INVESTIGATION INTO SYNTHESIS AND THE MICROSTRUCTURE OF SILVER NANOPARTICLES COATED WITH ALKANETHIOLS AND THIOL-FUNCTIONALIZED POLYMERS

FARHAD FAGHIHI

Ph.D., Amirkabir University of Technology, Iran, 2011

A Thesis

Submitted to the School of Graduate Studies

Of the University of Lethbridge

In Partial Fulfillment of the

Requirements for the Degree

Doctor of Philosophy

Chemistry and Biochemistry

University of Lethbridge

LETHBRIDGE, ALBERTA, CANADA

PREPARATION OF THESIS

FARHAD FAGHIHI

Date of Defense: May 20, 2015

Dr. P. Hazendonk Supervisor	Associate Professor	Ph.D.
Dr. M. Roussel Thesis Examination Committee Member	Professor	Ph.D.
Dr. P. Dibble Thesis Examination Committee Member	Associate Professor	Ph.D.
Dr. B. Seyed-Mahmoud Internal Examiner	Associate Professor	Ph.D.
Dr. E. Kemnitz External Examiner	Professor	Ph.D.
Dr. P. G. Hayes Chair, Thesis Examination Committee	Professor	Ph.D.

Dedication

To Sepideh and Adrina

Abstract

A comprehensive investigation into the synthesis and the characterization of discrete silver nanoparticles coated with alkanethiols and thiolate functionalized polymers is presented. Small and uniform alkanethiol capped silver nanoparticles were synthesized via the Brust and Schiffrin method. To improve the characteristics of the resulting nanoparticles, the intermediate stage of this reaction was investigated. The major precursor to the silver nanoparticles was identified and its microstructure was characterized.

Polymers bearing single or multiple thiolates were prepared by synthesis of well-defined precursors via RAFT polymerization and their subsequent post-polymerization modification. Nanoparticles stabilized with thiol-terminated PMMA were produced via a "grafting-to" process. A novel method was developed for the synthesis of small, uniform, and re-dispersible nanoparticles encapsulated with multiple-thiolate functional random copolymers of vinylbenzyl chloride. The effect of reaction conditions on the quality of these nanoparticles were evaluated. Adsorption of the copolymers on the nanoparticles were studied by ^{1}H NMR relaxation measurements.

Acknowledgments

I owe my deepest gratitude to Dr. Paul Hazendonk, my supervisor, for his guidance and support throughout the course of my graduate program.

I would like to thank my Ph.D. supervisory committee members, specifically Dr. Peter Dibble for his helpful discussion on the mechanisms of the reactions, and Dr. Marc Roussel for his comments on my thesis.

I am grateful to Mr. Tony Montina, the manager of Magnetic Resonance Facility at the University of Lethbridge, for his assistance with running NMR experiments.

I gratefully acknowledge the financial support provided by the University of Lethbridge, Alberta Innovates Technology Futures, and the Natural Sciences and Engineering Research Council of Canada.

Most importantly, I would like to express my special appreciation and thanks to my wife, Sepideh, for her love, support, patience, and encouragement.

Table of Contents

List of Tables

List of Figures

List of Schemes

Chapter 1. Introduction

The field of nanoparticles has been a rapidly developing area within the realm of nanotechnology, making these materials key components in a diverse range of scientific and technological disciplines. Nanoparticles are commonly defined as the particles with at least one dimension that is 100 nanometers or less in size. In general, the properties of materials are size dependent and change dramatically as their dimensions approach the nanoscales. Such a strong size dependence is dominated by two factors: substantial increase in surface area to volume ratio and quantum confinement effects. The ratio of surface area to volume of a particle increases markedly with reduction in its size, leading to a rapid growth in the percentage of surface atoms which experience different local environments compared to the bulk atoms. For example, a spherical cadmium sulfide nanoparticle with d=4 nm is composed of approximately 1500 atoms, approximately a third of which are located at the surface. This affects both the properties of an individual nanoparticle and its interactions with surrounding materials. Abundance of surface atoms is a critical factor in various applications of nanoparticles such as catalysis, and results in significantly enhanced interfacial interactions which have been widely exploited in fabrication of nanocomposites. Addition of 2 to 5 wt% nanoparticles has been shown to induce much larger improvement in the mechanical properties of a nanocomposite compared to the effect of 40 to 50 wt% of micron sized particles.

Quantum confinement is another key factor contributing to the size-dependent characteristics of nanoparticles that are sufficiently small compared to the wavelength of

the electron (1.23 nm for an electron with kinetic energy of 1 eV). These effects arise from confinement of electrons to a small regions of space, changing their energy levels and band gap and producing unusual properties relative to bulk materials. Blue shift in the light absorption of semiconductor nanoparticles as the result of reduction in their size and surface plasmon resonance of noble metal nanoparticles are examples of quantum size effects. Overall, the large increase in the proportion of surface atoms along with the emergence of the quantum confinement effects modify the electronic structure, physical (such as melting point), mechanical, optical, electrical, and magnetic properties of nanoscale particles, making them the materials of choice in a vast array of applications.

Organic-inorganic hybrid nanoparticles composed of a noble metal core and an organic shell have been intensively investigated due to their interesting properties that present a highly innovative platform for the development of novel nano-structured materials for photonics, electronics, energy, biochemical and medical applications[1-11]. The properties of these nanoparticles are strongly determined by the characteristics of the noble metal core, such as its size and shape, and the nature of the organic shell, which primarily serves to prevent aggregation of the metal nanocrystals. A diverse range of small-molecules and polymers with appropriate functional group(s) have been employed to stabilize the metal nanocrystals prepared by a variety of chemical reactions[7, 12-18]. Understanding the influence of reaction conditions on the characteristics of the metal core, synthesis of functional molecules that serve as their protective layer, as well as designing new preparative procedures are the major challenges in controlled manufacturing of the hybrid nanoparticles. These challenges are addressed in this thesis by detailed investigation into the synthesis of alkanethiol-capped silver nanoparticles, exploring various synthetic

strategies for preparation of thiol functionalized copolymers, and developing a novel and versatile method for production of polymer coated silver nanoparticles.

Amongst the numerous methods that have been explored for the synthesis of thiol-protected gold and silver nanoparticles, the two-phase synthesis proposed by Brust and Schiffrin[19] and its subsequent modifications[20] have been the predominant protocols for the preparation of these materials. Despite the success of the two-phase method in the synthesis of small and uniform gold nanoparticles, adaptation of this approach to silver has been hampered by the difficulty in obtaining pure product and poor solubility of the resulting nanoparticles. It is therefore of prime importance to identify and characterize the species formed during the two-phase synthesis of silver nanoparticles in order to improve yield, purity, and solubility of the product. To this end, a detailed investigation into the intermediate step of the two-phase method is presented in chapter 4. First, the fate of the reactants and the structural evolution of the intermediate compounds formed prior to the reduction step were closely monitored through comparison between samples obtained from various stages of the reaction using solution NMR and vibrational spectroscopies. This allows for the identification of intermediate species and further elucidation of the reaction mechanism. Next, the molecular dynamics and phase structure of the intermediate compounds were characterized in the solid state by examining a series of samples differing in reactant ratios. It was shown that the presence of various ionic species can be distinctly identified in the solid state through their influence on the microstructure of the complexes. Furthermore, the structure and dynamics of the alkanethiols grafted to the surface nanoparticles were studied by solid-state NMR.

Employing polymers as the protecting layer of the nanoparticles effectively stabilizes them against aggregation and expands their potential applications by providing access to the novel properties of the polymeric materials. Moreover the natural tendency of copolymers and polymer blends to form nanostructured morphologies can be exploited to control the ordering and spatial distribution of the nanoparticles. Analogous to the small-molecule capping agents, polymers effectively stabilize the nanoparticles if they contain functional groups that provide strong attractive interaction with the noble metal. Thiol functionalized polymers offer superior properties in stabilizing the silver nanocrystals owing to the high affinity of the thiol moiety to bond with silver. Synthesis of stable thiol-bearing polymers with well-defined physical and chemical microstructure is not straightforward and poses a major challenge in using these polymers in production of nanoparticles. This issue is addressed in chapter 5, where the results of reversible addition fragmentation chain transfer (RAFT) polymerization and their subsequent modification into thiol-bearing polymers are presented. First, controlled polymerization of methyl methacrylate and copolymers of vinylbenzyl chloride via RAFT process were studied and the resulting polymers were characterized. Then the post polymerization modification producing thiouronium (TU) functionalized copolymers and subsequent conversion of TU groups into thiolate moieties were described. This conversion was carried out through reaction of TU with either KOH or $NaBH_4$. The reaction with $NaBH_4$, which was found to be more facile and more flexible, was investigated in detail by monitoring the evolution of the copolymer functional groups during the reaction using NMR. Further insight into the mechanism of this post-polymerization modification process was obtained by investigation of the reaction between $NaBH_4$ and benzyl thiouronium, which is the small-molecule counterpart of TU-bearing vinylbenzyl repeating units.

In chapter 6, the synthetic strategies for preparation of silver nanoparticles stabilized with single-functional thiol-terminated PMMA and multi-functional random copolymers of VBC are discussed. Single-functional PMMA protected nanoparticles were synthesized by converting the dithioester residue of RAFT agents into thiol moiety via treatment with $NaBH_4$. Nanoparticles coated with copolymers bearing multiple thiolate groups were produced via a novel and versatile two-step method. Adsorption of copolymers on the surface of nanoparticles was verified by the changes in their dynamics (relative to the free copolymers), as was revealed by NMR relaxation times. The effect of reaction conditions on the average size, dispersity, and solubility of the nanoparticles prepared with this method were examined by conducting a series of experiments. The results of these experiments were explained by considering the influence of the reaction parameters on functionalization of the copolymers and formation of the silver nanocrystals. Moreover, the stability of the nanoparticles in solution and their re-dispersibility were evaluated by UV-visible spectroscopy and transmission electron microscopy.

In summary, the research presented in this thesis contributes to the better understanding of the underlying mechanism of the widely used two-phase method, leading to improvement in the quality of the resulting thiol-capped nanoparticles. Novel approaches are developed for synthesis of thiolate-functionalized copolymers and their subsequent application for production of small and relatively uniform silver nanoparticles. These methods can be generalized for a range of copolymer capping agents with diverse properties, thereby expand the applications of the resulting nanoparticles.

Chapter 2. Literature Review

2.1. Silver nanoparticles

The term "silver nanoparticle" widely refers to a range of nanosized structures of metallic silver such as spherical particles, nanoprisms, and nanowires. Although these materials are discoveries of the modern age, nanosilver has a long history of application. Documented examples of such applications dates back to over a thousand years ago, when the nanoparticles of silver were used to produce a deep yellow color in stained glasses and were incorporated into the coating of ceramic artifacts to give them an iridescent color. Moreover, fine particles of silver have long been known as an effective antibacterial agent being used to prevent and treat infections in the pre-antibiotic era.

Today silver is among the most commonly used metals in the field of nanotechnology due to its unique optical, electrical, medical, and biological characteristics. In the industrial sector, silver nanoparticles (SNP) have found their way into many public consumer products. Plastic, textile, fabric, coatings, health care, electronics, and cosmetics industries are currently utilizing these nanomaterials. SNP are widely incorporated into detergents, sanitizers and cleansers, personal health-care and cosmetic products, food storage containers, mold resistant coatings, a variety of fabrics including sportswear, underwear, sheets and mattress covers, and home appliances. Furthermore, the nanostructures made from silver have been the subject of extensive current research interest aiming at expanding their applications in modern fields of science and technology. A few examples of such applications include exploiting their surface plasmon resonance

absorption in fabrication of nanoscale sensors, surface enhanced Raman scattering, drug delivery vehicles, and light harvesting in solar cells, as well as using their superior electrical conductivity in production of transparent touch panels and conductive inks for printed circuit boards.

The majority of industrial, technological, and scientific applications of nanoparticles require them to maintain their nanometric size scale and remain as isolated particles. The extremely large surface area to volume ratio of metal nanoparticles results in their excessively high surface tension producing an intense energetic driving force for aggregation of adjacent particles into larger entities leading to loss of their desirable characteristics. It is therefore essential to disperse and fix these nanoparticles within a matrix material or passivate their surfaces by suitable organic stabilizing agents. A broad variety of ionic, molecular and macromolecular stabilizers containing proper functionalities (capable of establishing strong attractive interactions with silver) have been employed to form a protective layer on the metal surface. Such organic shells effectively prevent aggregation of the metallic cores and expand the potential applications of the resulting hybrid nanoparticle by providing access to the properties of the organic materials. The nature and the key characteristics of both the noble metal nanocrystal and the surface grafted layer are determined by the choice and details of the nanoparticle preparation method.

2.2. Preparation of silver nanoparticles

Numerous physical and chemical methods have been developed for the preparation of silver nanoparticles, having a wide variety of shapes, size distributions, and surface coatings. These methods can be broadly classified into the two major "top-down" and "bottom-up" categories. The top-down approaches involve production of SNP from the bulk materials via a range of physical and mechanical techniques such as milling, grinding, etching, laser ablation, vapor deposition, and photolithography. Amongst these methods, the mechanical techniques (e.g. milling and grinding) are significantly, simpler but suffer from lack of control over the shape and surface morphology of the nanoparticles. The more complicated laser ablation and lithographic procedures are capable of generating highly uniform ordered arrays of nanoparticles with great precision and reproducibility. These methods, however, require specialized equipment making them expensive for mass fabrication. Moreover, they are not suitable for production of surface coated hybrid nanoparticles.

The bottom-up approaches are based on chemical reactions to generate nanoparticles mainly from silver cation containing precursors. Compared to the more elaborate top-down methods (*e.g.* lithography), the chemical synthetic procedures are relatively simple and inexpensive for mass production. Moreover, they offer great potential for tuning the shape and size of the nanoparticles and tailoring their surface characteristics. Despite these advantages, a large number of the synthetic methods developed so far are not suitable for scale-up and industrial manufacturing of the nanoparticles. Another drawback of these techniques is the presence of residual chemicals, such as unreacted reagents and by-products, in the final product. Presence of these impurities, which might not be readily

removable, can hinder the application of chemically synthesized nanoparticles in medicines, catalysis, microelectronics and sensing devices.

The chemical synthesis of SNP generally involves reduction of the silver ions of a precursor compound into atomic species using chemical reagents or irradiation methods that provide free electrons. These silver atoms rapidly form growing metallic clusters, which are subsequently stabilized by surface active species known as capping agents. Based on this reaction scheme, the main reagents used in various bottom-up techniques are a silver salt precursor, a reducing agent, and a capping agent. The physical and chemical characteristics of the resulting nanoparticles are governed by many factors including the nature and concentration of the capping agents, the strength of the reducing agent, the polarity of the solvent, the reaction temperature, and the sequence and rate of feeding the reagents. Amongst all these parameters, the choice of the capping agent and its molar ratio to the silver salt have the most pronounced influence on the quality and properties of the noble metal nanoparticles. An efficient capping agent should be capable of establishing a strong interaction with the noble metal. The nature of bonding interactions can be physical (e.g. ionic interaction) as for ammonium bromide complexes or chemical (e.g. covalent bonding) as for alkanethiols.

Thiol-bearing molecules are commonly used as capping agents in the preparation of small and monodisperse silver and gold nanoparticles[12, 14, 19-21]. These surfactants firmly attach to the surface of the nanoparticle through the strong sulfur-metal bonding. The resulting protective shell formed around the metallic core effectively prevents their aggregation and provides long-term stability. Moreover, multi-functional thiol capping agent have been used to fine tune the surface characteristics of the nanoparticles for specific

purposes[22-23]. These features make thiol-bearing ligands very good candidates for adjusting the bulk and surface characteristics of noble metal nanoparticles for a range of applications. Examples of such applications include their usage as light harvesting elements to improve the conversion efficiency of photovoltaic devices[4-5, 24], in antimicrobial coatings that effectively inhibit the growth of *Escherichia coli* bacteria[11] and as additives in polymer nanocomposites for modification of their optical properties[25].

2.3. Alkanethiol-capped silver nanoparticles

2.3.1. Synthesis of alkanethiol-capped silver nanoparticles

Since its introduction in 1994, the two-phase synthesis proposed by Brust and Schiffrin[19] and its subsequent modifications[20], have been the predominant protocols for the preparation of alkanethiol passivated gold and silver nanoparticles. The conventional two phase method and most of its modifications involve two steps: 1) phase transfer and 2) reduction. In the first step, the noble metal ions, either monoatomic like Ag^+ or polyatomic like $[AuCl_4]^-$, are transferred from the aqueous phase to the organic solvent using a phase transfer catalyst, scheme 2.1-a. Tetraoctylammonium bromide (TOAB) is the most commonly used phase transfer catalyst for both gold and silver ions. Upon completion of the first step, the capping agent is added to the collected organic phase and this mixture is subsequently exposed to the aqueous solution of sodium borohydride to under vigorous stirring. During this step, the metal cations are reduced to atomic species, which rapidly aggregate into nanosized metallic clusters. The growth of these clusters is interrupted by surface adsorption of the capping agents leading to the formation of stable nanoparticles, scheme 2.1-b.

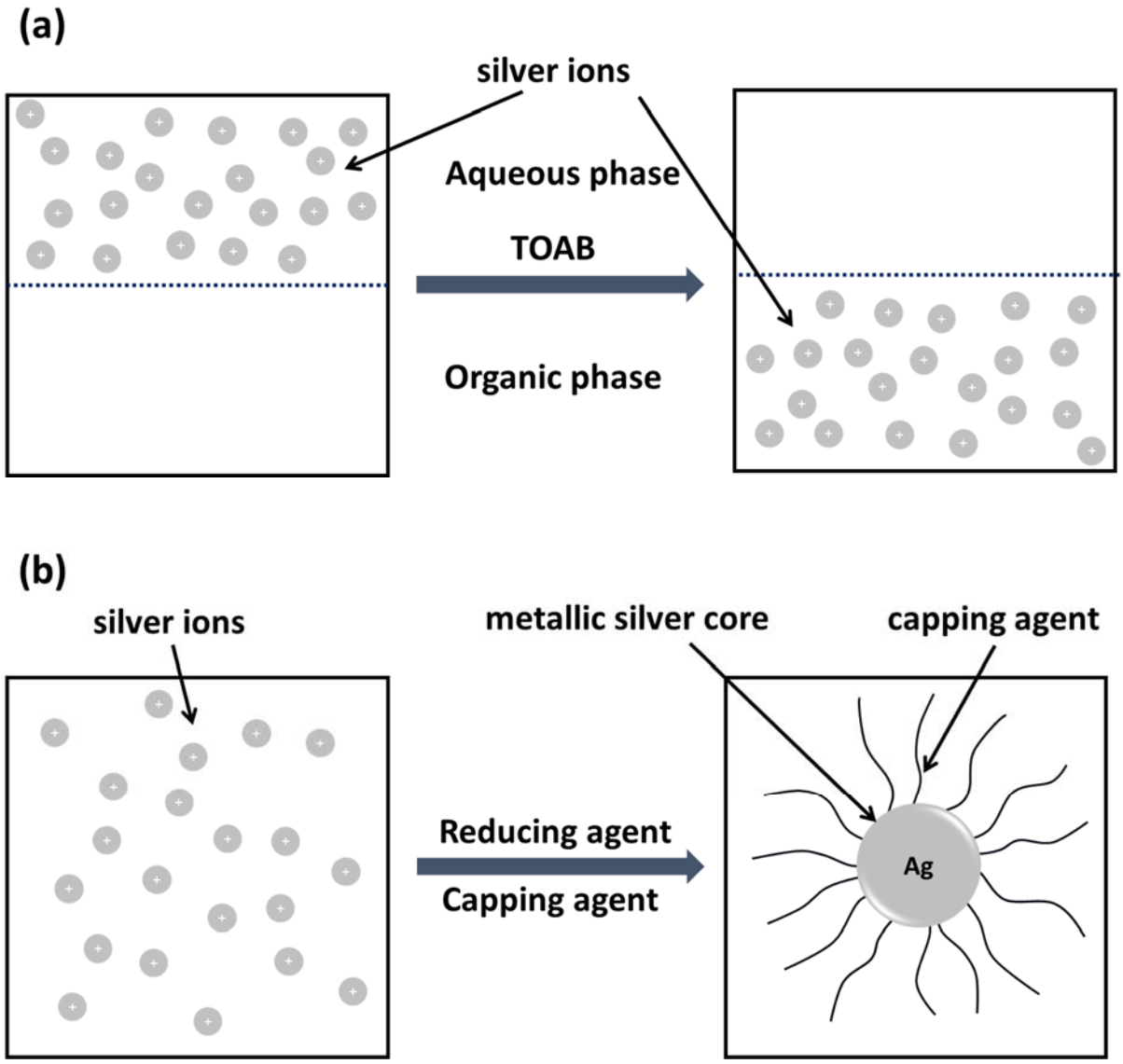

Scheme 2.1. Schematic representation of the two-phase method for synthesis of silver nanoparticles: (a) phase transfer step using tetraoctylammonium bromide (TOAB) and (b) Reduction step.

A major modification of the Brust and Schiffrin method has been developed where the whole reaction was performed in a single phase to eliminate the need for the phase transfer step[26]. The single phase methods rely upon using a solvent that dissolves both the capping agent and the silver salt. Such single phase approaches, however, can produce

significant amounts of by-products[27] and are not applicable for a large number of less polar thiol ligands which cannot be dissolved in a common solvent with silver salts. A successful example of the single phase procedure was developed by using dodecyl thiosulfate as the precursor of the capping agent and addition of ascorbic acid to the reaction mixture [14]. Alkyl thiosulfates, which convert into the corresponding alkyl thiolates upon coordination with silver, have improved solubility in polar solvents. The presence of ascorbic acid can in the reaction mixture prevents formation of Ag(I)-thiolate by-products.

The success of this approach in the preparation of small uniform nanoparticles has triggered interest in understanding its mechanism in more detail. Earlier studies into the mechanism of this reaction assumed that the polymer-like metal-alkanethiolate compounds are formed upon addition of the alkanethiol to the organic phase in the presence of the phase-transferred metal ions[28-29]. These polymer-like materials are subsequently reduced via $NaBH_4$ producing the alkanethiol-capped nanoparticles. Accordingly the following reaction mechanism was proposed for the synthesis of gold nanoparticles[29]:

$$AuCl_4^- \ (organic\ solvent) + RSH \ \rightarrow (-Au^ISR-)_n$$

$$(-Au^ISR-)_n + BH_4^- \rightarrow Au_x(SR)_y$$

Recent studies suggest that the tetraoctylammonium cation $[TOA]^+$ plays an important role in protecting the noble metal precursor during the intermediate stage of the reaction through complexation with the noble metal containing anion[27, 30]. Quantitative analysis of the ^1H NMR spectra of the phase-transferred solutions of the $AuCl_4^-$ ions with various amounts of dodecanethiol showed that adding two equivalents of the thiol changes the oxidation state of the gold ions and produces one equivalent of the $[TOA]^+[AuBr_2]^-$

complex and disulfides by-products[27]. The NMR signals of the $[TOA]^+[AuBr_2]^-$ complex did not change upon further increasing the concentration of dodecanethiol. The predominance of $[TOA]^+$-metal complexes as the precursor for the nanoparticles was further verified by Raman spectroscopy[30], where the gold-sulfur band, which is clearly evident for the Au(I)-thiolate compound, was not observed in the reaction mixture before reduction. Moreover, a significant shift in the peak position of the free water signal was observed in the ^1H NMR spectrum of the phase transferred $[AuCl_4]^-$. This shift was attributed to the encapsulation of water inside the inverse micelles formed in the phase transfer step. It was proposed that the nanoclusters of metal are initially formed inside these inverse micelles, temporarily protected by a shell of tetraoctylammonium ions. These ions are subsequently replaced by the alkanethiol molecules at later stages of the reaction.

Besides the knowledge of the chemical reactions involved in the synthesis of alkanethiol-capped silver nanoparticles, the knowledge of the mechanistic aspects of the nucleation and growth of silver nanoparticles is essential for designing a robust and scalable method for preparation of small, uniform, and stable nanoparticles. The alkanethiol passivated capped silver nanoparticles are formed via a two-step process in the presence of an excess amount of a strong reducing agent such as sodium borohydride[31-33]:

1- Nucleation: this step involves reduction of the silver cations into atomic species at an extremely rapid rate and subsequent emergence of the nuclei (primary particles) with the diameter of around 2nm[33].
2- Growth: larger particles are produced through aggregation of the nuclei. The growth is eventually ceased due to the surface adsorption of the capping agents.

According to the classical theory of nucleation, the primary particles form when the concentration of silver atoms (C) in the reaction medium increases above a certain threshold (C_0). Irreversible aggregation of the isolated atoms into crystalline nanoclusters (with diameter of D) results in drastic reduction of their concentration and generation of new surface with large excess energy (σ). The total change in free energy of the system associated with nucleation is therefore given by the sum of two contributions[31]:

$$\Delta G = -nk_BTln\left(\frac{C}{C_0}\right) + \pi D^2\sigma \qquad \text{Equation 1}$$

The rate of formation of primary particles ($\frac{dN_1}{dt}$), in a diffusion-controlled nucleation process, is accordingly described by the Fick's first law of diffusion:

$$\frac{dN_1}{dt} = k_rCexp\left(\frac{-\Delta G^*}{k_BT}\right); k_r = \frac{8k_BT}{3\eta_0} \qquad \text{Equation 2}$$

where ΔG^* is the free energy of nucleation and η_0 is the viscosity of the medium.

Under the commonly applied reaction conditions for synthesis of alkanethiol-silver nanoparticles, nucleation completes very rapidly. Upon completion of this step, the particles grow via aggregation of the naked nuclei, until the metal surface is passivated through interaction with the capping ligands. The disappearance rate of the primary particles is determined by their concentration (N_1), reaction temperature, and the interparticle interaction potential:

$$\frac{dN_1(t)}{dt} = -\frac{4k_BT}{3\eta_0R}\frac{N_1^2}{\int_{2R}^{\infty}\exp(\beta\Phi_T)r^{-2}dr} = -k_sN_1^2 \qquad \text{Equation 3}$$

where k_s is the binary aggregation rate constant. The influence of surface modification on the rate constant of this process is expressed as a contribution to Φ_T, which describes

particles interactions. For non-ionic surfactants such as alkanethiols, the stability of the nanoparticles is derived from self-assembly of the ligands on the surface of the growing particles, giving rise to steric repulsive interparticle interactions. Assuming that the establishment of this surface grafted layer is a diffusion limited process, the importance of the interparticle potential is conveniently represented by the stability ratio, W:

$$W = \frac{k_r}{k_s} = 2R \int_{2R}^{\infty} \exp(\beta \Phi_T)\, r^{-2} dr \qquad \text{Equation 4}$$

where k_r is the diffusion rate constant given in Equation 2 and r is interparticle distance. For $W \approx 1$ the particles are extremely unstable, implying that the attractive interaction (van der Waals forces) is the dominant term in the interparticle potential. In contrast, large values of W indicate the presence of strong interparticle repulsion and thus stable nanoparticles.

Based on the theoretical expressions describing the nucleation and growth processes, small and uniform nanoparticles can be obtained by lowering the number of nuclei to reduce the probability of their irreversible aggregation, decreasing the reaction temperature to slow down the rate of collision between particles, and increasing the concentration of surfactant to expedite establishment of a more densely packed stabilizing shell around the metallic core. These predictions were experimentally verified by systematic variation of the dodecanethiol/$AgNO_3$ and $NaBH_4$/$AgNO_3$ molar ratios in a series of reactions. It was observed that at low concentrations of dodecanethiol and the reducing agent, polydisperse, non-uniform nanoparticles with large average size were formed. In complete accordance with the theory, small and monodisperse spherical nanoparticles were produced at larger molar ratios where the surface coverage is complete. It was further shown that the ionic strength of the reaction medium does not affect the size

and uniformity of the particles, confirming the insignificant role of electrostatic interactions[31].

2.3.2. Characterization of the alkanethiol-capped silver nanoparticles

The intriguing applications of the thiolate-protected noble metal nanoparticles have prompted extensive investigation of their microstructure and properties. Various microscopy, spectroscopy, crystallography, calorimetry, and elemental analysis techniques have been employed to study the noble metal core, the organic shell, as well as the structure of the ordered arrays of nanoparticles. Transmission electron microscopy (TEM) has been so far the reference characterization technique that gives valuable information on individual nanoparticles and their aggregation state. A prominent feature of the thiol-capped noble metal nanoparticles shown by TEM, is their propensity to arrange into ordered, closed packed, two or three dimensional arrays[34-36]. Formation of such super-lattices is of great technological importance, specifically in photonic and electronic applications, as it provides access to the collective electronic and optical properties of the nanoparticles, while they maintain their individual size-dependent characteristics.

The self-organization of thiol protected nanoparticles is governed by several factors including attractive van der Waals forces between the neighboring particles, the interactions between the capping agents, and the entropic contribution. Additional contributions such as the external forces and the nanoparticle-substrate interaction should be considered when device manufacturing techniques like spin-coating are employed. The bonding state of nonanethiol grafted to the surface of silver nanoparticles was investigated by measuring the changes in in binding energies of the nonanethiol sulfur and the silver electrons using X-ray photoelectron spectroscopy (XPS)[34]. The binding energies in a

sample of passivated nanoparticles were found to be slightly larger than those of the neat nonanethiol and Ag^0. These energies were close to the values reported for silver sulfide, proving covalent bonding of sulfur to silver at the surface of the nanoparticle.

In an attempt to gain a fundamental understanding of the super-lattice formation, Korgel et al[35] studied various interactions effective in formation of 2D and 3D arrays of dodecanethiol-capped silver nanoparticles. The interparticle potential were calculated as a function of separation distance by factoring in two major interactions: the steric repulsion between the stabilizer shells and the van der Waals attraction between the metallic cores. The repulsive steric potential was estimated using the following expression:

$$E_{steric} \approx \frac{100\, R\delta_{SAM}^2}{(C-2R)\pi\delta_{thiol}^2} kTexp\left(\frac{-\pi(C-2R)}{\delta_{SAM}}\right) \qquad \text{Equation 5}$$

In this expression, C is the center-to-center distance, R is the particle radius, δ_{SAM} is the thickness of the absorbed layer, and δ_{thiol} is the diameter of the area occupied by the thiol which can be derived from the ligand surface coverage. The surface coverage was calculated from the surface area of the metallic core (TEM, particles were assumed to be spherical) and the weight fraction of the octadecanethiol shell (elemental analysis). The contribution of van der Waals forces to the interparticle potential was estimated using the Hamaker equation:

$$E_{VdW} = -\frac{A}{12}\left\{\frac{4R^2}{C^2-4R^2} + \frac{4R^2}{C^2} + 2\ln\left[\frac{C^2-4R^2}{C^2}\right]\right\} \qquad \text{Equation 6}$$

The Hamaker constant (A) was set to 1.95 eV for silver-silver attraction. The total interparticle potential curve has a weak minimum at C≈18 Å and increases sharply at smaller distances. This minimum is very close to the experimental average interparticle

distance (around 17 Å), determined from TEM and X-ray scattering. Interestingly the average separation is significantly smaller than the length of a fully extended octadecanethiol, suggesting that the alkane chains have some degree of conformational freedom and interdigitate with those grafted on the neighboring particles. Complementary information about the crystal structure and the actual shape of the individual nanoparticles and their ordering in the super-lattice was acquired through small angle X-ray scattering (SAXS) measurements. It was found that the silver core has a face-centered cubic unit cell which produces a nanocrystal with truncated icosahedral structure. This faceted shape of silver nanoparticles intensifies the interparticle attractive forces and facilitates their ordering. The influence of the nanocrystal structure on their interactions was evident in very dilute samples, in which the nanoparticles aggregated as dimers, trimers, or multimers. The results of TEM and SAXS experiments presented in this study confirmed that narrow size distribution of the nanoparticles and consistent surface coverage of the capping agent were crucial for formation of the super-lattice.

A complete understanding of the properties and behavior of alkanethiol-capped nanoparticles relies on characterization of the conformation, dynamics, and interactions of the capping ligands. FTIR spectroscopy is amongst the simplest experimental methods that provide basic information on the local molecular environment and conformation of the surface grafted alkanethiols. Restrictions of the vibrational motions of the bonds as well as changes in the relative population of the trans and gauche conformers have noticeable influence on the FTIR spectrum of the alkane chains. The extent of this effect depends on several factors such as the particle size and the surface density of the ligands. The effect of restricted motion was demonstrated by comparing FTIR spectra of free nonanethiols with

those adsorbed on silver nanoparticles (average diameter = 4.18 nm), where the latter does not contain several characteristic bands of the free thiol including the rocking modes of CH_2 and CH_3 moieties and C-S stretching vibration[34]. These changes, which were similarly observed for other capping agents, have been attributed to the limited mobility of the alkane chains confined in the 2-D array of the close packed particles.

Besides the disappearance of some IR bands, the variation of the wavenumber of several characteristic peaks has been commonly reported for the alkanethiol stabilized nanoparticles. The peak positions of the symmetric and asymmetric stretching vibrations of the methylene moieties are sensitive indicators of the ordering of the alkyl chains[26, 37]. Lower wave-numbers indicate larger population of *trans* conformation, implying higher degree of ordering within the alkyl chains. The sensitivity of these bands was exploited to determine the order-disorder transition of long chain alkanethiol (C>=14) capped gold nanoparticles[36]. The peak positions of the symmetric (initially at around 2850 cm^{-1}) and anti-symmetric (initially at around 2818 cm^{-1}) stretches shifted to larger wavenumbers by up to 6 cm^{-1} for the longest chain (C=18) upon increasing the temperature. This indicates the transition of the chains from the ordered (predominantly all-*trans* conformation) to the disordered (random sequences of *gauche* and *trans* conformations) state. The change is more prominent for the longer chains with larger population of *trans* bonds. These conclusion were corroborated with the results of DSC experiments.

A larger population of *trans* conformation within the grafted alkanethiols increases the probability of their close packing into ordered structures, which has a substantial effect on the solubility of the nanoparticles. Young et al. used FTIR spectroscopy to compare the ordering and packing of dodecanethiol chains adsorbed on silver nanoparticles prepared by

the two-phase and single phase methods[26]. Nanoparticles with comparable average size and size distribution were obtained from both methods. The CH_2 stretching vibration frequency of the single-phase sample was lower than that of the two-phase sample by 3 cm^{-1}, implying that the alkyl chains are more closely packed in the former. This was further confirmed by the appearance of well-resolved twisting-rocking and wagging modes in the 1150-1400 cm^{-1} region of the single-phase sample spectrum. It should be noted that the shifts in the asymmetric and symmetric methylene stretching modes of the thiol capping agents are generally smaller relative to those reported for self-assembled alkanethiol monolayers on the flat gold or silver surfaces. This has been attributed to the presence of a relatively larger fraction of the *gauche* defects in these ligands mainly due to their adsorption on a curved surface.

Complementary information on the bond motions of the surface grafted alkanethiols has been acquired using Raman spectroscopy. This technique can be specifically useful for characterization of the molecules on the surface of gold and silver nanoparticles as these metals can enhance the intensity of Raman signals through surface plasmon resonance. Such enhancement requires adjustment of the size and shape of the particles to match their plasmon resonance absorption with the frequency of the spectrometer laser. The surface enhanced Raman spectra of the alkanethiol molecules, absorbed on a gold substrate, contains two distinct peaks in the range of 600 to 750cm^{-1} pertaining to the stretching modes of the C-S bond adopting *trans* or *gauche* conformation, respectively[38]. The peak arising from the *trans* conformation is sharper and appears at higher wavenumbers. The time evolution of the octanethiol spectrum during its self-assembly on a gold surface revealed that sharper peaks emerged and intensified in the C-C region (900 to 1600 cm^{-1}) upon

progress of the self-assembly. Moreover, the $(C\text{-}S)_{trans}$ band appeared at a certain stage during the process, signifying the ordering of alkane molecules. The degree of ordering was shown to increase with increasing alkanethiols chain lengths[39].

Further insight into the various aspects of the hybrid noble metal nanoparticles such as the capping agent-metal bonding, the dynamics within the organic shell and the interparticle interactions has been provided via solution and solid state NMR spectroscopy. The adsorption of the alkanethiols on the rigid metal nanoparticles may results in significant variation of their NMR frequencies and line shapes in comparison to the free molecules. Several NMR studies on gold nanoparticles stabilized with alkanethiols of varying chain length has clearly shown that the frequency and width of both the ^{1}H and ^{13}C resonances of the CH_2 moieties changes with their position with respect to the gold-hydrocarbon interface[40]. The ^{13}C signals of the CH_2 groups become noticeably broader as they get closer to the nanoparticle surface, leading to the disappearance of the resonance of α, β, and in some cases γ carbons. However, the chemical shifts of the carbon nuclei located further from the surface remain mainly unchanged, indicating that the alkane chains extended into the solvent have a high degree of mobility. The peak positions and widths of these signals are also sensitive to the size of the nanoparticles. Dispersity in the size of the nanoparticle was shown to cause a distribution in carbon chemical shifts, thus resulting in heterogeneous broadening of the signals[40]. It was suggested that the discontinuity in the diamagnetic susceptibility at the gold-hydrocarbon interface and residual hetero-nuclear dipolar interactions in the alkanethiol monolayer are the major factors contributing to the observed line broadening. Such residual dipolar couplings are a direct consequence of the restricted reorientational motion of C-H bond vectors.

Solid-state NMR spectroscopy is a powerful tool for the characterization of dynamics of the surface-bond thiols, as well as their interactions with the metallic core of the nanoparticles. For the majority of thiol capping agents, ^{1}H solid-state NMR spectra do not provide much detail about their interactions and structures due to the overlap between the broad signals. ^{13}C solid-state NMR techniques, however, are not subject to this limitation as a result of the much wider chemical shift range of carbon. For tetradecanethiol ($C_{14}S$) capped gold nanoparticles, selective ^{13}C labelling of the α (C_1) and β (C_2) carbons was necessary to enhance the intensity and resolve these signals, which are otherwise not detectable due to extensive line broadening[41]. In the labelled $C_{14}S$/gold nanoparticles, C_1 and C_2 resonances were still broad and shifted to higher frequencies by 18 ppm and 12 ppm respectively relative to the free thiol peak positions. These changes in chemical shifts rule out the occurrence of weakly associated organo-sulfur species which may either be by-products of the synthesis, such as simple thiolates (RS^-Na^+ form) and alkyl disulfides, or air oxidation products, such as alkyl sulfonates. Moreover, the possibility of physical adsorption of the thiols on the metal surface was dismissed since the variation of C_1 and C_2 chemical shifts for the $C_{14}S$ thiolate salt (relative to the free thiol) are significantly smaller than those of the $C_{14}S$/gold colloids.

A possible origin of the observed changes in chemical shifts is the interaction between the near surface carbon nuclei and the conduction electrons of the metal particle, known as the Knight shift. Such interaction induces large variations in the NMR frequencies, specifically in metal clusters. The contribution of the Knight shift to the ^{13}C frequencies of the capping agents was ruled out[41] considering that: 1) the temperature dependence of longitudinal relaxations (T_1) of carbon signals do not exhibit Korringa

behaviour (linear relationship between T_1 and temperature), 2) similar changes were observed in chemical shifts of C_1 and C_2 of Au(I)-alkanethiolate $[Au(I)(SC_nH_{2n+1})]_n$ complexes in which the thiol is bonded to the ionic gold. It was therefore concluded that the changes in frequency of these carbon nuclei originated from the modification of their local electronic environment as a result of the gold-sulfur bonding. Moreover, an NMR hole burning experiment showed that the C_1 and C_2 peaks are heterogeneously broadened. This inhomogeneous broadening was attributed to the distribution of chemical shifts over a range of frequencies due to different chemisorption sites and non-spherical shapes of the nanoparticle. Thiolates adsorbed on different faces or the less symmetrical sites at edges of the nano-crystallites will exhibit different average chemical shifts. These NMR experiments, however, did not allow for a distinction between thiols grafted to nanoparticles and those forming complexes with ionic gold.

2.3.3. Stability and solubility of alkanethiol-capped nanoparticles

Long-term stability of the silver nanoparticles and their dispersibility as individual particles in compatible solvents or solid matrices are essential for their utilization in various applications. The colloidal stability of thiol-capped noble metal nanoparticles is provided by the tethered alkane chains through a steric stabilization mechanism. Their solubility is determined by the interactions of the capping ligands with the neighboring particles and the surrounding medium. The loss of stability is induced by two major processes: irreversible aggregation of the nanoparticles driven by their tendency to reduce the surface free energy and oxidation of the noble metal which is in the atomic state. It has been shown that the presence of a sufficiently dense layer of grafted alkanethiols can prevent or delay both of these processes.

Formation of the alkanethiol shell involves three steps: physical adsorption, sulfur-metal bonding, and rearrangement to establish the monolayer[42]. The adsorption process can be diffusion-limited or non-diffusion-limited based on the reaction conditions. The rate constant and activation energy of the thiol adsorption process was investigated through second harmonic generation (SHG) measurements[42]. The SHG light scattering from silver nanoparticles reduced with chemical adsorption of thiols due to the lower polarizability of the sulfur bonded silver atoms at the surface. This reduction was found to be proportional to the surface coverage of thiols, which allowed determination of the rate of the adsorption process. Quantitative correlation between the SHG intensity (I_{SHG}) and kinetics of thiol adsorption was derived starting from the Langmuir model:

$$T + ES \underset{k_d}{\overset{k_a}{\rightleftharpoons}} TS \qquad \text{Equation 7}$$

where T, ES, and TS denote the concentrations of thiol, vacant surface site, and occupied surface site, respectively. The rate constants of the adsorption and desorption processes are shown by k_a and k_d. The simple kinetic equations obtained from the Langmuir model combined with the empirical relation between I_{SHG} and the surface coverage[42] yielded the following expression describing dependence of the SHG intensity on the rate constants:

$$I_{SHG} = \left| b - q^* \left(1 - e^{-\frac{t}{\tau}}\right) e^{i\phi} \right|^2 \qquad \text{Equation 8}$$

in which b and q are fitting parameters, φ is a phase factor (measured in the experiment) and τ is the time constant which is related to k_a and k_d. Fitting this expression to the experimental data obtained at various temperatures gave the temperature dependence of the adsorption and desorption rate constants, from which their activation energy were

determined. This activation energy was attributed to the formation of the transition state during sulfur-silver bonding. It was suggested that under the commonly applied reaction conditions, diffusion and physical adsorption occur faster than the chemical bonding and the former is the rate-limiting step of the alkanethiol shell formation.

As shown by the NMR and FTIR studies[36-37, 40], the surface grafted alkanethiols have restricted mobility and tend to adopt an all-*trans* conformation, which facilitates interdigitation and ordered stacking of the capping ligands of the adjacent nanoparticles. These processes lead to the formation of strongly interacting three dimensional clusters of nanoparticles, which can drastically deter their solubility. The correlation between the solubility of the alkanethiol-capped silver nanoparticles and the enthalpy of the ligand disordering was studied through analysis of their thermal transitions[43]. DSC thermograms of these materials revealed a less intense transition at lower temperatures (around 65°C) for shorter alkane chains ($n<12$), and a higher temperature sharp reversible peak (around 130°C) which was attributed to the order-disorder transition of the capping ligands. Enthalpy of the order-disorder transition increased with the alkanethiol chain lengths. Odd-even effects were also observed for this transition, where the peak position shifted to higher temperatures for chains with an odd number of carbons (by around 10°C). The correlation between the solubility and the disordering enthalpy was verified by separation of the nanoparticles into soluble and insoluble fractions. The soluble particles had significantly lower disordering enthalpy. Based on these findings, the solubility was enhanced by coating the particles with a mixture of ligands with different chain lengths. The poly-functionalized particles had a single transition with lower enthalpy due to the disrupted ordering of the capping agents.

Besides the interdigitation of the capping ligands, the attractive interactions between the metallic cores of clustered nanoparticles provide a strong driving force for their irreversible aggregation and complete loss of solubility. The strength of these interactions directly correlates with the size of the particles and the interparticle distance. It was, for instance, shown that[15] the attraction potential between the cores of the neighboring particles increased from $0.6\times k_BT$ to $5\times k_BT$ when the length of capping ligand is reduced from octanethiol (n=8) to hexadecanethiol (n=16). The irreversible aggregation become more probable by desorption of the thiols from the surface of the dissolved nanoparticles to establish a dynamic equilibrium between adsorbed and free molecules. Desorption is more prominent in dilute solutions and polar solvents that are used to wash the nanoparticles. It is therefore recommended to avoid extensive washing of the nanoparticles and storing them in a solution containing added free thiols. Alternative approaches such as employing thiol capping agents with bulky groups that disturb their interdigitation[21] or crosslinking the organic protective shell[44] were exploited to enhance the solubility of nanoparticles.

Another major factor affecting the stability of the silver nanoparticles is their oxidative degradation. Atomic silver is known to be highly reactive towards atmospheric oxygen. The thiolate ligands are capable of slowing down this process. This was confirmed by the compositional analysis of the alkanethiol protected silver nanoparticles using X-ray photoelectron spectroscopy, which did not reveal presence of oxygen immediately after their preparation. Presence of oxygen can, however, indirectly trigger the oxidative degradation process. Alkanethiol-capped silver nanoparticles were reported to be stable under a nitrogen atmosphere while they underwent noticeable degradation after exposure

to air for 24 hours[45]. A large fraction of the initially ordered nanoparticles were fragmented into smaller particles, the number of which increased substantially after four days. This degradation process was drastically accelerated in a humid atmosphere and in the presence of excess free alkanethiols. The excess thiols, which are commonly added in a conventional preparation and are not efficiently removed by the work-up, were trapped in the surface grafted monolayers upon evaporation of the solvent. Considering the role of humidity and free thiols, the following set of reactions were proposed to be responsible for the degradation of silver nanoparticles:

$$\frac{1}{2}O_2 + 2H^+ + 2e^- \rightarrow H_2O$$

$$Ag \rightarrow Ag^+ + e^-$$

$$RSH + H_2O \rightarrow RS^- + H_3O^+$$

$$RSH + Ag^+ \rightarrow RSAg + H^+$$

The first reaction, which relies on the presence of water, is driven by the lower reduction potential of silver compared to that of O_2. The contribution of free alkanethiols to the corrosion process is through supplying H^+ according to the last two reactions. Unlike silver, gold nanoparticles have substantially higher stability due to the larger reduction potential of Au. Lower stability of silver nanoparticles compared to gold has been also reported elsewhere[46]. Moreover the silver nanoparticles are generally less soluble compared to their gold counterparts.

2.3.4. Ligand exchange on noble metal nanoparticles

The primary role of capping agents is providing stability for nanoparticles by preventing the aggregation of the noble metal nanocrystals. Furthermore, these organic molecules have a profound effect on surface related properties of the nanoparticles such as their solubility, compatibility with other materials, as well as their chemical reactivity. In most cases, the surface grafted capping ligands undergo a dynamic adsorption-desorption process, which increases the probability of nanoparticle aggregation, Figure 2.1. This problem is more prominent for ligands that are weakly bonded to the metal surface[47]. The stability of nanoparticles can be improved by exchanging such ligands with another surfactant capable of forming stronger bonds[48-50]. Alternatively, exchanging the capping agents with new multi-functional ligands, which may cause complications in the synthesis of the particles, allows for tailoring the surface characteristics and interfacial interactions of the resulting nanomaterials[23].

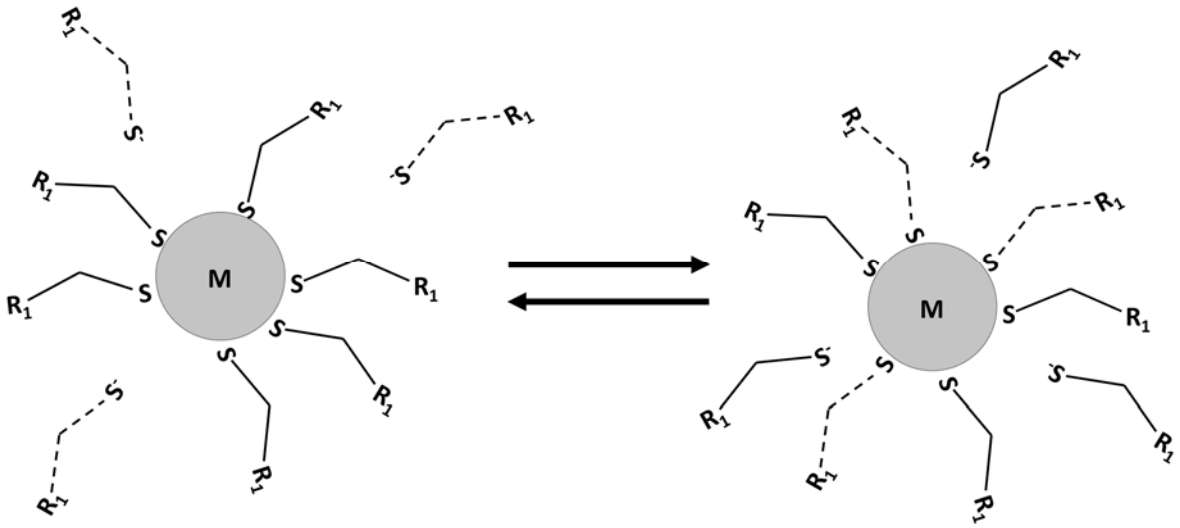

Figure 2.1. Schematic representation of the adsorption-desorption process of thiolate ligands. Dashed lines indicate the initially free ligands.

The ligand exchange reaction simply involves mixing of the new capping agent with the protected nanoparticles which leads to the replacement of the bound ligands by the incoming ligands, Figure 2.2. Similarly to the metal complexes, the ligand exchange process on nanoparticles can occur through associative, dissociative and interchange mechanisms[48]. The associative mechanism involves formation of an intermediate in which both the outgoing and the incoming ligands are attached to the nanoparticle; while in the dissociative pathway the outgoing ligand desorbs from the surface before binding of the incoming one. The interchange mechanism is a combination of the abovementioned processes. Despite some similarities, the ligand exchange on noble metal nanoparticles is more complicated than metal complexes due to the complexity of the electronic structure of nanoparticles, steric crowding at their surface, and dissimilarity of their surface sites.

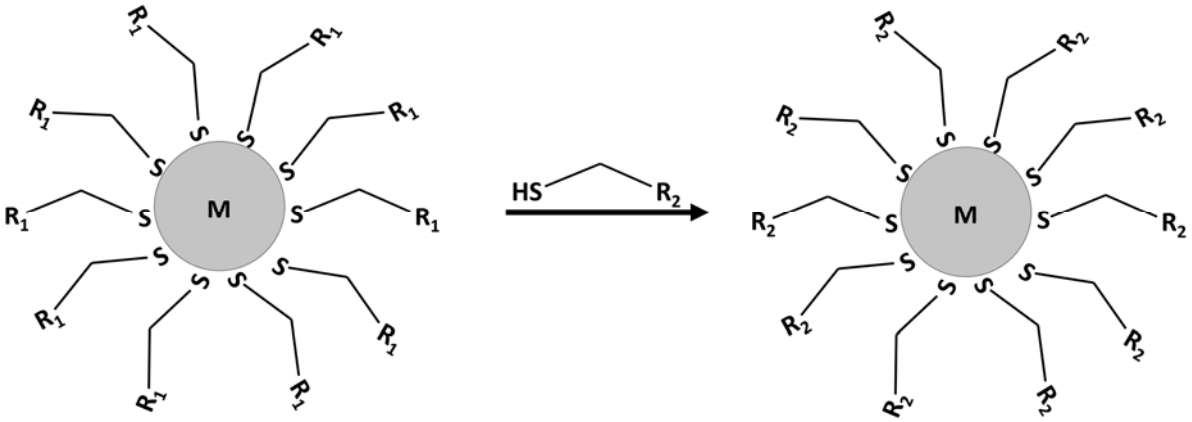

Figure 2.2. Schematic representation of ligand exchange reaction.

It was suggested that the rate of ligand exchange on the gold nanocrystal surface is faster at terrace edges and vertex sites (surface defects) and is slower at near-edge and interior terrace sites[51]. These differences in reactivity of the surface sites were associated with their electron densities and accessibility[52]. A comparison between several place-

exchange experiments, where gold nanoparticles capped with various alkanethiols were reacted with aromatic thiols, indicated that the rate of the process decreases as the alkanethiol chain length and the size of the aromatic ligand increase[51]. Investigation of the rate of exchange of ligands adsorbed on metal cores with different sizes showed that the reaction is relatively faster for smaller nanoparticles due to their larger surface curvature[53]. Application of the ligand exchange process for tuning the surface properties of noble metal nanoparticles was shown by employing this approach for synthesis of gold nanoparticles covered with mixed ω-functionalized alkanethiol ligands[23]. A self-assembled monolayer (SAM) of alkanethiols on the surface of a gold nanoparticle was replaced with a 3D-SAM of mixed ω-functionalized alkanethiols. The resulting nanoparticles exhibited catalytic activity owing to the presence of multiple functionalities on their surfaces.

2.4. Polymer-capped noble metal nanoparticles

Polymer coated noble metal nanoparticles have been the subject of recent research interest due to their unique optical, electronic and biological characteristics[7, 16-18, 54-56]. Employing polymers as the protecting layer of the nanoparticles effectively stabilizes them against aggregation and expands their potential applications by providing access to the novel properties of the polymeric materials. Moreover the natural tendency of copolymers and polymer blends to form nanostructured morphologies can be exploited to control the ordering and spatial distribution of the nanoparticles[57-59]. Polymer stabilized silver and gold nanoparticles have been mainly prepared either by growing the polymer from the surface of pre-made nanoparticles in "grafting-from" processes, or by using functional polymers as the capping agents during the synthesis of nanoparticles in "grafting-to" methods. In the

grafting-from approach, the nanoparticle surface is treated with chemical groups which are capable of initiating the polymerization reaction. Macromolecules are subsequently grown from these initiator sites upon exposing the nanoparticles to the monomer(s) under the proper reaction condition. The major drawback of this method is the difficulty of controlling the characteristics (such as molecular weight, polydispersity and configuration) of the surface-initiated polymer chains. This problem can be resolved by using the "grafting-to" methods in which pre-formed polymer chains with well-defined properties are directly adsorbed to the surface of the growing metal nanocrystals during their synthesis. The macromolecular nature of the capping agent, however, poses major challenges for achieving precise control over the size and dispersity of the nanoparticles.

The polymeric capping agents used in grafting-to methods should contain proper functional groups, capable of establishing a strong attractive interaction with the noble metal. A few examples of such functional polymers include thiolated poly(ethylene glycol)[16] and poly(methyl methacrylate)[7], poly(N-vinylpyrrolidone)[17, 55-56] (PVP), and poly(N-isopropylacrylamide)[18]. Water soluble gold and silver nanoparticles protected by poly(N-vinylpyrrolidone) (PVP) have been successfully synthesized through several different synthetic approaches. Huang and coworkers[56] prepared silver nanoparticles in aqueous medium using UV irradiation to reduce the silver ions in the presence of PVP. The average size and polydispersity of the colloidal particles were sensitive to the concentration of PVP, generally getting smaller up to a certain limit upon increasing concentration of the surfactant. The nature of the polymer-particle interactions was investigated through comparison between the binding energies of the pure and surface grafted PVP, determined by X-ray photoelectron spectroscopy. It was suggested that PVP is adsorbed on the

nanoparticle via the attractive interaction between silver and the oxygen atom of the pyrrolidone functionality. Alternatively, PVP stabilized nanoparticles have been produced by employing ethylene glycol as the reducing agent in a synthetic procedure known as the "polyol process". In this method, the silver salt and PVP are dissolved in ethylene glycol which acts as both the reaction solvent and the reducing agent. The reaction is performed at high temperatures (around 120°C) due to the slow reduction rate at room temperature. Systematic investigation of the influence of $AgNO_3$ and PVP concentrations on the average diameter and polydispersity revealed that PVP can effectively prevent sintering of the nanoparticles, however narrow size distributions were only obtained at an optimum PVP concentration. The quality (size, polydispersity and shape) of the nanoparticles prepared by this method is highly sensitive to the ratio and concentration of the reactants and the reaction conditions. This is partly due to the multiple roles of PVP which can function as reducing agent, besides its main role as the stabilizer[55].

Thiol functionalized polymers are another class of macromolecular surfactants that offer superior properties in stabilizing the noble metal nanoparticles. The thiol moiety is capable of establishing strong attractive interactions with the noble metals, allowing for firm grafting of the polymer chains to the nanoparticles. These polymers can contain a single thiol as a terminal group (located at the chain end) or bear multiple thiols as side groups along their backbone. A comprehensive review of the literature shows that the thiol-terminated polymers have been used predominantly, mainly due to the difficulties associated with synthesis of stable, well-defined polymer with multiple thiol functionalities. Several polymerization techniques including anionic polymerization and reversible addition fragmentation chain transfer (RAFT) polymerization provide easy

access to a terminal thiol group[60-69]. Niskanen et al[7] used RAFT polymerized n-butyl acrylate-methyl methacrylate random copolymer and its block copolymer containing a hydrophilic poly(acrylic acid) (PAA) block as the capping agent for synthesis of silver nanoparticles. The residue of the dithiobenzoate chain transfer agent at the chain end of these polymers was converted into a thiol functionality simultaneously with the reduction of silver cations. Several samples were prepared using various copolymers in which the terminal thiol was attached to either a hydrophobic or a hydrophilic repeating unit. Smaller and more uniform silver nanoparticles were produced using the block copolymer with thiol group attached to the PAA block. This was attributed to the lower molecular weight of this polymer and to the presence of a hydrophilic PAA segment.

Corbierre and coworkers[54] synthesized polystyrene (PS) and poly(ethylene glycol) (PEG) stabilized gold nanoparticles via the grafting-to method and studied their dispersion in polymer matrices with identical chemical compositions. Thiol terminated PS with various molecular weights were prepared by living anionic polymerization and used as the capping agent during the reduction of $HAuCl_4$ with triethylborohydride. The physical characteristics and surface properties of the nanoparticles were found to be strongly dependent on the molecular weight of the polymer. Smaller nanoparticles with more uniform size distribution were obtained using PS surfactant with lower molecular weight. Moreover, the surface grafting density of the polymer chains, determined from thermogravimetric analysis and TEM images (the gold cores were considered to be truncated octahedral), decreased drastically for longer polymer chains. Grafting density of the polymer ligands was suggested to be a key factor influencing their state of dispersion in polymer matrices that have identical chemical structure, but differ in molecular weight.

Nanoparticles protected with longer chains, which have lower ligand grafting density, showed complete dispersion within high molecular weight matrices. Partial aggregation was, however, observed for nanoparticles passivated by shorter chains due to the higher surface density of their ligands. This was attributed to the incomplete wetting of the densely packed surface grafted brushes by the higher molecular weight matrix polymer chains. An important conclusion of this work is that the faceted surface of the noble metal core has an important influence on the adsorption, grafting density and packing of the capping ligands. Adsorption of the polymer chains on the flat facets of the metal core is significantly different from the hypothetical smooth spherical surface. An example of such a difference is the presence of low density regions at the edges of the faceted morphology, while the grafting is essentially uniform on a spherical particle.

Besides the grafting methods, polymer stabilized noble metal nanoparticles can be alternatively produced within a polymeric matrix via in-situ synthetic procedures. The in-situ synthesis commonly involves swelling of the polymer, or a specific domain within the polymer matrix, with a solution of the metal salt precursor. Selective swelling is achieved by employing a solvent that preferentially interacts with the target domain. The metal salt is subsequently converted into nanoparticles by exposing the impregnated (loaded) polymer to a reducing agent. This approach is specifically useful for direct incorporation of the nanoparticles within the desired domain of block copolymers or multi-phase polymer blends[57-59, 70]. The phase morphology of such polymer matrices can serve as a template for arrangement of the nanoparticles. Moreover, the in-situ synthesis eliminates the need for subsequent dispersion of the nanoparticles, providing direct access to polymer-noble metal nanocomposites. In spite of these advantages, this approach suffers from major drawbacks

including lack of sufficient control over the size and uniformity of the nanoparticles, as well as presence of residual reactants and byproducts in the polymer matrix.

In-situ synthesis of noble metal nanoparticles in a copolymer matrix gives direct access to a nanocomposite with controlled nanoscale morphology. Precise ordering of the nanoparticles within the polymer matrix is a major challenge in production of nanocomposites for advanced technological applications. Exploiting the intrinsic tendency of block copolymers to form nanostructured phase morphology has been considered as a promising alternative to top-down nanoparticle ordering techniques such as nano-lithography. Block copolymers are composed of two or more covalently bound long sequences (blocks) of different monomers. They are classified based on the number and arrangement of their blocks. For example, block copolymers with two, three, and more than three blocks are respectively called diblock, triblock, and multiblock copolymers. From the thermodynamics point of view, the miscibility between blocks of the copolymer is determined by the change in the entropy and enthalpy of the system upon mixing. The entropy of mixing is conventionally separated into combinatorial and non-combinatorial contributions:

$$\Delta S_{mix} = \Delta S_{combinatorial} + \Delta S_{non-combinatorial} \qquad \text{Equation 9}$$

For a linear A-B diblock copolymers (A and B represent the comonomers composing each block), the combinatorial contribution term is given by:

$$\Delta S_{combinatorial} = kT\left[\frac{\varphi_A}{N_A}\ln(\varphi_A) + \frac{\varphi_B}{N_B}\ln(\varphi_B)\right] \qquad \text{Equation 10}$$

where $\varphi_A, \varphi_B, N_A,$ and N_B are the volume fractions and the degree of polymerization of A and B blocks. In the classic treatment, the enthalpy of mixing is considered proportional to the exchange interaction energy:

$$\Delta H_{mix} \propto \left[\epsilon_{AB} - \frac{\epsilon_{AA}+\epsilon_{BB}}{2}\right]/kT \qquad \text{Equation 11}$$

In the above equation ϵ_{ij} is the segmental attractive (<0) nearest-neighbour van der Waals interaction energy between segments *i* and *j*. The enthalpic and the non-combinatorial entropic contributions to the free energy of mixing are represented by the interaction parameter, χ:

$$\chi \propto \Delta H_{mix} + T\Delta S_{non-combinatorial} \qquad \text{Equation 12}$$

Using this parameter and treating the blocks as homopolymers of A and B, the free energy of mixing is given by:

$$\Delta G_{mix}/kT = \frac{\varphi_A}{N_A}\ln(\varphi_A) + \frac{\varphi_B}{N_B}\ln(\varphi_B) + \varphi_A\varphi_A\chi_{AB} \qquad \text{Equation 13}$$

Considering the fact that N_A and N_B are large numbers, the favourable contribution of combinatorial entropy to miscibility is rather negligible and miscibility requires negative or small positive interaction parameter that can originate from specific A-B segmental interactions, among other factors. Consequently most polymer pairs are immiscible and phase separate upon mixing due to lack of significant entropic gain and specific interactions.

Unlike homopolymer blends, the thermodynamically driven phase separation in an immiscible block copolymer is limited by the fact that the blocks in each chain are

covalently attached together. The block copolymers are therefore separated into periodic domains with characteristic size close to the size of the corresponding blocks. The final morphology of a block copolymer depends on the actual value of interaction parameter (χ), the length of blocks, the volume fraction of each component, and the surface properties of the substrate if the copolymer phase-separate on a surface. For example in a symmetric A-B diblock copolymer, a layered morphology is dominant when the volume fractions of the blocks are close to equal. A variety of morphologies were observed as the relative volume fractions of components change, Figure 2.3[71]. The size, shape and spacing of the ordered nano-domains in block copolymers are adjustable through changing the relative lengths of the blocks, their volume fractions, and tuning their interactions. Block copolymers are therefore suitable materials for ordering nanoparticles into 1-D, 2-D, or 3-D arrays.

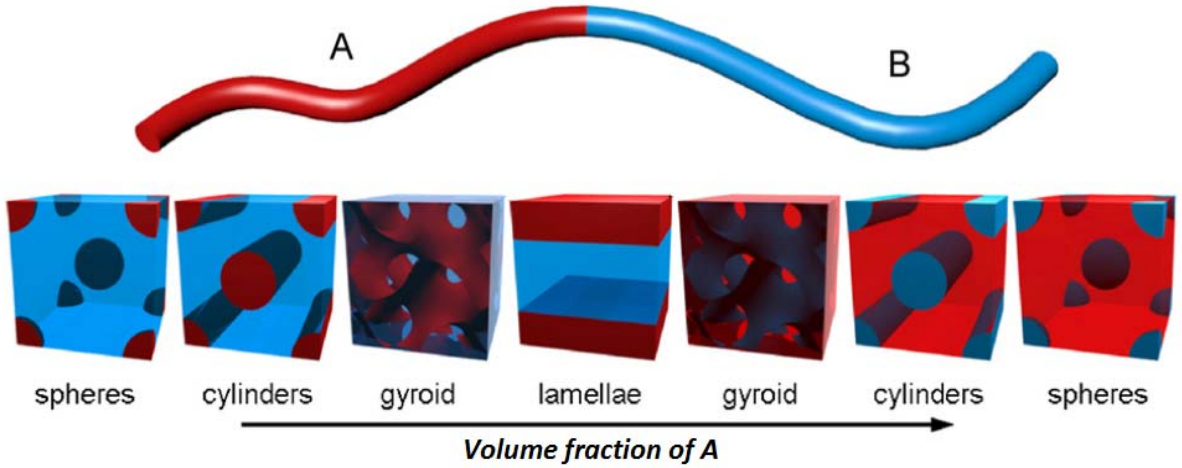

Figure 2.3. Schematic representation of various morphologies of a diblock copolymer as a function of the volume fraction of block A [From Ref. 63 with permission from The Royal Society of Chemistry].

Numerous examples of successful application of in-situ synthesis and ordering of nanoparticles within block copolymers have been reported[72-74]. Silver nanoparticles arranged in two-dimensional hexagonal patterns were synthesized via selective swelling of the hydrophilic domains of polystyrene-block-poly(acrylic acid) with silver salt[72]. The composition of the copolymer was adjusted to produce a continuous matrix of polystyrene blocks and isolated spherical domains of poly(acrylic acid) blocks, into which the silver nanoparticles were incorporated, Figure 2.4. A multilayered nanocomposite composed of alternating lamellae of polystyrene (PS) and gold-nanoparticle loaded poly(4-vinylpyridine) (P4VP), was produced by exploiting surface-directed phase separation of polystyrene-block-poly(4-vinylpyridine) (PS-b-P4VP) copolymer[73-74]. The lamellar morphology was achieved by depositing symmetric polystyrene-block-poly(4-vinylpyridine) (PS-b-P4VP) on silicon wafers or mica substrates and annealing the resulting thin film. Gold nanoparticles were incorporated by first immersing the polymer film into hydrogen tetrachloroaurate solution and then into sodium borohydride solution. TEM micrographs of the resulting nanocomposite film revealed that the gold nanoparticles were selectively positioned within the P4VP layers due to the favorable interaction of the pyridine moiety with the gold surface.

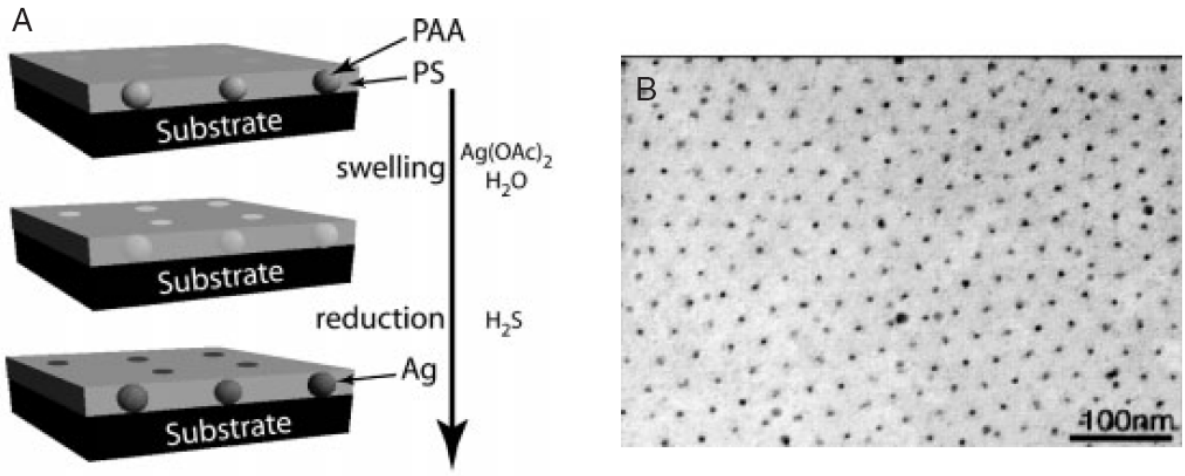

Figure 2.4. (A) Selective swelling of spherical poly(acrylic acid) (PAA) domains with silver salt solution and its subsequent reduction. (B) Transmission electron micrograph of the hexagonally arranged nanoparticles [From Advanced Materials, Vol. 17, 1331-1349 (2005). Reprinted by permission of John Wiley & Sons, Inc.].

In all of the abovementioned strategies (grafting to, grafting from, and in-situ methods), the characteristics of the polymeric component are crucial factors in production of nanoparticles with desired properties. Average molecular weight, polydispersity index, configuration, and the number and positions of active functional groups of the polymer have pronounced impacts on the size and uniformity of the nanoparticles as well as morphology of their nanocomposites. It is therefore of prime importance to employ polymerization and post-polymerization modification methods that yield tailored functionalized polymers.

2.5. Controlled synthesis of polymeric capping agents

Synthesis of homopolymers and copolymers with well-defined chemical and physical microstructure and narrow molecular weight distribution has been of great interest in polymer chemistry. Living polymerization techniques including ionic, coordination, and ring-opening polymerizations have been long known as the primary methods of choice for controlling the composition, architecture and molecular weight distribution of the polymer chains[75]. Despite their widespread application, the majority of these techniques require stringent reaction conditions as they are highly sensitive to the impurities and also they are not suitable for some functional monomers. More recently, a number of controlled radical polymerization (CRP) processes have emerged as alternative approaches for the synthesis of pseudo-living low-polydispersity polymers[76-77]. The major advantage of CRP processes such as atom-transfer radical polymerization (ATRP)[78], nitroxide mediated polymerization (NMP)[79] and reversible addition-fragmentation chain transfer polymerization (RAFT)[80] over the ionic processes is their high tolerance to the impurities and various unprotected functional groups. Such benefits offer a promising perspective for industrial application of the CRP techniques for production of well-defined polymers.

2.5.1. RAFT Polymerization

Reversible addition-fragmentation chain transfer (RAFT) polymerization, first introduced in 1995 by Moad and coworkers[81], has the benefits of being easily applicable to a wide range of monomers under a broad range of mild experimental conditions in bulk, solution (a range of non-polar to polar solvents), emulsion, and suspension. The RAFT process can be readily implemented by addition of an efficient chain transfer agent (CTA, also known as RAFT agent) into a conventional free radical polymerization reaction. The

success of this technique relies on the ability of the CTA to reversibly deactivate the major fraction of growing chains in the reaction mixture and ensure their uniform growth. Scheme 2 shows the general structure of a RAFT agent. In this structure, the R group must be a good leaving radical compared to the growing polymer chain and should readily react with the monomer to initiate a new chain. The Z group is responsible for providing sufficient stability to the intermediate radical formed during the addition-fragmentation step. Such stability is a prerequisite for formation of the radical intermediate, and therefore enhances the reactivity of the S=C bond toward radical addition. It should, however, be finely tuned, to allow the fragmentation reaction to occur at a reasonable rate and not impede the chain growth. Numerous RAFT agents have been developed so far containing various R and Z groups that meet the above criteria. These transfer agents have been classified based on the nature of the Z group, Scheme 2.2.

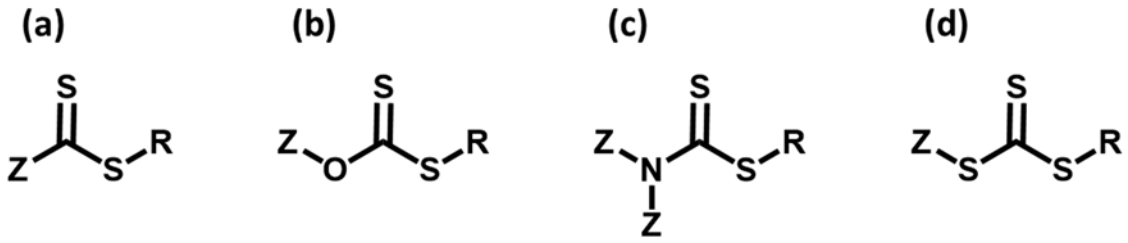

Scheme 2.2. General structure of various classes of common chain transfer agents employed in RAFT polymerization: (a) dithioester, (b) xanthates, (c) dithiocarbamates, and (d) trithiocarbonates.

The mechanism of the RFAT polymerization can be divided into three main steps of initiation, addition-fragmentation, and termination, Scheme 2.3. The key step in the RAFT process that differentiates it from conventional free radical polymerization is the

addition-fragmentation step. The following mechanism has been proposed for the RAFT reaction[82-83]:

1. *Reversible chain transfer*: The active end of a propagating chain reacts with the double bond of the chain transfer agent and forms an unstable intermediate compound, which stabilizes upon homolytic dissociation of the C-R bond. This process produces a temporarily deactivated chain (dormant species) and a free radical ($\dot{R}$). The rate coefficient for addition of the growing chain to the thiocarbonyl group of CTA is determined by the ability of the Z substituent to stabilize the intermediate. This step, where the RAFT agent is converted into a polymeric species, is also called the pre-equilibrium.
2. *Reinitiation*: The free radical released in the fragmentation step attacks a monomer to initiates a new chain.
3. *Chain equilibration*: Similar to the chain transfer step, a growing chain can react with the thiocarbonyl group of a dormant species, releasing the previously deactivated chain as an active macro-radical. This equilibrium process repeatedly turns each propagating chain on (active) and off (dormant). This step is also known as the main equilibrium.

The entire addition-fragmentation process significantly reduces the population of macro-radicals in the reaction medium to keep the termination rate negligible, giving rise to the living characteristic of the RAFT polymerization. More importantly it ensures uniform growth of all chains.

Initiation

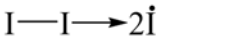

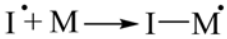

Propagation

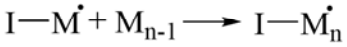

Re-initiation

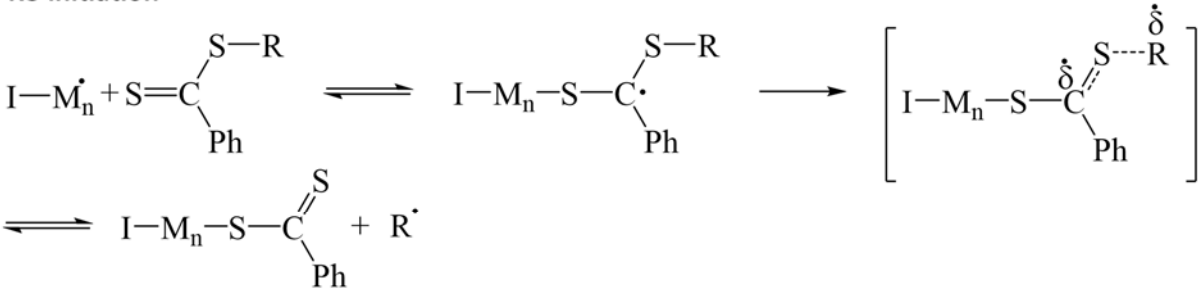

Chain equilibration

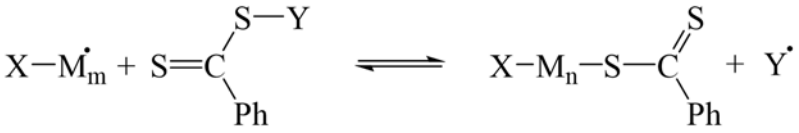

Termination

Scheme 2.3. Schematic representation of various steps of RAFT polymerization. In the chain equilibrium step, X is either I or R and Y can be either R or a dormant chain.

RAFT polymerization exhibits distinct kinetic features compared to conventional polymerization. The presence of the RAFT agent mostly brings about an inhibition period and rate retardation. This inhibition period, during which the polymerization is extremely slow, is essentially the time required to establish the pre-equilibrium[84], Figure 2.5.

Moreover the addition-fragmentation step reduces the overall rate of polymerization. In extreme cases, an incorrect choice of CTA can completely halt the reaction. The inhibition and rate retardation are caused by increased stability of the intermediate radical and inability of the leaving group to reinitiate the polymerization. These phenomena are mitigated by employing a suitable CTA that fragments rapidly and produces an efficient leaving radical group. For propagating radicals with lower reactivity (derived from reactive monomers such as styrene or MMA), a C=S bond with higher reactivity is required to ensure an acceptable propagation rate.

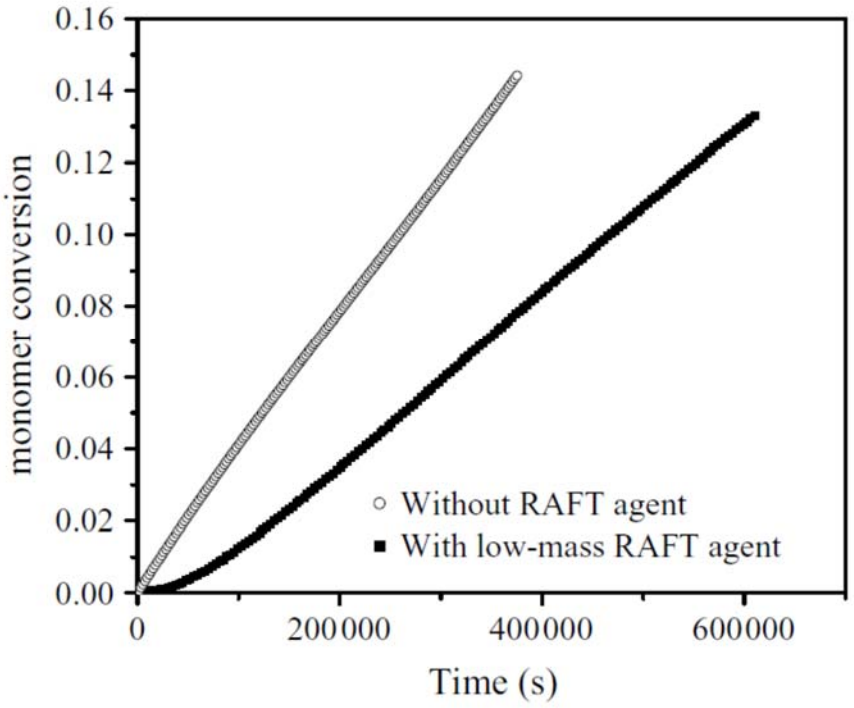

Figure 2.5. Time dependence of the monomer conversion in the bulk polymerization of styrene without (○) and with (■) small-molecule RAFT agent [From Handbook of RAFT polymerization, Chapter 3[84]. Reprinted by permission of John Wiley & Sons, Inc.].

The average degree of polymerization at any time during the reaction is equal to the number of consumed monomers divided by the total number of chains:

$$X_n = \frac{[M]_0 - [M]_t}{[T]_0 + df([I]_0 - [I]_t)} \quad \text{Equation 14}$$

where $[T]_0$ is the concentration of the chain transfer agent, d is the number of chains produced per radical–radical termination (for example d~1.67 and ~1.0 were reported for polymerization of MMA and styrene, respectively), f is the initiator efficiency and [I] is the concentration of the initiator. In ideal conditions, the population of radicals remains constant during the equilibrium state of RAFT polymerization. When the steady state condition is reached, the RAFT agent behaves just as a transfer agent which has no influence on the reaction rate. All of the growing chains at this stage are either derived from the initiator or from the $\dot{R}$ radicals. Ideally the number of living chains is equal to $[T]_0$ and the number of chains that undergo termination is equal to $df([I]_0 - [I]_t)$. The fraction of living chains is therefore given by:

$$L = \frac{[T]_0}{[T]_0 + df([I]_0 - [I]_t)} \quad \text{Equation 15}$$

If the molar ratio of the RAFT agent to the initiator is sufficiently large, the fraction of terminated chains is negligible. Under this circumstance, the average degree of polymerization simplifies to:

$$X_n = \frac{[M]_0 - [M]_t}{[T]_0} \quad \text{Equation 16}$$

The above equation states that the number average chain length and molecular weight increase linearly with monomer conversion. In fact in the RAFT process, unlike

conventional radical polymerization, many short chains are generated at the initial stages of the reaction which are periodically turned on and off. The relative rate of chain transfer to propagation determines the number of monomers added to a chain during its activation cycle. A rapid chain transfer rate and suitable choice of RAFT/initiator mole ratio is necessary for narrow molecular weight distribution and negligible termination. The latter was shown to have a major impact on the molecular weight and polydispersity index (PDI) of methyl methacrylate polymerized in the presence of a common dithiobenzoate (2-cyano-2-butyl dithiobenzoate) the RAFT agent[85]. It was observed that the molar mass reduced at lower initiator concentration. This could be a consequence of insufficient reaction time at the lower concentration. Lower initiator content, however, gives better control over the polymerization (narrower molecular weight distributions) due to the lower number of free radicals in the reaction mixture. More importantly it was indicated that increasing the RAFT agent to initiator mole ratio does not necessarily reduce the PDI, Figure 2.6. Under the applied reaction conditions the lowest polydispersity and an acceptable molecular weight was obtained at 1:0.25 molar ratio.

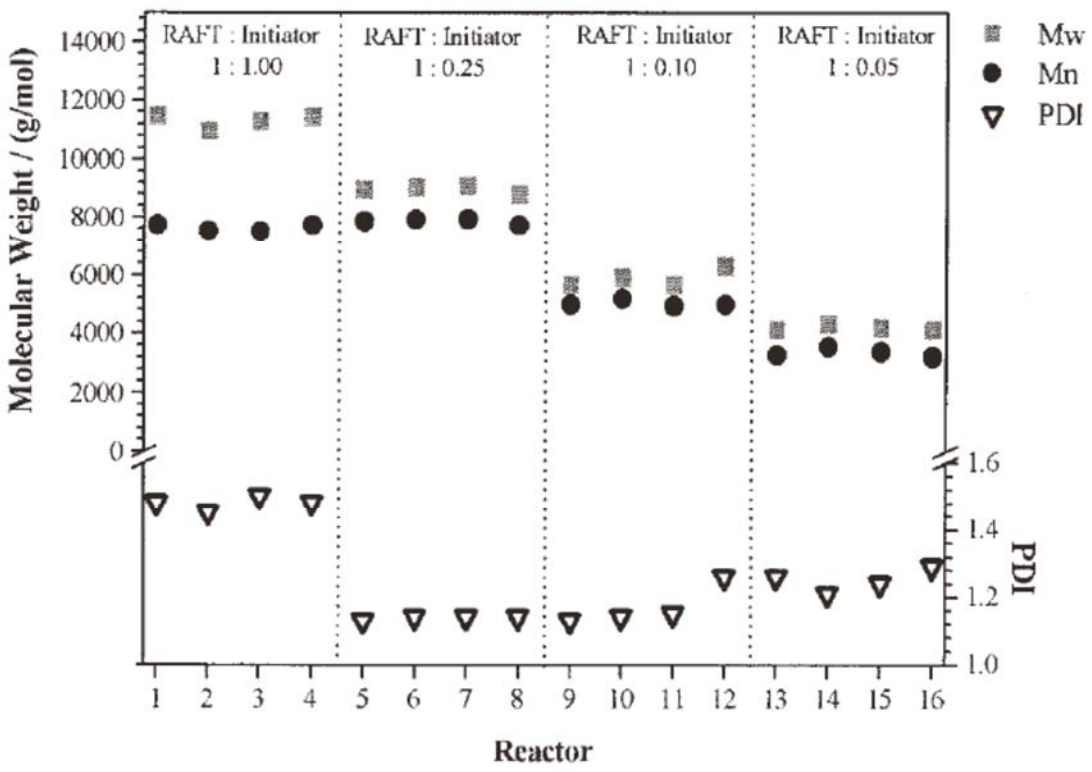

Figure 2.6. Dependence of the number average and weight average molecular weights of RAFT-polymerized poly(methyl methacrylate) on CTA to initiator mole ratios [From Journal of Polymer Science Part A: Polymer Chemistry, Vol. 42, 5775–5783 (2004). Reprinted by permission of John Wiley & Sons, Inc.].

The living characteristic of the polymers synthesized via the RAFT process renders this technique a suitable approach for preparation of a wide variety of block copolymers. The RAFT polymerized chains are predominantly terminated by the reactive residue of the CTA, thus can be readily extended by different monomers to produce di-block or multi-block copolymers. The chain extension reaction is commonly performed by employing the CTA-terminated block as the macro-RAFT agent in the polymerization of the second comonomer. This has been done by either addition of the comonomer at a certain point during the polymerization of the first block or starting a new reaction in presence of the

macro-RAFT agent. The success of this reaction in synthesis of an AB block copolymer relies on high transfer constant of the A-containing macro-CTA during the subsequent polymerization of the B block[86]. Such a high transfer rate is realized if the $\dot{A}$ radical is a better leaving group than the $\dot{B}$ radical, Scheme 2.4. For example, the transfer rate of the propagating methyl methacrylate chains (PMMA radical) to macro-RAFT agents of poly(acrylate ester) or a polystyrene were found to be very low. It was suggested that the active poly(acrylate ester) or polystyrene chains are poor leaving groups in comparison with the PMMA radical. This complication was avoided by first preparing the MMA block and subsequently extending it by styrene or acrylate monomer. Furthermore, it was emphasized that the amount of initiator should be as low as possible to avoid formation of homopolymer chains.

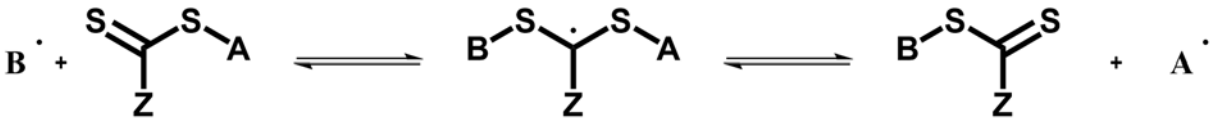

Scheme 2.4. Schematic representation of the chain transfer process to the macro-RAFT agent, releasing active A block that is extended with comonomer B to produce an AB di-block copolymer.

Several examples of successful extension of the first block with various comonomers were reported by Hoogenboom and coworkers[87]. Block copolymers of 1-ethoxyethyl acrylate (EEA) with several comonomers including methyl acrylate (MA), n-butyl acrylate (n-BA), MMA, and N,N-(dimethylamino) ethyl methacrylate were prepared by polymerization of the comonomer for three hours in the presence of a RAFT agent (2-cyano-2-butyl dithiobenzoate), followed by introduction of the EEA monomer to the reaction mixture. Azobisisobutyronitrile (AIBN) was used as the initiator and toluene as

the solvent. The monomer/RAFT/initiator ratio of 100/1/0.25 was found to be optimum for this set of reagents, providing adequate control over the molecular weight distribution (PDI≈1.2 to 1.3) without excessively reducing the rate of polymerization.

2.5.2. Thiol-functionalized polymers

Thiol bearing synthetic polymers, like their small-molecule counterparts, offer superior properties in stabilization of the noble metal nanoparticles. Thiol functionality can be incorporated into the polymer chains through direct polymerization of monomers containing protected thiol functionality or post-polymerization modification of various precursor polymers. Ideally, the first approach provide access to a polymer with well-defined chemical composition containing the desired number of thiol groups. Direct polymerization of thiol-containing monomers, however, is not trivial as they are only stable under certain reaction conditions and the thiol group can interfere with the polymerization process. Such complications severely restrict the choice of the comonomers and the polymerization technique and generally results in the formation of polymers with low molecular weights. Alternatively, chemical modification of preformed high molecular weight polymers has been employed to produce thiolated macromolecules with desired physical and mechanical properties. The success of this approach relies on the presence of proper moieties on the polymer chains that can be converted into thiol in a single or multiple steps reaction. This conversion is not a straightforward procedure due to several restricting factors including the limited accessibility of the reactive sites on the polymeric materials and high probability of side reactions such as crosslinking. Proper choice of the monomers, polymerization reaction, and the modification procedure are essential for efficient conversion of the functional groups on the precursor polymer into the thiol moieties.

Living ionic and controlled free radical polymerization methods allow for attaching certain functional groups to the polymer chain ends which can be transformed into thiol moiety through post-polymerization modification reactions. The precursor terminal group can be attached to the living end of the chain in the case of ionic polymerization[69] or might be the residue of initiator or chain transfer agent used in the controlled free radical methods[60, 66]. RAFT synthesized polymer chains are predominantly terminated by the dithioester residue of the transfer agent, which is convertible into the thiol group via several reactions such as alcoholysis, aminolysis, hydrolysis and reduction[60-62, 64]. Alcoholysis and aminolysis of a model dithioester (1-phenylethyl dithiobenzoate (PTB)) to produce 1-phenylethylthiol, was proposed to proceed through the following scheme[65]:

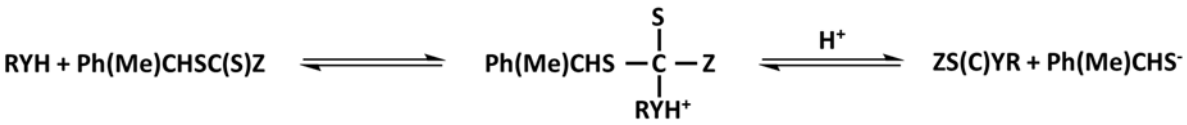

Scheme 2.5. Alcoholysis and aminolysis of a model dithioester. Y = NH, O, S; R = H, alkane; Z = Ph, OEt, Ph(Me)CHS.

If the dithioester group is located at the polymer chain end, the phenyl ethyl group should be replaced by the polymer chain. A major drawback of the aminolysis reaction is formation of larger molecular weight by-products as a consequence of oxidative disulfide coupling of two thiol-terminated homopolymers. Alternatively, the conversion of this model dithioester RAFT agent was performed using a range of strong to mild reducing agents, amongst which sodium borohydride was shown to give the highest yield of thiol. In addition to the choice of the reaction condition and the reducing agent, the yield of thiol depends on the size of the Z group and its ability to stabilize (more specifically its inductive

and resonance effects) the intermediate ion, scheme 5. The phenyl group has a very good ability to stabilize the intermediate but its steric hindrance reduces the probability of the favorable reaction and increases the probability of side reactions. Another important factor that needs to be considered is the efficiency of the RAFT agent in the polymerization measured by its chain transfer coefficient. The dithioxanthate (Scheme 2.2) compounds were readily converted into thiol with high yield; however, their efficiency as chain transfer agents was not satisfactory. Accordingly it was suggested that an optimum combination of both the chain transfer constant and the ease of conversion into thiol should be considered in the selection of the proper RAFT agent.

Dimerization of the terminal thiol groups to form disulfides can significantly diminish the yield of the RAFT agent conversion reaction. Various approaches have been proposed to reduce the probability of this undesirable side reaction. Spruell et al.[62] used sodium borohydride to convert the residue of dithio(1-cyano-1-methylethyl)-benzoate RAFT agent on poly(methyl methacrylate), polystyrene, and their block copolymers into a thiol group. Rigorous degassing of the reaction mixture was necessary to avoid disulfide formation. Addition of a large excess of tributylphosphine was found to be an efficient alternative approach to suppress oxidation of the thiols during the reaction performed under the ambient atmosphere. ^{1}H NMR and UV-visible spectroscopies confirmed the successful formation of thiol moieties which were further converted into the amine functionality via Michael addition. Nishi and coworkers[63] studied the influence of reducing agent and the reaction solvent on the conversion of dithiobenzoate end groups of polystyrene chains. Disappearance of ^{1}H NMR signals of the dithiobenzoate was observed for all of the applied reaction conditions; however, the resonances of the reduced end group were not identical

for the polymers modified by different protocols. Extensive dimerization of the polymer chains through disulfide formation was detected when using strong reducing agents such as super-hydride and propylamine. It was observed that reduction with sodium borohydride in aqueous THF under inert atmosphere proceeded slowly, but produced a stable thiol functionality. Efficient transformation of trithiocarbonates and dithioesters at short reaction times (less than 10 minutes) was conducted using hydrazine hydrate under ambient atmosphere[61]. The efficiency of this reagent was attributed to its strong nucleophilicity as well as its antioxidant characteristic which prevents the oxidative coupling of thiols.

Conversion of the terminal groups of the polymer chains into a thiol moiety suffers from nontrivial drawbacks, limiting the utility of the resulting polymeric capping agent for controlled synthesis of noble metal nanoparticles. Incomplete conversion, which is the case for all of the commonly used chain transfer agents, leaves a significant amount of polymer chains without the proper functionality. Even if the conversion is complete, the thiol to monomer mole ratio is extremely small (less than 1/100 for thiol-terminated PMMA with M_n > 10000 g/mol), as each polymer chain contains a single thiol group. Such an extremely small concentration of the active functionality reduces the probability of polymer-metal bonding at the early stages of particle growth, leading to poor control over the size, shape, and uniformity of the nanoparticles. To overcome this problem, polymers bearing multiple thiol functionalities along their backbones have been synthesized through alternative post-polymerization modification methods. These synthetic procedures rely on using functional monomers which are inert towards the polymerization and can subsequently transform into thiol-bearing units through a viable reaction pathway. Recent advances in controlled free radical polymerizations (CRP), specifically the more versatile RAFT and ATRP, allow for

using a wide range of functional monomers and designing their arrangement along the chains to obtain various copolymers with pre-determined number and positioning of the thiol groups.

Several functional monomers including maleic anhydride, vinylbenzaldehyde, glycidyl methacrylate, and vinylbenzyl chloride that are readily polymerizable via CRP methods, and are amenable to post-polymerization conversion into thiol bearing units. Narrow molecular weight distribution copolymers of maleic anhydride with styrene and substituted styrene (chlorostyrene, methoxystyrene and methylstyrene) comonomers were prepared by RAFT polymerization[88]. The anhydride side groups undergoe esterification reactions with alkyl alcohols in the presence of 4-(dimethylamino) pyridine as catalyst[89]. Employing mercapto-alcohols in this reaction provides access to thiol pendant groups. Aldehyde functional monomers such as 4-vinylbenzaldehyde have been successfully polymerized by RAFT process[90] yielding amine reactive precursor polymers. This reactivity of the aldehyde groups was exploited to graft cysteine on the polymer chains under mild condition to obtain thiol-functionalized macromolecules for biomedical applications[91]. Glycidyl methacrylate (GMA) is another example of a highly reactive functional monomer that can be easily polymerized via various CRP methods owing to its structural similarity with methyl methacrylate. The epoxide ring on this monomer is highly labile to nucleophilic attack by a large range of reagents due its ring strain. Depending on the reactivity of the nucleophile, the reaction proceeds either through the SN_2 (for strong nucleophiles) or SN_1 (for weak nucleophile, acid catalyzed) mechanism, scheme 2.6. Examples of such nucleophiles are Grignard reagents (R-MgX), alkyllithium, lithium aluminum hydride ($LiAlH_4$), hydroxide, and alkoxides.

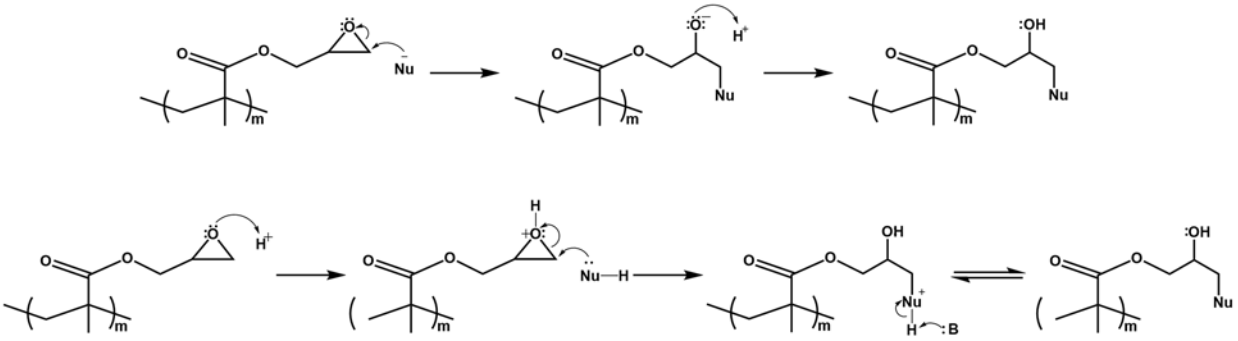

Scheme 2.6. Nucleophilic substitution reactions of epoxide ring with strong (top) and weak (bottom) nucleophiles followed by acidic work-up.

The epoxide ring on glycidyl methacrylate monomers was converted into a thiol functionality through reaction with sodium hydrosulfide[92-93]. This nucleophilic substitution proceeds through a second-order mechanism under basic conditions. The product was treated with a strong acid to protonate the negatively charged oxygen formed from opening of the epoxide ring. This resulted in formation of a neutral alcohol and a thiolate moiety. A major problem encountered in the post-polymerization modification of GMA containing copolymers is the possibility of intra or inter-molecular reactions between the glycidyl groups located on the same or on different chains, rendering a crosslinked polymer. Opening of the epoxide ring under the reaction conditions produces a highly nucleophilic O^- (or S^- in the case of reaction with NaSH) anion which can attack the intact epoxide rings. This reaction, which is analogous to the anionic ring opening polymerization of epoxide, leads to the undesired crosslinking of the polymer chains. The probability of this side reaction increases specifically in two-phase reaction media where the nucleophile (such as NaSH or amine) is in aqueous phase while the polymer is dissolved in an organic solvent.

2.5.3. Polymerization and modification of vinylbenzyl chloride

Vinylbenzyl chloride (VBC) is a highly versatile functional monomer for synthesis of reactive precursor polymers amenable to a wide range of post-polymerization modification reactions. The modified copolymers of VBC have been used in preparation of amphiphilic diblock or graft copolymers[94-97], ion-exchange and fuel cell membranes[98-101], monolithic scavenger resins[102], Janus nanoparticles[103], and antimicrobial colloidal systems[104] just to name a few applications. The VBC monomer owes its reactivity to the susceptibility of benzyl chloride side group to nucleophilic attack, Scheme 2.7. The partial positive charge on the benzylic carbon attached to the chlorine and the fact that chloride is a good leaving group facilitate the nucleophilic substitution of chloride with a range of mild to strong nucleophiles prior to or after its polymerization[105].

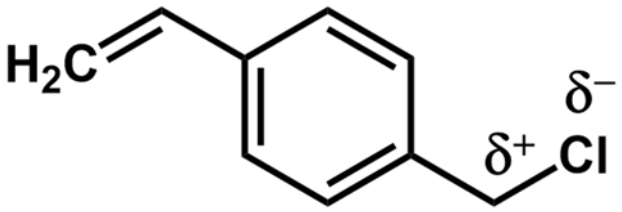

Scheme 2.7. Vinylbenzyl chloride monomer.

Several examples of successful substitution of the benzylic chloride with various functional groups have been presented. Krajnc et al replaced the chlorine on the crosslinked copolymer of VBC with divinylbenzene (DVB) by different amines including tris(2-aminoethyl)amine, 4-aminobutanol, tris(hydroxymethyl)aminomethane, and hexamethylenetetramine to produce monolithic scavenger resins containing both amine and hydroxyl functionalities[102]. The reaction was performed by either passing the amine solution (in DMF or ethanol) through a column containing the immobilized VBC-DVB

copolymer or by stirring the crosslinked polymer in amine solution at temperatures ranging from 40 to 60°C for 1 to 24 hours. A noticeable increase in the mole fraction of nitrogen and a decrease in the chlorine content of the modified polymer (determined by combustion elemental analysis) was observed as a function of the reaction time. The progress of the reaction was further confirmed by disappearance of the characteristic absorption of carbon-chlorine bond in the FTIR spectrum of the product. The intensity of this C-Cl band, which appears at around 1265 cm^{-1} in the FTIR spectrum of the unmodified homopolymer and copolymers of VBC, is a very good indicator of the extent of chloride substitution. Polymer colloids showing strong antimicrobial properties were prepared by treating crosslinked particles of VBC-DVB copolymer with (+)-usnic acid, which is a well-known biological antimicrobial agent[104]. Small copolymer particles (hydrodynamic radius=110 nm) synthesized via emulsion polymerization were allowed to react with usnic acid for 48 hours at room temperature in triethylamine. Under the basic condition provided by triethylamine, the phenoxide ions on deprotonated usnic acid can undergo nucleophilic substitution with the chlorine of the VBC units. It was also suggested that the benzyl chloride may react with triethylamine to produce cationic side groups which can strongly interact with hydroxyls of usnic acid. The bonding was verified by an increase in the hydrodynamic radius of the treated particles as well as changes in their Zeta potential, FTIR bands, and thermal weight loss. The VBC monomer can be alternatively modified before polymerization. An example of such modification is presented by Tseng and coworkers[106] where the monomer was treated with 2-dimethylethanolamine at room temperature to prepare a polymerizable surfactant for clay nanoparticles. It was shown that the tertiary amine replaces chlorine in VBC while the double bond remains intact. Vulnerability of the double bond to the

monomer modification reactions and the possibility of interference of the new functional group with the polymerization reactions are the two major issues limiting this approach.

Vinylbenzyl chloride has been readily polymerized via the common controlled free radical techniques to produce well-defined copolymers with various molecular structures. ABA and BAB triblock copolymers of styrene and VBC were synthesized through two-step RAFT polymerization in which the first block was used as the macro RAFT agent in the polymerization of the other blocks[107]. Azobisisobutyronitrile was used as the initiator in both the first and the second steps of the polymerization. The polydispersity indices (PDI) of the block copolymers were observed to increase from 1.2 for the first block to around 1.5 upon formation of the second block. The molecular weight distribution curves of the copolymers did not contain any separate peak or distinct shoulder, indicating that the second monomer did not form homopolymer chains. Presence of two distinct glass transition peaks in the DSC thermograms of the block copolymers indicated that they have microphase separated morphology. This copolymer was subsequently reacted with an excess of diethyl amine in THF at 70°C for 5 hours. The substitution of the chlorine atoms of the VBC units were studied by DSC and FTIR. The glass transition of the modified VBC blocks were shifted to higher temperature (from 150 to 160) while that of the PS block remained unchanged. Moreover, the modified polymer showed new FTIR bands at 2967 cm^{-1} and 2797 cm^{-1} pertaining to the CH_2 and CH_3 of the diethyl amine functionality and did not contain the characteristic peak of the chlorine group at 1265 cm^{-1}. Disappearance of C-Cl band was interpreted as complete conversion of the chloride. Couture and Ameduri[108] studied the kinetics of RAFT polymerization of VBC in presence of O-ethyl-S-(1-methyloxycarbonyl)ethyl xanthate and dibenzyl trithiocarbonate chain transfer agents.

The polymerization was performed either in bulk or in solution, changing the RAFT agent to initiator mole ratio while keeping the monomer to initiator mole ratio constant. Investigation of the monomer conversion, molecular weight and polydispersity using ^{1}H NMR and gel permeation chromatography revealed that the xanthate chain transfer agent does not provide sufficient control over the polymerization. The reaction conducted in presence of dibenzyl trithiocarbonate exhibited the characteristics of controlled radical polymerizations producing polymers having PDI ranging from 1.33 to 1.6.

Replacement of chlorine with thiol group on monomeric or polymerized VBC can be conducted via multi-step reactions. These synthetic procedures involve nucleophilic substitution of the chlorine with reagents such as thioacetate or thiourea, followed by deprotection of the thiol moiety, Scheme 2.8.

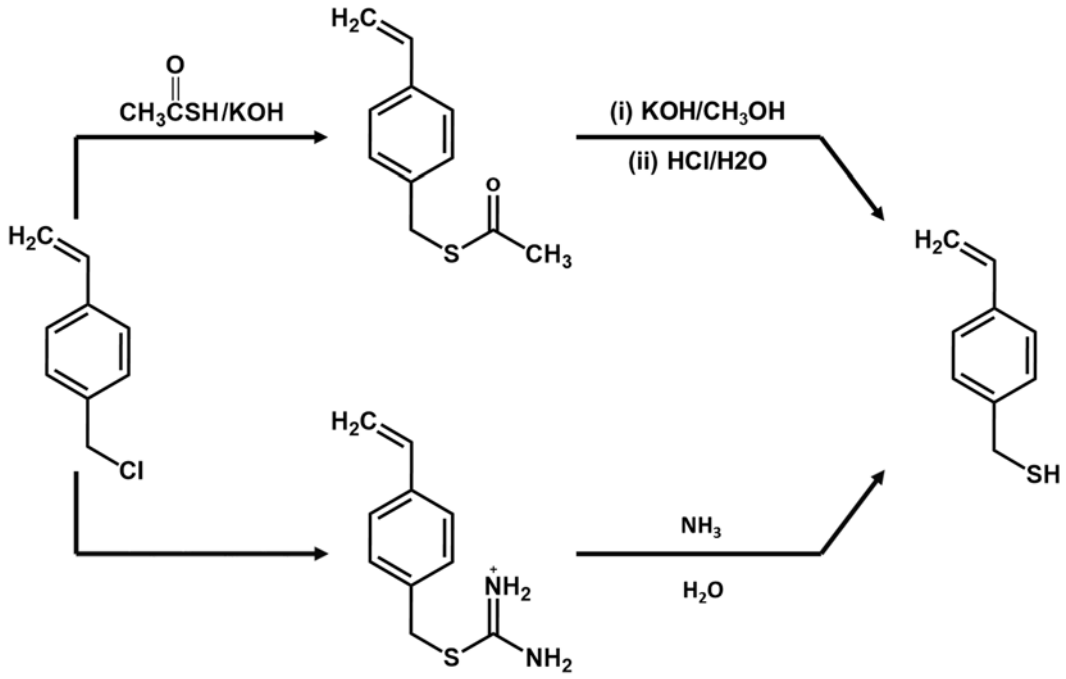

Scheme 2.8. Substitution of Cl group of VBC monomer via multi-step reactions with thioacetate (top) and thiourea (bottom)

Nucleophilic substitution of the halogen on alkyl halides with thiourea and subsequent hydrolysis of the resulting thiouronium salt is a well-established protocol for synthesis of small-molecule thiols. A similar approach is applicable to the benzyl chloride side group of VBC containing polymers through the mechanism presented in Scheme 2.9. Being a poor leaving group, the thiouronium functionality has a good resistance to nucleophilic attacks, thus providing stability for the intermediate polymer. Moreover, this group is not a good nucleophile due to the presence of a positive charge adjacent to sulfur, reducing the possibility of further undesirable reactions. Basic hydrolysis of this intermediate followed by acidic work-up results in formation of thiol bearing polymers. An example of such modification was presented for poly(vinylbenzyl chloride) chains grafted on poly(tetrafluoroethylene-co-hexafluoropropylene) membrane[109]. The reaction was performed by immersing the grafted film in the solution of thiourea in ethanol at 40 °C for 6 hours. The resulting thiouronium salt side groups were hydrolyzed in NaOH solution at room temperature for 8 hours and further washed with HCl to produce thiol functionalized polymer. Formation of the thiouronium intermediate and the thiol functional product was confirmed by FTIR spectroscopy and elemental analysis. The FTIR spectrum of the product showed the S-H stretching vibration of the thiol moiety and did not contain a C-Cl band. It should be mentioned that the thiol group on a polymer chain can readily undergo further undesirable reactions such as oxidation, leading to the loss of the functionality.

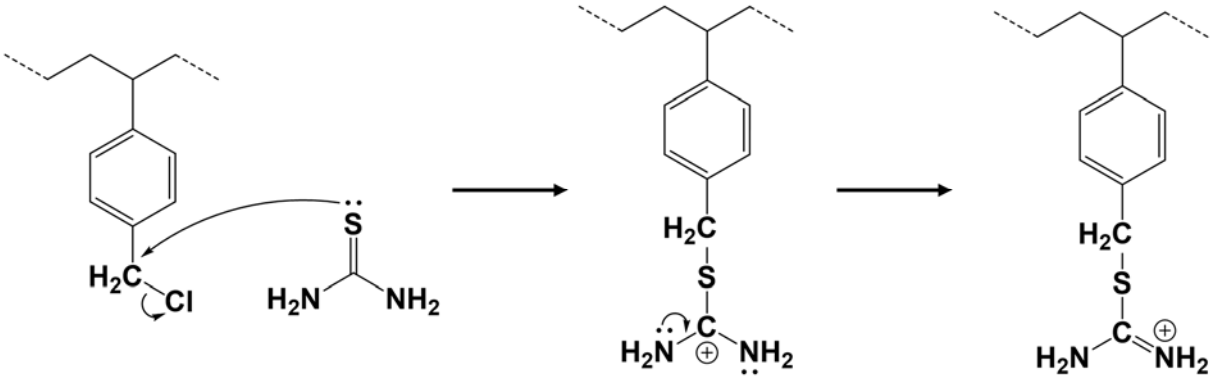

Scheme 2.9. Mechanism of nucleophilic substitution of the VBC chloride with thiouronium functionality

2.6. Applications of silver nanoparticles

Silver has long been known to have antimicrobial properties due to its toxic effects on living microorganisms. It was shown that silver can interact with proteins and DNA to interfere with their normal functionality. Due to the toxicity of the silver nanoparticles, it is very important to prevent their release into the environment by fixing them within the matrix material. An antimicrobial coating was made by incorporating silver nanoparticles into a matrix of thiol-terminated block copolymers of methyl methacrylate, *n*-butyl acrylate, and *tert*-butyl acrylate (*t*-BA) comonomers[7]. The *t*-BA repeating units were further converted into acrylic acid to produce a hydrophilic block. It was shown that a film formed from this copolymer on a glass slide released 0.16 μM/cm^2 silver ions into water during 6 days. This effectively inhibited the growth of *E. coli* bacteria without releasing toxic silver nanoparticles.

Noble metal nanoparticles are interesting materials for nanophotonics because their localized surface plasmon resonance (LSPR) occurs within the visible light frequency

range. Localized surface plasmons are collective oscillations of the free conduction electrons of the metallic nanomaterial upon interaction with the light field. When the frequency of the incident photons matches that of the surface plasmons, the spatially confined conduction electrons undergo coherent oscillations resulting in strong light absorption in the visible range and extensive enhancement of the local electromagnetic field in close proximity of the nanoparticles. These unique characteristics of the noble metal nanostructures open up a wide range of potential optical and photonic applications such as manufacturing of sensors[110], nanoscale detectors of chemicals and biological species[111], drug delivery vehicles[112], light filters[113], nonlinear optical switches[114], sub-wavelength waveguides[115], and magneto-optic data storage[116]. The local electric field enhancement have been exploited in surface enhanced Raman spectroscopy[3].

The frequency and bandwidth of the LSPR absorption depends on the size, shape and interactions of the nanoparticles as well as the refractive index and dielectric properties of their surrounding medium, which allows for fine tuning of their optical properties. Dependence of the LSPR frequency on the refractive index and dielectric constant of the surrounding medium and inter-particle spacing has been used in optical sensing applications[18]. Coating silver nanoparticles with stimuli-responsive polymers provides a practical approach for fabricating devices that are sensitive to the environmental parameters such as temperature and pH at very small length scales. Conformation or morphological changes in the grafted polymer chains in response to an external stimulant result in variation in their refractive index and/or dielectric constant which affect the LSPR frequency of the nanoparticles.

Poly(N-isopropylacrylamide), PNIPAM, is an example of well-studied temperature sensitive (thermo-responsive) polymer that can be directly attached to or polymerized from the surface of gold and silver nanoparticles. This polymer shows a lower critical solution temperature (LCST) phase behavior in water with a relatively narrow temperature range at around 32 °C. The PNIPAM chains in water switch between collapsed and swollen conformations upon passing through the transition temperature. This was shown to modify the effective refractive index of PNIPAM brushes grafted onto an array of gold nanodots leading to a red-shift in LSPR wavelength when the temperature was raised from below to above LCST[117].

Chapter 3. Methodology

3.1. Nuclear magnetic resonance (NMR) spectroscopy

NMR spectroscopy is a powerful tool for the characterization of a wide range of materials: from small molecules with simple structures to high molar mass macromolecules, and from isolated molecules to multi-component, multi-phase complex structures. Numerous NMR techniques, at various levels of complexity, have been developed in the last few decades to investigate the microstructural aspects, as well as the molecular and sub-molecular dynamics of materials in gas, solution, or solid states. Irrespective of their degree of complexity, all these techniques rely on the intrinsic spin of nuclei. A nucleus with spin quantum number (I) greater than 0 possesses nuclear spin angular momentum (**I**) which gives rise to the nuclear magnetic dipole moment (**μ**):

$$\boldsymbol{\mu} = \gamma \boldsymbol{I} \qquad \text{Equation 1}$$

where **I** and **μ** are vector quantities (bold face), and the proportionality constant, γ, is the gyromagnetic ratio which is a fundamental property of the nucleus. Interaction of the nuclear spins with an externally applied magnetic field lifts the degeneracy of energy levels, which is known as Zeeman splitting. The energies of these spin states are given by the following equation:

$$E_m = -\boldsymbol{\mu} \cdot \boldsymbol{B_0} = -\gamma I_z B_0 = -\hbar m_z \omega_0; \quad m_z = -I, -I+1, \ldots, +I \qquad \text{Equation 2}$$

where $\boldsymbol{B_0} = B_0\boldsymbol{k}$ is the external magnetic field arbitrarily chosen to be along the z axis ($\boldsymbol{k}$ is the unit vector), I_z is the z component of the spin angular momentum vector, and $\omega_0 = \gamma B_0$ is the Larmor frequency which is the angular frequency of spin precession. The total energy of the spin system is determined from the expectation value of the Hamiltonian operator, $\widehat{H}$ (the symbol ^ denotes an operator). The quantum mechanical counterpart of the above classical expression is the Zeeman Hamiltonian, which is the major contribution to the energy of a spin system:

$$\widehat{H}_z = -\gamma\hbar\hat{I}_z B_0 \qquad \text{Equation 3}$$

In this case $\hat{I}_z$ is the z component of the nuclear spin operator ($\hat{I}$).

In a system of non-interacting spin-1/2 nuclei (I = 1/2, such as ^{1}H and ^{13}C which are of interest in this study) there are two energy levels associated with quantum numbers m = +1/2 and m = -1/2, referred to as the Zeeman states (Scheme 3.1). The m = +1/2 and m = -1/2 states are referred to as α and β, respectively. At thermal equilibrium the population of spin states has a slight bias towards the lower energy state, which in aggregate gives rise to a net magnetization along $\mathbf{B_0}$. The relative population of the spins states is determined by the energy difference between them, $\Delta E = \hbar\omega_0$, and is given by the Boltzmann distribution:

$$\frac{N_{m=+1/2}}{N_{m=-1/2}} = e^{-\frac{\Delta E}{kT}} \qquad \text{Equation 4}$$

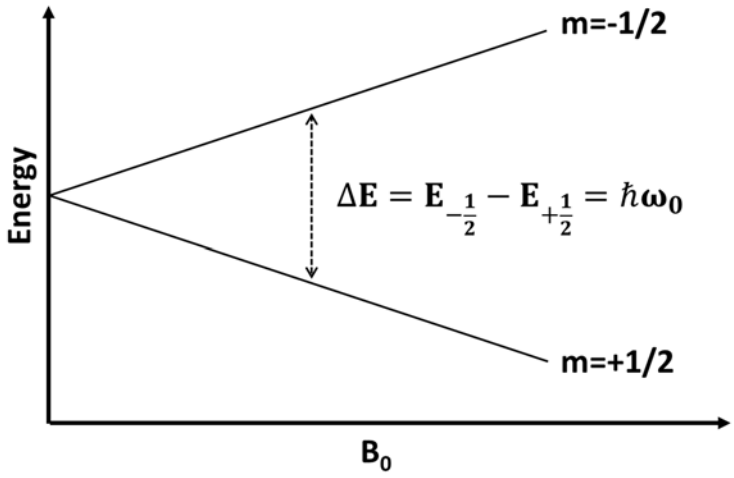

Scheme 3.1. Energy levels diagram of spin-1/2 nuclei showing the splitting between the states as a function of the magnitude of the external magnetic field.

The magnetic field of a radiofrequency (RF) pulse oscillating on resonance with the precession frequency of the nuclei has sufficient energy (*i.e.* equal to ΔE) to induce transitions between the states. Application of such RF pulses changes the orientation of the individual spin magnetic moments and rotates the induced magnetization in the x-y plane (transverse magnetization). This can be considered in terms of changes in the populations of spin states and generation of coherences between them. The transverse magnetization is detected by free induction giving rise to the NMR signals, which parametrically depend on the spin interactions governed by molecular structure (*e.g.* electronic environment, bond lengths, and geometry). Furthermore, the random fluctuations of the local magnetic interactions, which are modulated by random motion at various time scales, leads to loss of coherence between spin states and the re-establishment of the equilibrium spin populations. The relaxation behavior reveals the dynamic parameters that governs local motion.

The energy of the nuclear spin states is affected by the interactions with neighboring magnetic moments from nuclei and electrons[118-120]. The major spin interactions contributing to the Hamiltonian of a spin-1/2 system include shielding, direct dipole-dipole coupling, and scalar coupling (J-coupling):

$$\hat{H} = \hat{H}_z + \hat{H}_{cs} + \hat{H}_d + \hat{H}_j \qquad \text{Equation 5}$$

The shielding interaction arises from the local fields experienced by the nucleus induced by the electrons nearby. The externally applied magnetic field causes electrons to circulate generating a secondary magnetic field which opposes B_0. This local field is responsible for slight shifts in the Larmor frequency of nuclei located in different electronic environments. The shielding interaction and hence the resulting chemical shift depend on the orientation of the molecule with respect to $\mathbf{B_0}$:

$$\hat{H}_{cs} = -\gamma\hbar\hat{\boldsymbol{I}}.\boldsymbol{\sigma}.\boldsymbol{B_0} \qquad \text{Equation 6}$$

where $\boldsymbol{\sigma}$ the chemical shielding tensor describing the orientation dependence of the interaction. $\hat{H}_{cs}$ is more conveniently expressed in terms of the isotropic value ($\sigma_{iso} = 1/3(\sigma_{xx} + \sigma_{yy} + \sigma_{zz})$, σ_{ii}s are the principal values of the shielding tensor), the anisotropy (σ_{CSA}), and the asymmetry (η_{CSA}) of the shielding tensor:

$$\hat{H}_{CS} = \gamma\hat{I}_z B_0 \left\{\sigma_{iso} + \frac{1}{2}\sigma_{CSA}[(3\cos^2\theta - 1) + \eta_{CSA}\sin^2\theta\cos 2\phi]\right\} \qquad \text{Equation 7}$$

where the angles θ and φ describe the orientation of the chemical shielding tensor. Rapid tumbling of molecules in liquid-state and magic angle spinning (c.f. Section 3.3.1) of

samples in solid-state NMR, averages the effect of shielding on chemical shift to an orientation independent value known as isotropic chemical shift, δ_{iso}:

$$\delta_{iso} = \frac{\sigma_{iso}(ref) - \sigma_{iso}}{1 - \sigma_{iso}(ref)} \quad \text{Equation 8}$$

where $\sigma_{iso}(ref)$ is the isotropic shielding of a reference material. The isotropic chemical shift of each nucleus is predominantly determined by the structure of the electron density surrounding the nucleus.

The dipole-dipole or dipolar coupling is the direct interaction between magnetic moments of spins through space. The dipolar coupling of spins I and S varies with the I-S internuclear distance (r) and the orientation of internuclear vector relative to $\mathbf{B_0}$:

$$\widehat{H}_d = -2\hat{\boldsymbol{I}}.\boldsymbol{D}.\hat{\boldsymbol{S}} \quad \text{Equation 9}$$

The dipolar coupling tensor $\boldsymbol{D}$ describes the orientation dependence of the magnetic field of spin S at the site of spin I. The principal values of $\boldsymbol{D}$ are $-d/2$, $-d/2$, and $+d$ ($d = \hbar/r^3(\mu_0/4\pi)\gamma_I\gamma_S$ is dipolar coupling constant), which makes it a traceless tensor with isotropic value of zero. Hence in the liquid state rapid molecular motions average the dipolar couplings to zero. In the solid state, these couplings broaden of the NMR signals and also contribute strongly to spin-spin relaxation. Also note that dipolar couplings are referred to as either homonuclear or heteronuclear, depending on whether the spins are identical or different. The truncated homonuclear and heteronuclear dipolar coupling Hamiltonians are given by:

$$\widehat{H}_d^{homo} = -d\frac{1}{2}(3\cos^2\theta - 1)\left[3\hat{I}_z\hat{S}_z - \hat{\boldsymbol{I}}.\hat{\boldsymbol{S}}\right] \quad \text{Equation 10}$$

$$\widehat{H}_d^{hetero} = -d(3\cos^2\theta - 1)\hat{I}_z\hat{S}_z$$ Equation 11

Here the angle θ is determined by the orientation of the internuclear vector with respect to B_0.

Scalar coupling is best described as an indirect interaction between nuclear spin magnetic moments propagated by the bonding electrons. This interaction, typically is much weaker than the direct dipolar coupling and is orientationally dependent, but has a non-zero isotropic value, J_{jk}. The Hamiltonian of homonuclear and heteronuclear J-coupling in an isotropic liquid are given by:

Homonuclear: $\widehat{H}_j = 2\pi J_{jk}\hat{\boldsymbol{I}}_j.\hat{\boldsymbol{I}}_k$ Equation 12

Heteronuclear: $\widehat{H}_j = 2\pi J_{jk}\hat{I}_{jz}\hat{S}_{kz}$ Equation 13

The J-coupling is responsible for the splitting patterns most often observed in solution NMR spectra, which provides information about the type and number of nuclei that are linked together via a small number of bonds (< 4).

3.2. Solution-state NMR techniques

Solution state NMR is amongst the most widely used techniques for the characterization of isolated compounds. In the following, a brief description of the solution NMR experiments used in this study is presented. In-depth treatments are available in the literature[118, 121].

3.2.1. One dimensional ^{1}H and ^{13}C experiments: These NMR experiments provide the chemical shifts of the protons and carbon nuclei. ^{1}H spectrum is acquired in a short time and besides giving the chemical shifts of the protons at various positions, it shows splitting patterns arising from J-couplings which help in the assignment of the signals and determination of connectivity of the nuclei. The ^{1}H spectra of molecules with a large number of magnetically inequivalent protons, such as polymers, are usually very crowded due to the relatively small dispersion in the proton chemical shift. In polymers, protons with identical positions in repeating units vary slightly in chemical shift owing to differences in conformation along the chains. Consequently the corresponding signals are heterogeneously broadened.

^{13}C NMR has much larger chemical shift dispersion, which allows for noticeably improved resolution in its spectra as opposed to ^{1}H. The major disadvantage of carbon spectroscopy is poor signal to noise ratio resulting from the low natural abundance of the NMR active isotope, ^{13}C, which makes up only 1% of all carbon isotopes. Obtaining high quality ^{13}C NMR spectra with acceptable signal-to-noise ratio, therefore requires the collection of a larger number of scans in comparison with ^{1}H experiments, or the preparation of a highly concentrated sample. For polymers with typically limited solubility in common solvents, a very large number of scans should be acquired which imposes a long experiment time.

3.2.2. Distortionless enhancement by polarization transfer (DEPT): DEPT experiments are useful spectral editing methods allowing for differentiation between carbon signals arising from CH_3, CH_2, and CH groups. The experiment involves rotating the proton magnetization to the transverse plane by a 90° pulse, followed by ^{1}H

magnetization transfer to carbon and subsequent observation of the signals, Scheme 3.2. Magnetization transfer occurs through heteronuclear J-coupling between directly attached ^{1}H and ^{13}C nuclei, resulting in signal to noise enhancement of 4:1, in comparison with the ^{13}C direct polarization experiment. Moreover the recovery delay between successive scans is determined by T_1 of the proton, which reduces the experiment times. The type of selected carbon and the phase of its signal is determined by the flip angle of the final ^{1}H pulse. All the carbons with directly attached proton(s) appear in the case of a 45° pulse (DEPT-45). A flip angle of 90° gives only signals from CH groups (DEPT-90), and in the case of 135° the signals arising from CH and CH_3 carbons with opposing phase to those of CH_2 groups. Full assignment of these groups is possible by running a complete set of DEPT experiments.

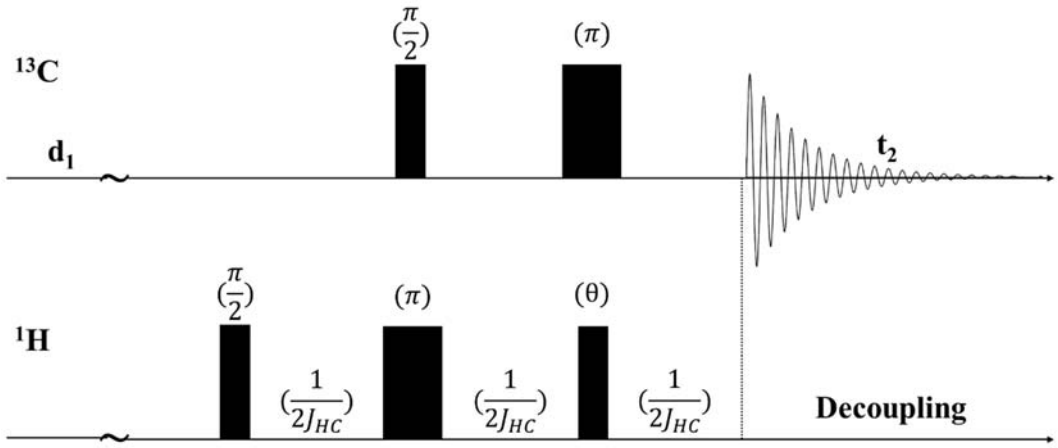

Scheme 3.2. Pulse sequence of DEPT experiment. J_{HC} is the isotropic value of ^{1}H-^{13}C heteronuclear J-coupling (Hertz). The angle θ depends on the type of DEPT experiment.

3.2.3. Two dimensional ^{1}H correlation spectroscopy (COSY): The COSY experiment is used to identify the protons coupled through scalar coupling thus indicating σ bond connectivity. The pulse sequence is composed of an initial 90° pulse which creates coherences, followed by an evolution period during which the coherences evolve under the

influence of J-couplings, and terminated with a 90° pulse after which the signal is recorded, Scheme 3.3. The spectrum obtained from two-dimensional Fourier transform of these signals contains diagonal peaks between the nuclei with identical chemical shifts and cross-peaks between the nuclei correlated with J-coupling. The cross-peaks indicates connectivity between the nuclei.

The two dimensional spectrum is acquired by dividing the evolution period (indirect dimension, t_1) into a number of fixed increments, and collecting the FID in the direct dimension (t_2 period) for each increment. High resolution, which is necessary to separate the cross-peaks in the crowded spectra of polymers, requires the sweep width (sw) in the indirect dimension to be as small as possible (only covering the spectral range of interest). Small sweep width increases the length of mixing period ($t_1 \propto 1/sw$), during which signals with short T_2 lose their intensity due to dephasing. This problem can be avoided at the expense of resolution by using large sweep width.

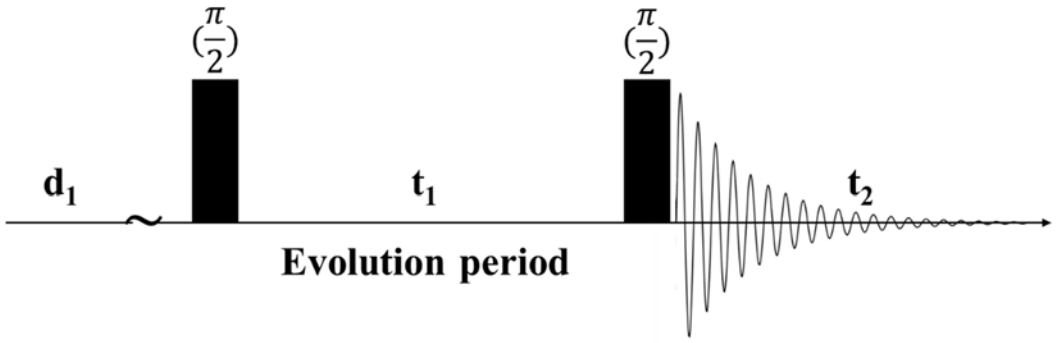

Scheme 3.3. Pulse sequence of ^{1}H COSY experiment. '$\mathbf{d_1}$' is the relaxation delay between the scans.

3.2.4. ^{1}H-^{13}C Heteronuclear single-quantum correlation spectroscopy (HSQC):

The HSQC experiment indicates correlations from protons to carbons connected by one bond. HSQC involves the excitation of the protons with an RF pulse, transfer of the magnetization from protons to carbons, evolution of the antiphase single quantum coherences in the carbon dimension, and conversion of these coherences to a transverse magnetization in the proton dimension which is subsequently recorded, Scheme 3.4. Exciting the protons, which have much larger equilibrium magnetization in comparison to carbons, leads to stronger signals thereby reducing the number of scans required to obtain the required signal-to-noise ratio. The magnetization transfer from protons to carbon is achieved via the INEPT sequence (shown in Scheme 3.4). During the τ period, coherences evolve under the effect of ^{1}H-^{13}C heteronuclear J-couplings and ^{13}C chemical shielding interaction. The latter effect is removed using the refocusing pulse on the ^{1}H channel at $\tau/2$. The evolution period is terminated by transfer of the magnetization back to the protons, via the reverse INEPT sequence. The signal is subsequently observed on ^{1}H with ^{13}C decoupling, which gives the advantage of shorter relaxation delays. This technique is very useful in the assignment of ^{1}H and ^{13}C signals and identifying connectivity between the corresponding atoms. When the ^{1}H spectrum is crowded, the HSQC experiment makes it possible to distinguish between overlapped proton signals by separating them by the chemical shift difference of their correlated carbons.

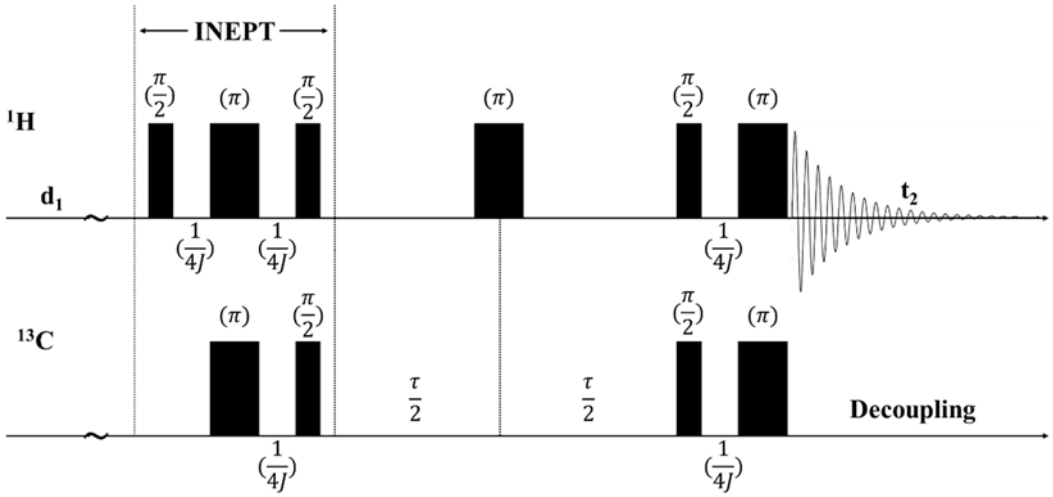

Scheme 3.4. Pulse sequence of ^{1}H-^{13}C HSQC experiment. J is the isotropic value of homonuclear J-coupling (Hertz).

3.2.5. ^{1}H-^{13}C Heteronuclear multiple-bond correlation spectroscopy (HMBC):

This experiment shows the correlations between the protons and carbons connected over 2 to 4 bonds, Scheme 3.5. The information obtained from HMBC is suitable for determining long range connectivity and is specifically useful for assigning resonances of quaternary carbons that do not appear in the HSQC spectrum.

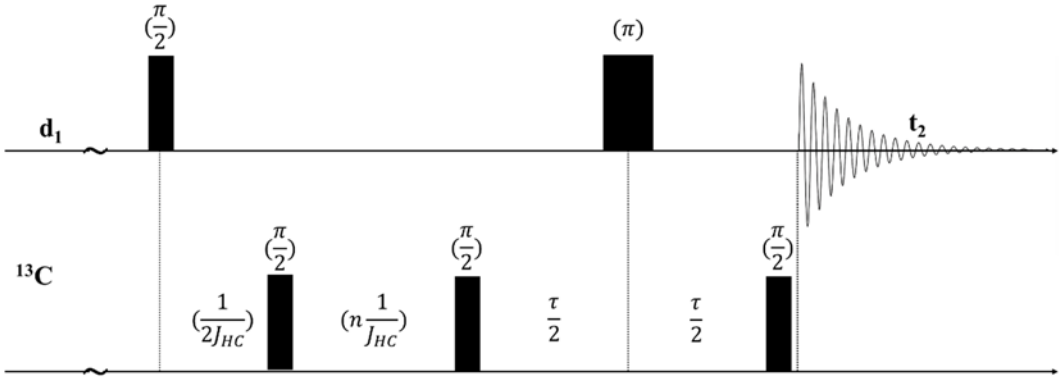

Scheme 3.5. Pulse sequence of ^{1}H-^{13}C HMBC experiment. J_{HC} is the isotropic value of heteronuclear J-coupling in (Hertz).

3.3. Solid-state NMR techniques

Solid-state NMR (SSNMR) spectroscopy is a versatile technique for the characterization of the molecular and phase structure in solid materials, as well as their molecular and sub-molecular dynamics[119, 122]. These aspects cannot be investigated by solution NMR, as dissolution disrupts the structure of solids and alters their molecular dynamics. Despite the vast capabilities of SSNMR techniques, implementation and optimization of these experiments to obtain high quality spectra is generally more involved than solution NMR methods. This is predominantly a consequence of the lack of rapid random molecular motion in the solid state, which results in presence of the orientation-dependent terms in the spin interactions. In what follows, some of the more common techniques used to improve the quality of SSNMR spectra are briefly discussed.

3.3.1. Magic angle spinning: This technique involves rapidly spinning the solid sample about an axis oriented at the magic angle θ_m=54.74° with respect to the external magnetic field, Scheme 3.6. Magic angle spinning (MAS) is the main approach to eliminate, or scale down, the anisotropy of the chemical shielding and the dipolar coupling interactions, which are responsible for line broadening of SSNMR signals. In an analogous manner to solution NMR, rapid spinning at θ_m averages these interaction to zero due to their dependence on a $(3\cos^2\theta - 1)$ term. The spinning rates used in this study are sufficiently high to completely suppress the chemical shielding anisotropy of both ^{1}H and ^{13}C and heteronuclear dipolar couplings of ^{13}C; however, they are not fast enough to effectively remove ^{1}H-^{1}H homonuclear couplings, giving rise to broad ^{1}H signals.

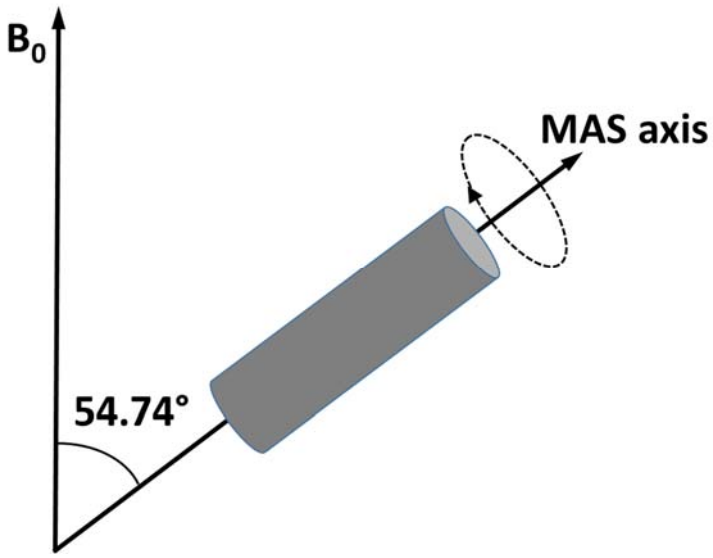

Scheme 3.6. Schematic representation of magic angle spinning.

3.3.2. Cross-polarization: This technique is most commonly employed to enhance the signal-to-noise ratio of the SSNMR spectra of nuclei with small equilibrium magnetizations. Nuclei with low natural abundance and/or small gyromagnetic ratio (γ) have intrinsically weak NMR signals. Furthermore these nuclei require relatively long times to reestablish their equilibrium magnetization once perturbed, and hence requires long recovery delays between successive scans. A combination of low signal intensity and long recovery delay results in poor signal-to-noise ratio of NMR spectra obtained by direct polarization (DP) of these nuclei. Enhanced signal-to-noise ratio at considerably shorter experiment times is achieved by transferring magnetization from an abundant spin (*I*) to a rare spin (*S*) through cross-polarization (CP). The theoretical maximum signal gain associated with CP (at the same number of scans as DP) is equal to γ_I/γ_S, which in the case of ^{1}H to ^{13}C CP is 4. A typical CP pulse sequence is composed of a 90° excitation pulse on spin *I*, after which the resulting transverse magnetization is subjected to simultaneous spin-locking fields on *I* and *S* for a period of time known as the contact time, Scheme 3.7.

The amplitude of these locking fields are set at the Hartmann-Hahn matching condition, where both nuclei precess at the same frequencies:

$$\gamma_I B_I = \gamma_S B_S \qquad \text{Equation 14}$$

where B_I and B_S are the magnetic fields of the spin-lock and contact pulses, respectively. During the matching conditions, magnetization transfer occurs from *I* to *S* through heteronuclear dipolar interaction over the contact period. The signal of S builds up via the exchange of magnetization between the two spins, and decays according to $T_{1\rho}$ of I. Achieving the highest signal-to-noise ratio in a CP experiment, therefore requires the optimization of the contact time to allow for maximum transfer before relaxation takes over. Generally the optimum contact time is not identical for all S nuclei within a test sample, making CP a qualitative technique (generally the peak area of each signal in a CP spectrum does not represent the quantity of the corresponding nuclei). CP is also used to establish correlations between *S* atoms located in close proximity to I nuclei. Typically in this case both nuclei are abundant isotopes such as ^{1}H, ^{19}F, and ^{31}P.

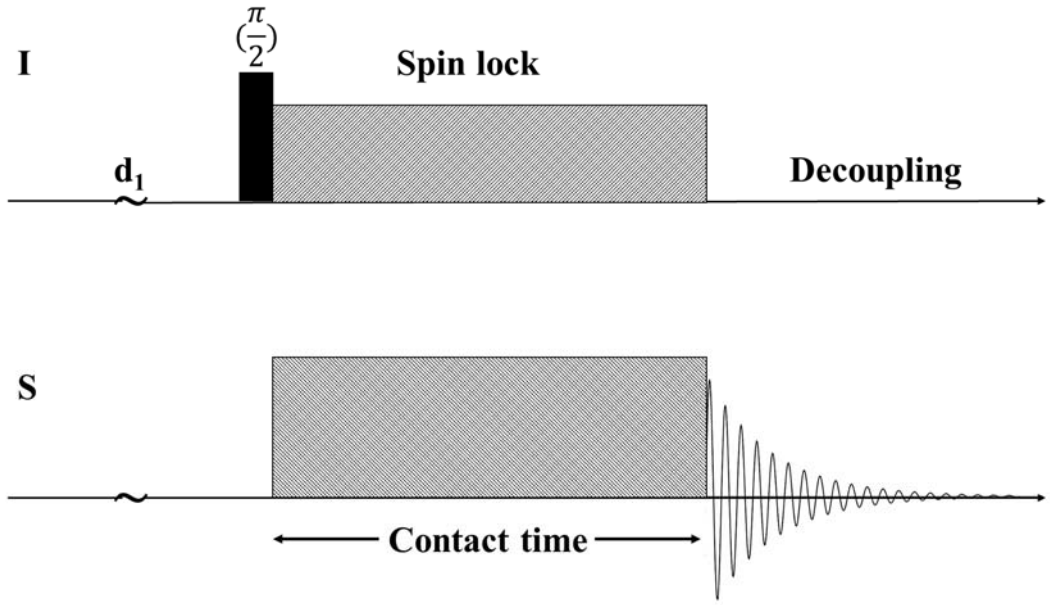

Scheme 3.7. Cross-polarization pulse sequence.

3.3.3. Heteronuclear dipolar decoupling: This technique is used to remove the heteronuclear dipolar coupling during signal acquisition to achieve optimal resolution and signal to noise ratio. In the case of ^{13}C NMR experiments, heteronuclear dipolar interaction with nearby ^{1}H nuclei leads to extensive line broadening. This effect is eliminated by the application of a decoupling RF field on the ^{1}H channel while an FID is recorded on the ^{13}C channel. The decoupling field rapidly rotates the orientation of the protons' magnetizations, averaging them to zero. Several methods have been developed for this purpose, including application of a continuous pulse in CW (continuous wave) decoupling or employing a series of pulses in TPPM (two-pulse phase modulation) decoupling. An efficient heteronuclear dipolar decoupling strategy significantly improves the resolution of the spectrum by reducing the linewidths and increases the signal to noise ratio.

3.4. Spin relaxation

NMR relaxation[123] involves the re-establishment of the spin system's equilibrium state after it was disturbed by the application of RF pulses. A pulse alters the relative population difference between the spin states and creates coherences between them. The populations of the spin states return to the Boltzmann distribution through a process known as longitudinal (spin-lattice) relaxation and the coherences decay via transverse (spin-spin) relaxation. The time constants of longitudinal and transverse relaxation processes are referred to as T_1 and T_2, respectively. Both processes are driven by randomly varying local magnetic fields that arise from the spin interactions modulated by molecular motion. NMR relaxation experiments are powerful techniques to investigate molecular dynamics and to characterize microstructure from the contrast between the motion in various phases or domains within materials.

The state of a spin system subjected to an externally applied static magnetic field changes in time under the influence of the various spin interactions contained in the Hamiltonian operator. The Hamiltonian of each interaction and the total Hamiltonian of a spin system can be divided into two parts:

$$\hat{H} = \hat{H}_0 + \hat{H}(t) \qquad \text{Equation 15}$$

where $\hat{H}_0$ is time-independent and $\hat{H}(t)$ is a random function of time. The time-dependent part originates from random thermal motions which change the orientation of internuclear vectors and electrons with respect to the external magnetic field. From a classical point of view, the variations of spin interactions induced by thermal motions give rise to a randomly fluctuating magnetic field, $\mathbf{B}_t$. Due to the random nature of the fluctuations, B_t averages to

zero over a sufficiently long time. Its magnitude is therefore considered in terms of its root mean square: $\langle B_t^2(t)\rangle^{1/2} \neq 0$. The time dependence of fluctuations is described by an auto-correlation function:

$$G(\tau) = \langle B_t(t)B_t(t+\tau)\rangle = \langle B_t^2(t)\rangle \exp(-\frac{|\tau|}{\tau_c}) \quad \text{Equation 16}$$

In this expression τ_c is the correlation time and $1/\tau_c$ is the correlation rate. The fluctuating field, although orders of magnitude smaller than $\mathbf{B}_0$, induces transitions between the spin states when $1/\tau_c$ approaches to the frequency of coherences of interest. For an uncoupled spin-1/2 system, the transition probability per unit time, from state α to β ($W_{\ominus}$) and from β to α ($W_{\oplus}$) are given by:

$$W_{\ominus} = W(1 - \frac{1}{2}B); W_{\oplus} = W(1 + \frac{1}{2}B); \quad \text{Equation 17}$$

$$W = \frac{1}{2}\langle B_t^2(t)\rangle J(\omega_0);\ B = \frac{\hbar\gamma B_0}{k_B T} \quad \text{Equation 18}$$

where $J(\omega_0) = 2\langle B_t^2\rangle \frac{\tau_c}{1+(\omega_0\tau_c)^2}$ is the spectral density function of B_t at ω_0. The transitions induced by the random field change the populations of the α and β spin states (ρ_α and ρ_β) according to the following equations:

$$\frac{d}{dt}\rho_\alpha = -W_{\ominus}\rho_\alpha + W_{\oplus}\rho_\beta\ ; \qquad \frac{d}{dt}\rho_\beta = +W_{\ominus}\rho_\alpha - W_{\oplus}\rho_\beta \quad \text{Equation 19}$$

Restoration of the total magnetization along the z axis is thus given by:

$$M_z = -2B^{-1}\left(\rho_\alpha - \rho_\beta\right) \Rightarrow M_z(\tau) = (M_z(0) - 1)e^{-2W\tau} + 1 \quad \text{Equation 20}$$

$\frac{1}{2W}$ is the characteristic time of the restoration process which is equal to T_1:

$$T^{-1} = 2W = \gamma^2\langle B_t^2\rangle J(\omega_0) = \gamma^2\langle B_t^2\rangle \frac{\tau_c}{1+(\omega_0\tau_c)^2} \qquad \text{Equation 21}$$

The above equation, describing the correlation time dependence of the transverse relaxation time of an uncoupled spin system, shows that T_1 passes through a minimum at $\tau_c = 1/\omega_0$ (Figure 3.1). In a coupled spin-1/2 system, the double and the zero quantum transitions between the coupled states, with characteristic frequencies of $2 * \omega_0$ and 0, contribute to the relaxation process in addition to the single quantum transitions. This makes the correlation time dependence of T_1 more complex, as motions much faster or slower than $1/\omega_0$ also influence the relaxation.

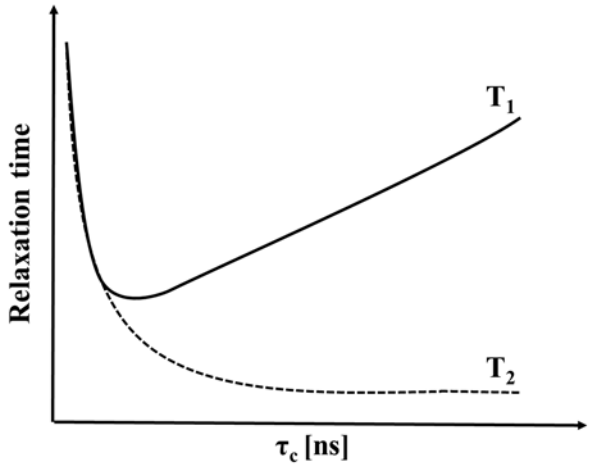

Figure 3.1. Variation of T_1 and T_2 as a function of the correlation time of motion.

Spin-spin relaxation is the irreversible loss of the transverse magnetization due to random interactions between the spins. In a simplified picture of this process, the transverse components of spin magnetization, oriented along the xy plane by the 90° pulse, lose their alignment with time (known as dephasing) leading to decay of NMR signal, while the

population of the spin states may still remain far from equilibrium. Dephasing occurs due to the slight differences in the frequencies of precession of the transverse spin magnetizations that resulted from the lack of uniformity in the local magnetic field throughout the spin system. The variation in the local magnetic field originates from time-independent interactions, giving rise to reversible (coherent) dephasing, in addition to time-dependent interactions that can cause irreversible (incoherent) dephasing. Transverse relaxation is the result of incoherent dephasing, which in the case of spin-1/2 nuclei is predominantly driven by dipolar couplings and the time-dependent part of the chemical shielding interaction. The strength of these orientation-dependent interactions, and thus T_2, are determined by the rate of motion. If molecular motion are much faster (short τ_c) than the time scale of each interaction, its corresponding local magnetic field is averaged over every possible orientation. An average over all orientations is zero, which leads to long T_2. When motion is slower (long τ_c), the averaging is less effective, resulting in stronger interactions thereby faster transverse relaxation, Figure 3.1.

3.4.1. Measurement of relaxation times

Inversion-recovery experiment. This technique is used to measure T_1 in both solution and solid-state NMR. The experiment involves the application of an inversion pulse (180°), followed by a variable delay (τ) period, during which the z magnetization is allowed to recover by spin-lattice relaxation, and terminated with a 90° observation pulse, Scheme 8. A series of spectra are collected, starting with a very short τ, where the signals are completely inverted, to very long delays (typically 5 to 7×T_1), where the signals are fully recovered, Figure 3.2. T_1 is determined by fitting the signal intensities as a function of τ to the following equation:

$$M_z(\tau) = M_\infty + (M_0 - M_\infty)\exp(-\frac{\tau}{T_1}) \qquad \text{Equation 22}$$

where M_0 is the intensity of the inverted signal at $\tau = 0$ and M_∞ is the intensity of the signal at equilibrium. For low natural aboundance nuclei, such as ^{13}C, the inversion recovery sequence can be applied prior to or after cross-polarization (CP) from an abundant nucleus. The former is used to measure T_1 of abundant nucleus and the latter is employed to obtain T_1 of a rare nucleus. In the case of post-CP inversion recovery, it is assumed that the magnetization is in the xy plane after CP, thus a 90° pulse is applied to flip it to the -z axis, Scheme 3.8.

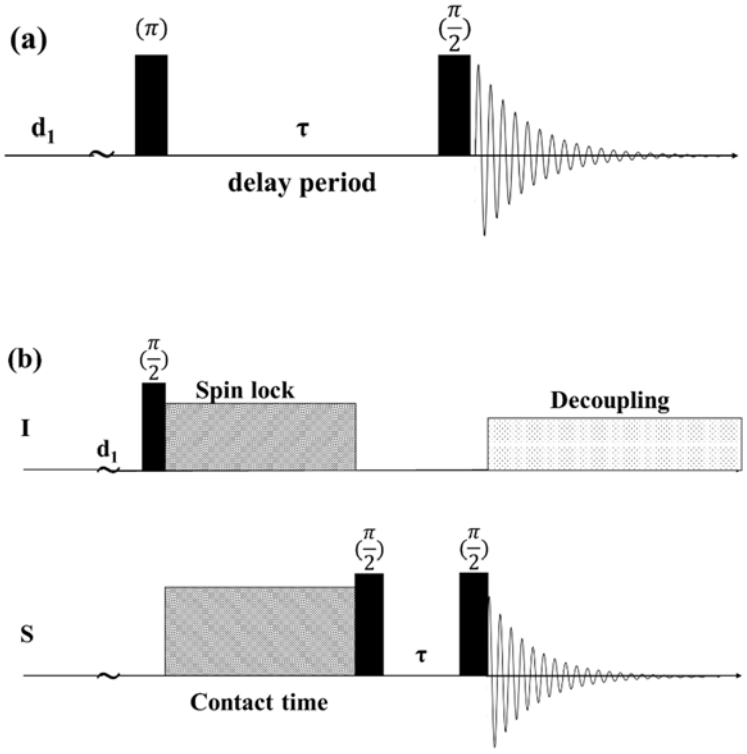

Scheme 3.8. Pulse sequences of (a) inversion-recovery and (b) post-CP inversion recovery experiments.

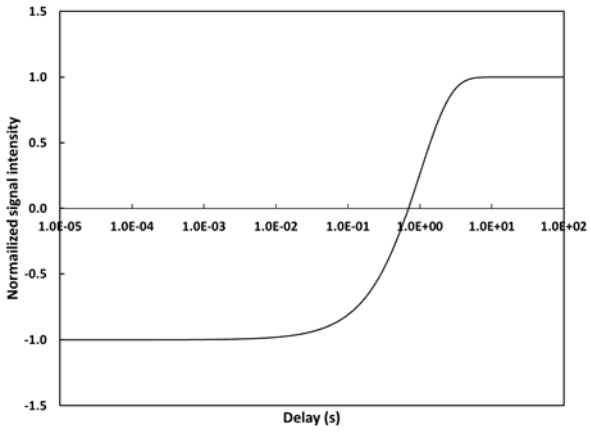

Figure 3.2. Normalized signal intensity as a function of delay time in an inversion-recovery experiment.

Hahn-echo. This is one of the most common techniques for the measurement of T_2 in the solid state. In this experiment the transverse magnetization, prepared by a 90° pulse, is allowed to evolve for a period of τ, after which a 180° pulse is applied followed by another τ period, Scheme 3.9. During the first delay period, the magnetization dephases by both coherent and incoherent processes. Rotation of the transverse magnetizations by 180° around the axis of first pulse, reverses sense of dephasing caused by coherent processes in the first delay period due to the isotropic chemical shielding and any inherent inhomogeneity of the external magnetic field, during the second delay period. This leads to the refocusing of the coherently dephased components of the transverse magnetization and the formation of an echo at 2τ. The loss of magnetization due to the incoherent processes, however, is not reversible which results in the decay of signal intensity. A series of spectra are collected with increasing delay period, from which the intensity of signal is extracted as a function of τ. T_2 is obtained by fitting an exponential decay function to the experimental data.

$$M(\tau) = M(0)epx(-\frac{\tau}{T_2})$$ Equation 23

If a signal is composed of two components with comparable intensities and significantly different T_2 values, a bi-exponential decay takes place. This occurs in materials where nuclei are located in domains with different dynamics, thus experiencing different rates of incoherent dephasing. Fitting a bi-exponential function to such a decay curve gives two T_2 values corresponding to the mobile and rigid environments. Like the inversion recovery pulse sequence, the 180° can be applied pre or post cross-polarization, Scheme 3.9.

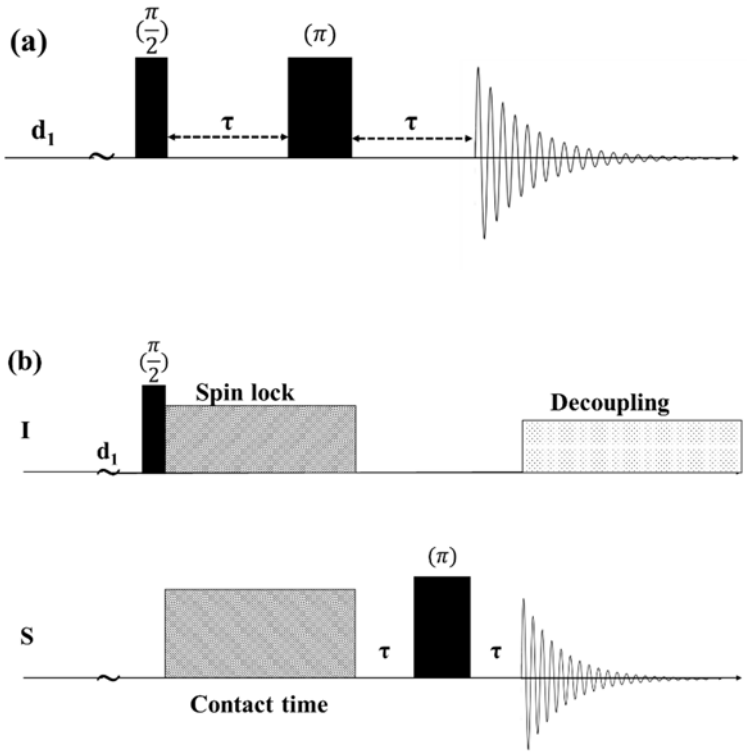

Scheme 3.9. Pulse sequences of (a) Hahn-echo and (b) post-CP Hahn-echo experiments.

Car-Purcell-Meiboom-Gill (CPMG) experiment. This technique is the other common approach to measure T_2. Analogously to the Hahn-echo experiment, a 180° pulse is applied to refocus the coherently dephased transverse magnetization and thereby create an echo, Scheme 3.10. In this experiment, a train of τ-180°-τ are applied n times, during which the transverse magnetization dephases only by incoherent processes. A spectrum is collected for each n = 1, …, n ($2n \times d_2 > 7 \times T_2$). T_2 is obtained by fitting an exponential decay function to the resulting signal intensity versus delay curves.

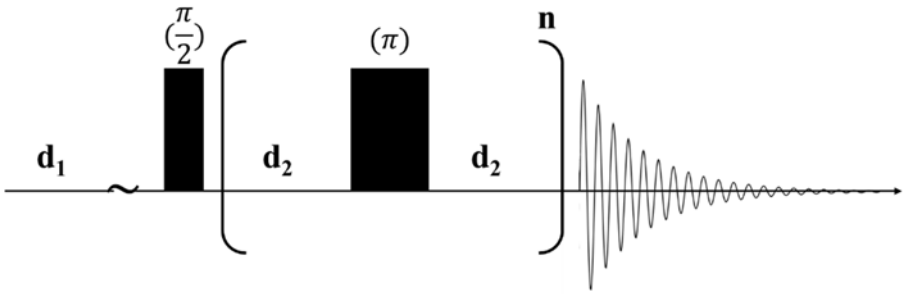

Scheme 3.10. Pulse sequences of CPMG experiment.

3.5. Fourier-transform infrared spectroscopy

FTIR spectroscopy is a well-established, widely used technique for characterization of the structure of organic compounds. A mode of internal vibration of a molecule can cause IR radiation to be absorbed if the motion leads to oscillation of the molecular dipole. Absorption occurs when such vibration is excited by on-resonance IR radiation. Molecules can have various modes of vibrations, involving symmetric and asymmetric stretches along the bond axis as well as bending modes such as scissoring, rocking, wagging, and twisting. The resonance frequencies of these modes are determined by the bond lengths, the bond

stiffness, and the masses of the atoms. For example, the vibration frequency of the stretching mode of a single bond is given by:

$$\nu \propto \sqrt{\frac{k}{\mu}} \text{ where } \mu = \frac{m_1 \cdot m_2}{m_1 + m_2} \qquad \text{Equation 24}$$

where ν is the wavenumber ($\nu = 1/\lambda$; λ is wavelength), k is the force constant of the bond, m_1 and m_2 are the masses of the atoms, and μ is the reduced mass. Modes with high symmetry that do not lead to oscillation of the molecular dipole can be detected using Raman spectroscopy.

In this study, FTIR spectroscopy was used to detect the presence of functionalities that are not observable by ^{1}H and ^{13}C NMR (*e.g.* NO_3^- anion), to characterize insoluble compounds (*e.g.* silver-nonanethiolate), and to investigate the transformations in functional groups. A major drawback of FTIR, which is more pronounced in the case of complex materials such as polymers, is that extensive overlap between various absorptions can obscure relatively weak characteristic bands of interest.

3.6. Ultraviolet-visible spectroscopy

This technique measures the absorption of ultraviolet and visible light by materials. UV-visible absorption by molecules occurs when the outer electrons are excited from the highest occupied molecular orbital (HOMO) to the lowest unoccupied molecular orbital (LUMO) by the incident light. According to the Beer-Lambert law, the absorbance (A) is directly proportional to the distance the light travels through the material (l), the molar absorptivity (ε), and the concentration of the absorbing material:

$$A = \frac{I}{I_0} = \varepsilon lc$$ Equation 25

Here, I_0 and I are intensities of the incident and the transmitted light, respectively.

An alternative origin of absorption in the visible spectral region, which is of special interest in this work, is the localized surface plasmon resonance of noble metal nanoparticles. Localized surface plasmons (LSP) are collective oscillations of the free conduction electrons in the metallic nanoparticles induced by interaction with light. When the frequency of the incident photons matches that of the LSP, the conduction electrons that are spatially confined to the boundaries of the nanoparticle, undergo coherent oscillations, Figure 3.3. This results in light absorption and enhancement of the local electromagnetic field at the surface of the nanoparticle. The resonance frequency is determined by several factors including the size and shape of the nanoparticles as well as the dielectric properties of their surrounding environment. In this work, UV-visible spectroscopy was used to confirm conversion of colored functional groups and study the LSPR of silver nanoparticles.

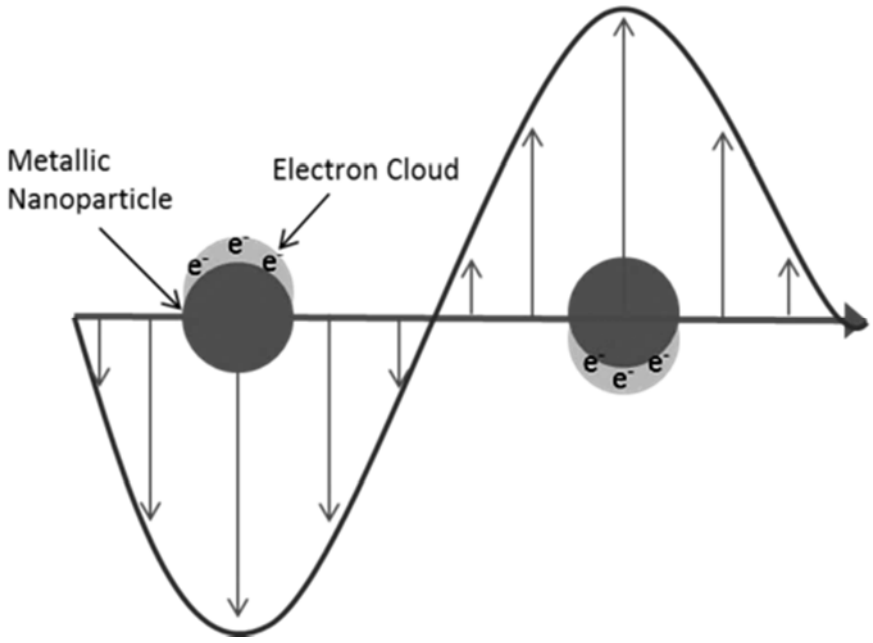

Figure 3.3. Schematic representation of LSPR upon interaction with light [Retrieved from http://nanocomposix.com/pages/plasmonics-and-nanophotonics].

3.6. Transmission electron microscopy (TEM)

TEM is a high resolution microscopy technique which provides information on ultrafine morphological and structural features of samples on the nanometer scale. This ability is afforded by utilizing a high energy beam of electrons for imaging, instead of a beam of light. Theoretically, the maximum resolution in optical microscopy is limited by the wavelength of photons. The de Broglie wavelength of electrons (λ_e) is orders of magnitude smaller than photons, thus allowing them to resolve features on a much smaller scale. For example, an electron with kinetic energy (E) of 1 eV, and a rest mass (m_0) of 0.511 μeV/c^2 (c is the speed of light) has de Broglie wavelength of 1.23 nm, which is about a thousand times smaller than a photon with the same kinetic energy:

$$\lambda_e \propto \frac{h}{\sqrt{2m_0E(1+\frac{E}{2m_0c^2})}}$$ Equation 26

A TEM image is formed from the changes in the intensity of the incident electron beam when it passes through the specimen. In the commonly employed "bright field" imaging mode, which is used in this work, variations in the intensity of the transmitted beam across the sample creates contrast between regions differing in electron density. Brighter spots in the image represent regions with lower electron density where a large fraction of the beam is transmitted, while darker spots show regions with high electron density where only a small fraction of the beam can pass through the sample. In this work, TEM was used to measure the size and dispersity of the silver nanoparticles, which appear as dark regions in the images due to the substantially higher electron density of the silver nanocrystals in comparison to their organic surfactants.

3.7. Differential scanning calorimetry (DSC)

DSC is widely used to measure the thermal properties of materials such as the temperature and enthalpy of phase transitions and heat capacities. These properties are determined by monitoring variations in flow of heat between the test specimen and a reference material. The instrument precisely measures the difference between the heat flows to the sample and the reference over a range of temperature or a period of time, while keeping both at the same temperature. The reference is a material with well-known thermal characteristics over the temperature range of the experiment. The difference in heat flows is thus associated with the change in temperature of the sample. The outcome of experiment

is normally represented by a plot of sample heat flow (q_s) versus temperature, known as DSC thermogram, Figure 3.4. If the sample remains in a given phase (*e.g.* solid or liquid, crystalline or amorphous), its heat capacity (c_p) is calculated from the slope of the thermogram:

$$c_p = \frac{1}{m}\frac{dq_s}{dT} \qquad \text{Equation 27}$$

where m is the mass of the sample. A change in the slope of the DSC thermogram usually indicates a second-order phase transition such as the glass transition in polymers. When the specimen undergoes a first-order phase transition, such as melting or crystallization, the heat flow required to keep its temperature the same as the reference varies depending on whether the process is endothermic or exothermic. This variation is associated with the enthalpy of the transition, which is determined from the area under the peak. It should be mentioned that besides the measurement of basic thermal properties, analysis of DSC thermograms acquired under various conditions, provides a host of information on the microstructure of crystalline, semi-crystalline, and amorphous materials.

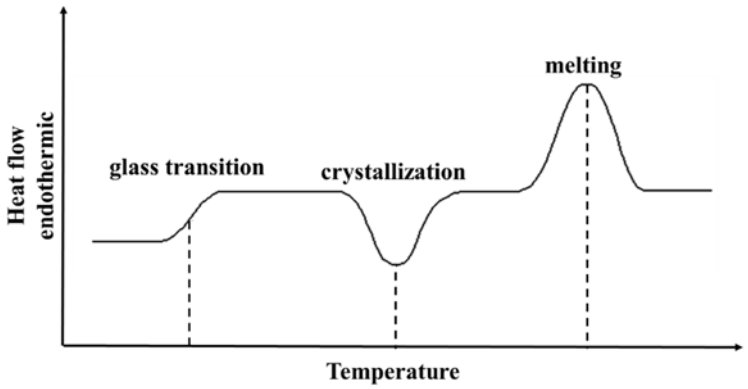

Figure 3.4. Schematic representation of a DSC thermogram showing first-order (crystallization and melting) and second-order (glass transition) transitions.

3.8. Gel permeation chromatography (GPC)

GPC is primarily used to determine the average molar mass and the molar mass distribution of polymers. Typically, all the polymer molecules within a sample do not have the same degree of polymerization and thus their molar mass varies. Accordingly, the molar mass of the sample is described by an average value, where the number average molar mass (M_n) and the weight average molar mass (M_w) are the most commonly used:

$$M_n = \frac{\sum M_i N_i}{\sum N_i} \qquad \text{Equation 28}$$

$$M_n = \frac{\sum M_i^2 N_i}{\sum M_i N_i} \qquad \text{Equation 29}$$

Here N_i is the number of molecules with molar mass of M_i.

When the polymer is dissolved in a good solvent, the hydrodynamic radius of each molecule is directly related with its molar mass[124]. In simple terms, molecules with higher molar masses can be represented by larger spheres. In the GPC experiment, the polymer molecules travel in the solvent (mobile phase) through a column packed with highly porous rigid particles (stationary phase). Low molar mass polymer molecules which have smaller hydrodynamic radii spend more time in the porous material while the larger high molar mass polymer molecules spend more time in the mobile. This provides the basic mechanism for separation of molecules with different molar masses. The retention time is determined by the fraction of time spent in the mobile phase, hence small molecules elute more slowly than the large ones. A basic GPC instrument gives retention time and the mole fraction of each group of molecules. The retention time is correlated with molar mass via comparison with a calibration curve obtained by performing the experiment on a set of reference

samples. Knowing the molar mass and mole fraction of each group, one can calculate various averages of molar mass and obtain the molar mass distribution curve, Figure 3.5.

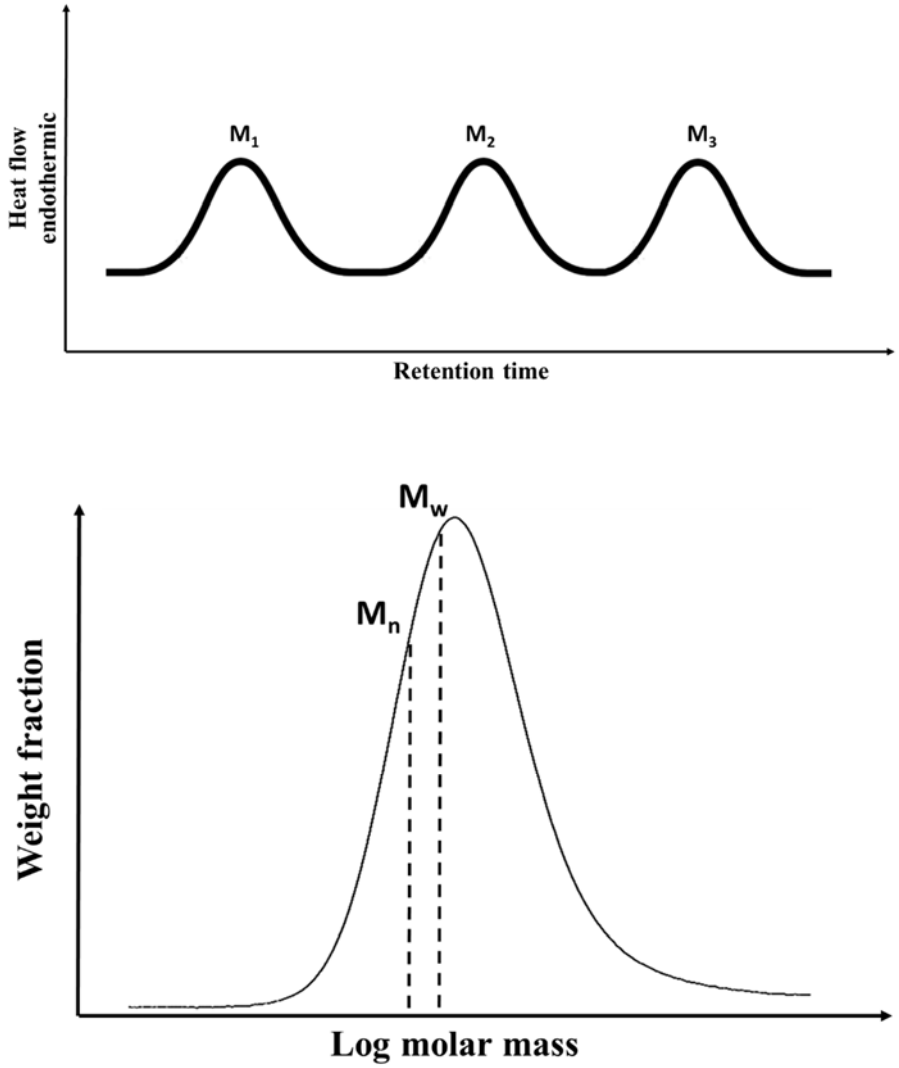

Figure 3.5. (Top) GPC traces of groups of polymer molecules with molar masses of $M_1 > M_2 > M_3$. (Bottom) Molar distribution of a polymer sample. The number and weight averages are shown on the distribution curve.

Chapter 4. Alkanethiol capped silver nanoparticles

Since its introduction in 1994, the two-phase synthetic procedure proposed by Brust and Schiffrin[19] and its subsequent modifications[20] have been the predominant protocols for the preparation of alkanethiol capped noble metal nanoparticles. Despite the success of this method in the synthesis of small and uniform gold nanoparticles, its application for silver has been hampered by the difficulty in obtaining pure product and poor solubility of the resulting nanoparticles. In this chapter, first a basic characterization of the alkanethiol-capped SNP prepared via the two-phase method is presented. This is followed by a detailed investigation into the intermediate step of this synthetic procedure[125]. Furthermore, the structure and dynamics of the surface grafted alkanethiols are studied.

4.1. Experimental

4.1.1. Materials

All reagents and solvents were purchased from Sigma-Aldrich and used as received. Deuterated NMR solvents used in this work were purchased from Cambridge Isotope Laboratories.

4.1.2. Synthesis

Alkanethiol protected silver nanoparticles. The silver nanoparticles (SNP) were prepared according to a slightly modified Brust and Schiffrin two-phase method. 15 ml of 0.03M silver nitrate ($AgNO_3$) solution in deionized water was stirred with 10 ml of 0.2 M

tetraoctylammonium bromide (TOAB) solution in toluene-d8 for 90 minutes. This process is referred to as the "phase-transfer step" throughout this thesis. More than 95% of the silver nitrate was transferred to the organic phase as determined by gravimetry. The organic phase (phase-transferred solution) was transferred to a clean round bottom flask into which 0.85ml nonanethiol (NT) or 0.125gr octadecanethiol (ODT) was added. To this 12ml of freshly prepared 0.43 M aqueous (deionized water) solution of sodium borohydride ($NaBH_4$) was added rapidly under vigorous stirring. After this mixture was stirred for three hours, the organic phase (dark brown) was separated from the clear aqueous phase. The product was first precipitated in ethanol, separated by centrifugation and then was washed copiously with chloroform, toluene, and water. The complete removal of TOAB and any unreacted alkanethiol was confirmed by solution NMR spectroscopy.

Phase-transferred and intermediate compounds. The product of the phase-transfer step was studied by examining three samples differing in the mole ratio of TOAB to $AgNO_3$. These samples were made according to the aforementioned procedure, where the amounts of TOAB and solvent were kept constant while varying the concentration of $AgNO_3$ to set the TOAB:$AgNO_3$ mole ratio to 4.4, 2, and 0.5. Toluene-d_8 was used as the solvent. The samples were denoted as AT-4, AT-2, and AT-0.5 respectively, Table 4.1. The AT-4 sample has exactly the same composition as the material obtained from the first step of the two-phase reaction. The intermediate compounds were prepared by adding 0.85 ml nonanethiol to AT-4 solution and stirring it for 24 hours. The duration of this step was much longer than in the conventional two-phase method to give sufficient time for any possible reaction between the phase-transferred material and nonanethiol. The samples taken from the reaction mixture after addition of nonanethiol were named ATNT-x (ATNT:

Ag/TOAB/Nonanethiol mixture), where x indicates the time (in hours) the sample was stirred with nonanethiol.

Table 4.1. Reactant ratios of the phase-transferred samples.

Sample name	AT-4	AT-2	AT-0.5
TOAB/AgNO3 mole ratio	4.4	2	0.5

Silver nonanethiolate (AgNT). AgNT was synthesized by mixing $AgNO_3$ (0.5 mmol) with nonanethiol (1 mmol) in 8 ml THF/water mixture (3:1) for 24 hours. The product was collected as a white powder after complete removal of the reaction solvent. This material is not soluble in water or common organic solvents.

Tetraoctylammonium bromide capped silver nanoparticles and ligand exchange. TOAB capped SNP were synthesized via reduction of the AT-4 without addition of alkanethiols. 14.6 mg AT-4 dissolved in 15 ml toluene was reduced by 3.2 ml of 0.08 M aqueous solution of $NaBH_4$. The reaction mixture was stirred overnight at room temperature. Ligand exchange was performed by adding 0.05 M solution (10 ml) of NT or ODT in toluene to the solution of TOAB-caped SNP, and stirring them for three hours.

4.1.3. Techniques

UV-visible spectroscopy. UV-visible spectra of dissolved test materials were recorded on a Cary 50 spectrophotometer. The experiments were conducted in the wavelength range of 300 nm to 700 nm at room temperature. For each spectrum, the baseline was corrected by subtracting the absorption of the cuvet and the pure solvent.

Transmission electron microscopy (TEM). TEM micrographs were obtained with a Hitachi H-7500 transmission electron microscope operating at 100 KV accelerating voltage. Each TEM sample was prepared by putting a drop of dilute nanoparticle solution on a 400-mesh carbon-coated copper grid. The excess solution was removed with filter paper and the grid was allowed to dry at room temperature overnight. Average particle size and size-dispersity were determined by measuring the Feret diameters of at least 200 nanoparticles for each sample using ImageJ software.

Solution-state NMR spectroscopy. NMR spectra were recorded at ambient temperature with a 300 MHz Bruker Avance II NMR spectrometer equipped with a 5 mm HX BBO probe. Higher resolution spectra were acquired on a Bruker Avance III HD 700 MHz NMR Spectrometer. Calculations based on five separate measurements on the same sample gives a standard deviation of 0.0012 for the ^{1}H NMR chemical shifts, which is very close to the non-zero-filled FID digital resolution of the experiments.

Fourier transform infrared (FTIR) spectroscopy. FTIR spectroscopy was performed at ambient temperature with a Bruker Alpha infrared spectrometer.

Raman spectroscopy. Raman spectra were collected on a Bruker RFS 100 FT Raman spectrometer with a quartz beam splitter using Nd:YAG laser for excitation. Measurements were done at room temperature with spectral resolution of 2 cm-1 and laser power of 150 mW.

Solid-state NMR (SSNMR) spectroscopy. SSNMR experiments were carried out on a 500 MHz widebore Varian Inova spectrometer equipped with 4 mm Varian T-3 HFXY probe at 8 kHz magic angle spinning rate and T = 20°C. The 90° pulse lengths were

calibrated to 3-3.5 μs for both ^{1}H and ^{13}C. All ^{13}C spectra were acquired through cross-polarization with a 2.4 ms contact time (optimized for maximum signal-to-noise ratio), using constant 1H locking field (60 kHz), and a ramped ^{13}C locking field (from 73 to 77 kHz). Longitudinal (T_1) and transverse (T_2) relaxation times of ^{13}C were measured via post-cross-polarization (post-CP) inversion-recovery and post-CP Hahn-echo experiments, respectively. The interpulse delays were rotor-synchronized in the Hahn-echo experiment by setting them to multiples of the rotor period.

Differential scanning calorimetry (DSC). DSC of samples dried at room temperature (to keep their thermal history consistent with other experiments) were carried out on a TA Q20 thermal analyzer (TA Instruments) over a temperature range of 20-150 °C. The scan rate was set at 10 °C/min, and dry nitrogen gas was used for temperature regulation and purging the sample compartment.

Elemental analysis (EA). Elemental analyses were performed using an Elementar Vario Microcube instrument.

4.2. Basic characterization of the alkanethiol-capped nanoparticles

Basic characteristics of the alkanethiol-capped SNP, including their shape, size and size distribution can be readily determined from transmission electron microscopy (TEM) and UV-visible spectroscopy. Typical TEM images of the nonanethiol-capped silver nanoparticles (SNPNT) and octadecanethiol-capped nanoparticles (SNPODT) are shown in Figure 4.1. Close examination of these TEM images reveals that both the SNPNT and SNPODT nanoparticles have faceted morphology with average diameters (determined

from measuring the Feret diameter of at least 600 particles) of 3.7±0.9 nm and 4.2±1.0 nm, respectively. The major fraction of each sample is composed of the nanoparticles with uniform size and shape which tend to arrange into ordered 2D and 3D lattices on the TEM grid. Such ordered structures are formed as a result of the interactions between the metallic cores and the surface grafted alkane chains on the neighboring nanoparticles which is facilitated by their faceted morphology. The average interparticle distances in the ordered regions are smaller than the length of a fully-extended (all-*trans* conformation) alkane chain, which can be attributed to the interdigitation of the capping ligands of the adjacent particles. Further information on the microstructure of the protecting layer has been obtained through FTIR and solid-state NMR spectroscopy.

The UV-visible spectra of the dissolved NT and ODT capped nanoparticles shows intense absorption peaks at wavelengths of 421nm and 433nm, respectively, due to the localized surface plasmon resonance of the silver core, Figure 4.2. This phenomenon, which originates from collective oscillation of the conduction electrons in resonance with the electric field of the incident light, provides a simple approach to verify the formation of SNP by UV-visible spectroscopy. The wavelength and shape of the absorption spectrum is determined by the average size and size distribution of the nanoparticles. For both capping agents, the surface plasmon resonance peaks are not completely symmetric, as the result of the nonuniform size and shape of the nanoparticles. The relative red shift of the SNPODT light absorption compared to that of SNPNT can be attributed to their larger average size, which was verified by TEM.

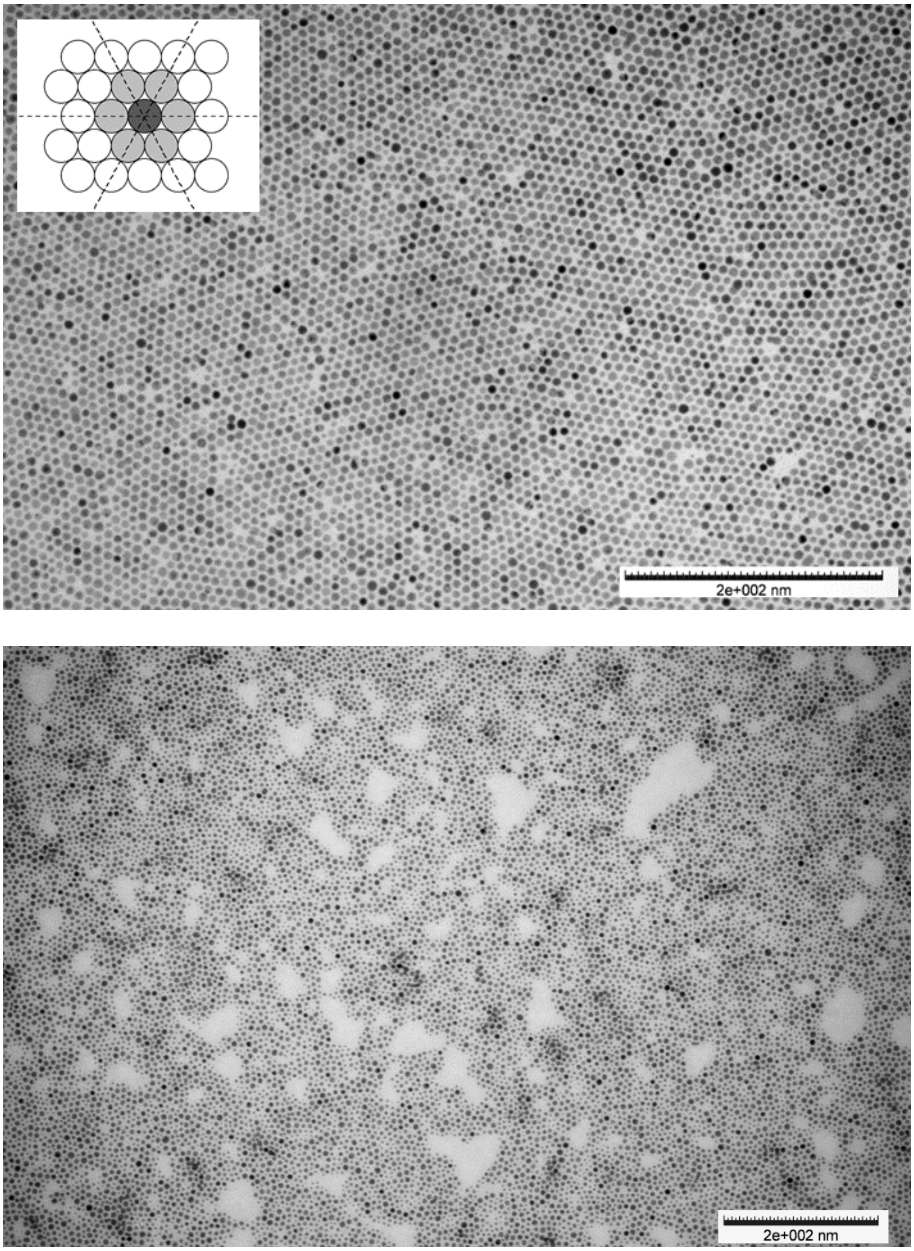

Figure 4.1. TEM micrographs of the SNPNT (top) and the SNPODT (bottom) samples. The inset shows a schematic representation of the 2D arrangement of the nanoparticles.

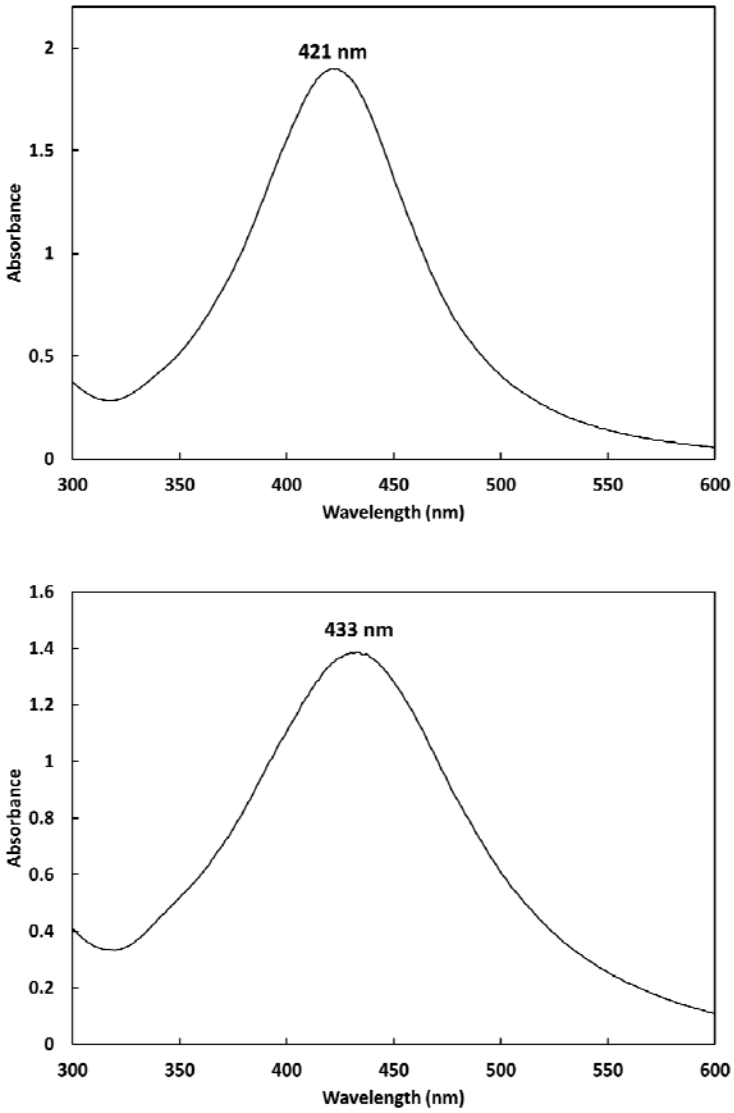

Figure 4.2. UV-visible spectra of (left) the SNPNT and (right) the SNPODT solutions in toluene.

The mole ratios of carbon, hydrogen and sulfur atoms in SNPNT and SNPODT samples, determined from elemental analysis, are presented in Table 4.2. The experimental mole ratios of these elements are in good agreement with those calculated from the chemical formula of the neat nonanethiol and octadecanethiol. Nitrogen was not detected in these samples implying that the phase transfer catalyst (tetraoctylammonium bromide)

was completely removed by the work-up procedure. The capping agent to silver mole ratios was determined by assuming that silver is the only undetected element in the nanoparticles. Interestingly, the mole ratios are the same for both SNPNT and SNPODT despite the difference in the initial ratios of the reactants used for preparation of these nanoparticles. These results indicate that, depending on the reaction conditions, only a certain mole fraction of the capping ligands are adsorbed on the nanoparticles. The fraction of surface grafted capping agents (grafting density) is determined by factors such as the rates of growth and stabilization of the nanoparticles, and their average size. The stability of the nanoparticles was evaluated by taking their TEM images after being exposed to air at room temperature for several months. The images show noticeable coalescence of nanoparticles which leads to formation of large and irregular clusters, Figure 4.3.

Table 4.2. Elemental analysis of the SNPNT and the SNPODT samples.

Mole ratios	Samples			
	SNPNT		SNPODT	
	Calculated*	Experimental**	Calculated*	Experimental**
C/H	0.45	0.47	0.47	0.48
C/S	9.00	8.91	18.00	18.61
H/S	20.00	18.88	38.00	38.40
Alkanethiol/Ag	0.79	1.00	0.79	0.89

* Values calculated based on the molecular formula of the alkanethiols and the initial amount of reactants used in the synthesis.

** Experimental values obtained from elemental analysis

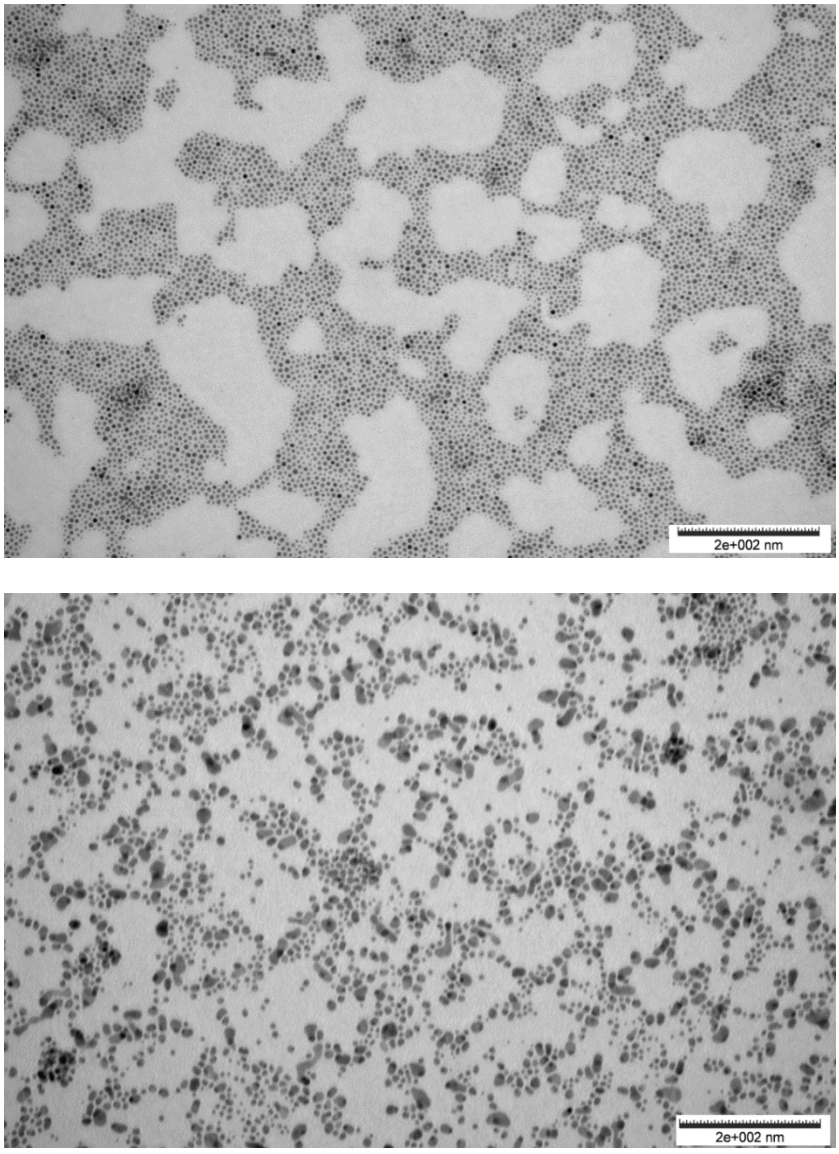

Figure 4.3. TEM micrographs of the SNPODT sample 1 day (top) and 10 months (bottom) after preparation. The images were taken from the same TEM grid.

4.3. Investigation of the two-phase method

As was shown in the previous section, the two-phase method produces small and uniform alkanethiol-capped SNP. These nanoparticles lose their stability during work-up and only a fraction of the dried product can be redispersed in a solvent. This is likely caused by the formation of insoluble by-products, such as Ag(I)-thiolate, during the reaction or

post-synthesis aggregation of the nanoparticles. It is therefore of prime importance to identify and characterize the species formed during the two-phase synthesis of silver nanoparticles in order to improve yield, stability, and solubility of the product.

4.3.1. Identification of the major reaction intermediate

High resolution NMR spectra of samples from the reaction mixture prior to the addition of reducing agent were obtained in toluene-d_8. Figure 4.4 shows the NMR spectra of TOAB and the phase-transferred solution (AT-4). The ^{1}H and ^{13}C resonances are labeled according to Scheme 4.1. Both samples were prepared with equal amounts of $[TOA]^+$ to avoid any variation in chemical shifts due to concentration differences. The sharp peak at 3.0 ppm originates from the residual water in the organic phase. As indicated in Figure 4.4, the signal of H_1, which is the closest proton to the ionic center of the $[TOA]^+$ group, is shifted from 3.553±0.001 ppm in TOAB to 3.349±0.001 ppm in the AT-4 sample. The frequency of H_2 also experiences a smaller change (from 1.673±0.001 ppm in TOAB to 1.632±0.001 ppm in AT-4, Table 4.3), while the chemical shifts of the protons located further from the ionic center remain relatively unaltered. The variation in frequency of H_1 upon formation of the phase-transferred product makes this signal a sensitive probe to detect structural changes in this material during the course of the reaction. Also note that the splitting pattern in the H_1 signal (AA′BB′ pattern) implies predominance of *trans* rotamer and hence restricted motion in the corresponding CH_2, which renders the protons magnetically nonequivalent. This magnetic nonequivalence fades by moving towards the octyl chain end, as the CH_2 moieties become more mobile.

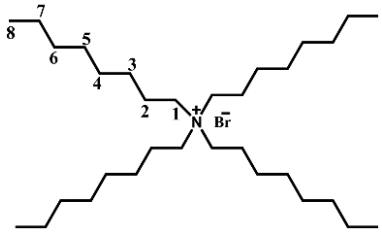

Scheme 4.1. Schematic representation of tetraoctylammonium bromide.

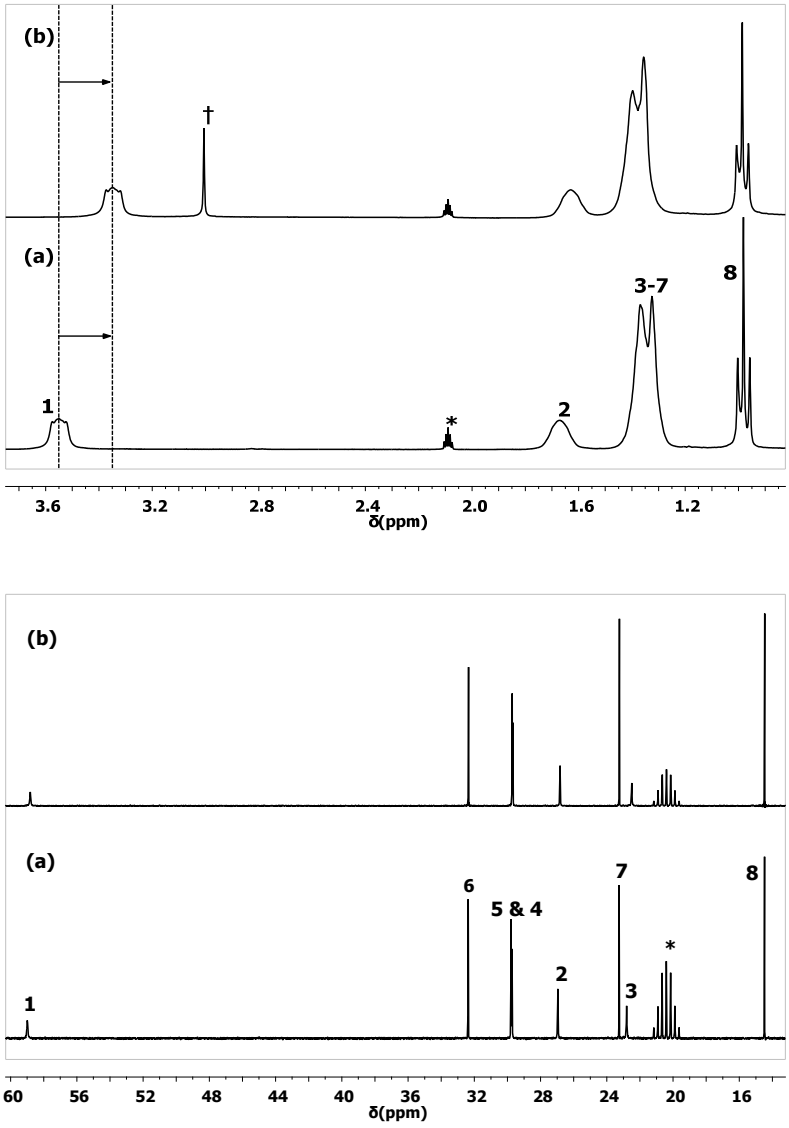

Figure 4.4. ^{1}H (top) and ^{13}C (bottom) NMR spectra of (a) TOAB and (b) AT-4 in toluene-δ_8. The solvent and residual water peaks are indicated by * and † [Adapted with permission from Ref 125. Copyright 2015 American Chemical Society].

Table 4.3. Chemical shifts of selected ^{1}H and ^{13}C signals of the TOAB and AT-4 samples.

	H_1 (ppm)	H_2 (ppm)	C_1 (ppm)	C_2 (ppm)	C_3 (ppm)
TOAB	3.55	1.67	58.98	26.95	22.81
AT-4	3.35	1.63	58.81	26.82	22.51

The ^{1}H NMR spectra of the reaction mixtures, nonanethiol and TOAB are shown in Figure 4.5. The chemical shifts and relative intensities of the octyl chain resonances in both ATNT-0 (the sample tested right after addition of nonanethiol) and ATNT-24 (the sample tested 24 hours after addition of nonanethiol) are identical to those of the complexes formed during phase transfer. The characteristic ^{1}H peaks of the residual water and nonanethiol, except for the resonance of SH hydrogen, remain unchanged up to 24 hours. The slight shift of the thiol signal to higher frequency might be due to its interaction with water. The stability of the complex in presence of nonanethiol is further verified in the ^{13}C NMR spectra of the AT-4 and the ATNT-24 (Figure 4.6). Similarly to the ^{1}H spectra, the carbon signals of octyl chains coincide in both samples and the position of the nonanethiol resonances do not change with respect to pure nonanethiol. The same trend was observed for the phase-transfer of $AuCl_4$ anions in the synthesis of gold nanoparticles[27].

The transfer of ionic species from the aqueous to the organic phase occurs via their complexation with $[TOA]^+$ during the phase-transfer step. Complexation of $[TOA]^+$with counterions differing in size and charge density (in comparison to Br^-) likely leads to changes in the average electronic environment of the proton and carbon nuclei of the octyl chains. As a result, one would expect differences in the ^{1}H and ^{13}C chemical shifts of

$[TOA]^+$ in different complexes, depending on the nature of the counterion and mobility in the octyl chains. This effect would be most pronounced for the nuclei proximal to the ionic center, which have restricted mobility compared to those located further down the chain. The observed difference between the chemical shifts of H_1 protons of AT-4 and TOAB, which is two orders of magnitude larger than the measurement uncertainty, therefore could be considered as evidence for the formation of new complexes in AT-4. This is consistent with the variations in the NMR frequency of H_1 protons upon complexation of $[TOA]^+$ with $[AuCl_4]^-$ in the synthesis of gold nanoparticles[27]. The observed insensitivity of H_1 chemical shift to addition of nonanethiol, thereby implies that the complexes formed during the phase-transfer remain unaltered prior to the reduction step.

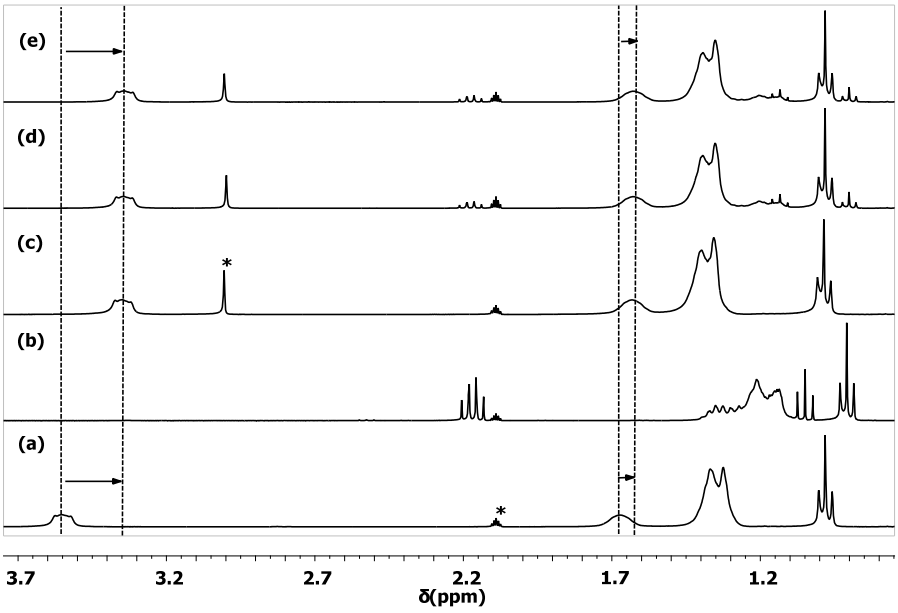

Figure 4.5. ^1H NMR spectra of (a) TOAB, (b) nonanethiol, (c) as-prepared AT-4, (d) ATNT-0, and (e) ATNT-24. The solvent (2.1 ppm) and the residual water (3.0 ppm) peaks are indicated by asterisks. The arrows show displacement of various H_1 signals [Adapted with permission from Ref 125. Copyright 2015 American Chemical Society].

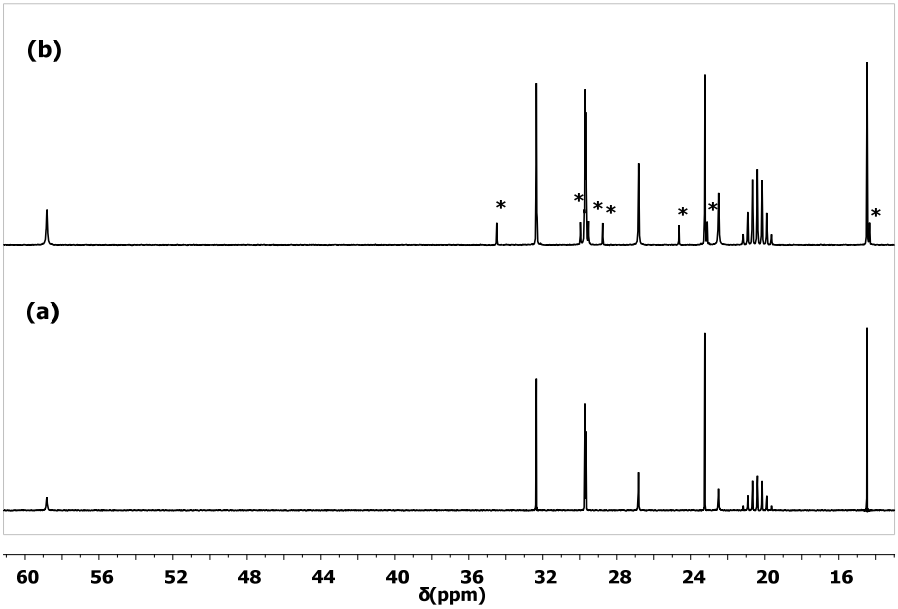

Figure 4.6. ^{13}C NMR spectra of (a) AT-4 and (b) ATNT-24 samples. The resolved peaks corresponding to nonanethiol in the ATNT-24 sample are indicated by asterisks [Adapted with permission from Ref 125. Copyright 2015 American Chemical Society].

Further investigation into the structural changes in the intermediate compounds formed prior to the addition of the reducing agent was pursued by Raman and FTIR spectroscopies. These methods allow for characterization of the insoluble AgNT, which may form upon addition of nonanethiol to the phase-transferred mixture, and comparison of this compound with the samples extracted from the reaction mixture. A comparison between the FTIR spectra of pure nonanethiol and AgNT (Figure 4.7, Table 4.4) shows that the symmetric and asymmetric methylene stretching modes of the latter (2846 and 2915 cm^{-1}) are shifted to lower wavenumbers and that sharp medium-intensity CH_2 wagging bands emerge at 1191, 1225 and 1262 cm^{-1} (indicated by asterisks in Figure 7). These changes indicate the predominance of all-*trans* segments in AgNT, which corresponds to a high degree of conformational ordering in the alkyl chains.[126-127] This conclusion is further

verified with the Raman spectrum of AgNT (Figure 4.8) where the $(C\text{-}S)_{gauche}$ stretch in pure nonanethiol at 655cm^{-1} is replaced by a sharp $(C\text{-}S)_{trans}$ mode at 720cm^{-1} with a concomitant increase in the relative intensities of the $(C\text{-}C)_{trans}$ bands (1062 and 1122cm^{-1})[128]. Moreover two new overlapping bands at 371 cm^{-1} and 383 cm^{-1} are observed in the frequency range commonly attributed to a stretching mode of the sulfur-silver bond[38-39].

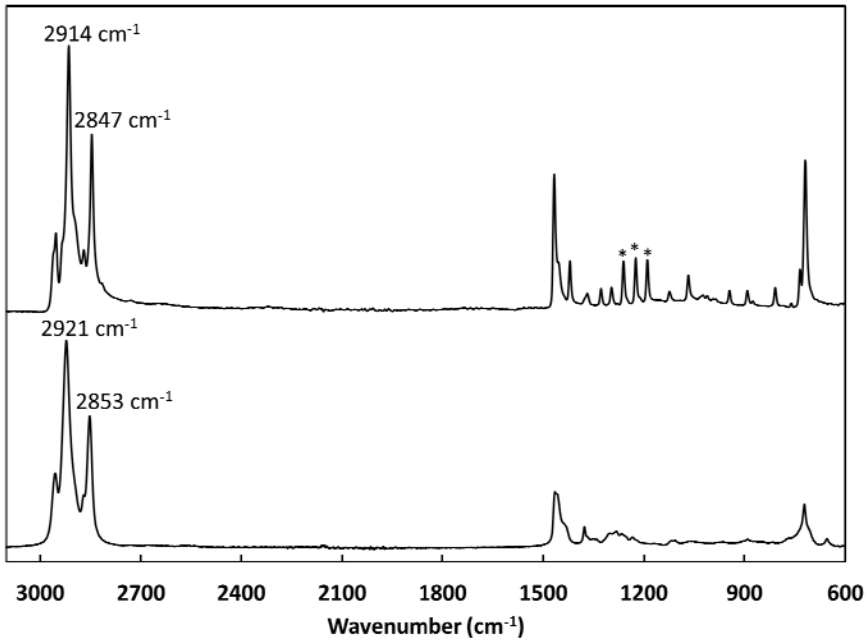

Figure 4.7. FTIR spectra of neat nonanethiol (bottom) and silver-nonanethiolate (AgNT) compound (top). Displacement of the methylene stretching modes and appearance of the new CH_2 wagging bands are indication of conformational ordering in AgNT [Adapted with permission from Ref 125. Copyright 2015 American Chemical Society].

Table 4.4. Selected FTIR bands of AgNT.

Wavenumber (cm^{-1})	718	1191	1225	1262	1467	2846	2915
Assignment	$\delta_{(CH2)}$	$\omega_{(CH2)}$	$\omega_{(CH2)}$	$\omega_{(CH2)}$	$\delta_{(CH)}$	$\nu_{s(CH)}$	$\nu_{as(CH)}$

δ: bending, ω: wagging, ν_s: symmetric stretching, ν_{as}: asymmetric stretching

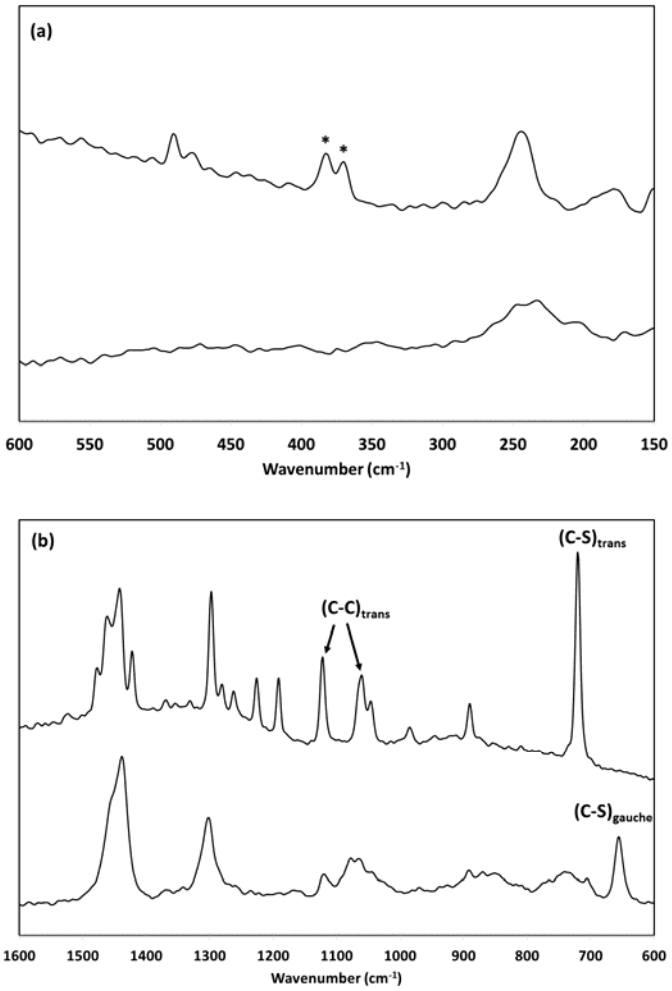

Figure 4.8. Raman spectra of (bottom) nonanethiol and (top) AgNT at (a) low wavenumber and (b) middle wavenumber regions. The absorptions marked by asterisks are within the frequency range commonly reported for the vibration of the sulfur-silver bond [Adapted with permission from Ref 125. Copyright 2015 American Chemical Society].

Figure 4.9 shows the FTIR spectra of the dried AT-4 and ATNT-24 samples in comparison with TOAB and AgNT. The spectrum of AT-4 is essentially the same as neat TOAB except for a relatively strong absorption appearing at 1341 cm^{-1}. This band corresponds to the N-O stretching modes of nitrate ions that are transferred to the organic phase through complexation with $[TOA]^+$. Consistent with the NMR results, the FTIR spectrum of ATNT-24 does not indicate changes that can be attributed to a reaction taking

place between the phase-transferred complexes and nonanethiol. Similarly, the Raman spectra ATNT-24 does not contain the characteristic bands of AgNT (Appendix, Figure A.1). Thus one can infer that, if the TOAB:$AgNO_3$ and TOAB:NT mole ratios are sufficiently large, the silver-containing $[TOA]^+$ complex remains unchanged prior to the reduction step, and thus is the major precursors to silver nanoparticles. Moreover, AgNT is not formed during the intermediate stage of this reaction. These conclusions are in accordance with the results of recent studies on the synthesis of gold nanoparticles that indicate $[TOA]^+[AuX_2]^-$ (X is halide) is the major metal precursor and noble metal-thiolate compounds are not formed under appropriate reaction condition[27, 30]. Unlike the gold precursor, which is produced from the reduction of $[TOA]^+[AuX_4]^-$ in presence of thiol, no perceptible changes in the structure of the phase-transferred silver complex occurs upon addition of thiol.

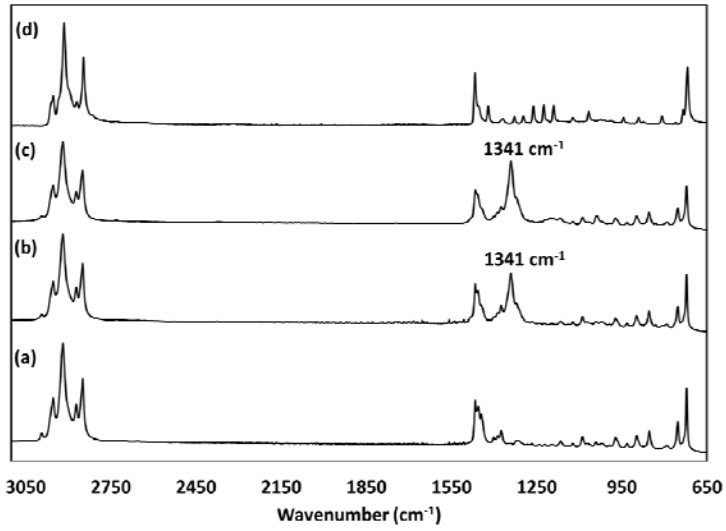

Figure 4.9. FTIR spectra of the (a) neat TOAB, (b) AT-4, (c) ATNT-24 and (d) AgNT samples. The strong band at 1341 cm^{-1} is assigned to the nitrate group [Adapted with permission from Ref 125. Copyright 2015 American Chemical Society].

4.3.2. Characterization of the phase transfer products

The structure and phase properties of the complexes formed in the phase transfer step, which are the major precursors to silver nanoparticles, were investigated by analyzing samples with a range of TOAB to $AgNO_3$ mole ratios. Selected regions from the FTIR spectra of neat TOAB and the complexes synthesized with mole ratios of TOAB/$AgNO_3$ of 4.4, 2, and 0.5 (AT-4, AT-2, and AT-0.5) are shown in Figure 4.10. The symmetric and asymmetric methylene stretches of TOAB at 2848 cm^{-1} and 2920 cm^{-1} are slightly shifted to higher wavenumbers (≈ 1 cm^{-1}) for AT-2 and AT-0.5 implying that the octyl chains in these compounds can have lower conformational ordering with respect to TAOB. The most conspicuous change occurs in the range of 1275 to 1500 cm^{-1}, where the intensity of the nitrate band (1341 cm^{-1}) increases linearly with the $AgNO_3$/TOAB ratio. The most conspicuous change occurs in the range of 1275 to 1500 cm^{-1}, where the relative intensity of the nitrate band at 1341 cm^{-1} increases and the characteristic band of pure TOAB at 1445 cm^{-1} weakens with reducing TOAB:$AgNO_3$ ratio. The relative intensity of the pure TOAB band (indicated by an arrow in Figure 4.10) to that of the nitrate band is a measure of the residual unmodified TOAB. Weakening of the 1445 cm^{-1} band indicates reduction in the concentration of residual TOAB.

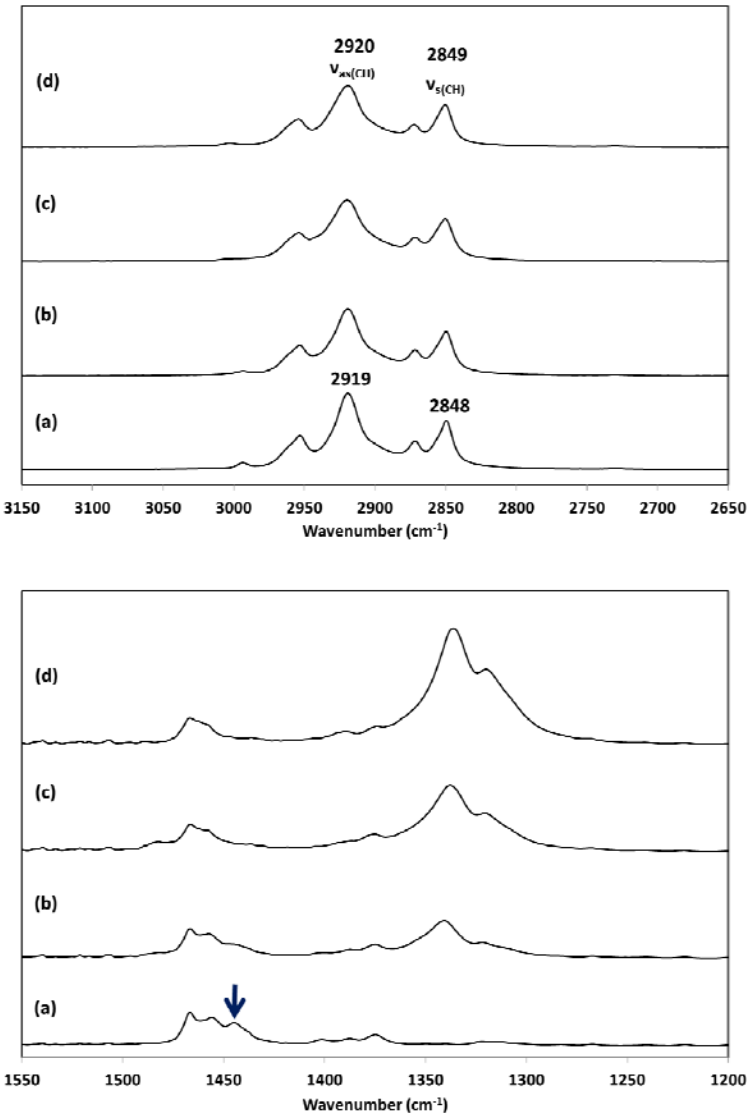

Figure 4.10. FTIR spectra of (a) TOAB, (b) AT-4, (c) AT-2, and (d) AT-0.5. (Top) methylene stretching region; (bottom) characteristic bands of the unreacted TOAB (indicated by an arrow) and the nitrate group [Adapted with permission from Ref 125. Copyright 2015 American Chemical Society].

More detailed information on the composition, structure, and dynamics of the phase-transferred complexes was obtained via ^{13}C solid-state NMR spectroscopy. Solution NMR only probes the dynamically averaged environment of the octyl chains, resulting from

rapid isotropic motion in the liquid state. Severely restricted dynamics in the solid state makes it possible to differentiate between distinct local environments. The solid-state ^{13}C spectra of the TOAB and AT-4 samples are shown in Figure 4.11 along with the ^{13}C solution spectrum of TOAB. As expected the solid state signals are shifted to higher chemical shifts (Table 4.5) due to the dominance of the all-*trans* segments in the alkyl chains leading to the loss of the γ-gauche shielding effect[129-131]. More importantly, in the ^{13}C spectrum of AT-4 one can see the emergence of new signals besides the relatively stronger signals of pure TOAB, Figure 4.12-a. The new signals can be divided into two subsets: a set of peaks which are shifted slightly to lower frequencies relative to those of TOAB resonances, and a group of signals experiencing relatively larger shifts to lower frequencies. Examples of these signals are clearly observable in the higher chemical shift region of the AT-4 spectrum (Figure 4.12-b), where there is a peak from the first subset close to the C_1 signal of the pure TOAB (indicated by asterisk in Figure 12-b) and a broad signal from the second subset shifted to a lower frequency by around 5 ppm with respect to C_1 (indicated by two asterisks in Figure 4.12-b). In AT-2, which contains the higher amount of Ag^+ and nitrate ions, the second subset of new signals are most pronounced. Closer examination of the less crowded spectral regions (from 14 to 17 ppm, 22 to 26 ppm and 28 to 31 ppm) in both the AT-4 and the AT-2 spectra, reveal that for each intense carbon signal, there are correspondingly two weaker peaks nearby (examples of these peaks are indicated with arrows in Figure 4.12-a). Interestingly, these new resonances disappear when further increasing the mole fraction of silver nitrate, as in AT-0.5, where the main peaks are shifted to lower frequencies with respect to those of TOAB.

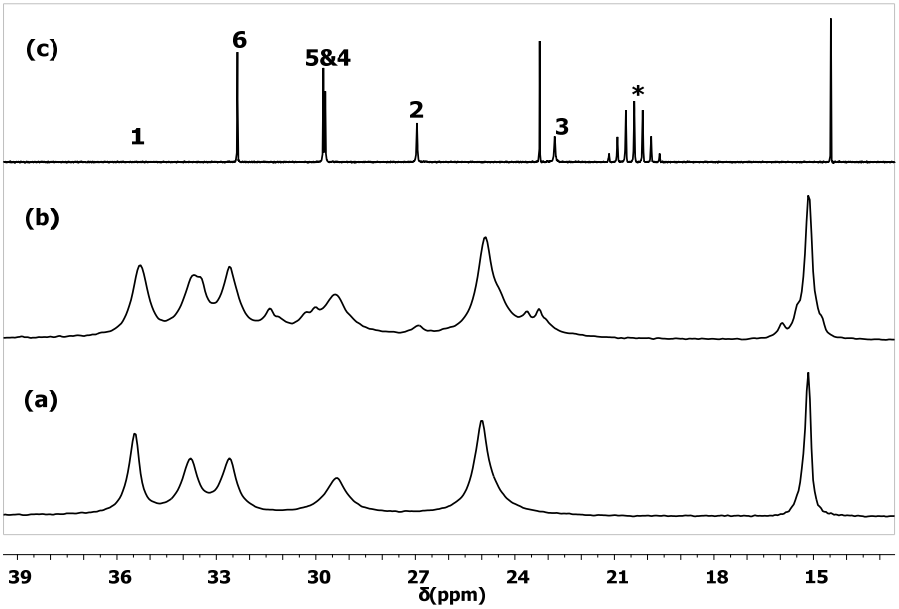

Figure 4.11. Solid state CP-MAS ^{13}C NMR spectra of (a) TOAB and (b) AT-4 at MAS=8 kHz. The ^{13}C solution state spectrum of TOAB (c) is shown for comparison (peak assignment follows Scheme 2 and the solvent signal is indicated by asterisk).

Table 4.5. ^{13}C NMR chemical shifts of TOAB in solution and solid state.

	C1	C2	C3	C4	C5	C6	C7	C8
$\delta_{solution}$ (ppm)	58.98	26.94	22.81	29.72	29.78	32.35	23.24	14.48
δ_{solid} (ppm)	63.39	29.38	24.98*	32.60	33.76	35.47	24.98*	15.14

* The same chemical shifts are reported for these signals due to their strong overlap.

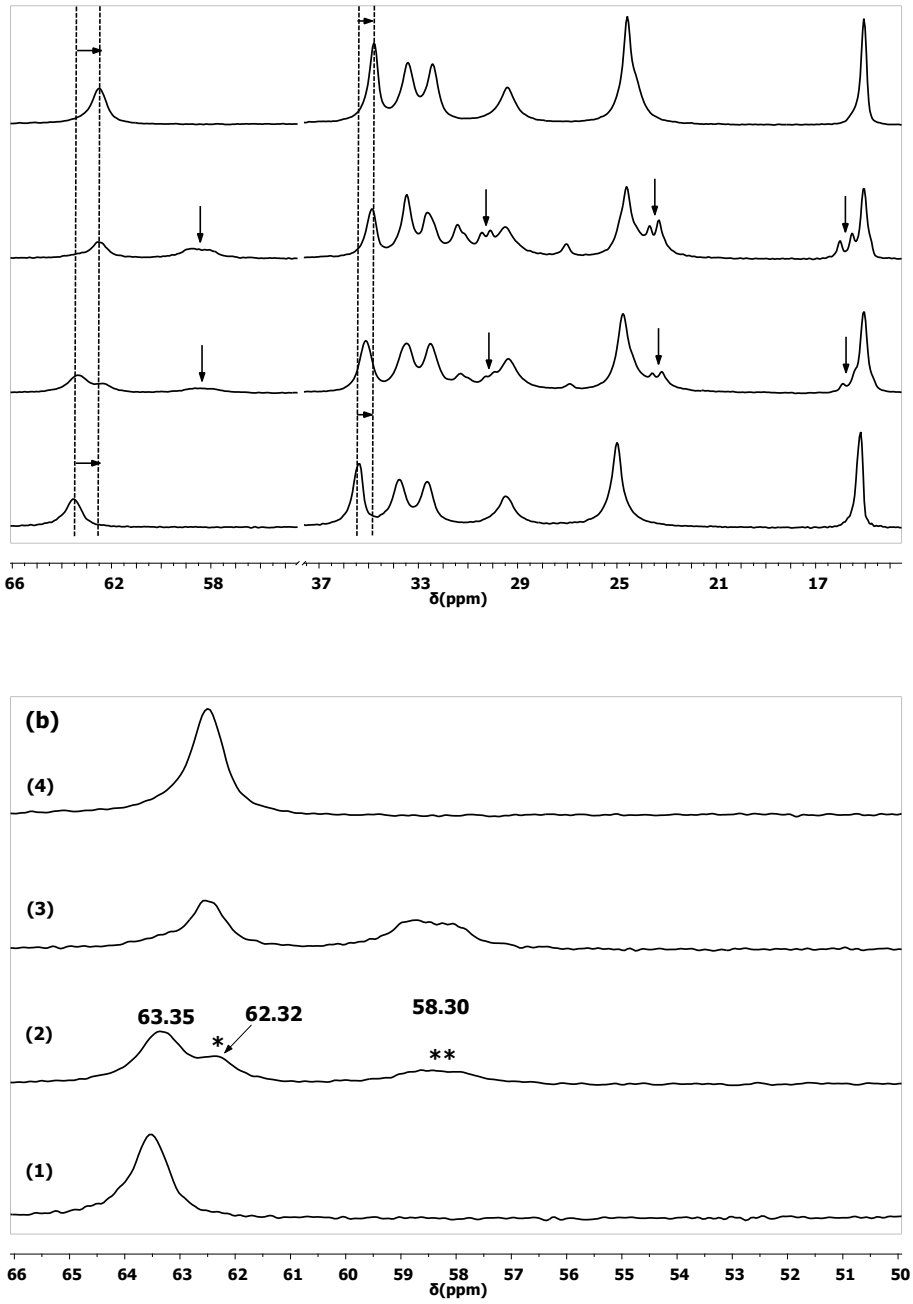

Figure 4.12. (a) ^{1}H-^{13}C CP-MAS NMR spectra of (1) TOAB, (2) AT-4, (3) AT-2, and (4) AT-0.5 at MAS=8 kHz. Some of the new signals are indicated by arrows. (b) High chemical shift region of these spectra showing signals from the new subsets [Adapted with permission from Ref 125. Copyright 2015 American Chemical Society].

Dynamics in the octyl chains were used to examine the solid-state phase structure of these systems using ^{13}C relaxation times. T_1 and T_2 values of selected signals of TOAB, AT-0.5, and the higher intensity subsets of AT-2 and AT-4 (obtained from the rotor synchronized post-CP Hahn-echo experiments) are presented in Table 4.5. C_1 and C_2 nuclei are the closest nuclei to the ionic center of $[TOA]^+$, thus exhibiting the fastest transverse decay rates (Figure 4.13-a, decay curves of AT-4 and AT-0.5 are not shown for clarity) and their T_2 values remain similar in all samples investigated. In contrast the T_1 values of C_1 and C_2 and both relaxation times (T_1 and T_2) of C_3 to C_7 show significant differences when comparing various samples (Figure 13-b). Apart from a few exceptions, the ^{13}C signals of TOAB exhibit the slowest rate of longitudinal relaxation (longest T_1) and the fastest dephasing rate of transverse magnetization (shortest T_2). Comparing the ^{13}C relaxation times of AT-4 and AT-2, one notes that generally the latter has shorter T_1s and longer T_2s.

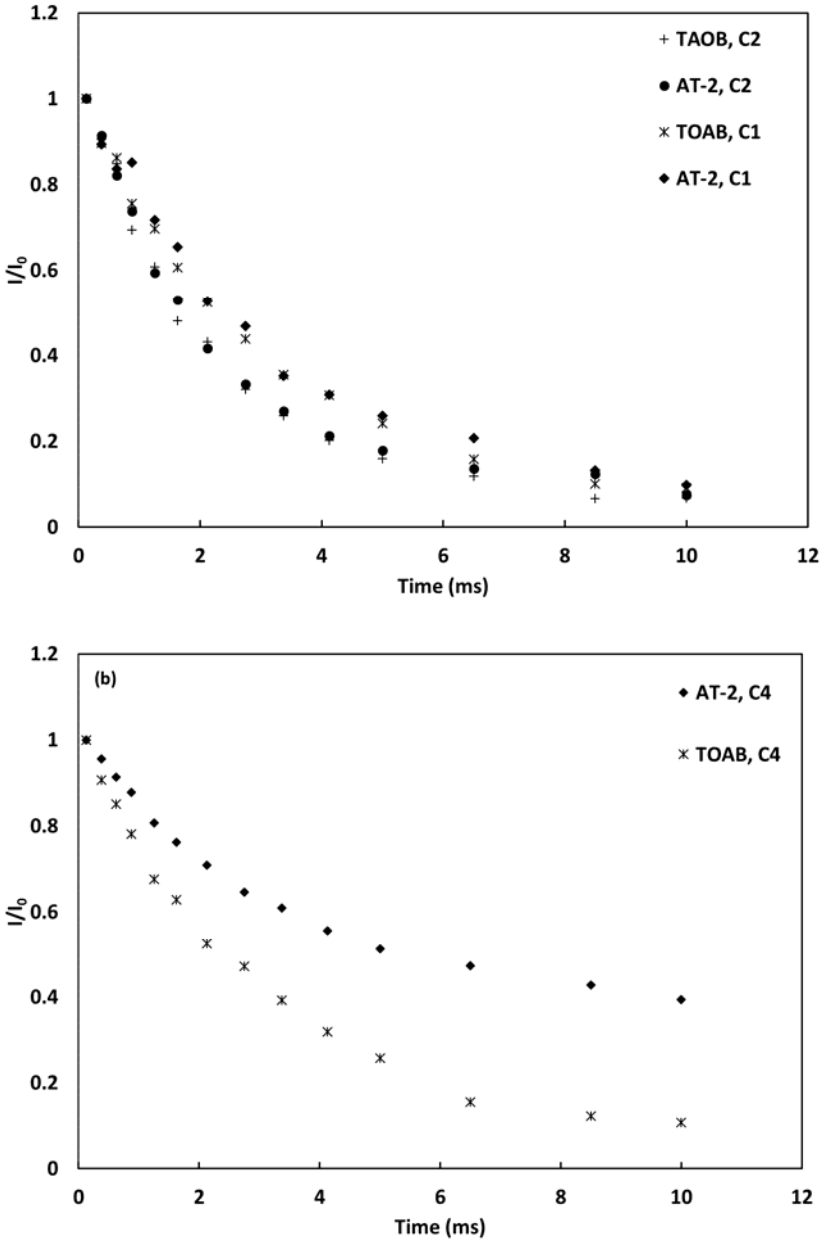

Figure 4.13. Transverse relaxation curves of the selected ^{13}C signals of the AT-2 and TOAB samples obtained from post-CP HE experiment at MAS = 8 kHz [Adapted with permission from Ref 125. Copyright 2015 American Chemical Society].

The influence of the local environment on the dynamics of the octyl chains can be examined more accurately by inspecting the T_1/T_2 ratios, Table 4.6. The T_1/T_2 ratios of all carbon nuclei, except for C_8, decrease from TOAB to AT-2. This trend is interrupted for

the AT-0.5 sample. The T_1/T_2 values of C_7 and C_6 carbons in this sample are similar to AT-2, while those of C_4 and C_2 are larger. The relaxation times of the weak subset of signals in AT-4 and AT-2 cannot be determined unambiguously due to spectral overlap. A reliable comparison however, can be made between the T_2 values of the well resolved resonances of AT-2 at 24.6 ppm (strong subset) and 23.3 ppm (weak subset) which have T_2 values of 7.72 ms and 10.23 ms, respectively, Figure 4.14.

Table 4.6. NMR relaxation times of selected ^{13}C nuclei.

Sample		C8	C7	C6	C4	C2
TOAB	Chemical shift (ppm)	15.2	25.0	35.5	32.6	29.4
	T_1 (s)	1.39	3.61	3.73	5.31	7.04
	T_2 (ms)	27.26	4.85	6.36	3.58	2.43
	$T_1.T_2^{-1}$ /10^3	**0.05**	**0.74**	**0.59**	**1.48**	**2.90**
AT-4	Chemical shift (ppm)	15.1	24.9	35.3	32.6	29.4
	T_1 (s)	1.37	2.66	2.54	2.78	3.26
	T_2 (ms)	31.15	5.47	6.62	5.45	2.44
	$T_1.T_2^{-1}$ /10^3	**0.04**	**0.49**	**0.38**	**0.51**	**1.34**
AT-2	Chemical shift (ppm)	15.0	24.6	34.9	32.6	29.4
	T_1 (s)	1.34	2.18	2.62	2.42	3.19
	T_2 (ms)	33.08	7.14	7.75	8.95	2.58
	$T_1.T_2^{-1}$ /10^3	**0.04**	**0.31**	**0.34**	**0.27**	**1.24**
AT-0.5	Chemical shift (ppm)	15.2	24.7	34.9	32.6	29.4
	T_1 (s)	1.35	2.55	2.63	4.27	6.85
	T_2 (ms)	34.58	7.43	8.37	5.17	2.56
	$T_1.T_2^{-1}$ /10^3	**0.04**	**0.34**	**0.31**	**0.83**	**2.67**

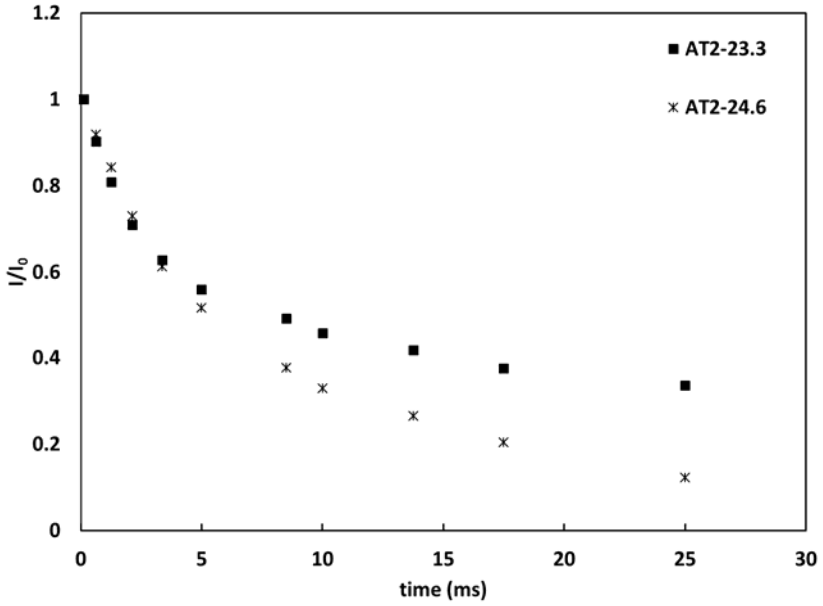

Figure 4.14. Transverse relaxation curves of selected signals form strong subset (24.6 ppm) and weak subset (23.3 ppm) of AT-2 sample [Adapted with permission from Ref 125. Copyright 2015 American Chemical Society].

Complementary information on the microstructure of TOAB and AT-n compounds was obtained using DSC, Figure 4.15. Neat TOAB has a major endothermic peak at 99°C, which is its melting transition, and a very weak endotherm near 50°C. This second transition corresponds with the emergence of a liquid-like phase composed of very mobile cations[132]. The DSC thermograms of AT-4 and AT-2 contain two broad transitions near 94°C and 47°C. The higher temperature transition in both AT-4 and AT-2 extends over a wider range of temperatures in comparison with the sharp melting endotherm in TOAB. Such broadening in thermal transitions is indicative of reduced ordering in the corresponding phases. The low temperature transition initially increases in intensity with increasing $AgNO_3$ concentration and eventually disappears in AT-0.5. The major transition

in AT-0.5 is shifted to higher temperature compared to TOAB, indicating larger lattice energies.

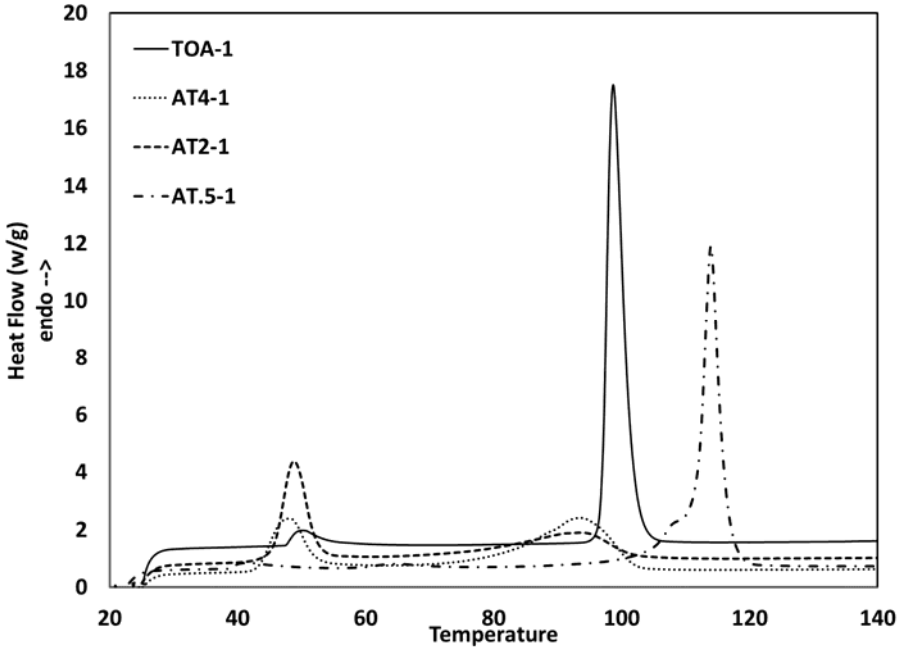

Figure 4.15. DSC thermograms of the neat TOAB and the phase-transferred compounds [Adapted with permission from Ref 125. Copyright 2015 American Chemical Society].

These observed changes in FTIR, NMR, and DCS of the phase-transferred compounds as a function of TOAB:$AgNO_3$ mole ratios can be correlated with the structure and phase properties of these materials. A comparison between the FTIR spectra of these samples with TOAB reveals that they contain nitrate anions. Moreover, there is a noticeable fraction of unmodified TOAB in AT-4, which is drastically reduced when decreasing the mole ratio to 2 and eventually reaches zero in AT-0.5. Coexistence of multiple species within these materials (Br^-, $[AgBr_2]^-$, and $[NO_3]^-$, see below for discussion) is expected to give rise to a heterogeneous phase structure. This hypothesis can be further examined by solid-state NMR spectroscopy, which allows for differentiation between distinct local

environments within the dried phase-transfer products. Emergence of two subsets of ^{13}C signals in the solid-state spectra of AT-4 and AT-2, along with the observed variations in their relative intensities as a function of TOAB:$AgNO_3$ mole ratios, suggest that the complexation process produces at least two distinct phases in which the octyl chains experience different local environments. At mole ratio of 0.5, there is a single set of signals at lower chemical shifts with respect to those of TOAB, implying that AT-0.5 has more uniform local environments which differ from pure TOAB. These conclusions are confirmed by DSC which shows two thermal transitions in AT-4 and AT-2, pertaining to two different phases. Analogous to the relative intensity of strong and weak subsets of NMR signals, the area under these peaks varies as a function TOAB:$AgNO_3$ mole ratio. Single thermal transition observed in the DSC thermogram of AT-0.5 corresponds with its relatively more uniform phase structure, inferred from solid-state NMR data.

Differences in phase structure between the AT-n samples and neat TOAB seems to have a noticeable impact on the dynamics of their octyl chains, which can be monitored via their ^{13}C transverse (T_2) and longitudinal (T_1) relaxation times. Less mobile environments, with long correlation times of motion with respect to the NMR time scale, $\tau=1/\omega_0$ (ω_0 is the Larmor frequency which is on the order of 10^8 Hz), experience fast dephasing of their transverse magnetization and slow recovery of their longitudinal magnetization. In this case T_1 increases, while T_2 decreases monotonically with correlation time. Domains with restricted motion therefore exhibit relatively shorter T_2 and longer T_1 values with respect to more mobile environments, resulting in a pronounced increase in their T_1/T_2 ratios. In all the samples, the T_1s and T_2s of successive carbons along the octyl chains respectively follow decreasing and increasing trends, due to their mobility increase. This has a dramatic

effect on T_1/T_2 ratios, varying by two orders of magnitude from the rigid C_2 to the highly mobile C_8. The reduction in T_1/T_2 ratios of C_2 to C_7 from TOAB to AT-2 indicates that the local motions of the octyl chains are more restricted in TOAB and become progressively less constrained in AT-4 and AT-2. Faster motions in the CH_2 groups correspond to a lower degree of conformational ordering of the octyl chains which results in reduction in their packing density. This is consistent with the broadening of the high temperature thermal transitions of AT-4 and AT-2 with respect to that of TOAB. The insensitivity of T_1/T_2 ratios of C_8 to the differences in local environments of $[TOA]^+$ in various samples is the result of its higher degree of motional freedom afforded by rapid rotation of the end chain methyl group. Unfortunately, this analysis of the ^{13}C relaxation times cannot be extended to compare the local motions within the domains giving rise to the weak and strong subsets of signals, as their T_1s and T_2s are not available.

The heterogeneous phase structure of the AT-4 and AT-2 compounds, inferred from their solid-state ^{13}C NMR spectra and their thermal behavior can be attributed to the coexistence of multiple ionic species in these complexes. In neat TOAB, the tetraoctylammonium cation interacts only with the Br^-, resulting in a single-phase microstructure. In this homogeneous environment, the octyl chains tend to preferentially adopt an *all-trans* conformation and thus pack into an ordered lattice. This densely packed (compared to the other samples studied here) microstructure maximizes the intermolecular attractive forces between the octyl chains thus restricting their local motion. During the phase-transfer process, Ag^+ combines with Br^- to form either $[AgBr_2]^-$ or AgBr, depending on the mole ratio of the reactants. The former is readily transferred to the organic phase

through complexation with $[TOA]^+$, while the latter tends to precipitate from the reaction mixture.

At a sufficiently large excess of bromide, which is the case for AT-4 and AT-2 samples, $[AgBr_2]^-$ is predominant owing to its significantly larger stability constant compared to $AgBr$[133]. Under this circumstance, there are at least two new counterions, $[AgBr_2]^-$ and $[NO_3]^-$, interacting with $[TOA]^+$. These samples also contain significant remnants of unreacted TOAB as confirmed by FTIR and elemental analysis. The coexistence of several counterions disrupts the dense packing of the octyl chains into an ordered lattice and gives rise to a heterogeneous phase morphology. The larger free volume in this less ordered phase increases the population of random *gauche-trans* conformations, allowing for increased freedom of local motion. This lower degree of ordering and enhanced mobility seen in AT-4 and AT-2 in comparison to TAOB, is consistent with broadening of their melting transition, increased intensity of their lower temperature transitions, slightly smaller chemical shift of their carbon nuclei, and reduction in their T_1/T_2 ratios. For the AT-0.5 sample, where the Br^-:Ag^+ mole ratio is less than one, the low concentration of bromide leads to the formation of silver bromide, which precipitates during the phase-transfer step. In this case, NO_3^- is the predominant counterion producing a material with a uniform phase structure, which is confirmed by a single set of NMR resonances and a single endothermic transition. The differences observed in solid-state NMR and DSC experiments between TOAB and AT-0.5 probably originates from the size difference between Br^- and NO_3^-.

4.3.3. Quality of the silver nanoparticles

TEM micrographs of the silver nanoparticles prepared from AT-4 (SNPAT-4) and AT-2 (SNPAT-2) via the two-phase method are presented in Figure 4.16. These images, taken from the samples after mild work-up (c.f. experimental section), show the presence of sheet-like structures alongside the individual nanoparticles. The average diameters (SNPAT-4: 3.7±0.9 nm SNPAT-2: 3.1±0.7 nm) and the dispersities of the nanoparticles are comparable in both samples. Sheet-like structures occur either as single or multiple stacked layers with clusters of nanoparticles located on the top of each layer or concentrated at their edges. Such structures could form in a process analogous to the initial stages of the latex film formation, where the alkanethiol-capped silver nanoparticles and impurities are brought together as the solvent evaporates. The resulting aggregates, though composed of various species, have some degree of ordering as the major fraction of the impurities contain octyl chains (confirmed by solution NMR) allowing them to pack together, and interdigitate with the nonanethiols adsorbed on the nanoparticles.

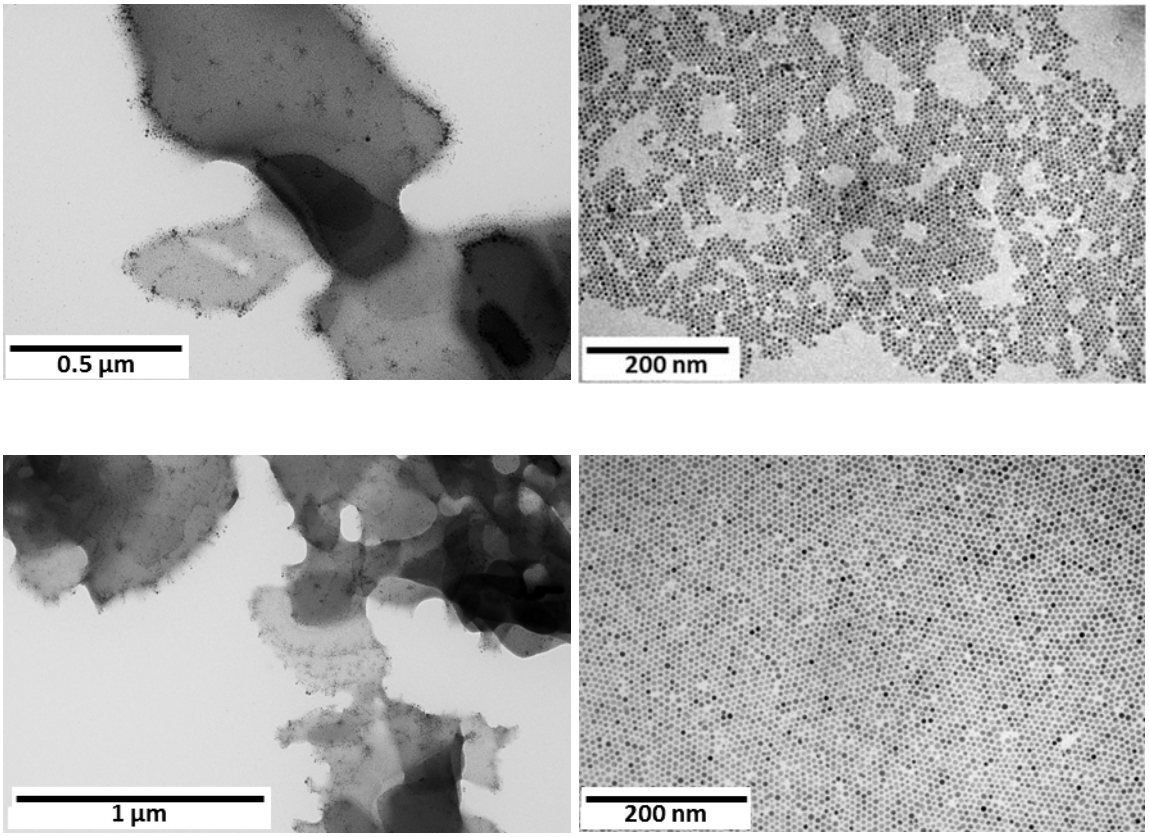

Figure 4.16. Sample TEM micrographs of SNPAT-4 (top) and SNPAT-2 (bottom) nanoparticles showing the layered sheet-like structures and individual particles [Adapted with permission from Ref 125. Copyright 2015 American Chemical Society].

The sheet-like structures are predominant in the TEM micrographs of the SNPAT-4 sample after being dried and re-dispersed in toluene, and furthermore have a higher degree of ordering with respect to the original product (before drying and re-dispersing), Figure 4.17. When compared to SNPAT-4, the images taken of dried and re-dispersed SNPAT-2 contain a significantly larger proportion of isolated nanoparticles. These observations suggest that residual $[TOA]^+$ facilitates the formation of the sheet-like structures from the impurities and nanoparticles, consequently leading to irreversible aggregation that impairs their solubility. Furthermore, the slightly smaller and more

uniform SNPAT-2 nanoparticles indicate that a large excess of TOAB does not ensure higher stability for the nanoparticles at the initial stages of their formation. It is therefore advantageous to reduce the TOAB/$AgNO_3$ molar ratio to 2 to simplify the purification procedure and to mitigate the aggregation. Further reduction of this ratio, as in the AT-0.5 sample, results in inefficient phase-transfer, where mostly silver bromide is formed which subsequently precipitates from the reaction medium.

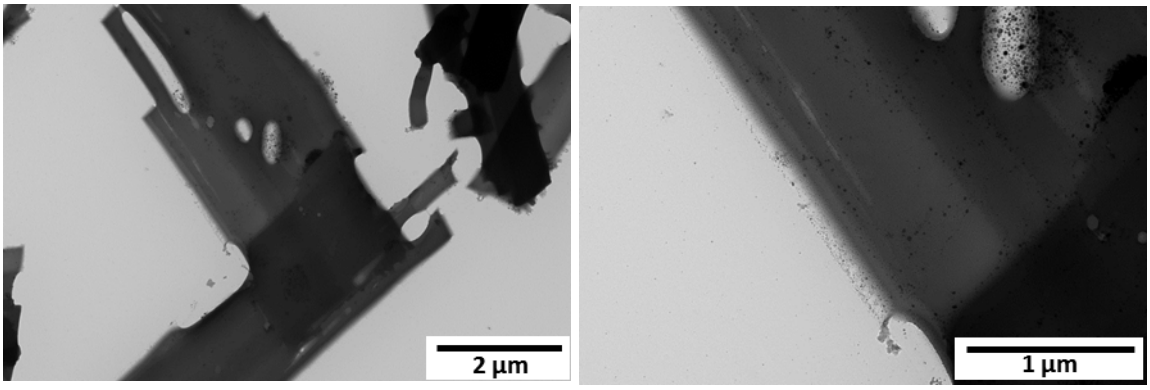

Figure 4.17. TEM micrographs of ordered sheet-like structures in the dried and re-dispersed SNPAT-4 sample at two different magnifications: 7000 (left) and 20000 (right) [Adapted with permission from Ref 125. Copyright 2015 American Chemical Society].

4.4. Solid-state NMR characterization of alkanethiol-capped SNP

The microstructure of the surface grafted alkanethiols is a major determining factor in stability of the nanoparticles, their arrangement into ordered structures, and their interactions with surrounding material. Solid-state NMR techniques are powerful tools for characterization of the microstructural features of the capping ligands, as well as the investigation of their interactions with the noble metal core. Figure 4.18 shows the ^{13}C SSNMR spectrum of octadecanethiol (ODT) in comparison to its solution state spectrum. Expectedly, all of the solid-state resonances appear at higher chemical shifts due to the dominance of the all-*trans* conformation within the alkyl chains. These nuclei experience reduced shielding effect as a result of maximized spatial separation between the groups located in γ position with respect to each other. The ^{13}C signals of ODT shift to higher frequencies upon adsorption on the nanoparticles, Figure 4.19. These changes in peak positions (Table 4.7), which are more pronounced for the nuclei closer to the thiol group, are smaller than those observed when comparing the resonance frequencies of ODT in the solution and in the solid state. Interestingly, the C_1 signal of neat ODT at 26.4ppm is either missing or experiencing a large shift to higher frequencies in the spectrum of the nanoparticle. Moreover, the methyl signal of the SNPODT is composed of at least three overlapping peaks that are separated by about 45 Hz. Similar variations in chemical shift are observed when comparing the solid-state ^{13}C spectrum of SNPNT with the solution-state spectrum of the neat nonanethiol, Figure 4.20. The displacement of signals toward higher frequencies, however, is slightly greater for this sample, Table 4.7. These changes in peak positions, along with the disappearance of the C_1 signal in both SNPNT and SNPODT, confirm that these samples do not contain free alkanethiols. This was further

verified by ^{1}H solution NMR spectra of these samples, where the characteristic signals of free capping ligands were not observed.

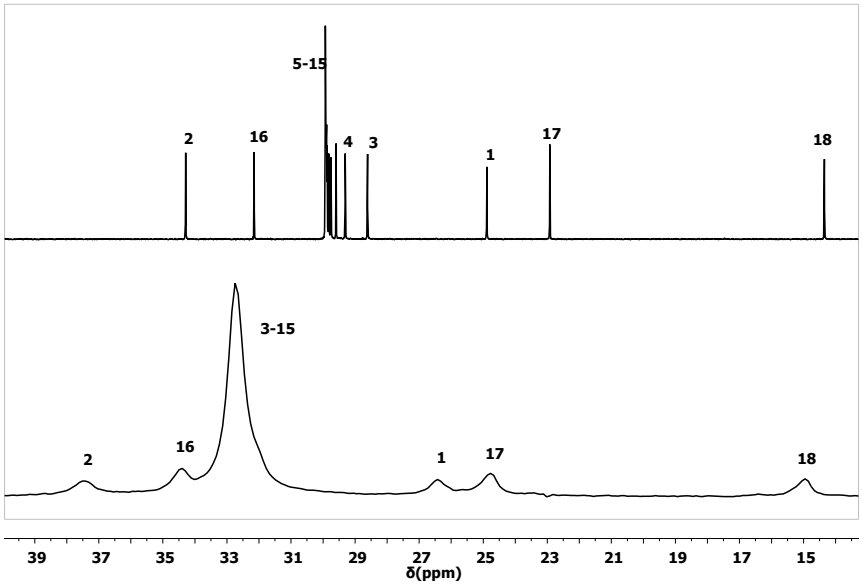

Figure 4.18. ^{13}C NMR spectrum of octadecanethiol (top) in chloroform-d and (bottom) in the solid state at MAS=8 kHz.

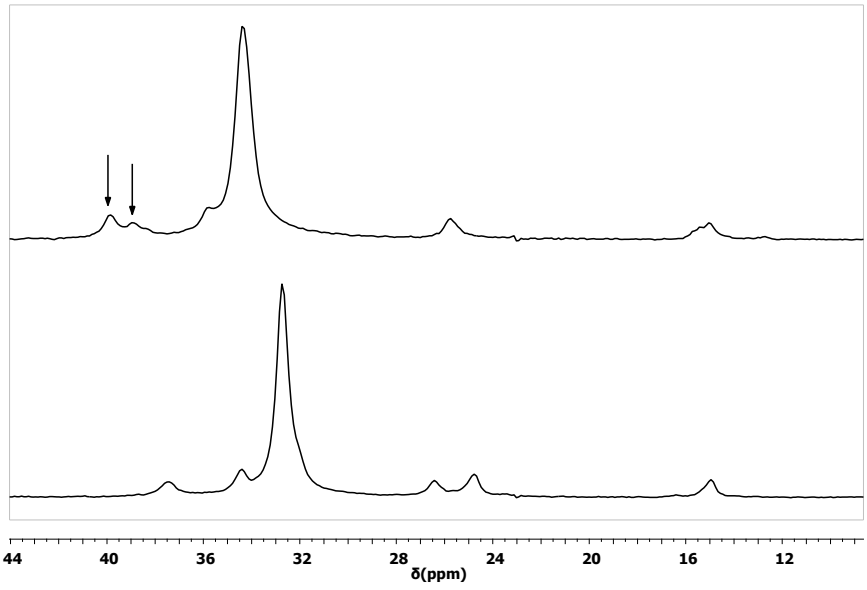

Figure 4.19. Solid-state CP-MAS ^{13}C spectra of ODT and SNPODT at MAS=8 kHz.

Table 4.7. Relative changes in ^{13}C resonances of alkanethiols in solid state and on silver nanoparticles.

Samples	Chemical shift differences			
		$(\delta_s - \delta_d)$	$(\delta_a - \delta_s)$	$(\delta_a - \delta_d)$
Nonanethiol	C_4-C_6	----	----	5.12
	C_7	----	----	3.96
	C_8	----	----	3.11
	C_9	----	----	1.38
Octadecanethiol	C_4-C_{15}	2.92	1.64	4.56
	C_{16}	2.26	1.36	3.62
	C_{17}	1.85	0.99	2.84
	C_{18}	0.6	0.08	0.68

δ_d: chemical shift in solution state; δ_s: chemical shift of free alkanethiol in solid state; δ_a: chemical shift of the adsorbed alkanethiol in solid state

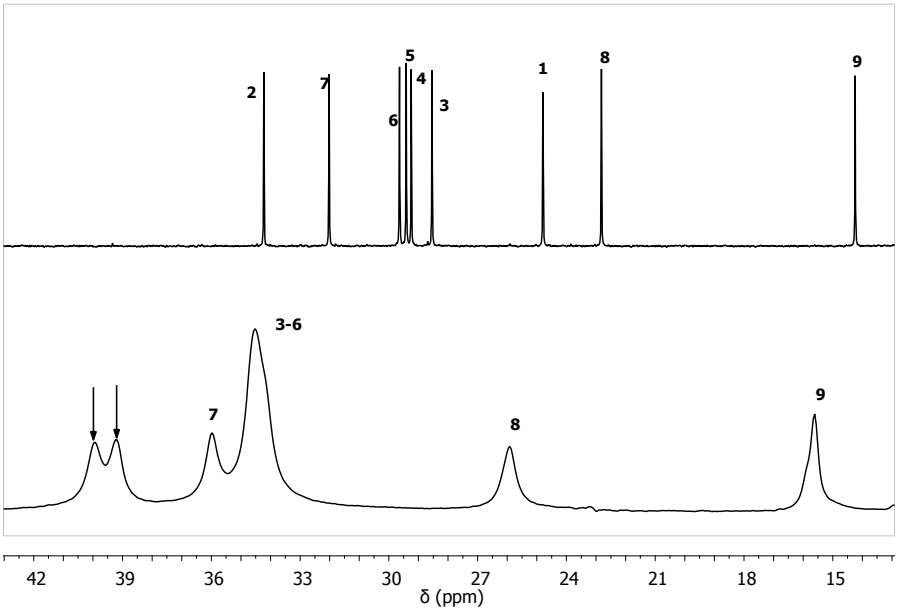

Figure 4.20. Solid-state ^{13}C CP-MAS (MAS=8 kHz) spectrum of the SNPNT sample (bottom) in comparison to the neat nonanethiol in chloroform-d (top).

A characteristic feature of the ^{13}C spectra of the surface grafted nonanethiol and octadecanethiol is the apparent disappearance of their C_1 signals, which has also been reported for the alkanethiol-capped gold nanoparticles[37, 40]. These spectra contain two signals at around 40 ppm (indicated by arrows in Figures 4.19 and 4.20), at least one of which has no corresponding signal in the solution and solid state spectra of the neat alkanethiols. This new signal might originates from the C_1 of the adsorbed alkanethiols, which has shifted to a higher frequency by around 13 ppm with respect to its chemical shift in the free alkanethiol. Although the origin of this new signal cannot be determined unambiguously, spectral integration can provide useful information regarding its possible origin. For reliable comparison, all the integrals of each spectrum are normalized to the area of its CH_3 signal. The normalized areas of the known signals show close correspondence with the number of their associated carbon nuclei. For example, if the area under the C_{18} (Figure 4.18) peak is set to 1, the normalized areas of C_1, C_{17} and C_3-C_{15} are 1.01, 1.08, and 13.25, respectively. Moreover, the total area (sum of the normalized signal areas) is 18 for ODT and is 9 for AgNT, which corresponds to the number of carbons in each sample, thus confirming the accuracy of the integration. Interestingly, the total areas of the SNPNT and SNPODT signals are 9 and 18, respectively. This integration analysis therefore implies that the C_1 signal is not missing from the spectra of the nanoparticle samples, but it is undergoing a much larger shift in frequency in comparison to the other carbon nuclei.

The observed shifts of the surface grafted alkanethiol ^{13}C signals to higher frequencies might originates from a Knight shift induced by the metallic silver nanoclusters, conformational ordering of the self-assembled alkane chains, or the inductive

effect of sulfur-silver binding on the nearby methylene group. Knight shift refers to the changes in chemical shifts of nuclei located within or in a close proximity of a metallic environment. A change in spin orientation of the conduction electrons of silver in the presence of the external magnetic field strongly affects the local field within the metallic core of the nanoparticles. This effect might be experienced by the hydrogen and carbon nuclei located close to the metal surface, resulting in noticeable de-shielding of their resonances. The possibility of a Knight shift contribution was examined by comparing the solid-state ^{13}C spectrum SNPNT with that of the non-metallic Ag(I)-nonanethiolate (AgNT). The 1:1 sulfur to silver mole ratio (obtained from elemental analysis, Table 4.8) confirms that the AgNT sample does not contain metallic silver, thus its resonance frequencies are not affected by a Knight shift. Figure 4.21 shows that, except for minor differences between the C_9 peaks in these samples, other signals have analogous shapes and positions. The striking similarity between these two compounds rules out the possibility of a Knight shift contribution to the ^{13}C resonance frequencies of the alkanethiols adsorbed on the nanoparticles.

Table 4.8. Mass and mole percentage of sulfur and silver atoms in AgNT.

	Mass %	Mole %
Sulfur	11.64	3.25
Silver	40.5	3.35

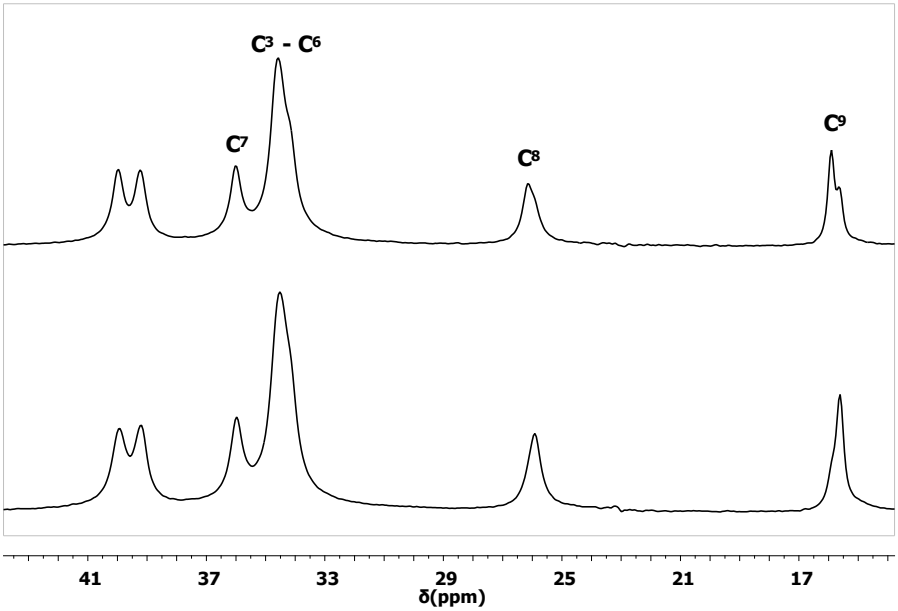

Figure 4.21. Solid-state CP-MAS ^{13}C spectra of the AgNT (top) and the SNPNT (bottom) at MAS=8 kHz.

Alternatively, the changes in chemical shifts, which are comparable to those reported for alkanethiol-capped gold nanoparticles[37, 41], can be the result of an increase in the population of *trans* conformations within the surface grafted alkane chains. Considering that the neat ODT is close to its melting point (30-33 °C) at the test temperature, it may contain a noticeable fraction of gauche conformers. Strong adsorption of the ODT chains on the metal nanocrystals has a strong influence on their conformations. As was observed in the TEM images, the nanoparticles tend to arrange into ordered aggregates through interdigitation of the capping ligands of the adjacent particles. Formation of such aggregates requires that a major fraction of alkane chains adopt an all-*trans* conformation. This leads to the loss of the γ-gauche shielding effect and a consequent increase in the NMR frequencies. The effect of conformational ordering on the ^{13}C chemical shifts of the capping agents is further illustrated by the slight shift of the peak positions to lower frequencies at

elevated temperature, due to the reduction in population of *trans* conformations, Figure 4.22. It should be mentioned that if the new signal originates from the C_1, its relatively large displacement is mainly caused by factors other than conformational ordering.

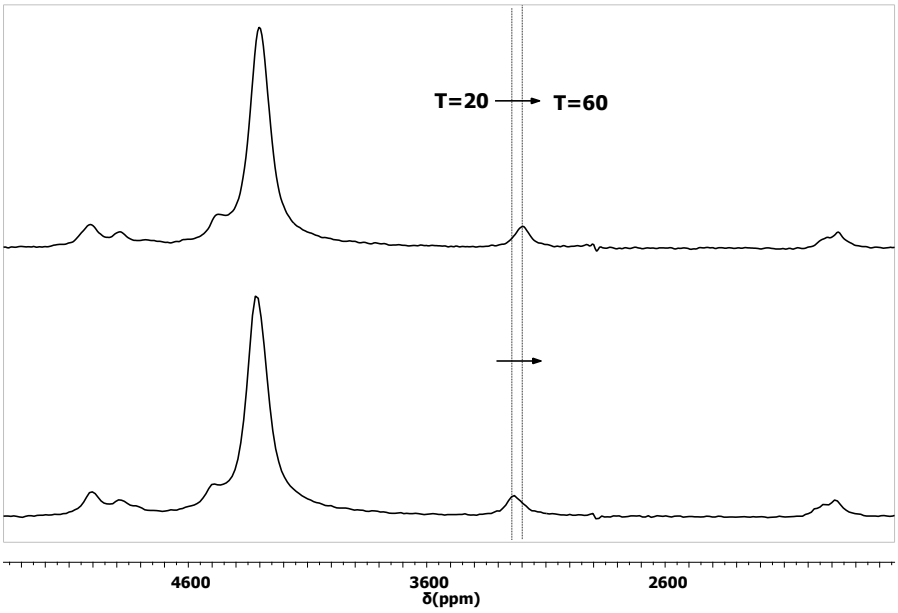

Figure 4.22. Solid-state CP-MAS ^{13}C spectra of the SNPODT at T=20˚C (bottom) and T=65˚C (top).

Adsorption of the alkanethiols on the nanoparticles and their subsequent interdigitation in the solid state have a noticeable influence on their dynamics, probed by their ^{13}C transverse (T_2) and longitudinal (T_1) relaxation times. The longitudinal and transverse relaxation times of selected ^{13}C nuclei of neat ODT and SNPODT are presented in Table 4.9. The carbons of bonded alkanethiols have relatively longer T_1s, shorter T_2s and larger T_1/T_2 ratios, implying slower motions within these chains. Such reduced mobility is induced by grafting of the alkane chains to the rigid surface of the silver nanocrystals as well as the interdigitation of capping ligands within the arrays or clusters of nanoparticles.

This is in complete agreement with the predominance of the all-*trans* conformation in SNPODT and SNPNT samples.

Table 4.9. Relaxation times and T_1/T_2 ratios of SNPODT vs ODT.

	ODT		SNPODT	
	C_{17}	$C_3 - C_{15}$	C_{17}	$C_3 - C_{15}$
T_1 (s)	8.75	9.33	9.29	9.51
T_2 (ms)	2.18	1.97	1.33	1.25
$T_1.T_2^{-1}/10^3$	**4.01**	**4.74**	**6.98**	**7.61**

4.5. TOAB-capped SNP and ligand exchange

Silver nanoparticles protected with TOAB, which primarily acts the phase transfer agent, were prepared using lower concentrations of the reactants and under mild reducing condition, with respect to the two-phase method described above, to avoid aggregation of the nanoparticles. Visual examination of the TOAB-capped SNP (TOAB-SNP) solution collected from the reaction mixture did not reveal observable aggregates. A sample TEM micrograph of these nanoparticles, taken within a few hours of their synthesis, is presented in Figure 4.23. As it is evident in this image, the sample is composed of a group of smaller isolated nanoparticles and a group of larger nanoparticles that tend to form clusters. Quantitative particle size analysis shows a bimodal nanoparticle size distribution with two maxima at 3.17 nm and 8.67 nm, Figure 4.24.

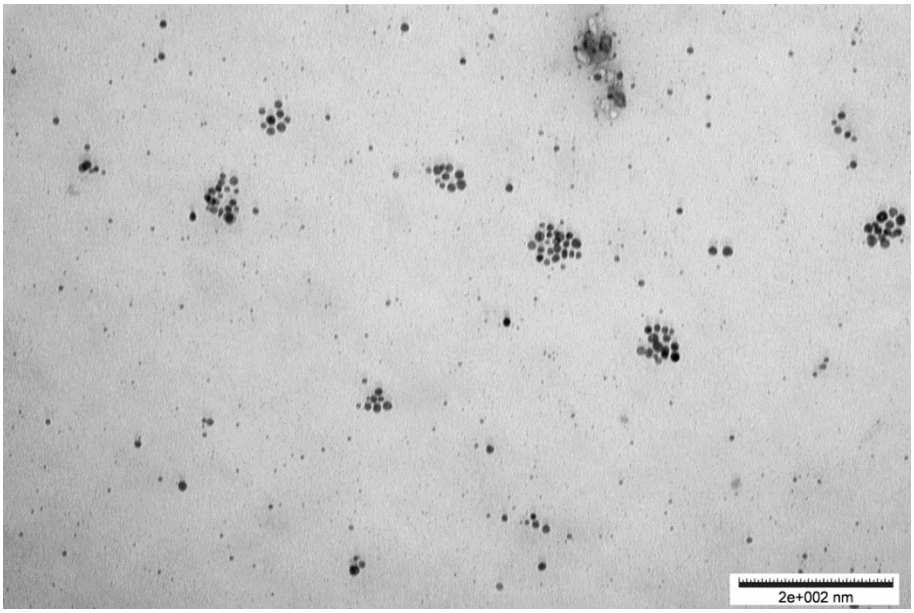

Figure 4.23. TEM micrograph of TOAB-SNP.

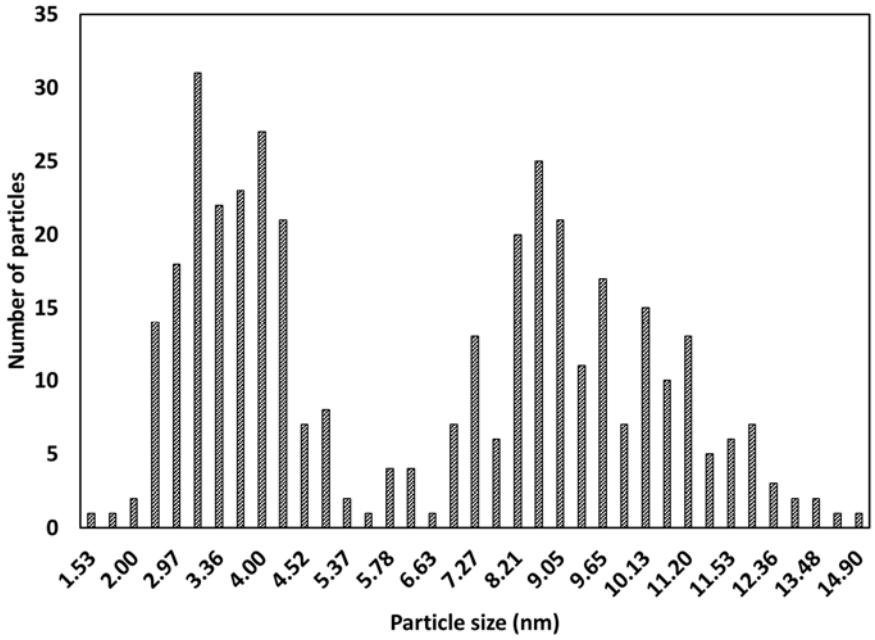

Figure 4.24. Particle size distribution of TOAB-SNP showing two maxima at 3.17 nm and 8.67 nm.

The UV-visible spectrum of this sample (Figure 4.25) shows a single peak at 418 nm, which is blue shifted with respect to the light absorption maxima of more uniform SNPNT (421 nm, d_{avg} = 3.7±0.9 nm) and SNPODT (436 nm, d_{avg} = 4.2±1.0 nm), implying that the surface plasmon resonance absorption of TOAB-SNP is primarily dominated by the smaller nanoparticles. It should be mentioned that, besides the size of noble metal core, the light absorption is also affected by the electronic properties of the capping ligand. The stability of TOAB-SNP solution stored for 4 days at ambient conditions was examined by monitoring the changes in its UV-visible spectrum, Figure 4.25. The peak wavelength does not change in comparison to the initial solution, while the absorption intensity decreases by around 32% upon storage. Lower absorbance can be attributed to the irreversible aggregation of particles, which is consistent with the presence of observable precipitates in the stored sample. The precipitation, however, does not affect the average size of the soluble fraction of nanoparticles, as was confirmed by TEM micrograph of the stored sample (Appendix, Figure A.2). The nanoparticles completely lose their solubility upon removal of the reaction solvent, implying that $[TOA]^+$ ligands are considerably less efficient than alkanethiols in stabilizing the noble metal nanocrystals.

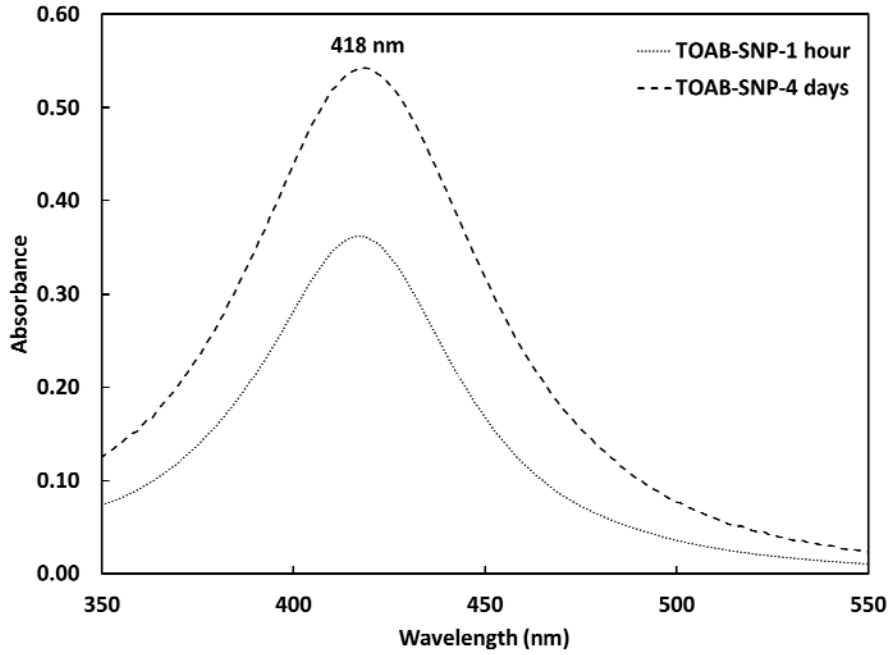

Figure 4.25. UV-visible spectra of the TOAB-capped SNP solution in toluene recorded immediately after their synthesis and after storage at ambient condition for 4 days.

Theoretically, the $[TOA]^+$ ligands can be readily substituted with alkanethiols, due to the stronger bonding of thiols with the silver nanoparticles (this was confirmed by higher stability of the alkanethiol capped SNP). In practice, however, this ligand exchange process led to excessive aggregation of the nanoparticles. A large fraction of the TOAB-SNP (more than 80 wt%) precipitated during the ligand exchange with nonanethiol or octadecanethiol. This might be due to the desorption of the weakly bonded $[TOA]^+$ ligands prior to the adsorption of alkanethiols, known as dissociative exchange mechanism[48]. If the time interval between dissociation of the original ligands and association of the incoming ones is sufficiently long, the naked nanoparticles undergo irreversible aggregation. TEM micrograph of the soluble fraction of the ligand exchanged product shows large clusters of the nanoparticles, Figure 4.26. Such clusters are formed as the result of extensive interdigitation between the surface grafted alkanethiols.

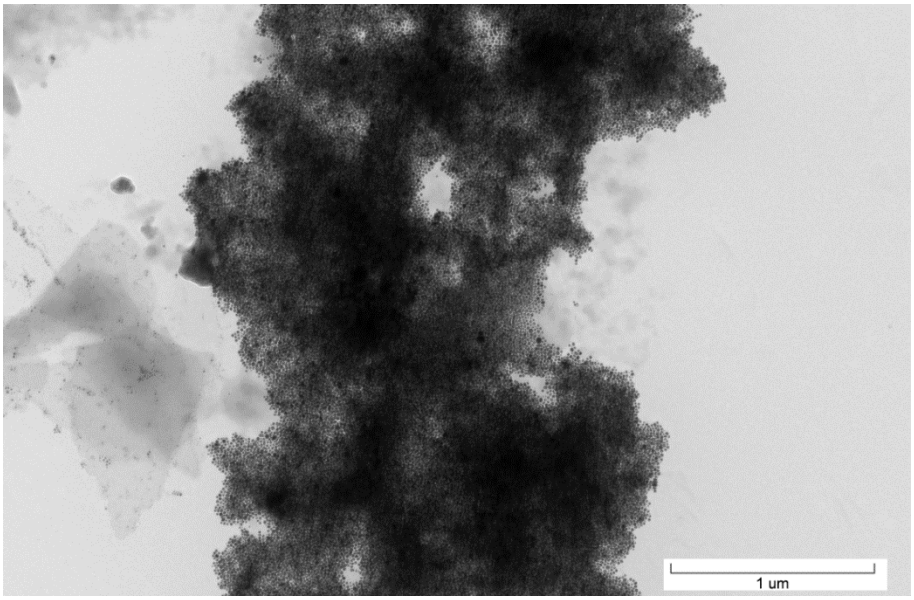

Figure 4.26. TEM micrograph of the TOAB-capped nanoparticles after ligand exchange with nonanethiol, showing a large cluster of the nanoparticles.

4.6. Conclusions

Small and uniform nonanethiol and octadecanethiol capped SNP were successfully synthesized via a slight modification of the Brust and Schiffrin two-phase method. TEM micrographs showed that the resulting silver nanocrystals have a faceted morphology and arrange into 2D or 3D structures, in which the surface grafted alkane chains of the neighboring particles are interdigitated. An intense light absorption peak was observed in the UV-visible spectra of the nanoparticles solutions, arising from localized surface plasmon resonance of the conduction electrons in the silver nanocrystals. The wavelength of this peak was correlated with the size of the nanoparticles, where a decrease in average size caused a blue-shift in the peak position.

Samples taken from the intermediate stage of the two-phase method were characterized by NMR and vibrational spectroscopies, and compared with unmodified TAOB and AgNT, to identify the major intermediate of the two phase reaction. Interaction of $[TOA]^+$ with the new anionic species during the phase-transfer step resulted in distinct shifts in the ^1H and ^{13}C NMR resonances and the appearance of new bands in the FTIR spectra. Further changes in the characteristic NMR, FTIR, and Raman signals of the phase-transferred complexes did not occur the in presence of nonanethiol. Moreover, comparisons between AgNT and the samples from the reaction mixture did not reveal evidence of the formation of thiolate prior to the reduction step. It was thus concluded that at sufficiently large TOAB:$AgNO_3$ and TOAB:NT mole ratios, the silver-TOAB complex is the predominant intermediate compound and thus must be the precursor to the silver nanoparticles.

Observations on the chemical shifts, dynamics, and thermal transitions of the samples prepared with a variety of mole ratios of the reactants provided new insights into the phase structure and composition of the reaction intermediate. Solid-state NMR and DSC experiments showed that with excess amounts of TOAB (TOAB:$AgNO_3 \geq 2$), the product of the phase-transfer step has at least two distinct phases whose proportions depend on the TOAB:$AgNO_3$ mole ratio. The octyl chains within these new phases experience lower conformational order accompanied with enhanced mobility when compared to neat TOAB. This results from interactions between $[TOA]^+$ and a multitude of counterions, such as NO_3^-, $[AgBr_2]^-$, and Br^- (from unreacted TOAB), which disturbs the ordered packing of the octyl chains. Lower concentrations of TOAB (TOAB:$AgNO_3 < 2$) resulted in inefficient phase transfer and formation of insoluble silver bromide that precipitated from the reaction

mixture. The reduction of the TAOB:$AgNO_3$ mole ratio from 4.4 (which is commonly used in the two-phase methods) to 2 did not significantly affect the average size and uniformity of the nanoparticles. This modification to the synthetic procedure simplifies the purification process and improves the solubility of the dried nanoparticles, without compromising the small size and dispersity of the nanoparticles produced.

Information on the microstructure and dynamics of the surface grafted alkanethiols was acquired by solid-state NMR spectroscopy. In comparison to the neat ODT, the ^{13}C SSNMR spectrum of SNPODT showed noticeable shifts of the resonances to higher frequencies, disappearance or relatively large displacement of the C_1 signal, and emergence of a new signal. This new signal was also observed in the ^{13}C spectrum of SNPNT. Integration analysis of ODT, SNPODT and SNPNT spectra suggested that the new signal might be due to the C_1 of the surface bonded ODT chains, shifted by around 13 ppm. Higher chemical shifts of C_4 to C_{18} signals of SNPODT were attributed to the predominance of the all-trans conformations within the interdigitated stacks of the alkane chains. Such microstructure of the adsorbed ODTs is consistent with slower dynamics in these ligands, as revealed by relatively larger (with respect to free ODT) T_1/T_2 ratios of their carbon nuclei.

Silver nanoparticles with limited stability were produced by employing $[TOA]^+$ (phase transfer agent) as the capping ligand. Although the resulting SNP are less uniform and less stable than the alkanethiol-capped SNP, their successful synthesis indicates the important role of $[TOA]^+$ ligands in providing stability to the noble metal nanoclusters at the early stages of the two-phase method.

Chapter 5. Polymerization and post-polymerization modification

Thiol functionalized polymers offer superior properties in stabilizing the silver nanocrystals owing to the high affinity of the thiol moiety to bond with silver. Synthesis of stable thiol-bearing polymers with well-defined physical and chemical microstructure is not straightforward and poses a major challenge in using these polymers in the production of nanoparticles. Here, synthesis of well-defined polymers via the RAFT process and their subsequent post-polymerization modification into thiol-functionalized macromolecules are discussed.

5.1. Experimental procedure

5.1.1. Materials

All reagents and solvents were purchased from Sigma-Aldrich and used as received. Deuterated NMR solvents used in this work were purchased from Cambridge Isotope Laboratories.

5.1.2. Synthesis

Poly(methyl methacrylate) (PMMA). Reversible addition fragmentation chain transfer (RAFT) polymerization of the methyl methacrylate monomer was performed in toluene under inert atmosphere using benzoyl peroxide (BPO) as the initiator and 4-cyano-4-(phenylcarbonothioylthio)pentanoic acid (CPPA, Scheme 5.1) as the chain transfer agent (CTA). The optimum condition for RAFT polymerization of MMA was determined by

changing the CTA to initiator mole ratio and the reaction temperature. The CTA/initiator mole ratio was set to 2, 4, 8, and 10 by varying the amount of initiator at constant monomer and initiator concentrations. In a typical polymerization, 3.1mg BPO and the proper amount of the CTA were first dissolved in 3ml of toluene. To this 3ml, MMA (1500:1 monomer to initiator molar ratio) was added at room temperature. The reaction mixture was degassed under vacuum several times and then immersed into an oil bath. The polymerization was allowed to continue under an inert atmosphere for 24 hours at T=70°C. The product was precipitated from toluene in ethanol, washed several times and dried under vacuum to remove unreacted monomers or residual solvents.

Conventional free radical polymerization of MMA was conducted under the same reaction condition employed for RAFT, using 150:1 monomer to initiator (M/I) mole ratio (no chain transfer agent was added). The concentration of the initiator was increased to compensate for the free radicals that are produced by CTA in the RAFT process.

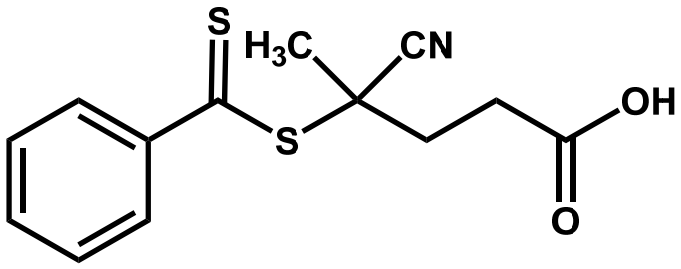

Scheme 5.1. 4-Cyano-4-(phenylcarbonothioylthio)pentanoic acid (CPPA) RAFT agent.

Homopolymer and copolymer of glycidyl methacrylate (GMA). Poly(glycidyl methacrylate) was synthesized via RAFT polymerization using M/I=500 and CTA/I=4, at T=70°C under an inert atmosphere. MMA/GMA random copolymer with 85:15 comonomers mole ratio was prepared using the same reactant ratios and reaction

conditions. The product was precipitated from toluene in ethanol, washed with ethanol and dried under vacuum to remove unreacted monomers or residual solvents.

and copolymers of vinylbenzyl chloride (VBC). RAFT polymerization of vinylbenzyl chloride (VBC) was conducted using both CPPA and 4-Cyano-4-[(dodecylsulfanylthiocarbonyl) sulfanyl] pentanoic acid (CDSPA, Scheme 5.2) chain transfer agents. In both cases the M/I and CTA to initiator mole ratio (CTA/I) were set to 350 and 3, respectively. The reaction mixture was degassed under vacuum several times and then immersed into an oil bath. The reaction was allowed to continue under an inert atmosphere for 48 hours at T=70°C. The M/I was reduced to 100 for free radical polymerization of VBC. The homopolymer is denoted as PVBC.

Random copolymers of MMA with VBC, containing 15 or 5 mole% of the latter, were produced via RAFT polymerization using M/I=350 and CTA/I=3. In a typical polymerization for synthesis of the copolymer with 15 mole% VBC, 2.5 mL MMA, 0.5 mL VBC, 18.8 mg BPO, and 64.9 mg of CTA were dissolved in 4 mL toluene in a round bottom flask. The flask was connected to a vacuum line and the mixture was degassed several times. The reaction was carried out at T=70°C for 48 hours under an inert atmosphere. The resulting polymers are denoted as MV15 and MV5, depending on the initial mole percentage of VBC. Free radical polymerizations were carried out by decreasing the M/I to 100. The same reactant ratios and reaction conditions were used to prepare copolymers of VBC (15 mole%) with styrene and butyl acrylate.

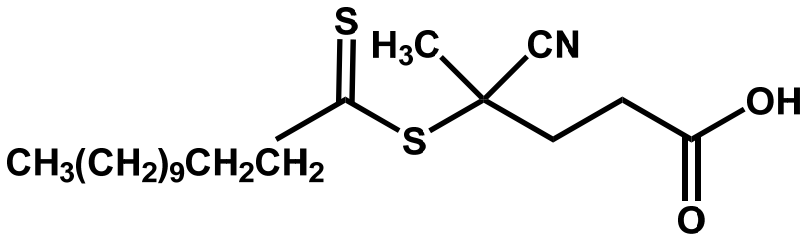

Scheme 5.2. 4-Cyano-4-[(dodecylsulfanylthiocarbonyl) sulfanyl] pentanoic acid (CDSPA) RAFT agent.

Thiouronium functionalized homopolymer and copolymers of VBC. The chloride side groups on VBC repeating units of PVBC and VBC random copolymers were substituted with thiouronium (TU) functionalities via reaction of the polymer with thiourea. An excess amount of thiourea, with respect to the molar concentration of VBC units, was used to ensure complete substitution of all chlorides. These copolymers are denoted by adding "TU" to their names; for example MV15TU is the thiouronium functionalized MV15 random copolymer.

Thiol-terminated PMMA. The residue of the CTA at the polymer chain end was reduced in the presence of excess sodium borohydride. The polymer and $NaBH_4$ were both dissolved in 5:1 THF/water mixture. The polymer solution changed color a short time after addition of $NaBH_4$. The reaction was continued for 24 hours at ambient condition. The product was separated by precipitation and washed several times.

Thiol-functionalized copolymers of VBC. The TU side groups on the copolymer chains were converted into thiolates via hydrolysis by KOH or reaction with $NaBH_4$. Both modification reactions were conducted in DMSO/water mixture at elevated temperature. In a typical reaction, KOH or $NaBH_4$ dissolved in the DMSO/water mixture was added to the

copolymer solution under an inert atmosphere and stirred for 1 hour at T=60°C. The mole ratios of KOH or $NaBH_4$ to VBC units were set to 7 and 4.4 respectively.

Benzyl thiouronium and benzyl thiolate. Benzyl thiouronium (BTU) was produced through reaction of benzyl chloride (BC) with an excess amount of thiourea (thiourea/BC mole ratio=1.5), under the same reaction conditions used for synthesis of TU functionalized copolymers. The reaction of TU groups with $NaBH_4$ was studied inside an NMR spectrometer at T=60°C, using $NaBH_4$/BTU mole ratio of 2 and DMSO-d_6 as the reaction medium.

5.1.3. Techniques

UV-visible spectroscopy. UV-visible spectra of dissolved test materials were recorded on a Cary 50 spectrophotometer. The experiments were conducted in the wavelength range of 300 nm to 700 nm at room temperature. For each spectrum, the baseline was corrected by subtracting the absorption of the cuvette and the pure solvent.

Solution-state NMR spectroscopy. NMR spectra were recorded at ambient temperature with a 300 MHz Bruker Avance II NMR spectrometer equipped with a 5 mm HX BBO probe. Higher resolution spectra were acquired on a Bruker Avance III HD 700 MHz NMR Spectrometer. Calculation based on five separate measurements on the same sample gives a standard deviation of 0.0012 for the ^{1}H NMR chemical shifts, which is very close to the non-zero-filled FID digital resolution of the experiments.

Fourier transform infrared (FTIR) spectroscopy. FTIR spectroscopy was performed at ambient temperature with a Bruker Alpha infrared spectrometer.

Solid-state NMR (SSNMR) spectroscopy. SSNMR experiments were carried out on a 500 MHz widebore Varian Inova spectrometer equipped with 4 mm Varian T-3 HFXY at 8 kHz magic angle spinning rate and T = 20°C. The 90° pulse lengths were calibrated to 3-3.5 μs for both ^{1}H and ^{13}C. All ^{13}C spectra were acquired through cross-polarization with a 2.4 ms contact time (optimized for maximum signal-to-noise ratio), using constant 1H locking field (60 kHz), and a ramped ^{13}C locking field (from 73 to 77 kHz).

Gel permeation chromatography (GPC). GPC experiments were performed using a Malvern Viscotek GPCmax instrument equipped with five detectors: refractive index, intrinsic viscosity, differential pressure, low angle light scattering, and right angle light scattering detectors. Monodisperse polystyrene with M_n=99000 g/mol was used as the only reference required to calibrate the instrument.

5.2. Poly(methyl methacrylate)

efficiency of the chain transfer agent (4-Cyano-4-(phenylcarbonothioylthio)pentanoic acid; CPPA) in controlling the molecular weight and polydispersity of poly(methyl methacrylate) (PMMA) was examined by systematically changing the chain transfer agent (CTA) to initiator (I) mole ratio, at a constant concentration of the initiator, in a series of polymerization reactions. The molecular weights of RAFT polymerized products reduced drastically at larger concentrations of CTA, due to the increase in the number of active macroradicals present in the polymerization medium, Table 5.1. Polymers with narrow molar mass distribution, with PDI of less than 1.07, were obtained at the CTA/I ratios of 8 and 10. Acceptable control over the polymerization (PDI≈1.1) was also achieved at CTA/I=4 by decreasing the concentration of the initiator

and reducing the reaction temperature. The living nature of these polymers (their ability for reactivation under appropriate reaction condition; refer to Chapter 2, section 2.5.1) was verified by employing them as macro-RAFT agents in polymerization of methyl methacrylate (MMA). The PMMA chains prepared with CTA/I=10 were uniformly extended with new MMA monomer in the presence of an appropriate amount of initiator. The resulting polymer has an increased molar mass while maintain its narrow molecular weight distribution (PDI=1.11), Figure 5.1.

Table 5.1. Molar mass and polydispersity index as a function of CTA/initiator molar ratio.

	0:1	2:1	4:1	8:1	10:1
M_n / 10^3(g/mol)	70.3	52.8	41.8	20.2	16.2
M_w / 10^3 (g/mol)	161.9	78.4	47.4	21.6	16.7
PDI	2.30	1.48	1.14	1.06	1.03

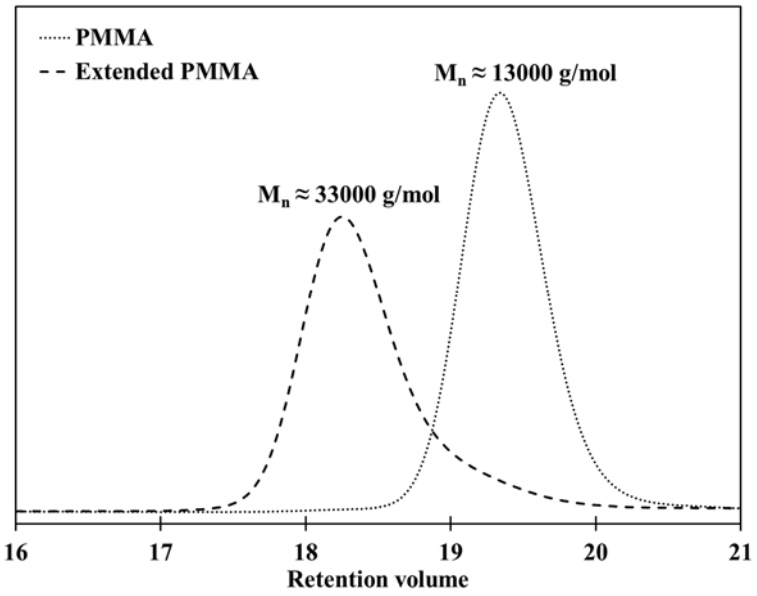

Figure 5.1. GPC traces of the 10:1 PMMA and the extended PMMA samples.

Configuration of the 10:1 PMMA (CTA/I=10) was probed by ^{1}H solution NMR in $CDCl_3$, Figure 5.2. The signal assignment was confirmed by a 2D ^{1}H COSY NMR experiment (Appendix, Figure A.3). Figure 2 shows signals arising from sequences of meso-racemic ("mr", Scheme 3) additions which are characteristic of an atactic configuration. Moreover, close examination of this spectrum reveals several weak resonances which are not present in the spectrum of the PMMA synthesized via conventional free radical polymerization, Figure 5.3. A comparison with the ^{1}H spectrum of the RAFT agent indicates that these weak signals are originated from the dithioester fragments attached to the polymer chain ends. These terminal groups have a characteristic light absorption band at $\lambda \approx 509$ nm in the UV-visible spectrum of the polymer solution, Figure 5.4. This was confirmed by a comparison between the UV-visible spectrum of the RAFT PMMA solution, FRP (free radical polymerization) PMMA which does not have any absorption in the visible light region, and the neat CTA that has an absorption at $\lambda \approx 511$ nm. The changes in the intensity of this peak is a distinctive indicator of conversion of the terminal group during the post polymerization modification reactions.

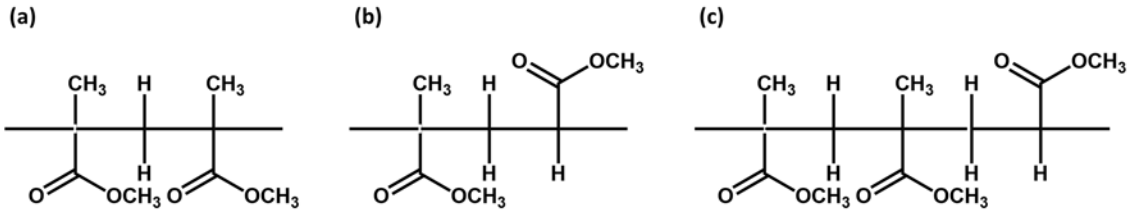

Scheme 5.3. Meso (a), racemic (b), and meso-racemic (c) additions of MMA monomers.

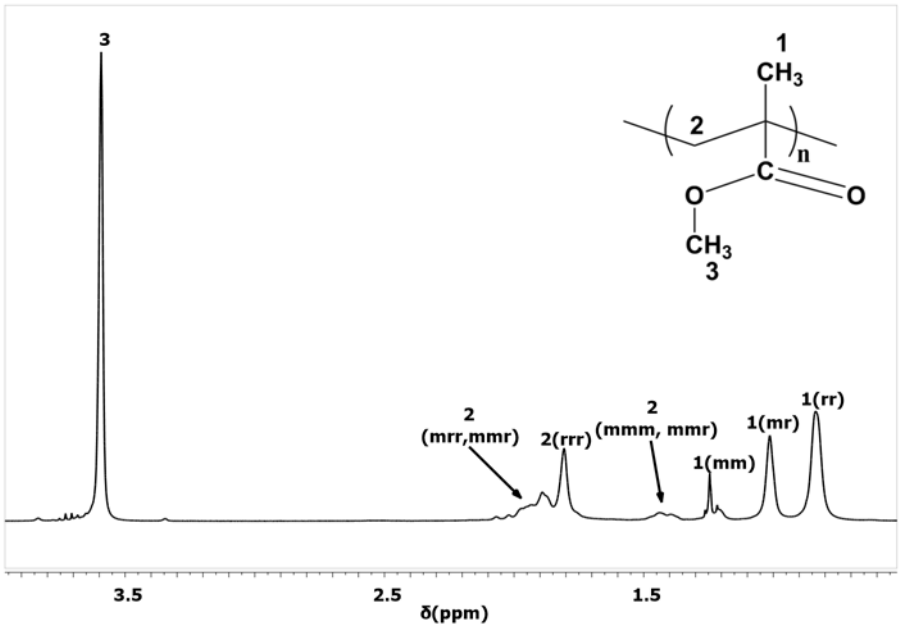

Figure 5.2. [1]H NMR spectrum of the 10:1 PMMA sample in deuterated chloroform. "m" stands for meso and "r" stands for racemic isomers.

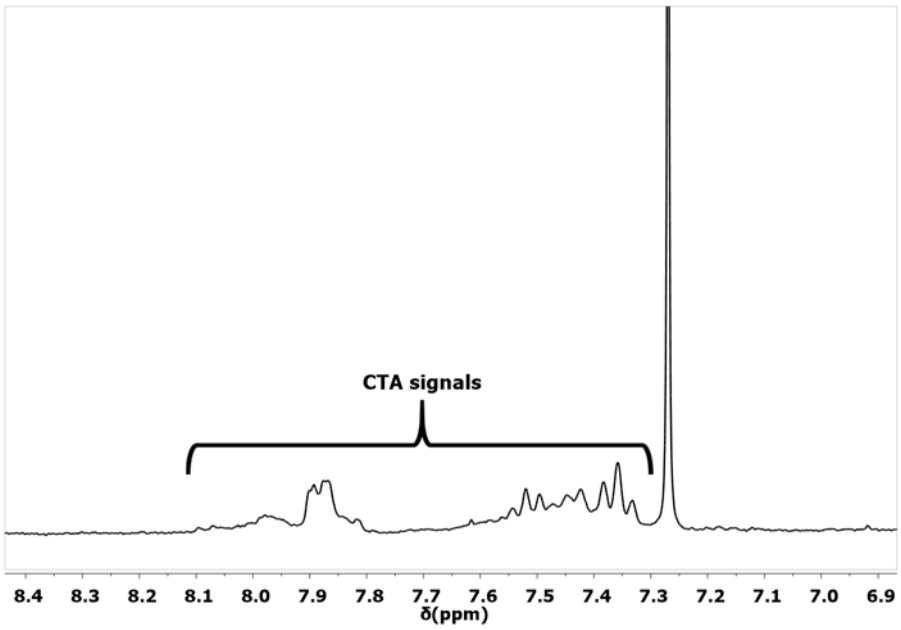

Figure 5.3. selected region from [1]H NMR spectrum of 10:1 PMMA showing residue of the CTA.

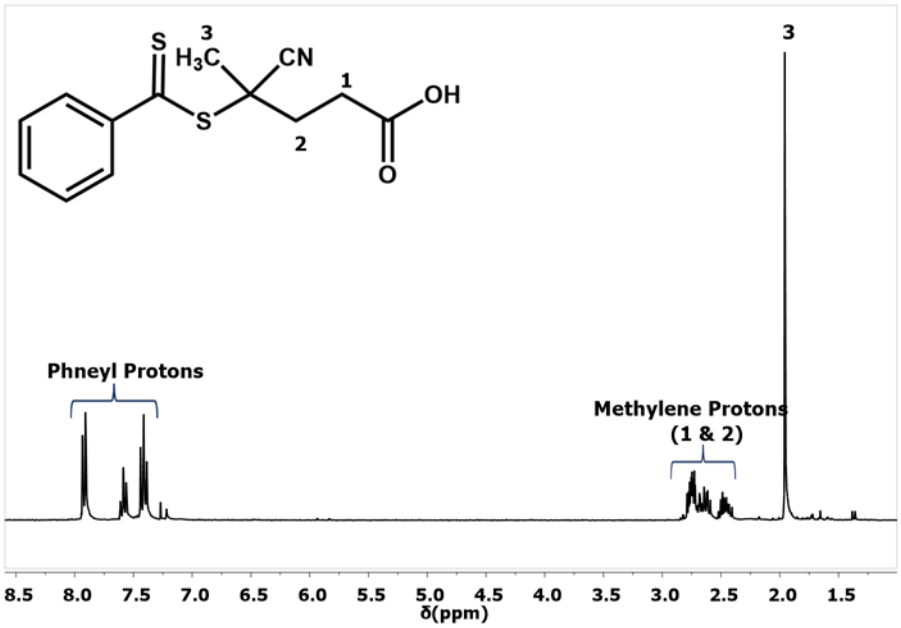

Figure 5.3. (Continued) the spectrum of 4-Cyano-4-(phenylcarbonothioylthio) pentanoic acid in $CDCl_3$. The signal assignments were done by performing 2D ^1H COSY experiment and integration analysis.

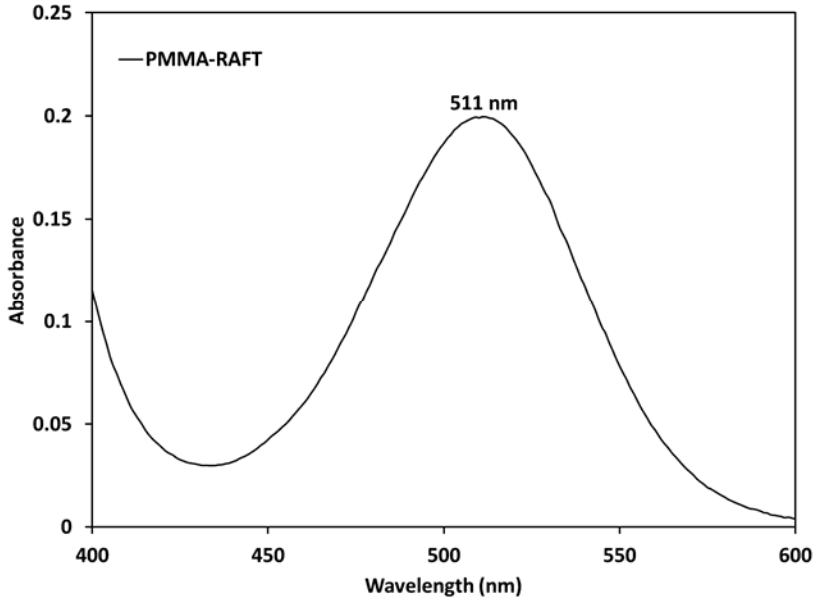

Figure 5.4. UV-visible spectrum of the 10:1 PMMA solution in THF.

5.3. Homopolymer and copolymer of glycidyl methacrylate

Despite structural similarity between glycidyl methacrylate (GMA) and MMA monomers, employment of the same RAFT agent (CPPA) used for synthesis of PMMA did not yield satisfactory control over the polymerization of GMA. Poly(glycidyl methacrylate) (PGMA) synthesized in presence of CPPA has a PDI of 1.6 (in contrast to PDI=1.03 for RAFT PMMA) which is still less than that of the PGMA made via conventional free radical method (PDI=2.24). This indicates moderate efficiency of the chain transfer agent for controlled polymerization of GMA. The characteristic ^{1}H NMR and FTIR peaks of the epoxide ring are shown in Figures 5.5 and 5.6. In comparison with PMMA, the FTIR spectrum of PGMA contains medium intensity bands at 909 cm^{-1} and 848 cm^{-1} which are characteristic of the epoxide ring, Table 5.2.

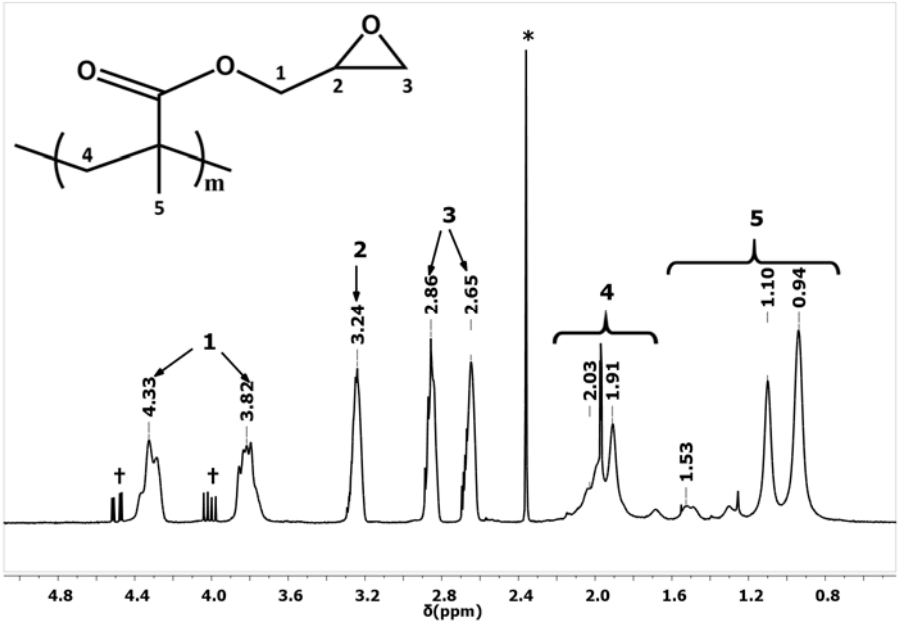

Figure 5.5. ^{1}H NMR spectrum of PGMA. The residual polymerization solvent (toluene) and monomer signals are respectively indicated by * and †.

Table 5.2. Selected FTIR bands of PGMA.

Wavenumber (cm^{-1})	1720	1000-12600	909 & 848
Assignment	ν(C=O) ester carbonyl	ν(C-O) ester	ν(C-O-C) epoxy ring

ν: stretching vibration

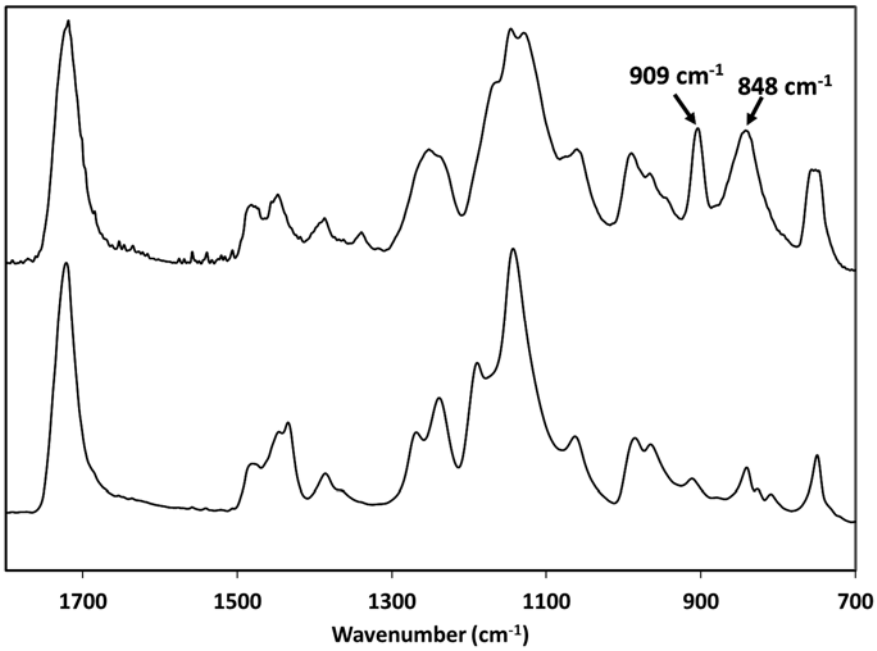

Figure 5.6. FTIR spectrum of PGMA (top) in comparison to the spectrum of PMMA (bottom).

A random copolymer of MMA and GMA, containing 15 mole% of the latter in the initial reaction mixture (MG15), was successfully prepared via RAFT polymerization. The actual mole fraction of GMA repeating units in this copolymer, determined by integration of the ^{1}H signals, was 11.6 %. The difference in the mole fractions of the GMA monomer and the repeating units can be attributed to the larger reactivity ratio of GMA[134] (1.24) compared to MMA (0.85) and lower efficiency of chain transfer to this comonomer.

5.4. Homopolymer and copolymers of vinylbenzyl chloride

polymerization of vinylbenzyl chloride (VBC) was conducted using both CPPA (4-Cyano-4-(phenylcarbonothioylthio) pentanoic acid) and CDSPA (4-Cyano-4-[(dodecylsulfanylthiocarbonyl) sulfanyl] pentanoic acid) chain transfer agents. The polymers synthesized in the presence of CPPA and CDSPA have PDIs of 1.58 and 1.46, respectively. Although these values are noticeably smaller than the PDI of poly(vinylbenzyl chloride) (PVBC) prepared via the conventional free radical process (2.64), they are significantly greater than those of RAFT-polymerized PMMA. This implies inadequate efficiency of the RAFT agents employed in controlling the polymerization of VBC. The ^{1}H and ^{13}C NMR and FTIR spectra of PVBC are presented in Figures 5.7 and 5.8. The FTIR spectrum contains a strong band at 670 cm^{-1}, bending vibration of the aromatic C-H bonds at 824cm^{-1}, the C-Cl bond stretching at 1264 cm^{-1}, stretching modes of aromatic C=C bonds at 1421, 1442, and 1510 cm^{-1}, and C-H stretching vibrations at 2850, 2920, and 3024 cm^{-1}. The intensity of the C-Cl band decreases dramatically upon substitution with chlorine, thus it is a very useful indicator of the progress in post-polymerization modification of the VBC repeating units.

Table 5.3. ^{1}H and ^{13}C signals of PVBC.

^{1}H shifts (ppm)	1.40	1.71	4.55	6.42	6.50	7.07
Assignment	H_1	H_2	H_3	H_4	H_4	H_4
^{13}C shifts (ppm)	43.77	40.43	46.49	128.12	135.09	145.41
Assignment	C_1	C_2	C_3	C_4	C_5	C_6

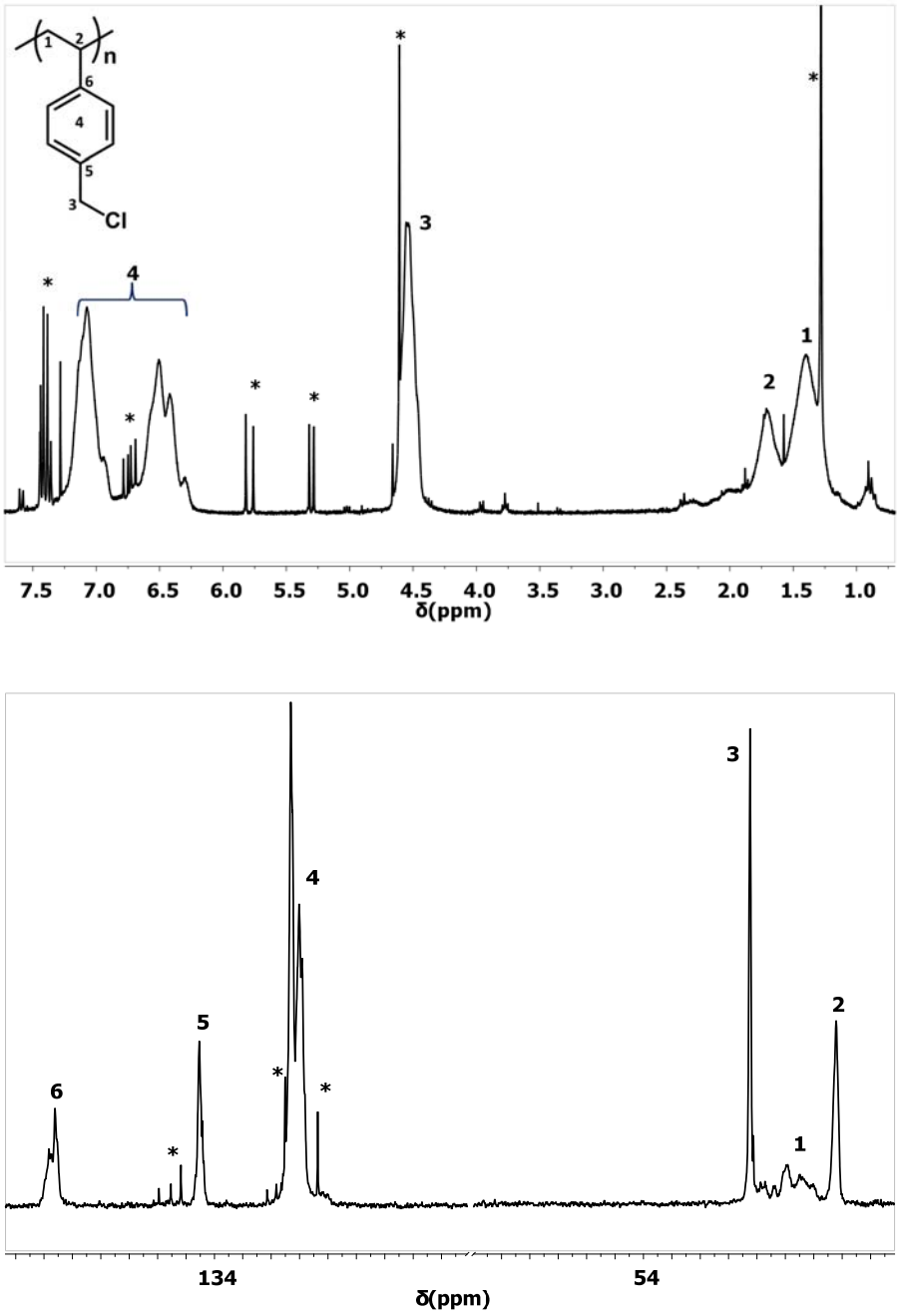

Figure 5.7. Solution state ^{1}H (top) and ^{13}C (bottom) NMR spectra of PVBC in chloroform-d.

The signals of residual monomers are shown with asterisks.

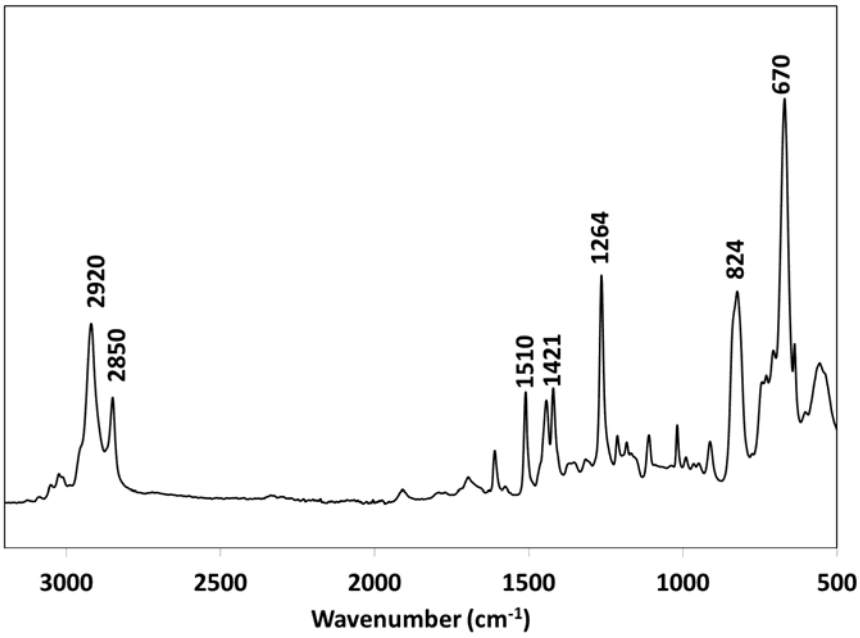

Figure 5.8. FTIR spectrum of PVBC.

Table 5.4. Selected FTIR bands of PVBC.

Wavenumber (cm^{-1})	670	824	1264	1421	1442	1510	2850	2920
Assignment	$\delta_{(C-H)}$ Phenyl	$\delta_{(C-H)}$ Phenyl	$\nu_{(C-Cl)}$	$\nu_{(C=C)}$	$\nu_{(C=C)}$	$\nu_{(C=C)}$	$\nu_{s(C-H)}$	$\nu_{as(C-H)}$

δ: bending, ν_s: symmetric stretching, ν_{as}: asymmetric stretching

The chlorine of the VBC repeating unit can be substituted with a thiol functionality via a two-step post-polymerization modification reaction starting with the first nucleophilic substitution of Cl with thiourea and subsequent hydrolysis, Scheme 5.4. This is a well-established procedure for synthesis of thiol-bearing small molecules. The first step proceeds through an SN2 mechanism yielding a thiouronium salt side group. In contrast to the unmodified polymer, the thiouronium functionalized PVBC (PVBC-TU) is partially

soluble in water and also dissolves readily in polar solvents such as DMSO. The FTIR spectrum of PVBC-TU, in comparison with that of the neat PVBC, is shown in Figure 5.9. Selected FTIR bands of neat thiourea are presented in Table 5.5 for comparison. The PVBC-TU polymer contains a broad absorption ranging from 3100 cm^{-1} to 3350 cm^{-1} (N-H stretching modes), a strong C=N stretching band at 1642 cm^{-1} with a shoulder at 1605 cm^{-1} (N-H bending), which are all characteristics of the thiouronium side group. The band at 1401 cm^{-1} arises from the C=S stretching vibration of residual thiourea, Table 5.5. The sharp C-Cl vibration band at 1264 cm^{-1} in PVBC is noticeably weaker and shifted to a lower wavenumber (1250 cm^{-1}) in PVBC-TU, indicating the substitution of a fraction of chlorines.

The ^{1}H NMR spectrum of PVBC-TU dissolved in D_2O contains a new signal at 8.62 ppm that is assigned to the NH_2 protons of the thiouronium group. The broad intense peak at 7.15 ppm originates from the overlap of the neat thiourea NH_2 signal at 7.22 ppm and the phenyl ring resonance at 7.08 ppm, thus indicating the presence of a significant amount of residual thiourea, Figure 5.10. The presence of the C-Cl band in the FTIR spectrum along with the relatively weak ^{1}H NMR signal of TU side groups implies that the substitution reaction does not proceed to completion and the modified PVBC retains a considerable fraction of unreacted VBC chlorines. Such incomplete conversion is mainly caused by high concentration of the reactive sites on the VBC homopolymer which severely reduces their accessibility. As the reaction proceeds, substitution of chlorines with the bulky TU anions decreases availability of the remaining unmodified VBC units. Moreover, the polymer progressively loses its solubility in the reaction medium, which further lowers the reactivity of the polymer.

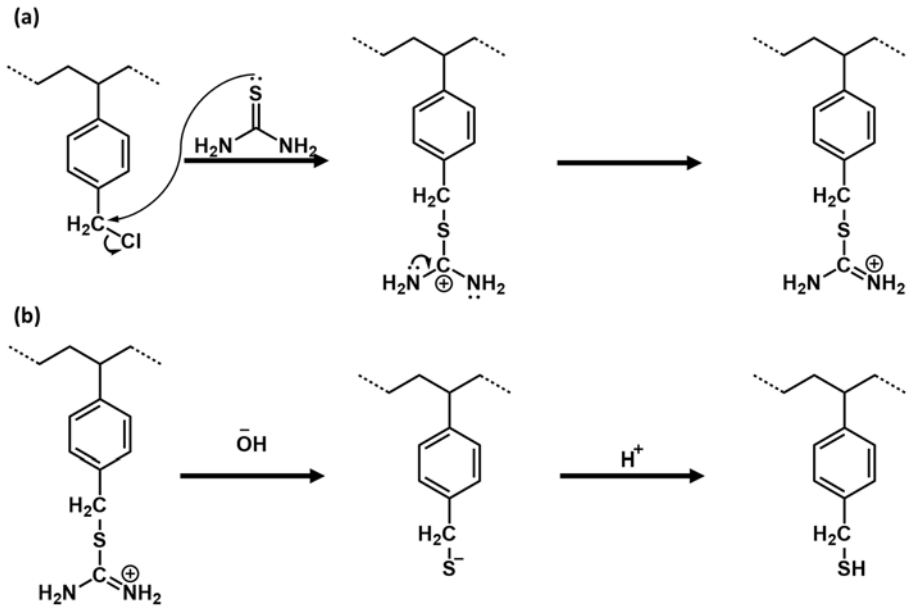

Scheme 5.4. Schematic representation of (a) nucleophilic substitution of VBC chlorine with thiouronium and (b) basic hydrolysis of TU side group followed by acid treatment to obtain thiol moiety.

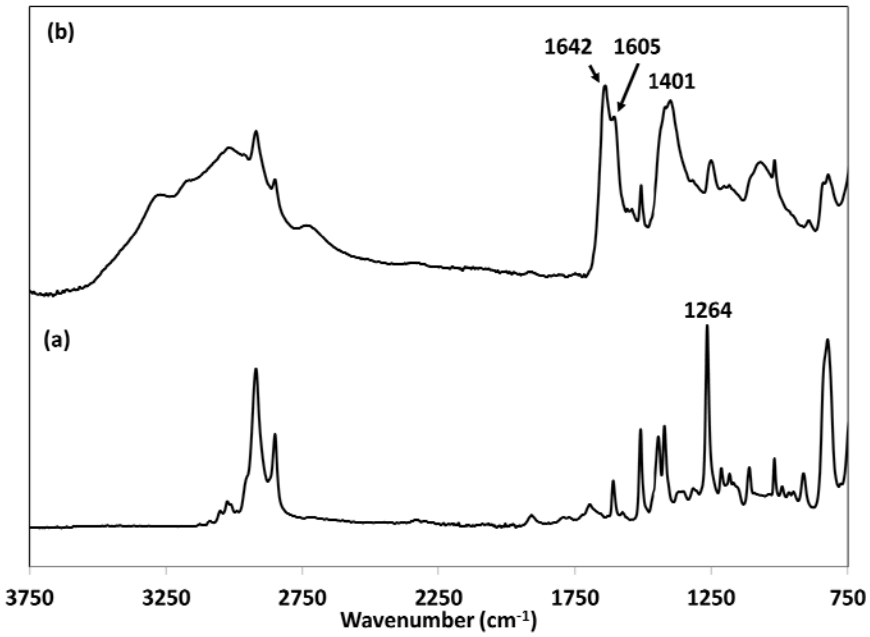

Figure 5.9. FTIR spectra of (a) PVBC and (b) PVBC-TU.

Table 5.5. Selected FTIR bands of neat thiourea[135].

Wavenumber (cm^{-1})	1410	1640	1689–1650	3200-3400
Assignment	$\nu_{(C=S)}$	$\delta_{(N-H)}$	$\nu_{(C=N)}$	$\nu_{(N-H)}$

δ: bending, ν: stretching

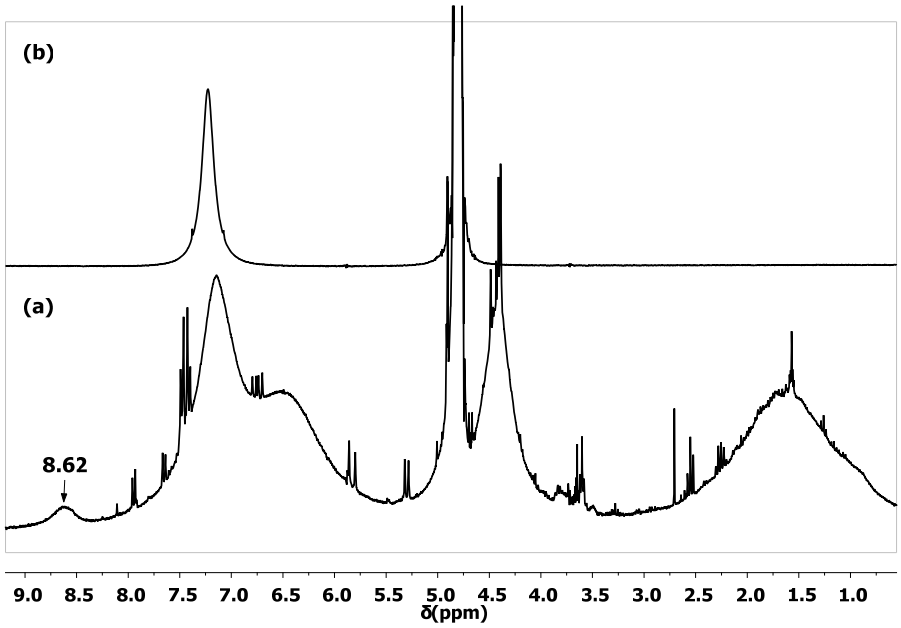

Figure 5.10. ^{1}H NMR spectra of (a) PVBC-TU and (b) neat thiourea in D_2O.

Basic hydrolysis of PVBC performed under a variety of reaction conditions failed to produce a soluble thiol functionalized polymer. This reaction yielded a crosslinked network of polymer which only swells in compatible solvents, therefore cannot be further employed as the capping agent in the preparation of isolated nanoparticles. The insoluble material is formed as a result of side reactions leading to inter and intra-molecular bonding between the polymer chains. Examples of such side reactions include, but are not limited to, the formation of disulfide bonds between the thiolate groups (disulfide might be more

stable than thiolate in the presence of oxygen) and nucleophilic attack of thiolates to the benzylic methylene of the residual benzyl chloride groups. The covalent bonds resulting from these reactions attach (crosslink) the polymer chains together to form an insoluble network. The probability of these side reactions can be reduced by decreasing the concentration of reactive sites along the polymer chain through random copolymerization of VBC with an unreactive monomer such as methyl methacrylate. Random distribution of the VBC units along the copolymer chains further enhances the accessibility of the benzyl chlorides, thus facilitating their substitution by TU groups.

VBC was copolymerized with methyl methacrylate, styrene, and butyl acrylate (BA) comonomers to produce random copolymers with a range of physical and mechanical properties. Molecular weights, polydispersity indices, and the compositions of the MV15, SV15, and BV15 copolymers synthesized via FRP and RAFT (using CDSPA as the chain transfer agent) polymerizations are presented in Table 5.6. The RAFT agent employed provides good control over the copolymerization of VBC with MMA consistently, producing a copolymer with narrower molecular weight distribution and smaller average molar mass than the FRP product, Figure 5.11. The actual mole fraction of the VBC units in the RAFT synthesized MV15 is 5.2% larger than the initial concentration of this monomer in the reaction mixture. This difference can be attributed to the higher probability of the chain transfer reaction to the RAFT agent from a macro-radical with an active MMA site (MMA^*), than a macro-radical bearing an active VBC. The relatively higher tendency of MMA^* to react with the original or macro RAFT agents increases their probability of conversion into dormant species, thus resulting in a larger fraction of the VBC-terminated active chains.

Table 5.6. Basic characteristics of VBC random copolymers.

	M_n / 10^3 (g/mol)		PDI		VBC mole fraction* (%)	
	FRP	RAFT	FRP	RAFT	FRP	RAFT
MV15	31.2	14.2	2.31	1.29	15.4	20.2
SV15	32.8	9.5	2.64	1.58	15.3	18.1
BV15	38.7	10.8	2.51	1.93	NA**	NA**

* Determined from ^{1}H NMR spectra of the copolymers

** These comonomers do not form random copolymers

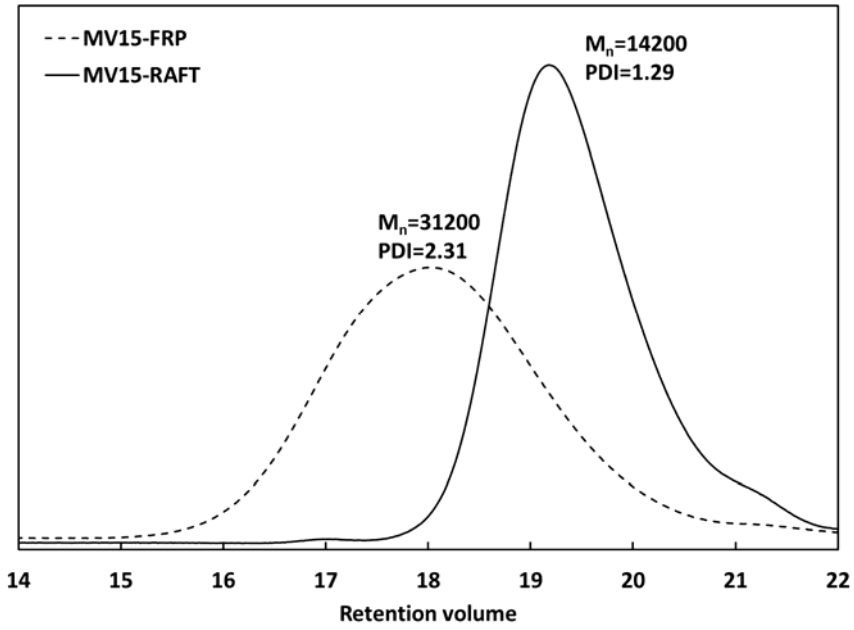

Figure 5.11. GPC traces of the MV15 copolymer prepared via conventional free radical polymerization (MV15-FRP) and RAFT polymerization (MV15-RAFT).

The CDSPA chain transfer agent is less efficient in controlling the copolymerization of VBC with styrene, as is evident from the PDI of this copolymer, and is completely inefficient in the case of the VBC/BA reaction. Further insight into the influence of the

RAFT agent on the styrene/VBC copolymerization was obtained by monitoring the changes in concentrations of the reactants and products during the reaction. Figure 5.12 shows the monomer conversion as a function of the reaction time for the FRP and RAFT polymerization of SV15. These reactions were conducted at T = 75 °C inside an NMR tube, using identical concentrations of comonomers and initiator, and a CTA/initiator ratio of 3 for the RAFT process. The monomer conversion in the FRP reaction is around 77% when it reaches a plateau at long reaction times. The conversions of both comonomers follow similar trends, which is in agreement with their random addition to the copolymer chains. Introduction of the CTA into the reaction mixture induces an inhibition period[82, 84] and reduces the overall rate of polymerization (-d[M]/dt, where [M] is the monomer concentration), which is especially apparent during the early stages of the reaction where the slope of the conversion curve reduces from 1.6×10^{-3} s^{-1} for FRP to 0.9×10^{-3} s^{-1} for RAFT. Moreover, the maximum monomer conversion of the RAFT process is limited to 33%. This maximum is reached after a relatively short time (≈ 15 hours), beyond which the reaction does not proceed.

Inspection of the NMR spectra at early stages of the polymerization shows that the sharp P_3 signal of the CTA, which arises from the closest protons to the reaction site on CTA, disappear after a relatively short time, Figure 5.13. Presence of the inhibition period, along with variations in the NMR signals of the RAFT agent imply that the initial radical transfer from the short propagating chains to the CTA occurs successfully. The low monomer conversion is either caused by the extremely high stability of the intermediate radical (Scheme 5.5-a), or is more probably the result of very slow radical transfer from an active chain to a macro-RAFT agent (Scheme 5.5-b). The latter leads to termination of the

propagating chains and stops the polymerization. In the case of the BA/VBC copolymer, monitoring the free radical polymerization showed that VBC monomers polymerize at a noticeably higher rate than BA, indicating that at least a large fraction of these comonomers do not form random copolymers, Figure 5.14.

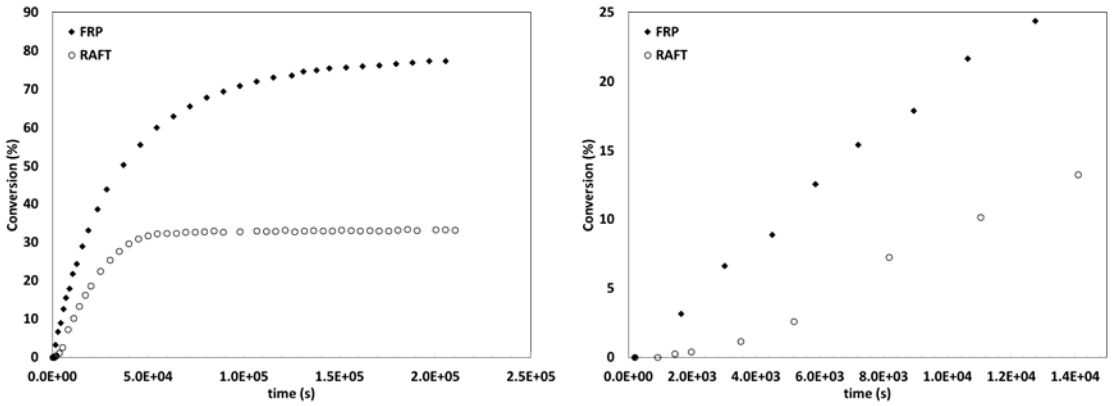

Figure 5.12. Monomer conversion as a function of time during the FRP and RAFT copolymerization of SV15. The inhibition period (right) at the start of the RAFT polymerization.

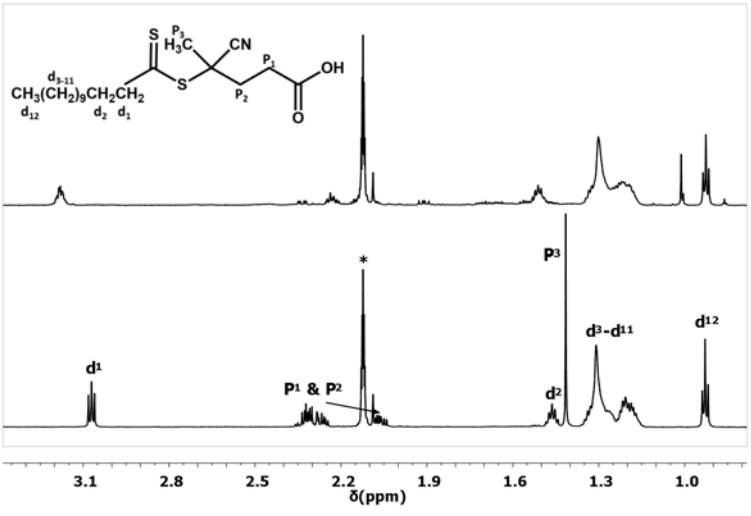

Figure 5.13. Selected region from ^{1}H NMR spectra of the SV15 RAFT polymerization mixture at t=0 (bottom) and t=3522 s (top). The solvent signal (toluene-d_8) is marked by asterisk.

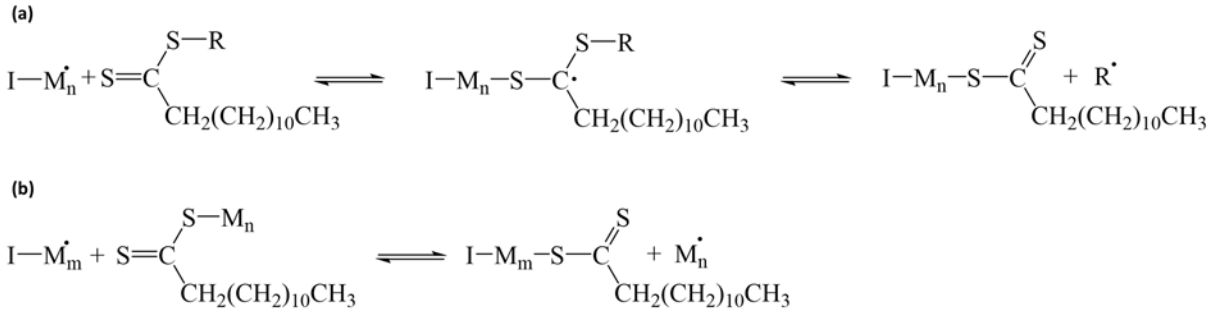

Scheme 5.5. (a) Radical transfer from a propagating chain to an unreacted RAFT agent and (b) transfer from a propagating chain to a macro-RAFT agent which reactivates a dormant chain.

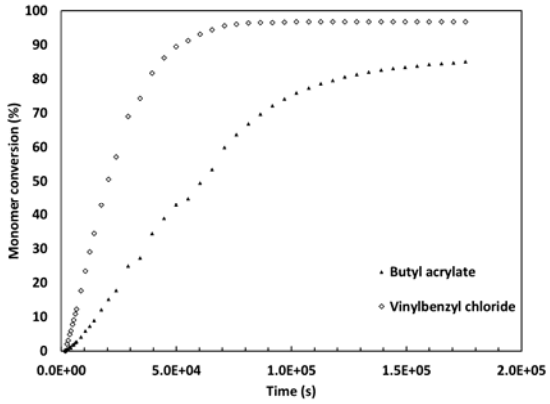

Figure 5.14. Monomer conversion during free radical polymerization of BA/VBC.

The ^{1}H and ^{13}C solution NMR spectra of the MV15 copolymer are shown in Figures 5.15. All the signals, except for the proton resonance at 2.94 ppm and the carbon resonance at 51.09 ppm, were assigned based on comparison with the spectra of MMA and VBC homopolymers. These new signals reveal information regarding the configuration of the copolymer chains. The proton signal at 2.94 ppm has no cross-peak in the COSY spectrum (Appendix, Figure A.4) and is correlated with the new carbon signal at 51.09 ppm in the HSQC spectrum of MV15, Figure 5.16. Further information on the origin of the new ^{13}C signal was obtained from DEPT experiments, showing that it is originating from either methyl side groups of MMA repeating units, Figure 5.17. The peak area of these methyl

signals confirms that the new resonance arises from a portion of the P_4 groups (CH_3 on the ester side-chain) experiencing different shielding environment. The changes in ^1H and ^{13}C chemical shifts in these groups are due to their proximity to the aromatic ring of the nearby VBC units. Considering that the concentration of VBC is 5.67 times smaller than that of MMA, and the reactivity ratios of these comonomers are less than one[136], it is expected that the VBC monomers randomly distribute as isolated units between sequences of MMA. The ester side groups on an MMA unit adjacent to a VBC experiences a different electronic environment resulting from the ring current, compared to those located next to another MMA. The methyl on such an ester group is located in the diamagnetic shielding zone of the proximal phenyl ring leading to lower chemical shifts of its signal (P_4^*). Interestingly the resonance of aromatic protons in MV15 are shifted to higher frequencies, compared to the PVBC, as they are not affected by a neighboring phenyl ring. The peak area ratio of P_4^* to P_4 is close to 1:4 indicating that nearly all of the VBC units are connected to MMA, thereby confirming the random distribution of the comonomers.

Table 5.7. ^1H and ^{13}C signals of MV15.

^1H shifts (ppm)	0.83	1.02	1.39	1.64	1.80	1.99	2.50	2.94	3.60	4.53	7.00	7.23
^1H Nuclei	P_1	P_1	V_1	P_2	P_2	V_2	V_2	P_4^*	P_4	V_3	V_4	V_4
^{13}C shifts (ppm)	16.42	37.33	44.64	46.07	51.09	51.76	52.87	54.33	128.35	135.36	145.54	177.31
^{13}C Nuclei	P_1	V_2	P_3	V_3	P_4^*	P_4	V_1	P_2	V_4	V_5	V_6	P_5

* These are the P4 signals of the MMA units bonded to a VBC unit

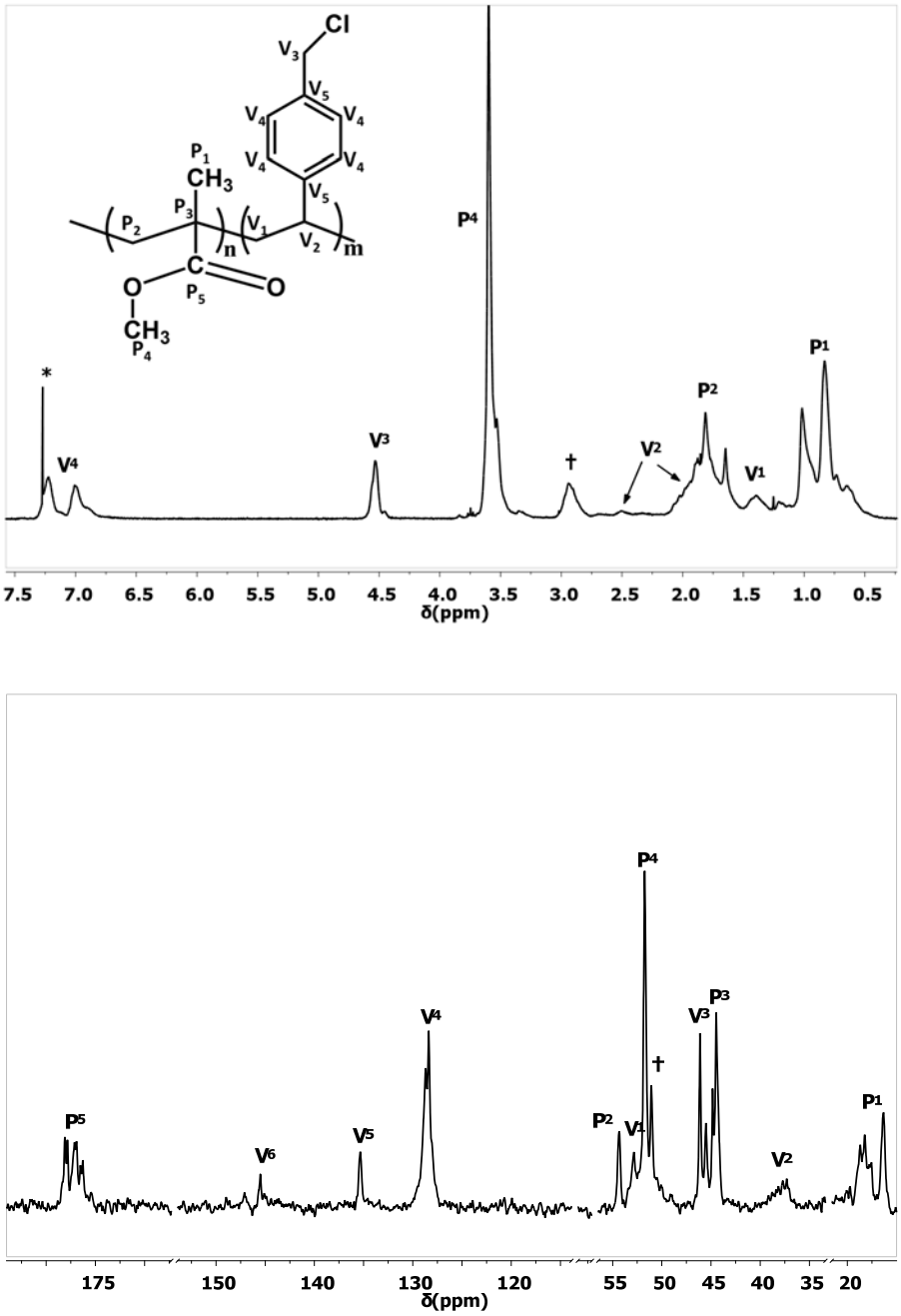

Figure 5.15. ^{1}H and ^{13}C NMR spectra of the MV15 copolymer in chloroform-d. The new proton and carbon signals are indicated by †.

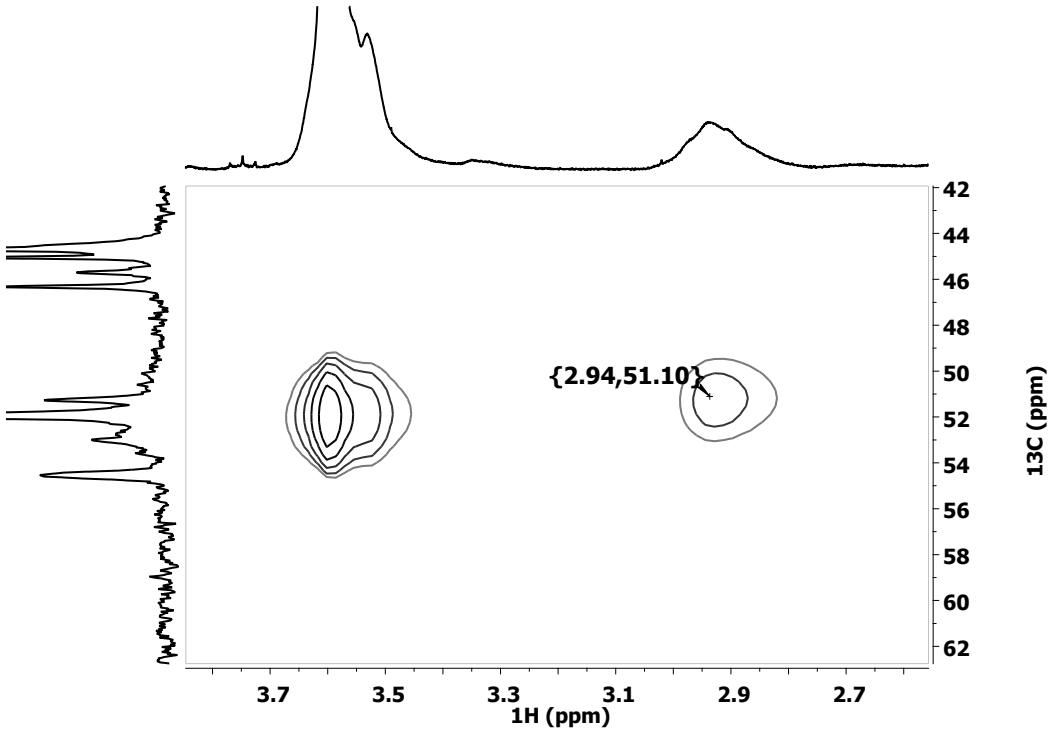

Figure 5.16. HSQC spectrum of the MV15 in chloroform-d.

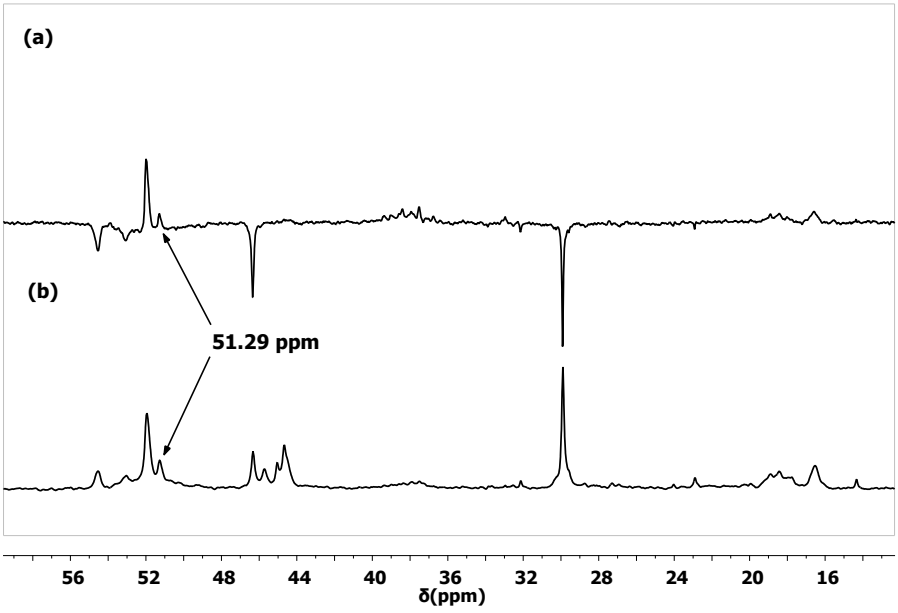

Figure 5. 17. (a) DEPT-135 and (b) ^{13}C NMR spectra of MV15 in chloroform-d.

Post polymerization modification of the MV15 with thiourea, to produce thiouronium functionalized copolymer (MV15TU), drastically reduces the solubility of the polymer in organic solvents of moderate polarity, such as THF and chloroform. This polymer also has limited solubility in water (significantly less than PVBC), but dissolves in DMSO and THF/water mixtures. Solution NMR spectra of the MV15TU in DMSO-d_6 are shown in Figure 5.18. The ^{1}H spectrum contains a new signal at 9.33 ppm that originates from the NH_2 hydrogens of the thiouronium side group. These hydrogens are strongly deshielded, in contrast to the neat thiourea (7.22 ppm), due to the positive charge delocalization in the NH_2 moieties, Scheme 4. The peak area of this resonance is twice that of the benzylic CH_2 signal, indicating that the substitution reaction proceeds almost to completion. The ^{13}C spectrum clearly reveals the structural changes in the modified copolymer, where the signal of benzylic CH_2 shifts from 46.3 ppm in the MV15 to 34.3 ppm in MV15TU due to the substitution of its neighboring group. This assignment was confirmed by a 2D HSQC experiment on MV15TU which shows a correlation between the carbon at 34.3 ppm and the proton at 2.94 ppm (benzylic CH_2). The new ^{13}C peak at 169.7 arises from the thiouronium carbon. The assignments were further verified using DEPT experiments allowing for distinction between C, CH, CH_2, and CH_3 moieties (Appendix, Figure A.5). The NMR spectra of the SV15TU and BV15TU copolymers show changes similar to those observed in MV15TU, upon reaction with thiourea. The ^{1}H spectra of both SV15TU and BV15TU contain two signals, with slightly different chemical shifts, that are very close to the benzylic CH_2 signal of the unmodified copolymers, Figure 5.19. Inspection of the ^{13}C and 2D HSQC spectra of SV15TU and BV15TU shows that one of these signals arise from the CH_2 side group of the modified vinylbenzyl units, while the

other one belongs to the residual (unmodified) VBCs. The fraction of substituted chlorines are 50% for SV15TU and 69% for BV15TU, calculated from integration analysis.

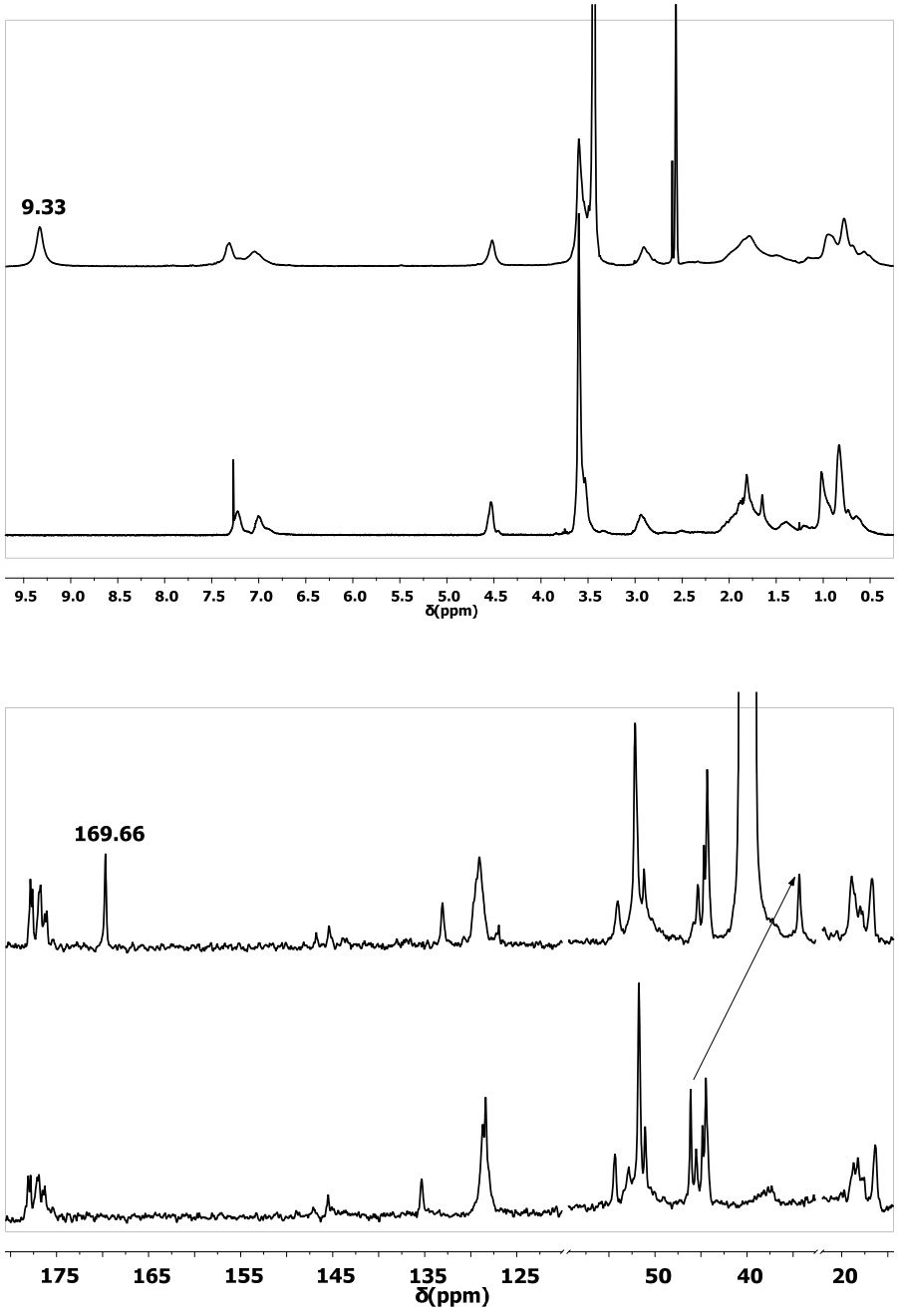

Figure 5.18. ^{1}H and ^{13}C NMR spectra of MV15TU in DMSO-d_6 in comparison to the unmodified copolymer.

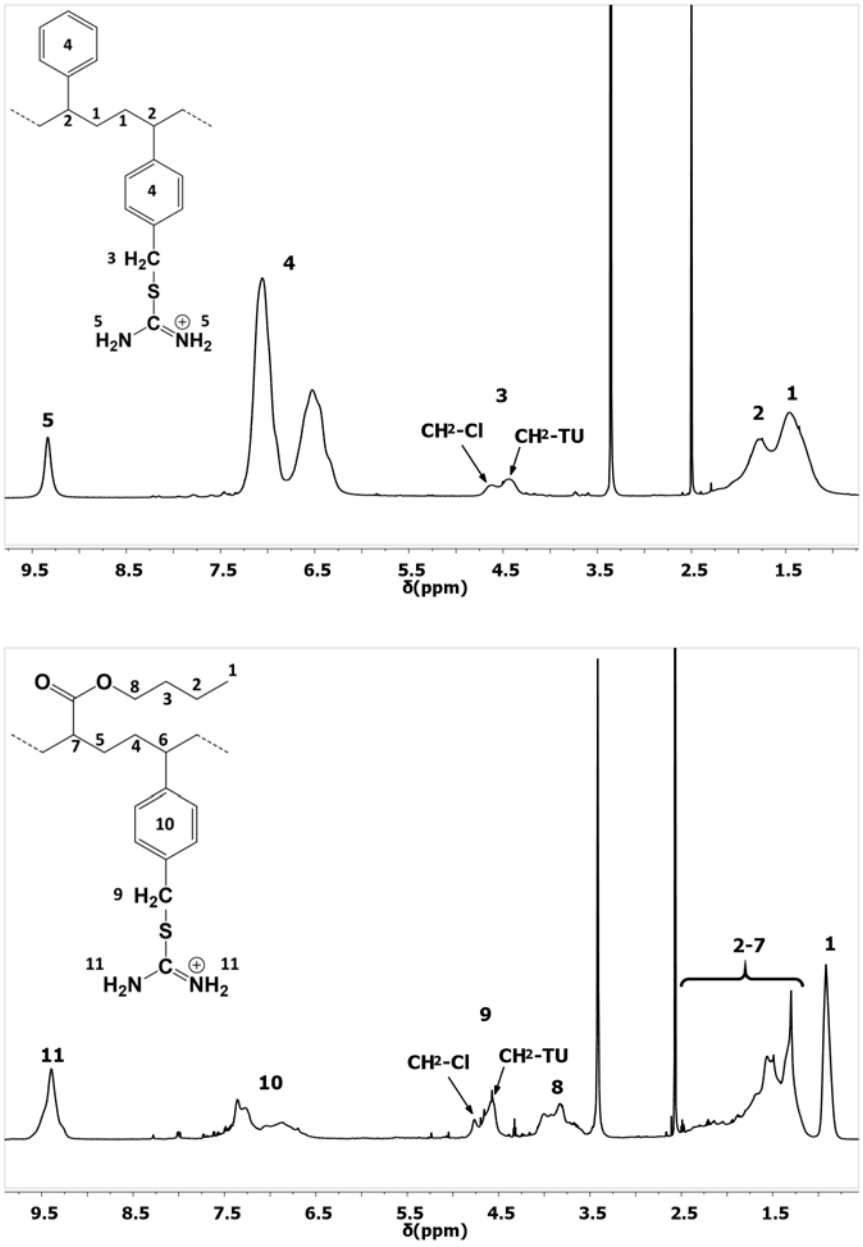

Figure 5.19. ^{1}H NMR spectra of (left) SV15-TU and (right) BV15-TU in DMSO-d_6. The signals of benzylic CH_2 moieties next to chlorine and TU are indicated by arrows.

Substitution of the benzylic chlorine with a thiouronium group was further verified by FTIR spectroscopy, Figure 5.20. The FTIR spectrum of the modified copolymer contains a broad N-H stretching band at around 3200 to 3350 cm^{-1} and strong N-H bending mode at 1650 cm^{-1}. The latter have significant overlap with the C=N stretch which emerges

in the same region. The FTIR spectrum of the TU functionalized SV15 contains C-Cl band with reduced intensity, which further confirms incomplete modification of this copolymer.

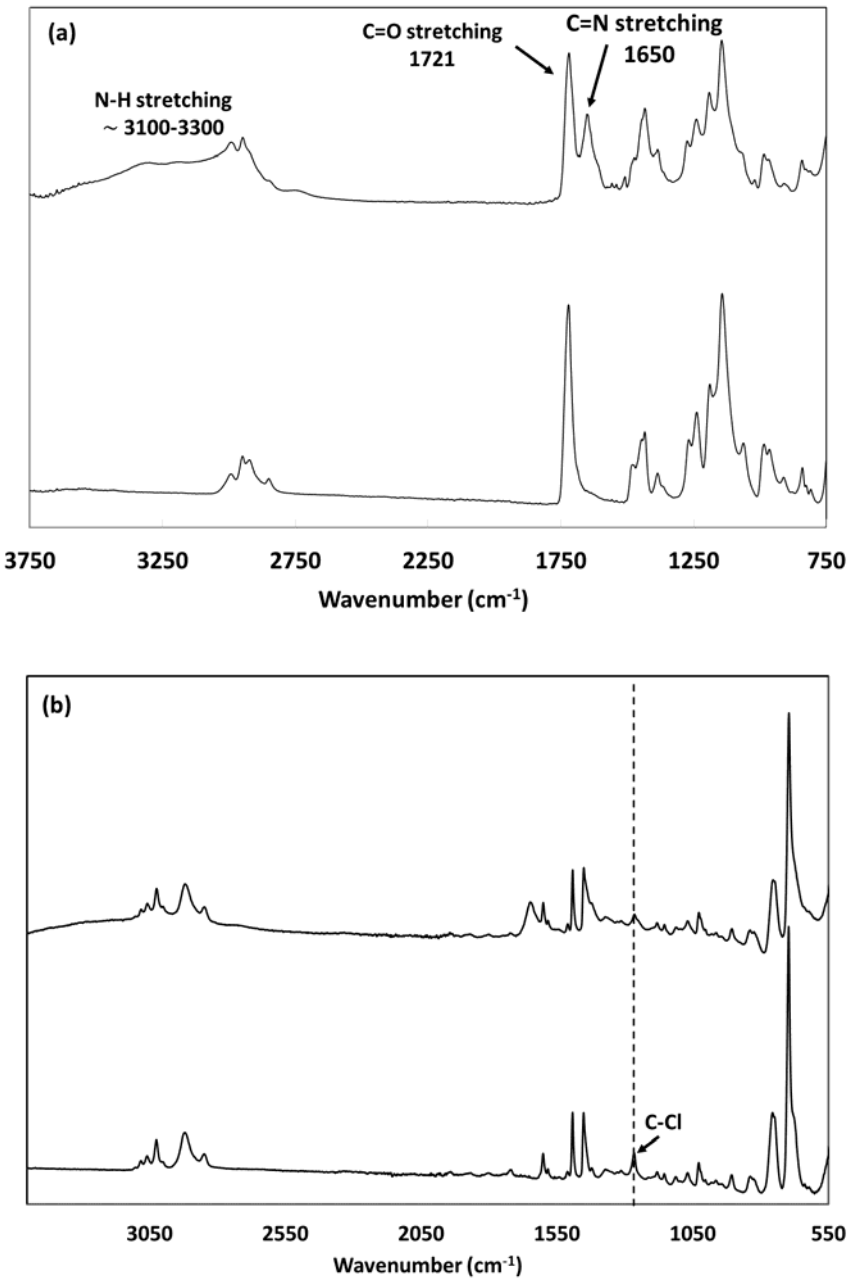

Figure 5.20. FTIR spectra of (a, top) MV15TU and (b, top) SV15-TU in comparison to the unmodified copolymers (bottom spectra). The dashed line shows the C-Cl band in SV15 and SV15-TU.

5.4. Thiol functionalized polymers

Conversion of the dithioester residues of the chain transfer agents, which are present as terminal groups on the RAFT-polymerized chains, provide an easy access to thiol-terminated polymers. As was confirmed by ^{1}H NMR spectroscopy, the RAFT-synthesized PMMA chains contain phenyl dithioester groups (Figure 5.3), that can be converted into thiolates through reaction with sodium borohydride ($NaBH_4$), Scheme 5.6[60, 64]. Conversion of the phenyl dithioester terminal groups were confirmed by the absence of the aromatic protons signals in the NMR spectrum and disappearance of the light absorption peak of dithioester from the UV-visible spectrum of the $NaBH_4$ treated RAFT-PMMA, Figures 5.21 and 5.22. The resulting thiolates can further form disulfides in presence of oxygen. The extremely small mole fraction of the dithioester groups and the product of their reaction makes it impossible to trace any changes in the NMR spectrum due to the formation of thiolate or disulfide species.

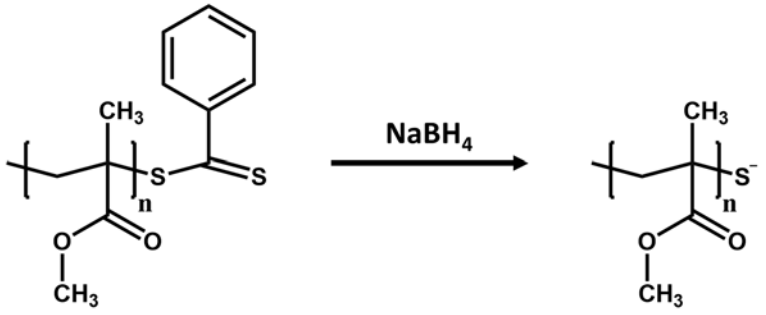

Scheme 5.6. Conversion of the dithioester group into thiol functionality through reduction by $NaBH_4$.

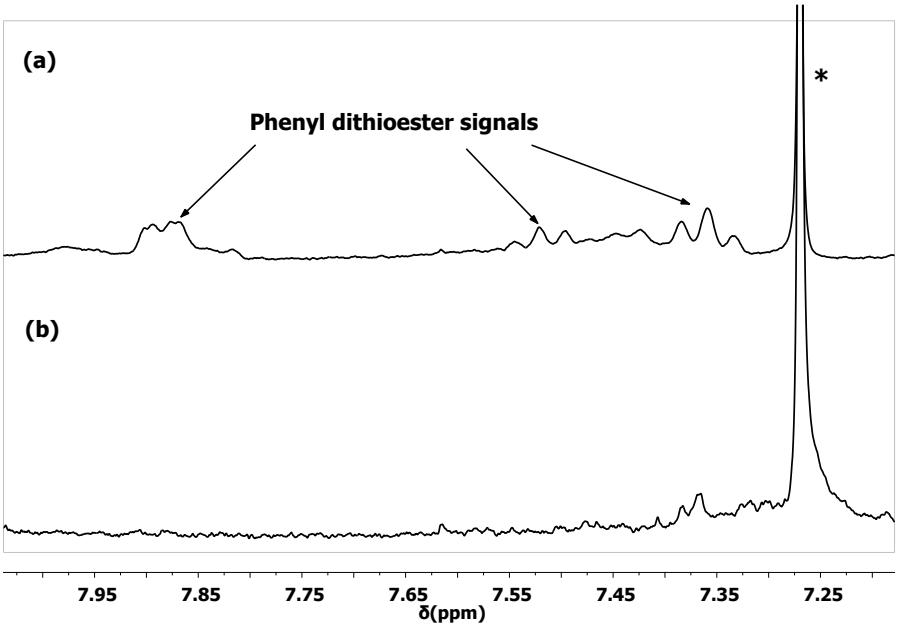

Figure 5.21. Selected region from ^{1}H NMR spectrum of the RAFT- PMMA (a) before and (b) after reaction with $NaBH_4$. The solvent signal, $CDCl_3$, is indicated by an asterisk.

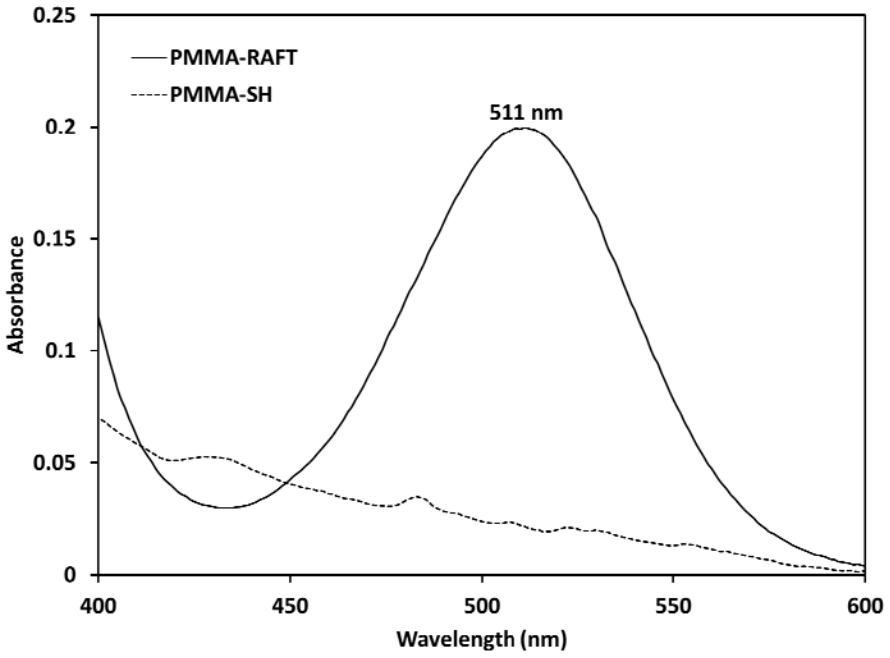

Figure 5.22. UV-visible spectra of the RAFT-polymerized PMMA before and after reaction with $NaBH_4$.

Polymers bearing multiple thiol moieties, distributed as side groups throughout the chains, are accessible through further modification of the thiouronium (TU) functional copolymers. Conversion of the TU group into thiol moiety through base catalyzed hydrolysis is a well-established step in the synthesis of small-molecule thiols. Basic hydrolysis of TU generates thiolate moiety and urea according to the Scheme 5.4. Treatment of the products with strong acid converts thiolates into thiol groups and further hydrolyzes urea. The hydrolysis of urea yields intermediates such as ammonium, cyanate, or ammonium carbamate which are eventually transformed into NH_3 and CO_2 at sufficiently high temperature, Scheme 5.7.

$$\mathbf{CO(NH_2)_2} \rightleftharpoons \mathbf{[NH_4]^+ + [OCN]^-}$$

$$\mathbf{[OCN]^- + [H_3O]^+ \longrightarrow NH_3 + CO_2}$$

Scheme 5.7. Proposed reaction pathways for acid catalyzed hydrolysis of urea.

Basic hydrolysis of the TU side groups into thiols becomes substantially more difficult to achieve for high molecular weight polymers due to their limited solubility, reduced accessibility of the reactive sites, and the possibility of inter or intra-molecular side reactions rendering a crosslinked polymer network which cannot be employed as the capping agent for synthesis of noble metal nanoparticles. All of the TU-functionalized random copolymers investigated in this study are composed of two segments with disparate solubility: sequences of the major comonomer (MMA, St, and BA) dissolve in low to medium polarity solvents, while the isolated vinylbenzyl thiouronium units tend to dissolve in highly polar solvents. Presence of the ionic TU side groups along the copolymer chains hinders their dissolution in moderately polar solvents such as THF and chloroform.

Solubility testing shows that these copolymers dissolve in a limited number of relatively high polarity media including THF/water mixture and DMSO, which are capable of interacting with both the ionic and non-ionic segments of the copolymer chains. Even in such solvents, addition of an aqueous solution of strong inorganic base to the MV15TU solution, which is essential for complete hydrolysis, may disrupt the attractive interactions of the solvent with the ionic side-groups leading to the precipitation of the polymer. This problem can be avoided by a suitable choice of reaction solvent, using a copolymer with lower molecular weight, and adjusting the concentration of the base solution.

The optimal reaction conditions under which the hydrolysis product maintains its solubility was determined by varying the solvent (DMSO or THF/water mixture), concentration of the base, and molecular weight of the copolymer. In comparison to DMSO, a THF/water mixture dissolves the TU functionalized copolymers more readily, and it is removed much faster owing to its lower boiling point. The exact THF to water ratio depends on the mole fraction of TU groups and the nature of the comonomer, *e.g.* MV15TU dissolves in a mixture with 5:1 THF:water ratio. Experiments on MV15TU and SV15TU showed that despite the good solubility of the copolymer, partial or complete precipitation occurred upon addition of aqueous KOH, depending on its concentration. The product of the reaction conducted in a THF/water mixture is not soluble in common low, medium, or high polarity solvents including toluene, chloroform, THF, acetone, THF/water, or DMSO.

The IR absorption of thiouronium side groups at 1651 cm^{-1} (N-H bending) has either disappeared or been obscured by the strong band at 1558 cm^{-1}, Figure 5.23. The new peaks at 1398 cm^{-1} and 1558 cm^{-1} may originate from the reaction byproducts. Several reactions

conducted under a variety of conditions leads to the conclusion that employing two-component solvents significantly complicates the synthetic procedure. Strong affinity of the reagents or products to one of the solvents can cause partial or complete phase separation, which hinders the desired reaction and facilitates the formation of byproducts.

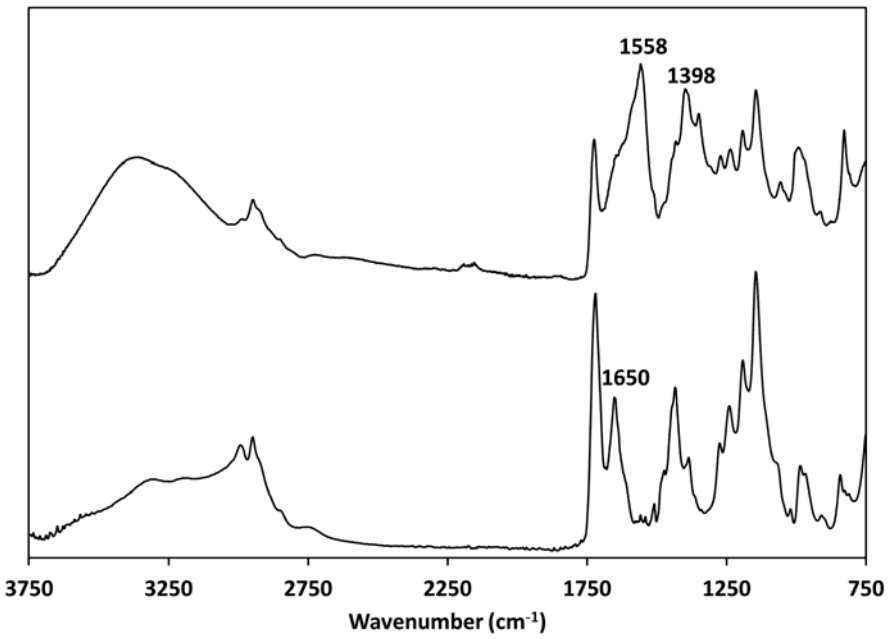

Figure 5.23. FTIR spectra of MV15TU hydrolyzed in THF/water mixture (top) and MV15TU (bottom).

Precipitation of MV15TU was avoided by using DMSO as the solvent, carefully adjusting the concentration of KOH solution, and removing oxygen from the reaction environment. Even under these reaction conditions, increasing the molecular weight of MV15TU from M_n=14.2 kg/mole to M_n=31.2 kg/mole, or reducing the mole fraction of TU groups resulted in precipitation. Figure 5.24 shows the ^{1}H and ^{13}C NMR spectra of the hydrolysis products prior to and after treatment with HCl. Besides the presence of several sharp signals arising from small molecule by-products (this was confirmed by comparing

the ^{1}H spectra of product before and after work-up, Appendix, Figure A.6), the characteristic signals of the thiouronium NH_2 (9.26 ppm) and the benzylic CH_2 (^{1}H 4.45 ppm, ^{13}C 34.31 ppm) of MV15TU are missing from the spectrum of the hydrolyzed copolymer. The spectrum of the intermediate product contains several new resonances including relatively sharp signals at 1.55 ppm, 1.91 ppm, and 2.01 ppm (indicated by * in Figure 5.24-b). The ^{1}H COSY spectrum of this sample shows cross-peaks between the signals at 1.55 ppm and 2.01 ppm and correlation between the former and the residual water signal at 3.39 ppm, Figure 5.25. Such correlations with water are attributed to the hydrogen bonding with concomitant proton interchange. These signals disappear upon acid treatment, suggesting that they are associated with an intermediate species. The HSQC spectrum of the final product has correlation between the ^{1}H at 2.42 ppm and ^{13}C at 36.99 ppm (indicated by † in Figure 5.24), which are very close to the chemical shifts of the V_2 group (see Table 5.7) on the copolymer backbone and, as shown by DEPT experiment, originate from a CH moiety. Accordingly, these signals might be assigned to the V_2 moiety, which are obscured by the strong solvent peaks in both ^{1}H and ^{13}C spectra of MV15TU. These results indicate that neither the intermediate, nor the final product have well-resolved NMR signals that can be assigned to the benzylic CH_2 of the thiolate or the thiol bearing copolymer. Furthermore, note that hydrolysis of SV15TU and BV15TU via the same procedure yields insoluble product which cannot be used as the capping agent for synthesis of isolated silver nanoparticles.

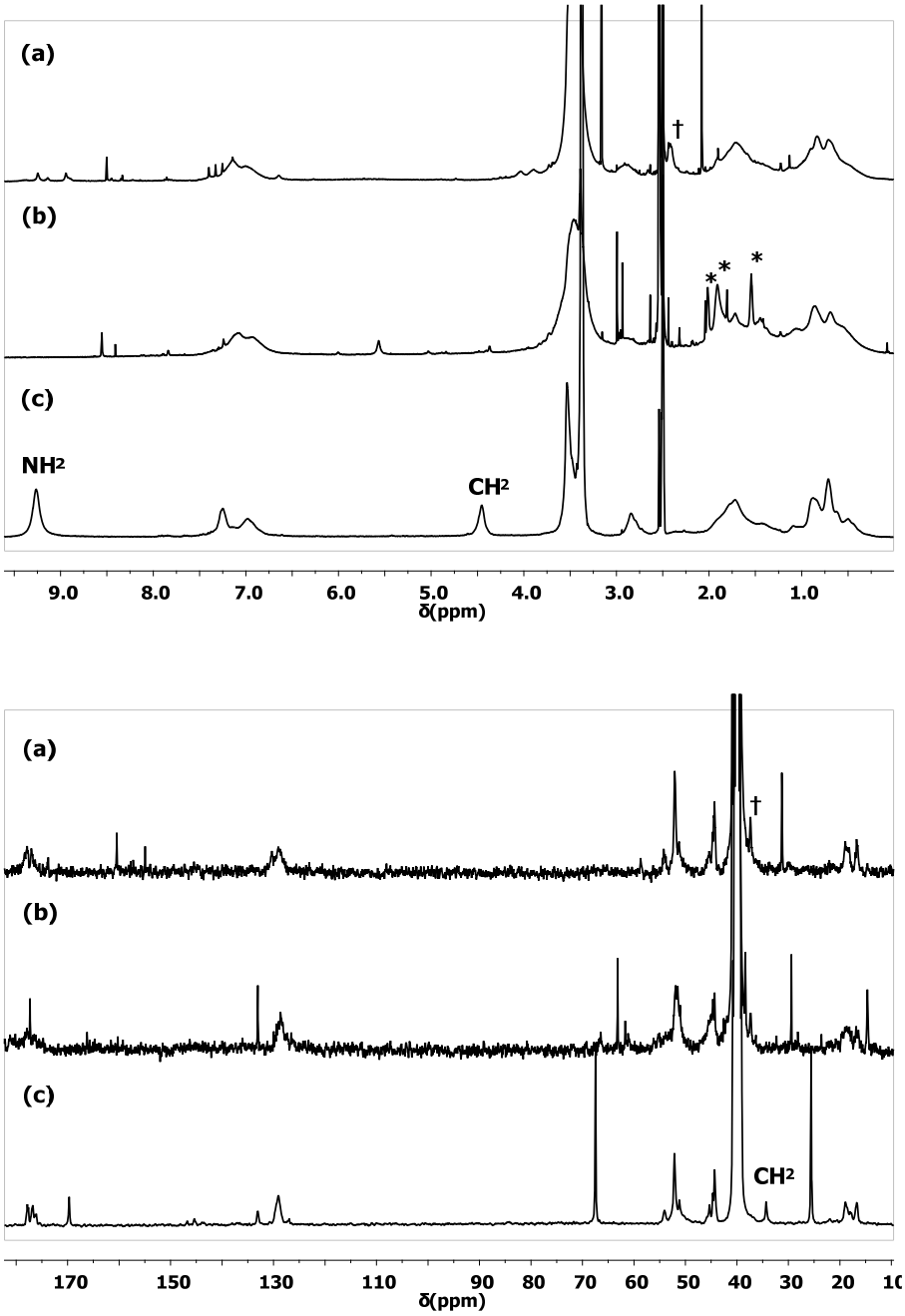

Figure 5.24. ^{1}H and ^{13}C NMR spectra of the base hydrolyzed MV15TU (a) after and (b) before acid treatment in comparison with the neat copolymer (c) dissolved in DMSO-d_6.

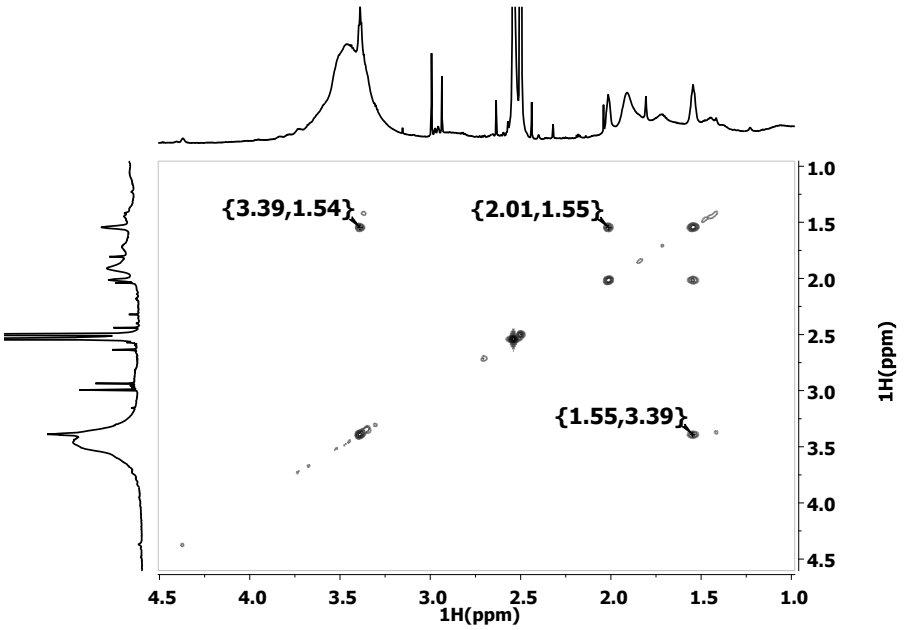

Figure 5.25. 2D COSY spectrum of the product of MV15TU hydrolysis in DMSO-d_6.

An alternative to basic hydrolysis is reduction of the thiouronium side group to thiol using sodium borohydride[137]. The modification of MV15TU copolymer in presence of sodium borohydride ($NaBH_4$) was monitored by ^1H NMR (the reaction was conducted in deuterated solvent). ^1H NMR spectra acquired at different stages of this reaction at T=60°C are presented in Figure 5.26. Addition of sodium borohydride is seen as a strong multiplet pattern from 0.07 ppm to -0.75 ppm. The observed multiplet pattern is the result of protons coupling to two NMR active isotopes of boron: ^{10}B (spin=3, natural aboundance≈20%) and ^{11}B (spin=3/2, natural aboundance≈80%), where the $\gamma_{11B}/\gamma_{10B} \approx 3$. The prominent quartet corresponds to the coupling to the ^{11}B isotopes, whereas the weaker septet is due to coupling to the ^{10}B. The ^1H resonances of the copolymer backbone and side-groups of the MMA repeating units do not changes throughout the entire reaction, implying that they remain unaltered under the applied reaction conditions. In contrast, the thiouronium functionality and its neighboring benzylic CH_2 group are strongly affected, as their characteristic

resonances at 9.23 ppm and 4.46 ppm (marked by arrows in Figure 21) are lost in the first spectrum acquired five minutes after $NaBH_4$ addition. The influence of this reaction is felt in the phenyl ring, where the signals are shifted slightly to lower frequencies. Moreover, the peak area of the residual water at 3.18 ppm decreases by 19% after 90 minutes.

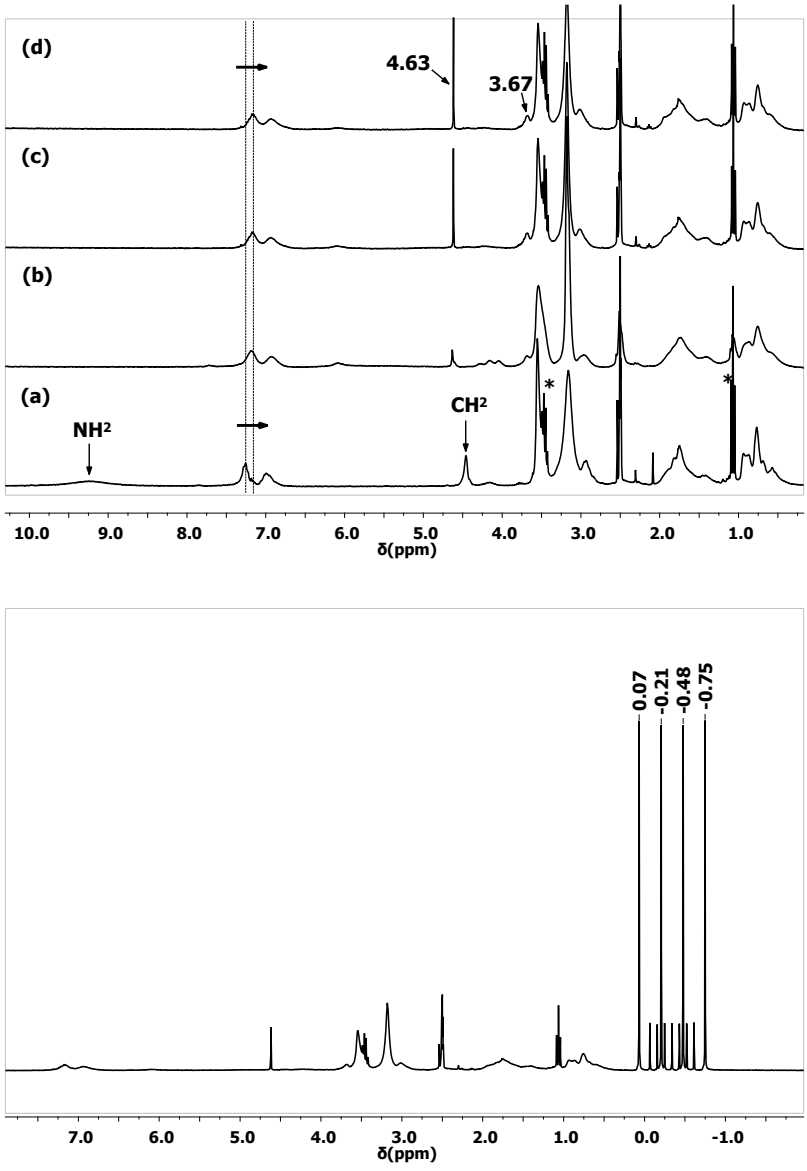

Figure 5.26. (Top) ^1H NMR spectra of MV15TU/ $NaBH_4$ reaction mixture acquired at (a) t=0, (b) t=5 min, (c) t=60 min, and (d) t=90 min at T=60°C. (Bottom) NMR spectrum at t=30 min showing the signals of $NaBH_4$. The reaction was conducted in DMSO-d_6.

The ^{1}H NMR spectra of the modified copolymer contain several new signals, including those at 3.67 ppm and 4.63 ppm. Unfortunately, it is difficult to determine the origin of these signals as the copolymer precipitates from the reaction mixture within a few hours at T=60°C. More details, specifically on the initial stages of the reaction, was revealed by inspecting the variation of the NMR signals during the reaction conducted at T=21°C. The reaction rate is significantly slower at this temperature and the modified copolymer remains soluble for a sufficiently long time to acquire ^{13}C and two-dimensional NMR spectra. Similarly to the reaction conducted at high temperature, the signals of the thiouronium NH_2 and the benzylic CH_2 groups are lost shortly after $NaBH_4$ addition, Figure 5.27. Several new resonances that appear at the initial stages of the reaction eventually disappear over time, suggesting that they correspond to the intermediate structures. The new signal at 3.67 ppm, which is clearly perceptible in the spectrum acquired 5 minutes after $NaBH_4$ addition at T=60°C, emerges after a few hours at the lower temperature and becomes more intense over time. At this stage of the reaction, the ^{13}C NMR spectrum reveals a new signal at 27.50 ppm, Figure 5.28. Phase-sensitive ^{13}C-^{1}H HSQC experiment (Figure 5.29) indicates that this CH_2 carbon is correlated to protons giving rise to the new ^{1}H signal at 3.67 ppm.

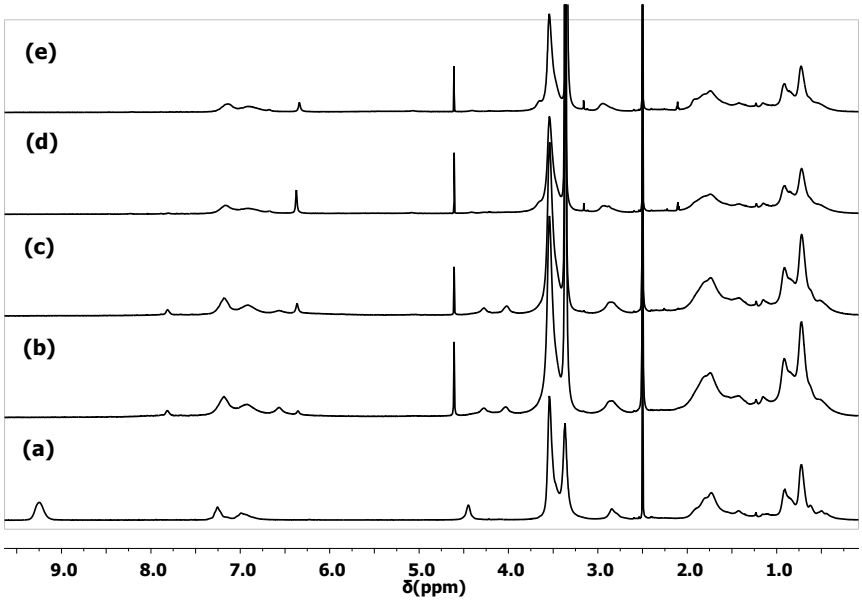

Figure 5.27. ^{1}H NMR spectra of MV15TU/ $NaBH_4$ reaction mixture acquired at (a) t=0, (b) t=5 min, (c) t=60 min, (d) after 2 days, and (e) after 5 days at T=22°C. The reaction was conducted inside an NMR spectrometer in DMSO-d_6.

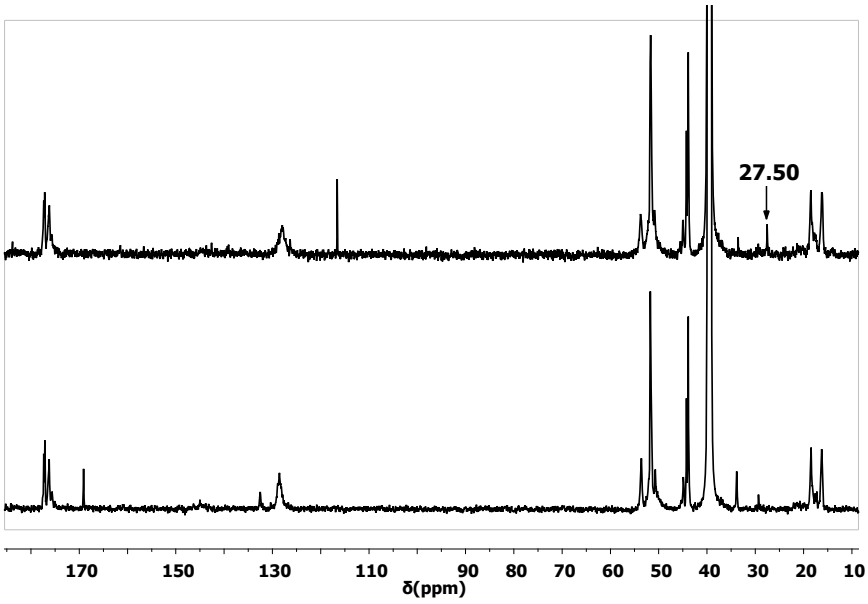

Figure 5.28. ^{13}C NMR spectra of (top) MV15TU/ $NaBH_4$ reaction mixture acquired after 2 days in comparison to MV15TU (bottom) in DMSO-d_6.

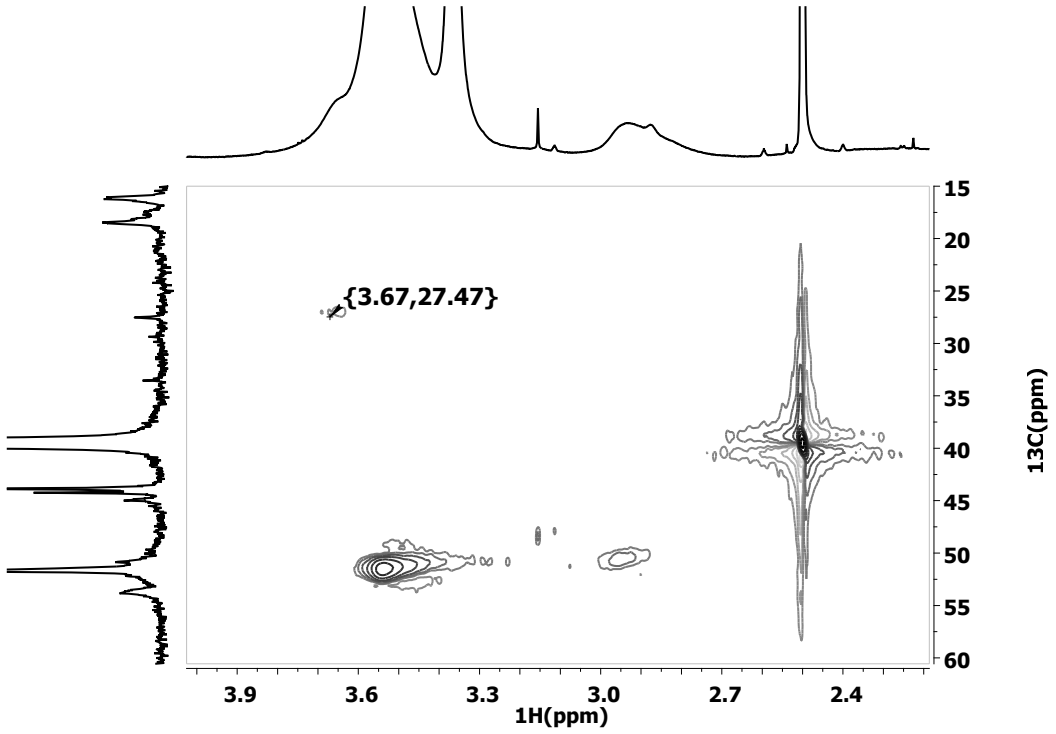

Figure 5.29. 2D NMR HSQC spectrum of MV15TU/ $NaBH_4$ reaction mixture acquired at T=22 °C in DMSO-d_6.

Although the above NMR experiments provide preliminary information on the reaction of TU groups with $NaBH_4$, the detailed structural information of the modified copolymer cannot be determined solely on the basis of these experiments as a consequence of extensive spectral overlap and the insolubility of the final product. The FTIR spectrum of the modified copolymer (Figure 5.30) clearly shows the disappearance of the NH2 bands of the thiouronium side group (N-H bending at 1651 cm^{-1} and N-H stretching at 3200 to 3300 cm^{-1}), does not shed light onto the structure of the modified side group. Consequently, it was necessary to obtain further details on the reduction of the TU side groups in the presence of $NaBH_4$ by investigating the reaction of its small-molecule counterpart, benzyl thiouronium (BTU). In comparison to the polymer, ^{1}H and ^{13}C NMR spectra of BTU, which was synthesized by reaction between benzyl chloride and thiourea, contain fewer, as well

as better-resolved signals due to its simpler molecular structure, Figure 5.31. Thus it is substantially easier to monitor its reduction with $NaBH_4$ via NMR spectroscopy. Figure 5.32 shows selected ^1H NMR spectra of the reaction mixture at 60°C over one hour. Similarly to the polymer, the characteristic signal of the thiouronium NH_2 groups at 9.38 ppm disappears and the resonance of benzylic CH_2 at 4.57 ppm becomes noticeably weaker a short time (5 minutes) after addition of the reducing agent. New signals emerge at 3.66 ppm and 4.07 ppm, the intensities of which vary as a function of the reaction time.

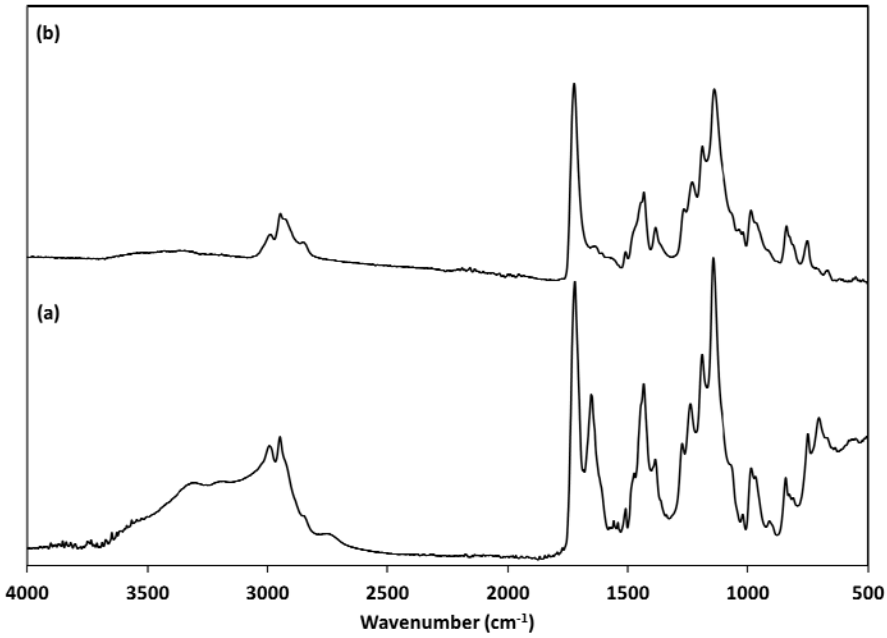

Figure 5.30. FTIR spectra of (a) MV15TU and (b) the dried MV15TU- $NaBH_4$.

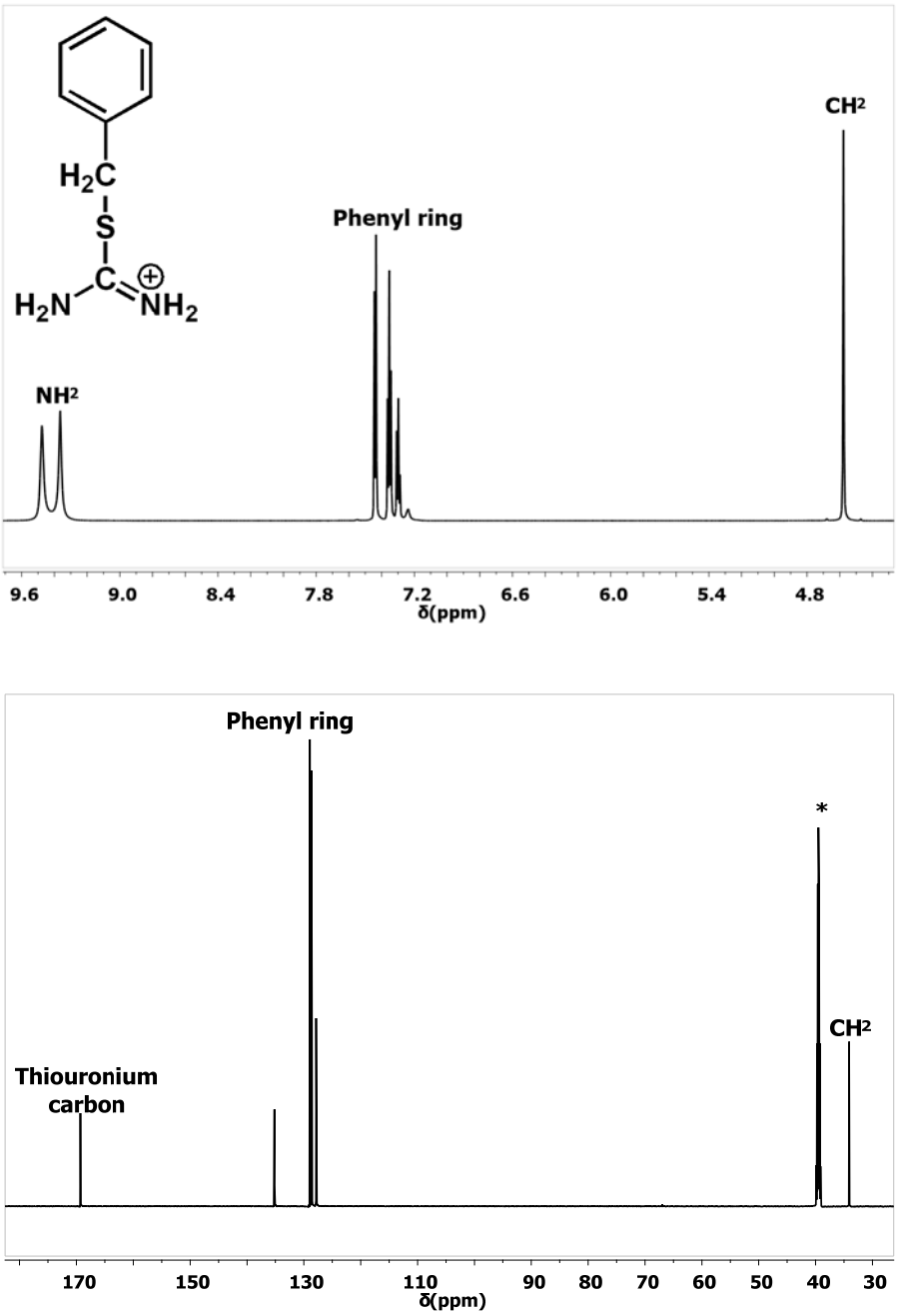

Figure 5.31. ^{1}H (top) and ^{13}C (bottom) NMR spectra of BTU in DMSO-d_6. The solvent peak is marked by asterisk.

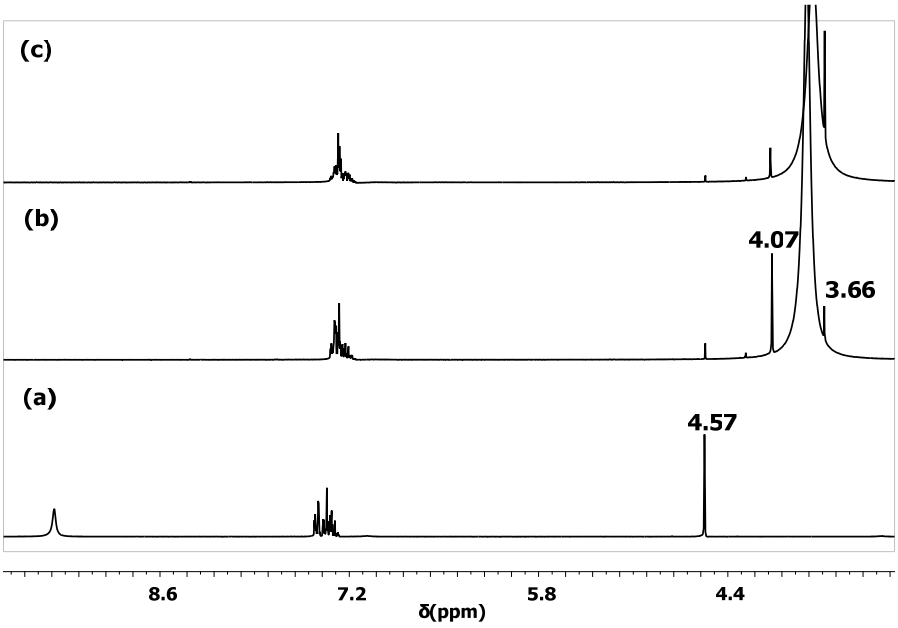

Figure 5.32. ^{1}H NMR spectra of BTU/ $NaBH_4$ reaction mixture at (a) t=0, (b) t=5 min, and (c) t=60 min acquired at T=60 °C in DMSO-d_6.

The origin of the new signals was determined by following evolution of the ^{1}H and ^{13}C NMR resonances over the long reaction time and with the help of homonuclear, as well as heteronuclear 2D experiments. Interestingly, the spectra acquired at room temperature show the presence of two separate signals at 3.64 ppm and 3.67 ppm (indicated by *), in contrast to the single peak at 3.66 ppm observed at T=60°C, Figure 5.33. The intensities of the new ^{1}H resonances at 4.07 and 3.67 ppm decrease as the reaction proceeds, eventually approaching zero at long reaction time (16 days), while the signal at 3.64 ppm becomes progressively more intense. The ^{13}C spectra collected at room temperature also contain several new signals, including the resonances at 28.30 ppm, 34.57 ppm, 42.24 ppm, 137.77 ppm, and 141.93 ppm, either gaining or losing intensity over time. Two-dimensional HSQC (Figure 5.34) and HMBC experiments (Appendix, Figure A.7) confirm that the changes in

intensity of the ^{13}C signals are consistent with the variations observed in their correlated ^{1}H signals, Table 5.8.

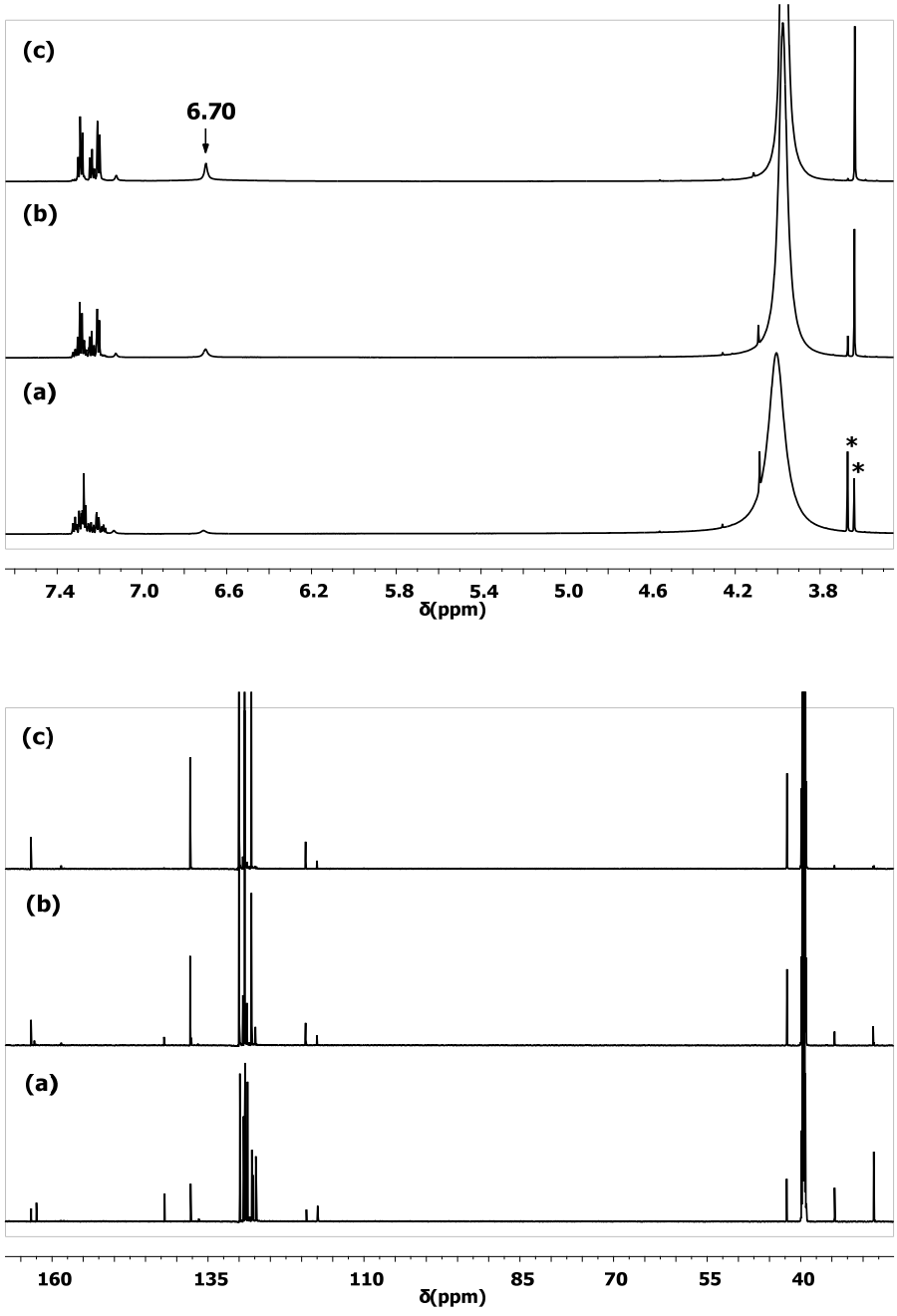

Figure 5.33. NMR spectra of BTU/ $NaBH_4$ reaction mixture after (a) 5 hours, (b) 4 days, and (c) 16 days at T=60 °C in DMSO-d_6.

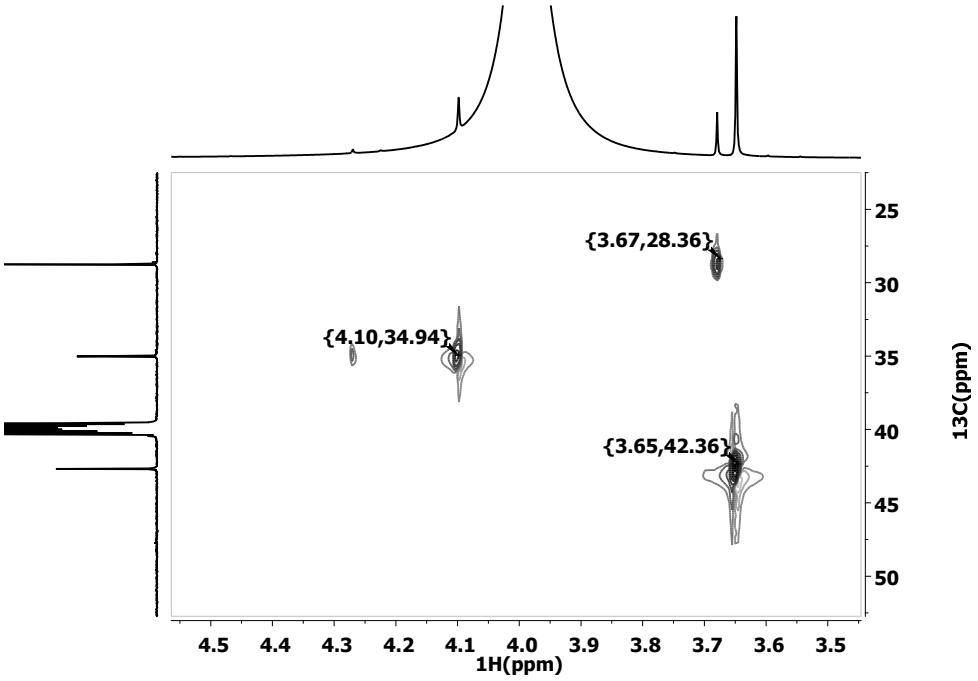

Figure 5.34. 2D HSQC spectrum of BCTU/$NaBH_4$ reaction mixture acquired at T=22 °C in DMSO-d_6.

Table 5.8. Single bond and multiple correlation between ^{1}H and ^{13}C signals of BTU/$NaBH_4$ reaction product.

^{13}C signal	28.30 ppm	34.57 ppm	42.24 ppm	137.77 ppm	141.93 ppm
Correlated ^{1}H – HSQC	3.67 ppm	4.07 ppm	3.64 ppm	----*	----*
Correlated ^{1}H – HMBC	Aromatic region	Aromatic region	Aromatic region	3.64 ppm	3.67 ppm

* These are quaternary carbons

The ^{1}H-^{1}H COSY spectrum collected after 5 hours reaction time at T=22°C (Figure 5.35) shows cross peaks between the three new peaks at 3.64, 3.67, and 4.07 ppm and different set of signals within the aromatic region. As these sets do not have correlation with each other, they must arise from separate species. In fact the ^{1}H signals at 3.67 ppm and 3.64 ppm and their associated proton and carbon peaks correspond with the chemical shifts reported in the literature for benzyl thiolate and benzyl disulfide, respectively. Interestingly, the COSY spectrum contains relatively weak cross peaks between these two proton signals (3.67 ppm and 3.64 ppm, indicated in Figure 35), although they originate from different compounds. The presence of these cross peaks can be rationalized by considering the possibility that chemical exchange occurs between the thiolate and the disulfide. This reversible exchange process favors the formation of disulfide, which is the stable species in the presence of atmospheric oxygen, thus resulting in an increase in the intensity of its neighboring CH_2 signals.

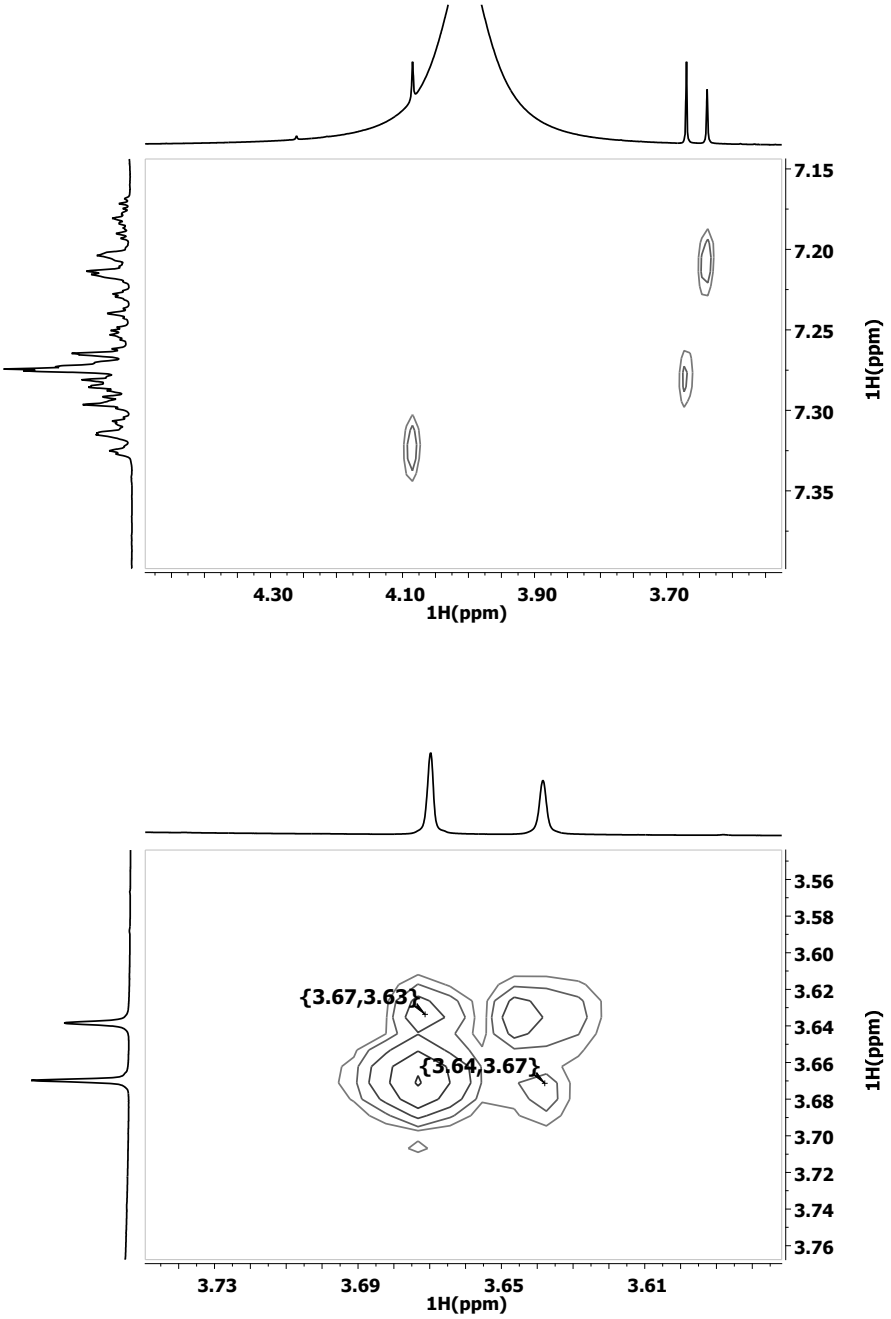

Figure 5.35. COSY spectrum of BTU/$NaBH_4$ reaction mixture collected after 5 hours at T=22°C in DMSO-d_6 showing (top) correlation between peaks at 3.64, 3.67, and 4.07 ppm and different sets of signals within the aromatic region, and (bottom) the cross-peaks between proton signals at 3.67 ppm and 3.64 ppm.

Feasible reaction pathways for formation of benzyl thiolate in the presence of excess of sodium borohydride and water are proposed in Scheme 5.8. The first pathway (scheme 8-a) involves nucleophilic attack of the hydride anion on the electron deficient carbon of the thiouronium group, while the second one is simply base-catalyzed hydrolysis of the thiouronium. The disappearance of NH_2^+ signal alongside the noticeable reduction in the intensity of the benzylic CH_2 signal in the first spectra of both BTU and the copolymer, imply that the first step of the reaction (addition of hydride or hydroxide on the thiouronium carbon) proceeds rapidly, even at room temperature. The resulting intermediate compounds might be too unstable to be observed in the NMR spectra of the reaction mixture. The more stable intermediate gives rise to the signal at 4.07 ppm and its associated resonances (Table 8), gains intensity during initial stages of the reaction, but eventually disappears as the reaction proceeds. The identity of these intermediates cannot be unambiguously determined from the NMR results alone. Both proposed reactions generate byproducts, such as formamide (^1H signals at 7.2, 7.5, and 8.2 ppm), which may form via the first pathway, or urea (^1H signal at 5.6 ppm) which is a known product of the basic hydrolysis of thiouronium. Characteristic NMR signals of either of these byproducts were not detected at any stage of the reaction, however, a new relatively broad proton signal is seen at 6.71 ppm that gains intensity over time. This signal, which does not have cross peaks in COSY and HSQC experiments, is tentatively assigned to a byproduct. It should be noted that both urea and formamide are known to undergo further conversion into other species (refer to Scheme 8) in the presence of water, at alkaline pH and elevated temperature[138].

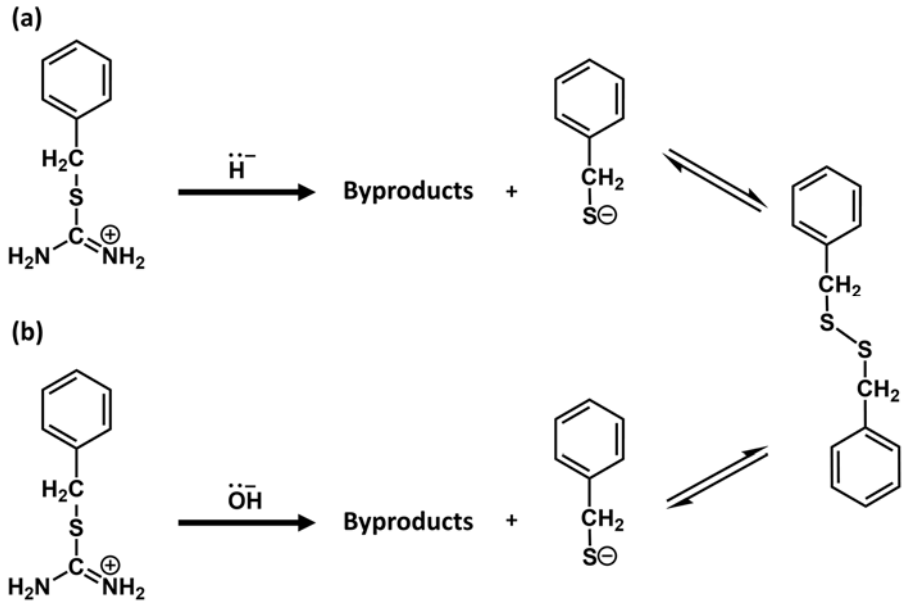

Scheme 5.8. Possible pathways for the reaction between BTU and $NaBH_4$ in presence of water. The hydroxide in (b) is produced as the result of combination of hydride with water. The small molecule byproducts can undergo further conversion in the alkaline reaction medium.

A comparison between the ^{1}H spectra of the BTU/$NaBH_4$ and the MV15TU/$NaBH_4$ reaction mixtures, shows that the modified copolymer has a new signal at 3.67 ppm, which is very close to the benzylic CH_2 peaks of both the thiolate and the disulfide species, Figure 5.36. Correlation between this proton and a ^{13}C resonance at 27.50 ppm, observed in the HSQC spectrum of the copolymer at T=21°C, confirms that it originates from CH_2 side groups attached to the thiolate moiety. Further conversion of thiolates into disulfides renders a crosslinked polymer network that precipitates from the reaction medium, and thus is not amenable to analysis by solution NMR techniques. Formation of disulfide bridges is further corroborated by inspection of the ^{13}C solid-state NMR spectrum of the precipitated copolymer, Figure 5.37. The modified copolymer has a new signal at 40.7 ppm which corresponds with the resonance of the CH_2 groups next to the disulfide bond.

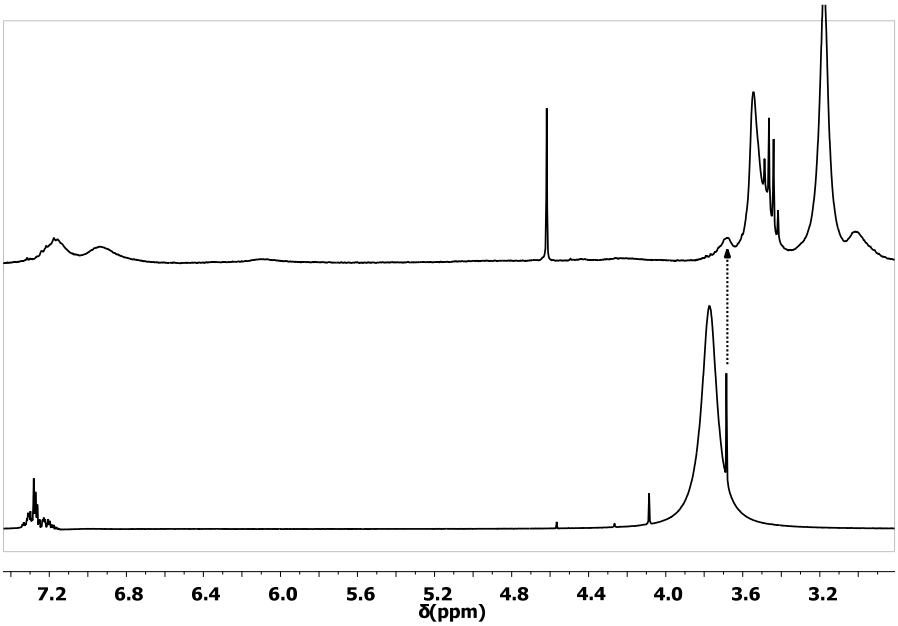

Figure 5.36. Comparison between the ^{1}H spectra of the BTU/$NaBH_4$ and the MV15TU/$NaBH_4$ reaction mixtures acquired at T=60°C in DMSO-d_6. The new signals are indicated by an arrow.

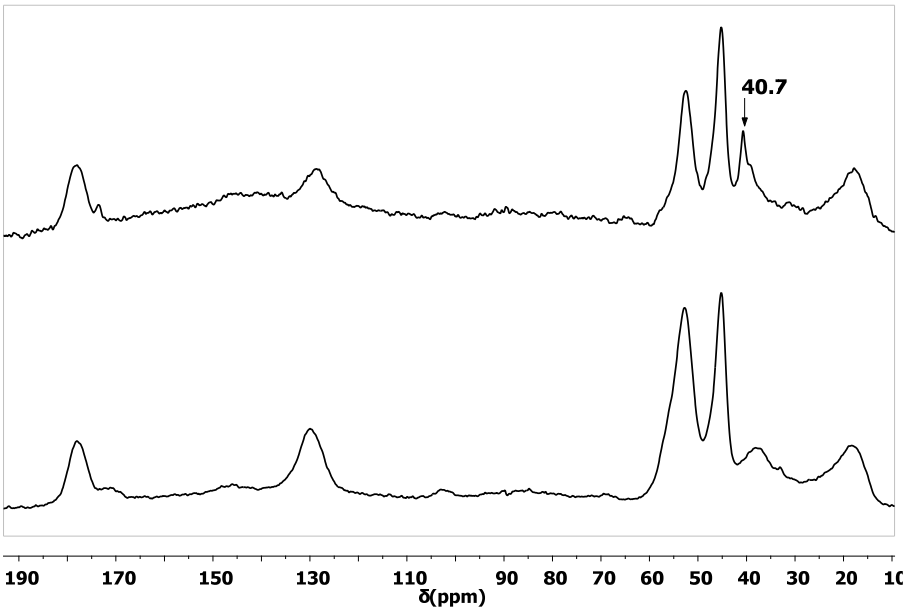

Figure 5.37. ^{13}C CP-MAS solid-state NMR spectra of (top) dried product of MV15-TU/ $NaBH_4$ reaction in comparison to unmodified MV15-TU (bottom) showing a new signal at 40.7 ppm.

5.5. Conclusions

The chain transfer agents employed for RAFT polymerization of MMA and its random copolymers with VBC (MV15 and MV5) provided very good control over the average molar mass and molar mass distributions of these polymers. Random addition of the comonomers in MV15 was confirmed by NMR which revealed new (not present in the spectra of PMMA and PVBC) ^{1}H and ^{13}C signals arising from the ester side group of MMA repeating units connected to VBC units. Integration of the 1H peak indicated that almost all VBCs were attached to MMA monomers. The living nature of the polymer chains terminated with the dithioester portion of the CTA was confirmed by its utilization as the macromolecular RAFT agent in a separate polymerization reaction. The terminal dithioester groups were converted into thiolate functionalities via reduction with $NaBH_4$, providing access to thiol-terminated PMMA.

The homopolymer of VBC and its copolymer with styrene (SV15) synthesized in the presence of CPPA or CDSPA chain transfer agents had higher polydispersity indices in comparison with PMMA and MV15, indicating lower efficiency of the RAFT agents in controlling the polymerization of these monomers. Monitoring the copolymerization of SV15 via NMR revealed that the maximum monomer conversion in the RAFT process was limited to 33%, while 77% was achieved via FRP. Such a low monomer conversion might be attributed to the high stability of the intermediate radical (Scheme 5-a) or slow radical transfer from an active chain to a macro-RAFT agent (Scheme 5-b). NMR investigation of BA/VBC free radical polymerization showed that, at least a large fraction of these monomers, do not incorporate into random copolymer chains.

Homopolymer and copolymers of VBC bearing multiple thiol functionalities were synthesized by nucleophilic substitution of the chlorines with TU groups, followed by conversion of TU into thiolate by basic hydrolysis or reduction with $NaBH_4$. The substitution reaction on PVBC did not proceed to completion, as confirmed by presence of the C-Cl band in the FTIR spectrum of the modified polymer. This was attributed to the high concentration of the reactive sites on PVBC, which severely reduces their accessibility as the reaction proceeds. Basic hydrolysis of PVBC yielded an insoluble product which was not suitable for further application as the capping agents of nanoparticles. The insoluble material is produced as a result of side reactions (such as formation of disulfide bonds and nucleophilic attack of thiolates on the residual benzyl chloride groups) leading to inter and intra-molecular bonding between the polymer chains.

Complete substitution of Cl with TU was achieved on the MV15 copolymer, where the accessibility of benzyl chloride groups is enhanced by the random distribution of VBC units between the sequences of unreactive MMA monomers. This was verified by integration analysis of the ^{1}H NMR spectrum of MV15TU and a comparison between its ^{13}C chemical shifts and those of MV15. Despite the lower concentration and random distribution of the reactive units in MV15TU chains, introduction of KOH for basic hydrolysis, could induce rapid precipitation of the copolymer from the reaction medium. Precipitation was avoided by conducting the reaction in DMSO under an inert atmosphere, using a RAFT copolymer with lower molar mass, and carefully adjusting the concentration of the base solution. NMR spectra of the intermediate and the final product of the MV15TU hydrolysis did not reveal well-resolved signal(s) that can be assigned to the benzylic CH_2

of the thiolate bearing copolymer. Moreover, hydrolysis of SV15TU and BV1-TU via the same procedure produced insoluble material.

Conversion of the thiouronium side group into thiolate by reduction with $NaBH_4$ was found to be more facile and more flexible in comparison to the basic hydrolysis. The reaction was monitored by NMR at two temperatures. The ^1H NMR spectra acquired at T=60°C showed that the copolymer backbone and side-groups of the MMA units remained unaltered, while signals of the TU functionality and its neighboring benzylic CH_2 disappeared rapidly and those of the phenyl ring shifted slightly to the lower frequencies upon addition of $NaBH_4$. Moreover, new ^1H signals emerged in the spectrum of the modified copolymer, including those at 3.67 ppm and 4.63 ppm. ^{13}C and 2D phase-sensitive HSQC spectra of the reaction conducted at T=21°C, revealed a new ^{13}C signal at 27.50 ppm arising from the CH_2 carbon directly bonded to protons giving rise to the ^1H peak at 3.67 ppm. FTIR of the modified MV15TU showed the disappearance of the thiouronium bands, however it did not shed light into the structure of the modified side group.

Further insight into the mechanism of the above reaction was obtained by investigation of the reduction of benzyl thiouronium, which is the small-molecule counterpart of the TU-bearing vinylbenzyl repeating units. Monitoring this reaction via 1D and 2D NMR experiments, showed that the TU groups are first converted into thiolates, which subsequently undergo a reversible exchange with disulfides. The ^1H and ^{13}C signals of CH_2 groups attached to the disulfides gained intensity over time, while those of the CH_2 moieties next to thiolate became weaker and eventually disappeared. A comparison between the NMR spectra of the BTU/$NaBH_4$ and the MV15TU/$NaBH_4$ reaction mixtures, indicated that the new ^1H signal of the modified copolymer at 3.67 ppm and its correlated

^{13}C signal at 27.50 ppm originate from CH_2 side groups attached to the thiolate moiety. Precipitation of the copolymer from the reaction medium at long reaction times was attributed to the conversion of thiolates into disulfides, which form crosslinks between the copolymer chains.

Chapter 6. Polymer capped silver nanoparticles

Thiol-bearing macromolecules, like their small-molecule counterparts, can impart superior stability to the noble metal nanoparticles, afforded by strong sulfur-metal bonding. Hypothetically, these materials can be used as the capping agent for synthesis of nanoparticles in procedures similar to those employed for low molar mass thiol functionalized compounds. However, several factors, including extremely high molar mass, slow molecular dynamics, steric obstruction of the reactive sites, and limited solubility, add considerable complexity to the application of polymers as the capping agents. Here various synthetic strategies for the preparation of silver nanoparticles stabilized with single-functional thiol-terminated or multi-functional polymers are presented. The efficiency of each method in producing small and uniform nanoparticles is evaluated by characterization of the size, dispersity, and solubility of the resulting nanoparticles.

6.1. Experimental

6.1.1. Materials

All reagents and solvents were purchased from Sigma-Aldrich and used as received. Deuterated NMR solvents used in this work were purchased from Cambridge Isotope Laboratories.

6.1.2. Synthesis

Thiol-terminated PMMA capped SNP: Thiol-terminated PMMA was first dissolved in either 1:1 THF/ethanol mixture or 5:1 THF/water mixture. Silver nitrate was added to this solution and stirred for 30 minutes. A solution of $NaBH_4$ was then added to the reaction mixture under vigorous stirring. Stirring was continued for 24 hours at room temperature. The solution of nanoparticles in the reaction solvent was diluted by addition of THF to adjust the concentration for UV-visible spectroscopy and TEM.

Copolymer capped SNP. Silver nanoparticles protected with modified copolymers of VBC were produced via a two-steps synthetic procedures. First, the TU-functionalized copolymer was treated with KOH or $NaBH_4$ for a certain period of time at elevated temperature. This process is called the "pretreatment step". In the second step, a solution of silver nitrate was added to the product of pretreatment and silver ions were reduced by $NaBH_4$ (reduction step).

The pretreatment with KOH was carried out with a KOH/TU mole ratio of 7, at T=80°C for 15 minutes. $NaBH_4$ and $AgNO_3$ solutions were subsequently injected into the reaction mixture, which was cooled down to room temperature. The entire reaction was conducted under inert atmosphere to avoid precipitation of the copolymer.

For pretreatment with $NaBH_4$, the $NaBH_4$/TU mole ratio and the duration of the first step were varied in a series of experiments, Table 6.1. Moreover $NaBH_4$ was either added once at the start of pretreatment (1-step addition) or added twice, once at the start of pretreatment and once at the start of the reduction steps (2-steps). This reaction was conducted under atmospheric air.

Table 6.1. Various reactant ratios and experimental conditions used for pretreatment with $NaBH_4$.

Experiments	$NaBH_4$/TU mole ratio, pretreatment time, $NaBH_4$ addition steps				
Series 1	$NaBH_4$/TU	2.63	4.39	9.36	17.54
	Pre. time (min)	15	15	15	15
	$NaBH_4$ steps	1 step	1 step	1 step	1 step
Series 2	$NaBH_4$/TU	4.39	4.39	4.39	4.39
	Pre. time (min)	15	45	90	150
	$NaBH_4$ steps	1 step	1 step	1 step	1 step
Series 3	$NaBH_4$/TU	4.39	4.39	4.39	4.39
	Pre. time (min)	90	150	90	150
	$NaBH_4$ steps	1 step	2 steps	1 step	2 steps

6.1.3 Techniques

UV-visible spectroscopy. UV-visible spectra of dissolved test materials were recorded on a Cary 50 spectrophotometer. The experiments were conducted in the wavelength range of 300 nm to 700 nm at room temperature. For each spectrum, the baseline was corrected by subtracting the absorption of the cuvette and the pure solvent.

Transmission electron microscopy (TEM). TEM micrographs were obtained with a Hitachi H-7500 transmission electron microscope operating at 100 kV accelerating voltage. Each TEM sample was prepared by putting a drop of dilute nanoparticle solution on a 400-mesh carbon-coated copper grid. The excess solution was removed with filter paper and

the grid was allowed to dry at room temperature overnight. Average particle size and size-dispersity were determined by measuring the Feret diameters of at least 200 nanoparticles for each sample using ImageJ software.

Solution-state NMR spectroscopy. NMR spectra were recorded at ambient temperature on a Bruker Avance III HD 700 MHz NMR spectrometer. Calculation based on five separate measurements on the same sample gives an standard deviation of 0.0012 for the ^{1}H NMR chemical shifts, which is very close to the non-zero-filled FID digital resolution of the experiments.

6.2. Thiol-terminated PMMA capped SNP

Figures 6.1 and 6.2 show the TEM micrograph and the UV-visible spectrum of the silver nanoparticles stabilized with thiol-terminated PMMA. This capping agent was prepared by reduction of the RAFT-polymerized PMMA by $NaBH_4$ to convert the dithioester fragment of the RAFT agent into a thiol moiety [refer to Chapter 2, Section 2.5.2]. The average diameter and polydispersity of the resulting nanoparticles are 5.86 nm and 1.98 nm, respectively. Despite the successful synthesis of nanoparticles, employing thiol-terminated PMMA or its copolymer with styrene and butyl acrylate, suffers from major drawbacks including very small initial mole fraction of the dithioester groups, their incomplete conversion into thiolate and limited solubility of the polymer in a solvent that can dissolve the silver salt. These factors decreases the efficiency of the polymers in stabilizing the nanoparticles, which results in formation of large and nonuniform nanoparticles. This problem can be partially alleviated by using a smaller concentration of

silver nitrate to maintain a sufficiently large thiolate/Ag^+ mole ratio. Lowering the concentration of silver nitrate, however, reduces the number of nanoparticles produced.

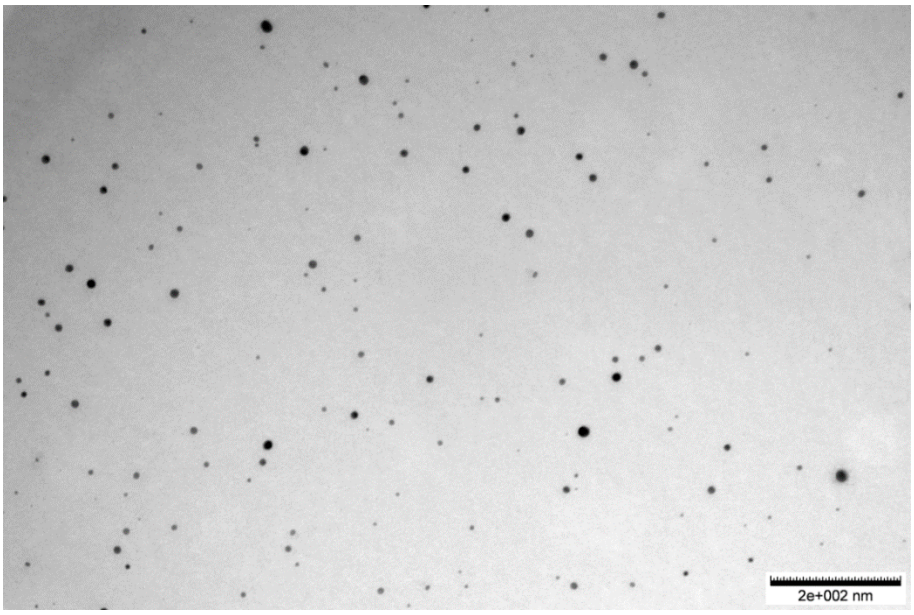

Figure 6.1. TEM micrograph of the thiol-terminated PMMA capped silver nanoparticles.

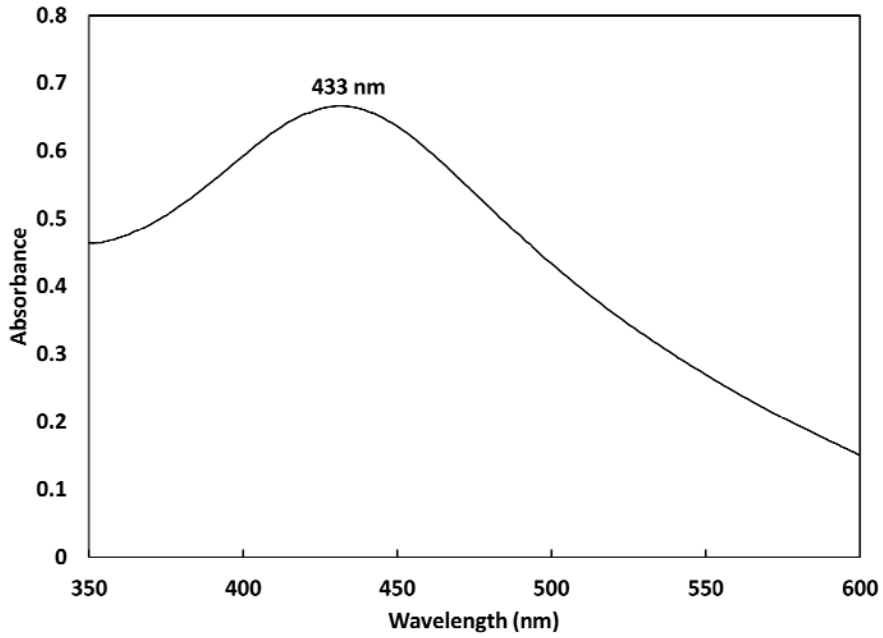

Figure 6.2. UV-visible spectrum of thiol-terminated PMMA capped silver nanoparticles.

6.3. Silver nanoparticles coated with modified VBC copolymers

Better control over the size and the dispersity of the SNP is provided by employing polymeric capping agents bearing multiple thiol functionalities. In the previous chapter two methods were proposed for the conversion of the thiouronium (TU) groups on the functionalized random copolymers of VBC to thiolates. The conversion was performed via basic hydrolysis of the TU side groups or reaction with $NaBH_4$. The nanoparticles coated with hydrolyzed MV15TU copolymer have an average diameter of 3.98±1.16 nm, Figure 6.3. Detailed investigation of the basic hydrolysis of MV15TU showed that the reaction product has a high propensity to the formation of an insoluble product during the reaction or upon solvent removal. This loss of solubility was avoided by the careful control of the reactant concentrations, addition of the reducing agent and silver salt to the reaction medium immediately after the hydrolysis, and by conducting the synthesis at elevated temperature under an inert atmosphere. Despite all these precautions, this method is not applicable to the TU functionalized random copolymers of VBC with styrene (SV15TU) and with butyl acrylate (BVTU) due to the polymer precipitation. Moreover, presence of KOH and water in the reaction mixture may result in conversion of silver cations into Ag(I) oxide[139-140], Scheme 6.1. Formation of the silver oxide (light brown aggregates in DMSO) was observed when $AgNO_3$ was added before $NaBH_4$ or when a low concentration of $NaBH_4$ was used.

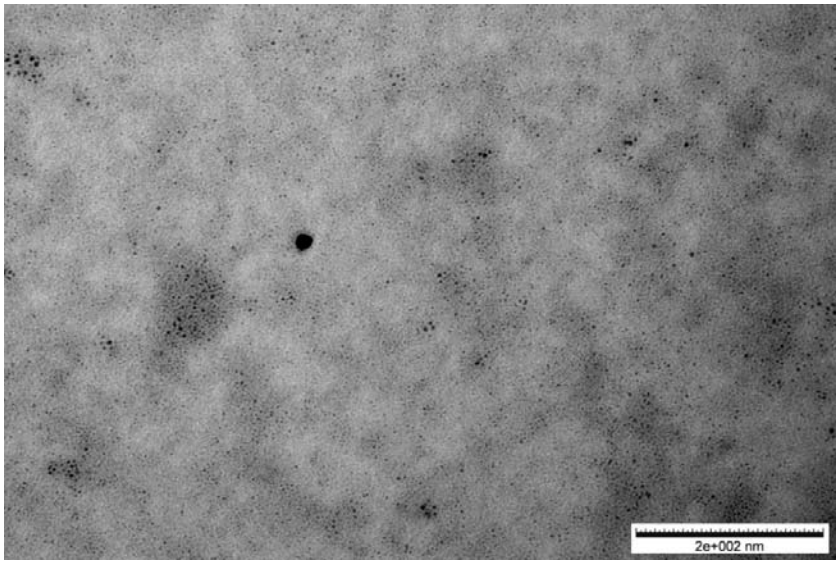

Figure 6.3. TEM micrograph of the nanoparticles coated with hydrolyzed MV15TU copolymer.

$$AgNO_3 + KOH \longrightarrow AgOH + KNO_3$$

$$2AgOH \longrightarrow Ag_2O + H_2O$$

Scheme 6.1. Conversion of silver cations into silver oxide in presence of KOH and water.

As was shown in the previous chapter, TU groups on the modified random copolymers of VBC are transformed into thiolate via reduction with $NaBH_4$. The resulting thiolated copolymers, however, were not sufficiently stable to be separated from the reaction mixture without significant loss of its active functionalities and solubility. This insoluble material is formed as the result of the conversion of the thiolate moieties into disulfide bridges, rendering a crosslinked polymer network that cannot be used as a capping agent for the silver nanoparticles. Under the appropriate conditions, however, the thiolate groups remain intact in the reaction mixture for a sufficiently long period, during which they are able to bind to the metal surface. Sulfur-silver binding stabilizes the nanoparticles

via surface grafting of the copolymers and hinders disulfide formation. Based on this hypothesis, a synthetic procedure was developed to employ the $NaBH_4$ treated copolymers as the capping agent for silver nanoparticles within their limited period of stability (the copolymers precipitate after a few hours if not grafted to the nanoparticles). This procedure involves modification of the copolymer with $NaBH_4$ in a pre-treatment step, which is followed by the introduction of the silver cations to the reaction medium in the reduction step. Figure 6.4 shows the TEM image of MV15 encapsulated SNP produced by this method. This sample was prepared by single step addition of $NaBH_4$ using $NaBH_4$/TU and TU/SN mole ratios of 4.39 and 1.3, respectively. The pretreatment step was conducted at T = 60 °C for 15 minutes, after which the reduction step was continued for 4 hours. The resulting nanoparticles have an average diameter of 2.73 nm with a dispersity (characterized by the standard deviation of the nanoparticle diameters) of 0.31 nm.

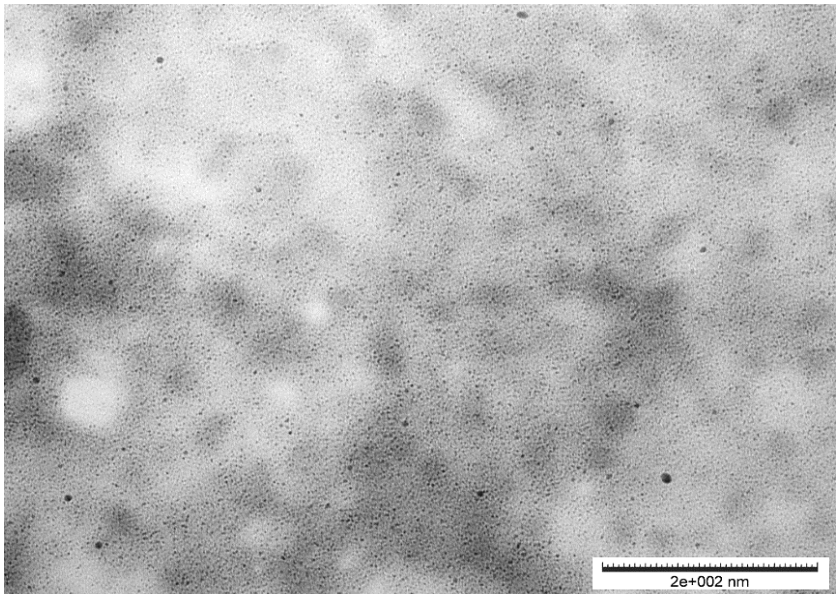

Figure 6.4. TEM micrograph of the MV15-SNP synthesized with $NaBH_4$/TU=4.39, TU/$AgNO_3$=1.3, and pretreatment time of 15 minutes.

Unlike the basic hydrolysis method, this approach does not require strict reaction conditions (such as high reaction temperature throughout the entire reaction and inert atmosphere) and is applicable to a range of VBC copolymers, allowing for the customization of the physical properties of the resulting nanoparticles. Based on our observations on the synthesis of alkanethiol-capped SNP and the post-polymerization modification of VBC copolymers with $NaBH_4$, the average size and the size distribution of the polymer coated nanoparticles are predominantly determined by the following factors:

- The mole percentage of VBC comonomer and the fraction of chlorides substituted by TU groups in the modification process. A large mole percentage of VBC increases the probability of undesirable side reactions such as crosslinking, while a small percentage may compromise the efficiency of the polymer as a multi-functional capping agent.

- The initial concentration of $NaBH_4$ at the pre-treatment step which primarily affects the rate of reaction. At constant copolymer concentration, this factor can be expressed as the $NaBH_4$/TU mole ratio.

- The duration of the pre-treatment step, which is a major factor in determining the conversion (how much of TU is transformed to thiolate), yield and selectivity (the mole ratio of thiolate to disulfide) of the reaction.

- The mole ratio of the TU side groups on the polymer chains to the silver salt ($AgNO_3$).

- The reducing strength of the reaction medium at the start of the second step, when the silver salt is added. This is determined by the initial concentration of $NaBH_4$

and the manner in which it is added (whether it is added in a single or in multiple steps during the reaction).

- The reaction temperature in both the pre-treatment and the reduction steps.

Most of the abovementioned factors are interrelated, in the sense that they affect the same basic aspects of the reaction. For example the concentrations of TU groups and $NaBH_4$, duration of the pretreatment step, and the reaction temperature affect both the rate and the conversion of the reaction. The large number of interrelated variables, make it very difficult to determine the optimum preparation conditions. Here a simpler approach was used to evaluate the effect of some of the reaction parameters on the size and uniformity of the nanoparticles. A series of experiments were performed in which only one factor was varied, while the rest were kept constant with the reference sample.

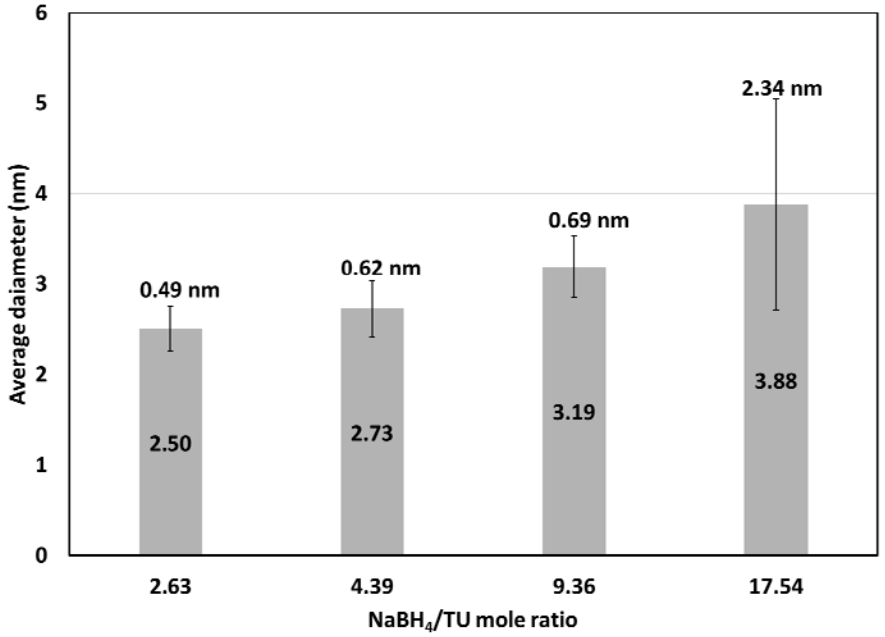

Figure 6.5. The effect of $NaBH_4$/TU mole ratio on the average size (shown at the center of each column) and dispersity (shown on top of the error bars) of the nanoparticle diameters.

Figure 6.5 shows the influence of $NaBH_4$/TU mole ratio on the average size and dispersity of the nanoparticles. The average diameter of the particles increases from 2.50 nm to 3.88 nm by increasing the concentration of the reducing agent. The particles also become noticeably less uniform in size at the highest $NaBH_4$/TU ratio. A noticeable proportion of the nanoparticles prepared with $NaBH_4$/TU=17.54 are larger than 6 nm (Feret diameter, $d_F > 6$ nm), which is the largest diameter in the other samples of this series, Figure 6.6. Variations in the mean diameter and dispersity of the nanoparticles as a function of pretreatment time are exhibited in Figure 6.7. An increase in duration of the pretreatment step from 15 minutes to 90 minutes, while maintaining concentrations constant, results in the formation of larger nanoparticles with slightly increased dispersity. Further increasing the time of pretreatment to 150 minutes, does not lead to significant change in the average diameter; however, it approximately doubled the dispersity with respect to that of the sample prepared with 90 minutes pretreatment. A small amount of aggregated copolymer was present in the reaction mixture at the later stages of the pretreatment step, when it was extended from 90 to 150 minutes, which had to be removed prior to the reduction step. The reducing strength of the reaction medium was adjusted by replenishing the $NaBH_4$ concentration at the start of the reduction step. A noticeable decrease in the average diameter of the nanoparticles is observed when $NaBH_4$ is added in two steps, Figure 6.8. A stronger reducing environment has also a pronounced effect on the dispersity of the sample prepared with 150 minutes pretreatment time, producing nanoparticles with smaller dispersity.

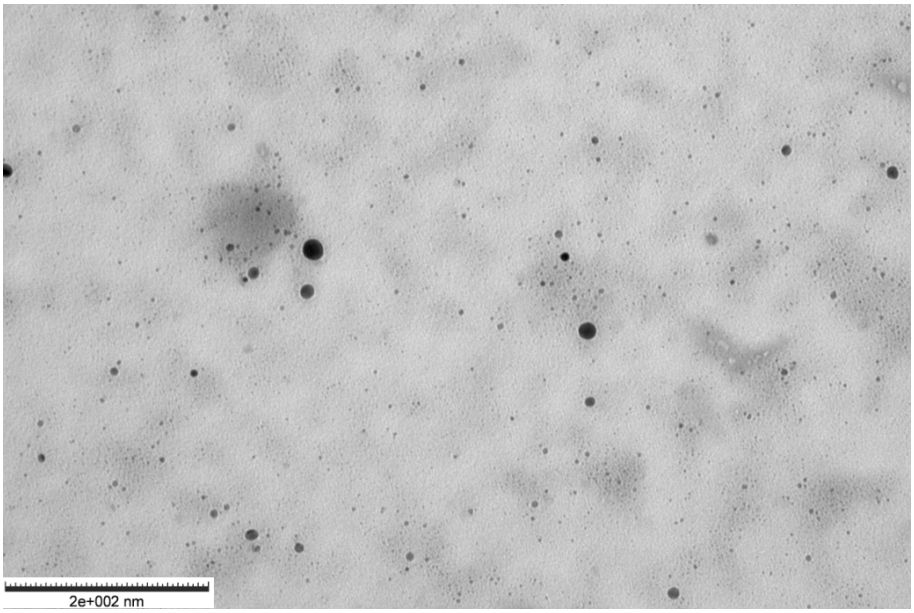

Figure 6.6. TEM micrograph of the MV15-SNP synthesized with $NaBH_4$/TU = 17.54, TU/$AgNO_3$ = 1.3, and pretreatment time of 15 minutes.

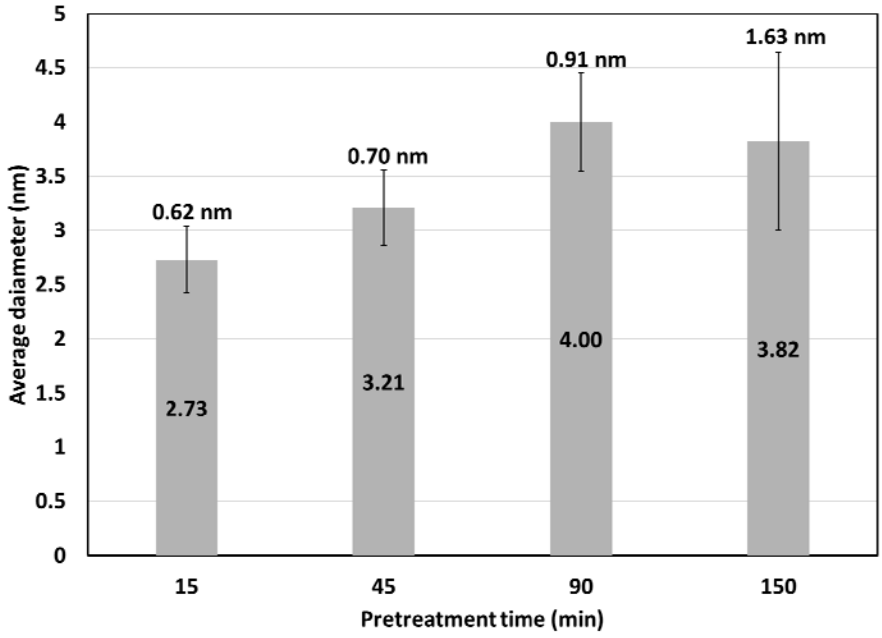

Figure 6.7. The effect of pretreatment time on the average size (shown at the center of each column) and dispersity (shown on top of the error bars) of the nanoparticle diameters.

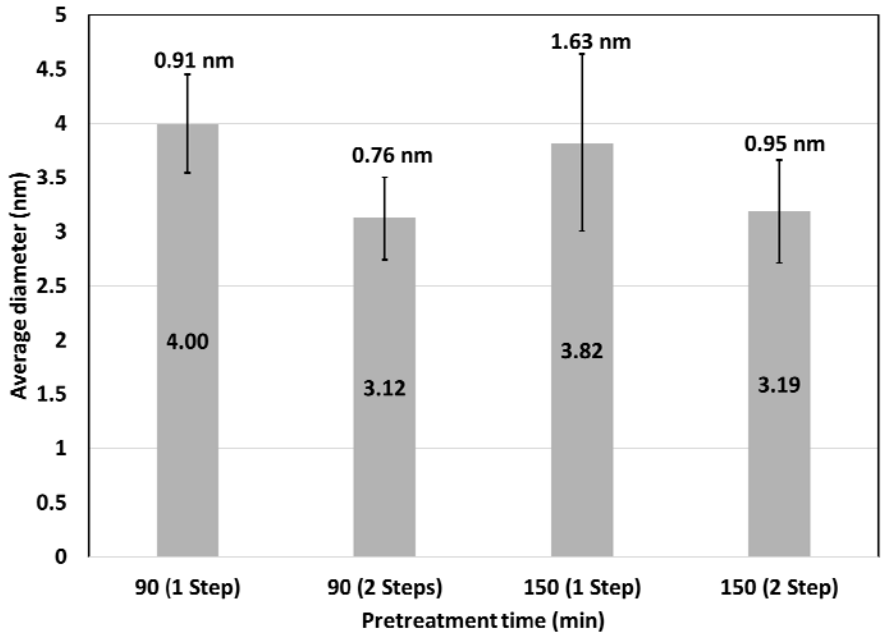

Figure 6.8. The effect of two-step addition of $NaBH_4$ on the average size (shown at the center of each column) and dispersity (shown on top of the error bars) of the nanoparticles diameters.

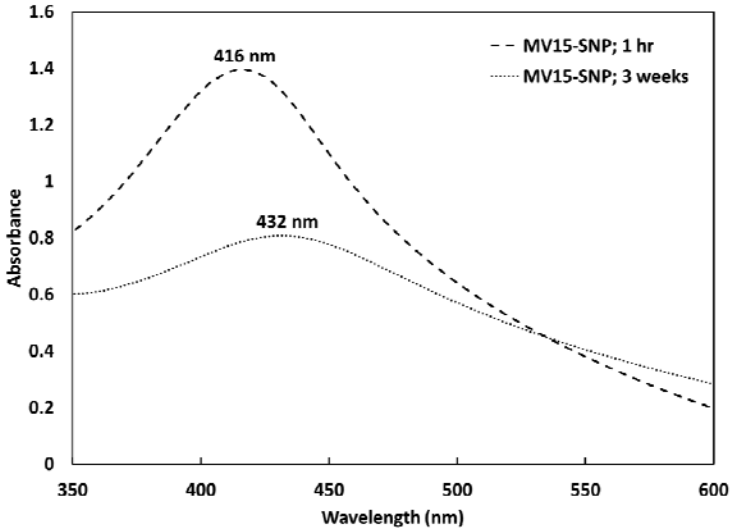

Figure 6.9. UV-visible spectra of the freshly prepared MV15-SNP solution and the same solution stored under ambient condition for three weeks. The nanoparticles were synthesized with pretreatment time = 90 min and two-step addition of $NaBH_4$.

All nanoparticle samples remained soluble in the reaction mixture (the mixture was diluted by solvent addition) for at least two weeks without forming any perceptible aggregates. The stability of the nanoparticles in solution was studied by inspecting the changes in their UV-visible absorption with time. The absorption spectra of these polymer coated nanoparticles has a strong peak in the range of 426 to 408 nm, arising from the surface plasmon resonance of the silver nanocrystals. Figure 6.9 shows the UV-visible spectra of the freshly prepared nanoparticle solution (using a pretreatment time = 90 min and the two-step addition of $NaBH_4$) and the solution stored under ambient conditions for three weeks. The absorption band shows a conspicuous red shift from 416 nm in the fresh sample, to 432 nm in the aged sample, implying formation of larger nanoparticles due to the coalescence of the smaller ones. Further ageing of this sample for two months had a negligible effect on the wavelength and intensity of its absorption band (Appendix, Figure A.8), which indicates that the rate of particle coalescence decreased dramatically over time.

Many potential applications of the nanoparticles, including their incorporation into various matrices, relies on the solubility of the dried nanoparticles. The mass percentage of the soluble fraction of the dried nanoparticles is presented in Table 6.2. The soluble fraction of the samples prepared with single step addition of $NaBH_4$ increases initially with pretreatment time from 15 minutes to 90 minutes and then declines upon further increasing to 150 minutes. The two-step addition of the reducing agent significantly improves the solubility of the dried nanoparticles. For example, up to 93 mass% of the nanoparticles synthesized with pretreatment time of 90 minutes and two-step addition of $NaBH_4$, was successfully redissolved in DMSO. These nanoparticles were characterized by UV-visible spectroscopy and TEM, Figures 6.10 and 6.11. The TEM micrograph shows an increase in

the average diameter from 3.12 nm for the original sample to 3.74 nm and a pronounced loss of uniformity (dispersity = 2.39 nm) for the dried nanoparticles. Moreover, this sample had a high incidence of very large particles, with diameters up to 27 nm. The presence of these large particles is responsible for the red shift of the light absorption band from 416 nm to 422 nm.

Table 6.2. The mass percentages of the dried nanoparticles soluble fraction. All the samples were prepared with $NaBH_4$/TU=4.39.

	$15^{*} - 1^{**}$	$90^{*} - 1^{**}$	$150^{*} - 1^{**}$	$90^{*} - 2^{**}$	$150^{*} - 2^{**}$
Soluble fraction	63 %	76%	69%	93%	87%

* The duration of the pretreatment step in minutes

** The number of steps of $NaBH_4$ addition

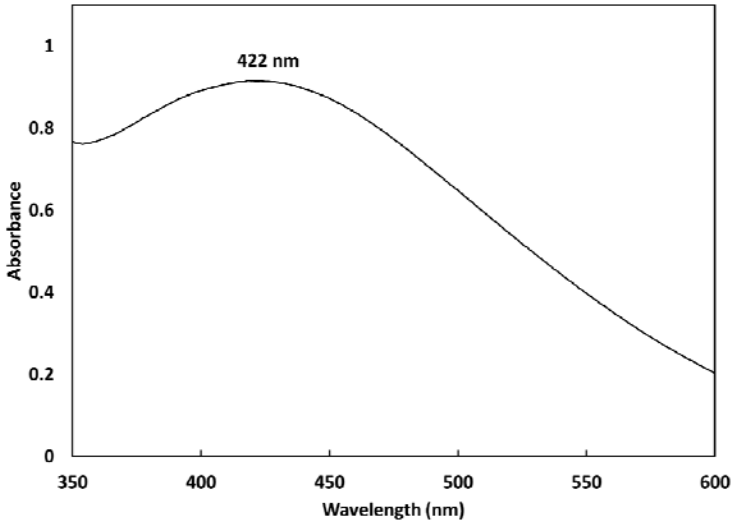

Figure 6.10. UV-visible spectrum of the dried and re-dispersed nanoparticles. The sample was synthesized with pretreatment time of 90 minutes, and two-step addition of $NaBH_4$.

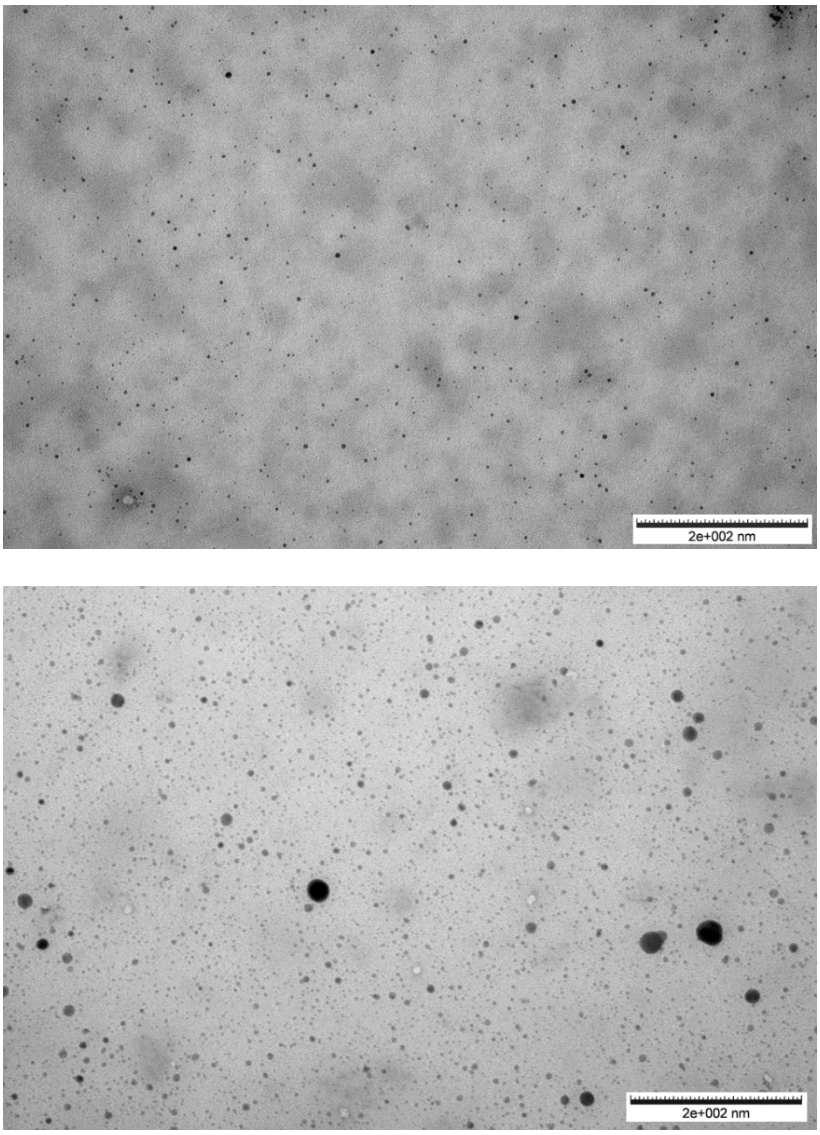

Figure 6.11. TEM micrograph of the MV15-SNP prior (top) and after being dried and re-dissolved (bottom). The sample was synthesized with $NaBH_4$/TU = 4.39 and TU/SN = 1.3.

The solubility of the dried nanoparticles was further enhanced either by performing the pre-treatment step under inert atmosphere or by employing a copolymer containing 5 mole% TU groups (MV5TU) as the capping agent. Treatment of MV15TU with $NaBH_4$ under an inert atmosphere reduces the probability of oxidation of thiolate to disulfide, thus

preventing the formation of crosslinked polymer chains. The average diameter (3.22 ± 0.36 nm) of the nanoparticles prepared under an inert atmosphere with 90 minutes pretreatment time and two-step addition of $NaBH_4$ is similar to the mean size of the sample made in the presence of oxygen, Figure 6.12. Performing the pre-treatment in the absence of oxygen, however, increases the soluble fraction to approximately 96%. Near complete solubility was achieved by employing MV5TU to stabilize the nanoparticles (90 minutes pretreatment time and two-step addition of $NaBH_4$). These nanoparticles remain soluble throughout multiple cycles of solvent removal and dissolution. The MV5TU-SNP (nanoparticles coated with MV5TU) have larger average diameter (4.30 nm) and dispersity (1.66 nm) in comparison with MV15TU-SNP prepared under the same reaction conditions, Figure 6.13. This is the result of the lower concentration of TU functionalities in MV5TU which reduces the thiolate/$AgNO_3$ mole ratio.

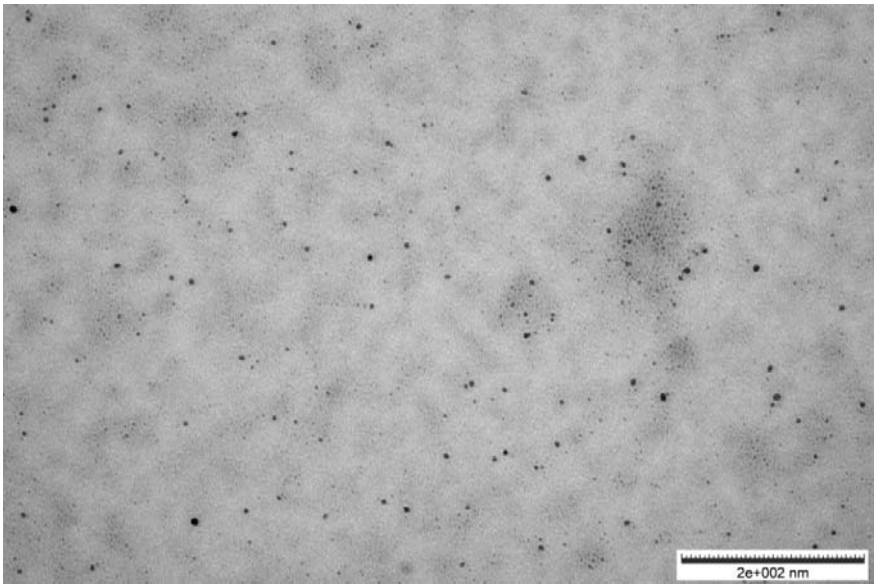

Figure 6.12. TEM micrograph of the MV15-SNP synthesized with $NaBH_4$/TU = 4.39, TU/SN = 1.3, pretreatment time of 90 minutes, and two-step addition of $NaBH_4$ under inert atmosphere.

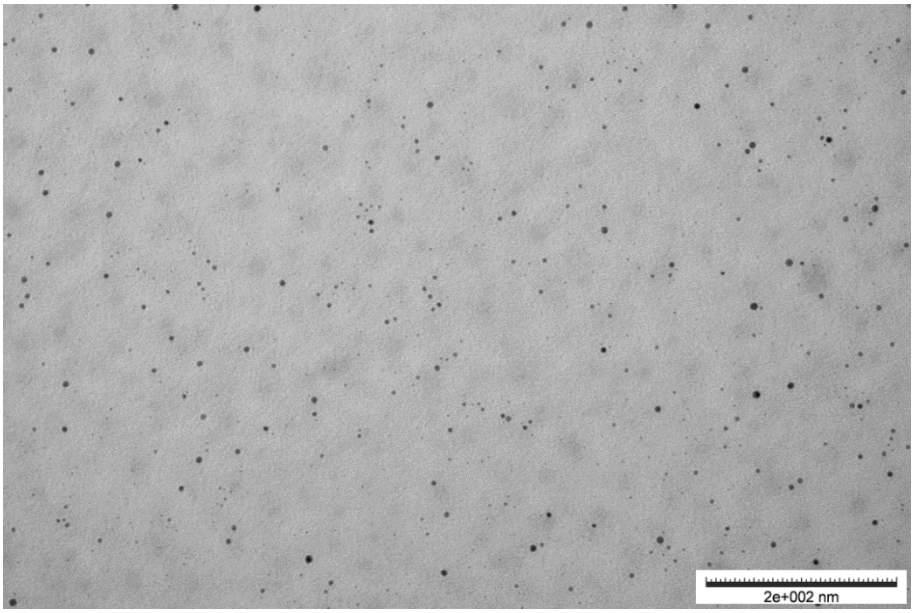

Figure 6.13. TEM micrograph of the silver nanoparticles encapsulated with MV5 copolymer.

As confirmed by NMR investigation of the pretreatment step, the TU groups react rapidly with $NaBH_4$ to produce intermediate species that are subsequently transformed into thiolates at a slower rate. These thiolate moieties undergo reversible exchange with disulfide, which tends to gradually shift towards the disulfides. The formation of intermolecular disulfide bridges produces longer, branched polymer chains that continue to grow into an insoluble crosslinked network. The occurrence of disulfide bonding is negligibly small at the early stages of the reaction, due to the very low concentration of the thiolates. At later stages, however, three active side groups were seen to coexist on the copolymer chains: the intermediate, thiolates, and disulfides. The concentration of the intermediate species decreases monotonically, while the amount of thiolates first increases and at some point starts to decline as its conversion to disulfide become dominant. The optimum conditions in the pretreatment step are achieved when the concentration of thiolates is near its maximum, and the incidence of disulfide bridging is not large enough

to adversely affect the polymer solubility. As the reaction is much slower at T = 22°C (temperature of the reduction step), we can assume that the concentration of thiolate in the reduction step is a function of its rate of formation and conversion into disulfides during the pretreatment. At optimum pretreatment conditions, the highest thiolate/Ag^+ mole ratio is achieved, which minimize the size and dispersity of the particles. Moreover, smaller and more uniform nanoparticles may form by increasing the reduction strength of the reaction medium[31, 33]. The observed changes in the size, dispersity, and solubility of the nanoparticles as a function of the experimental conditions are therefore attributed to their influence on concentration of the thiolate groups and reducing strength of the reaction medium.

An increase in the average size and dispersity of the nanoparticles with the duration of the pretreatment step (single-step addition of $NaBH_4$) can result from the diminished concentration of the thiolates and the lower reducing strength of the reaction medium at longer pretreatment times. The nanoparticles prepared with 15 minutes pretreatment are even smaller and more uniform than those made in a stronger reducing environment provided by two-step addition of $NaBH_4$. This implies that the concentration of thiolate moieties decreases significantly with increasing length of the pretreatment step. The noticeable improvement in the uniformity of the particles prepared via two-step $NaBH_4$ addition can be attributed to the higher reducing strength during the second step. Faster reduction of the silver cations is also responsible for the smaller average diameter of these nanoparticles, with respect to those made with single-step addition. The concentration of the thiolate groups also has a crucial impact on the solubility of the dried nanoparticles. The loss of solubility is mainly caused by the formation of intermolecular disulfide bonds

between the free thiolates (those that are not grafted to the surface of nanoparticles), the concentration of which is determined by the initial concentration of the thiolates at the reduction step and the metal surface area available for their grafting. Larger initial concentration increases the population of the free thiolates and accordingly increases the rate of their conversion into disulfide bridges. This explains the lower solubility of the nanoparticles obtained using the shortest pretreatment time and complete solubility of the MV5 coated nanoparticles. The higher soluble fraction of the samples produced with two-step addition of $NaBH_4$, in comparison to the single-step samples, is due to their smaller particle size which correspondingly provides larger metal surface area for grafting, thereby preventing the thiolates from being converted into disulfides.

Adsorption of the copolymer on the metal surface was investigated through examining the dynamics in the free and the grafted chains using ^1H NMR measurements. The longitudinal (T_1) and transverse (T_2) relaxation times of ^1H are driven by the molecular motion occurring on the time scales of the spin interactions[118, 123]. Previously (Chapter 3, section 3.4) it was explained that T_1 initially reduces with increasing τ (correlation time of motion), passes through a minimum at $\tau_0 = 1/\omega_0$ (ω_0 is the Larmor frequency which is on the order of 10^8 Hz), and subsequently increases for $\tau > \tau_0$ (Chapter 3, Figure 3.1). In contrast, T_2 decreases monotonically with correlation time of the motions that influence dephasing of the transverse magnetization. Also note that the variation of T_1 and T_2 as a function of inverse temperature (1/T) is similar to their dependence on the correlation time, owing to the inverse relation between τ and T. When $\tau > \tau_0$, the effect of temperature or the rate of motion on NMR relaxation times is more pronouncedly observed as the variation in T_1/T_2 ratio.

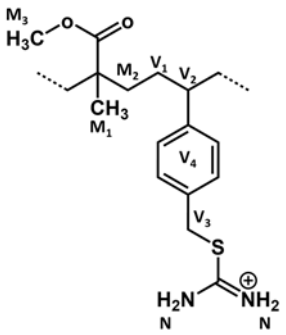

Scheme 6.2. Schematic representation of MV15TU.

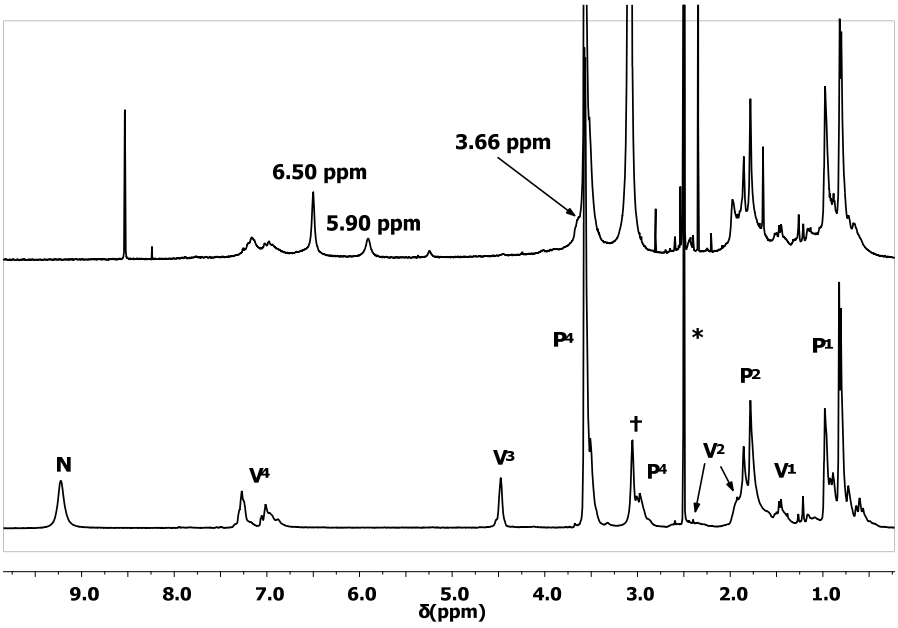

Figure 6.14. ^{1}H NMR spectra of (bottom) MV15TU copolymer and (top) the MV15 capped nanoparticles re-dissolved in DMSO-d_6. The copolymer signals are assigned according to the scheme 6.2. The solvent and residual water signals are indicated by * and †, respectively.

Figure 6.14 shows the ^{1}H solution NMR spectrum of the redispersed MV15-capped nanoparticles in DMSO-d_6. As was shown previously [Chapter 5, Section 5.3], the characteristic resonances of NH_2 groups and the benzylic CH_2, indicated by N and V_3 in Figure 14, disappear upon treatment of MV15TU copolymer with $NaBH_4$. The ^{1}H spectrum

of the nanoparticles reveals several new signals, most of which are arising from byproducts. Through comparison with the ^1H spectrum of the MV15TU/$NaBH_4$ (Figure 5.36), the new signal at 3.66 ppm, which has a strong overlap with P_4 signal, is assigned to the methyl protons adjacent to the thiolate moiety. The origin of the peaks at 5.90 ppm and 6.50 ppm is not clear as they have no correlation with other protons or carbon signals in the COSY and HSQC spectra of this sample.

Solution-state ^1H NMR relaxation curves and the relaxation times of selected signals of MV15TU and MV15-SNP at three temperatures are presented in Figure 6.15 and Table 6.3. The T_2s of all signals and the T_1s of P_2 (1.75 ppm at T=22°C) and P_1 (0.73 ppm at T=22°C) decrease monotonically with increasing the temperature from 22°C to 80°C. The T_1 of the aromatic protons at 7.14 ppm, however, increases with temperature. These observations imply that relaxation of the two nuclei with lower frequencies is driven by motion with long correlation times ($\tau > \tau_0$), whereas relaxation of the aromatic signals is dominated by motion faster than τ_0. Adsorption of the polymer chains on the rigid silver surface imposes severe restriction on their dynamics, reducing the rate of bond rotation. A comparison between the redispersed nanoparticles and the unreacted MV15TU shows that, irrespective of the test temperature, the ^1H signals of the former have shorter transverse relaxation times than the latter. Moreover, the P_1 and P_2 resonances of the redispersed nanoparticles have relatively longer T_1s, while the resonances of their aromatic protons have shorter T_1 times. This is consistent with their aforementioned temperature dependence, which indicated that the T_1s of P_1 and P_2 are in the slow motion regime, while the T_1 of the aromatic protons is in the fast motion regime. The observed differences between the T_1s and T_2s of MV15TU and MV15-SNP indicate that the correlation times of local motion,

responsible for relaxations of the nuclei located at various positions (main chain and side groups on MMA and VBC units), are consistently longer in the nanoparticle sample. Slower dynamics can result from grafting of the copolymer chains to the nanoparticles from multiple points along the chain. Large differences between the T_1/T_2 ratios of the free and grafted copolymers, which persist at elevated temperatures, further confirm strong bonding of the chain to the metal surface. The temperature dependence of the chemical shifts, line width, intensity, and relaxation times of the NMR signals are completely reversible, showing that the thiolate-silver bonds remain intact and the copolymers effectively stabilize the nanoparticles at T = 80 °C.

Table 6.3. ^{1}H NMR relaxation times of MV15TU and MV15-SNP at various temperatures.

Sample		T = 22			T = 50			T = 80		
	Chemical shift (ppm)	7.14	1.75	0.73	7.14	1.76	0.77	7.15	1.78	0.80
MV15TU	T_1 (s)	1.6	1.2	1.0	1.9	0.9	0.6	2.1	0.7	0.4
	T_2 (ms)	44.6	14.0	24.7	122.4	28.7	48.7	248.6	70.9	114.0
	T_1/T_2	**35.8**	**86.2**	**41.3**	**15.7**	**32.9**	**11.5**	**8.5**	**9.9**	**3.6**
MV15-SNP	T_1 (s)	1.5	1.4	1.2	1.6	1.0	0.7	1.9	0.8	0.5
	T_2 (ms)	11.9	8.0	13.9	43.2	24.7	53.3	98.6	60.3	97.7
	T_1/T_2	**124.5**	**171.3**	**82.7**	**37.9**	**40.9**	**12.9**	**19.3**	**13.0**	**4.9**

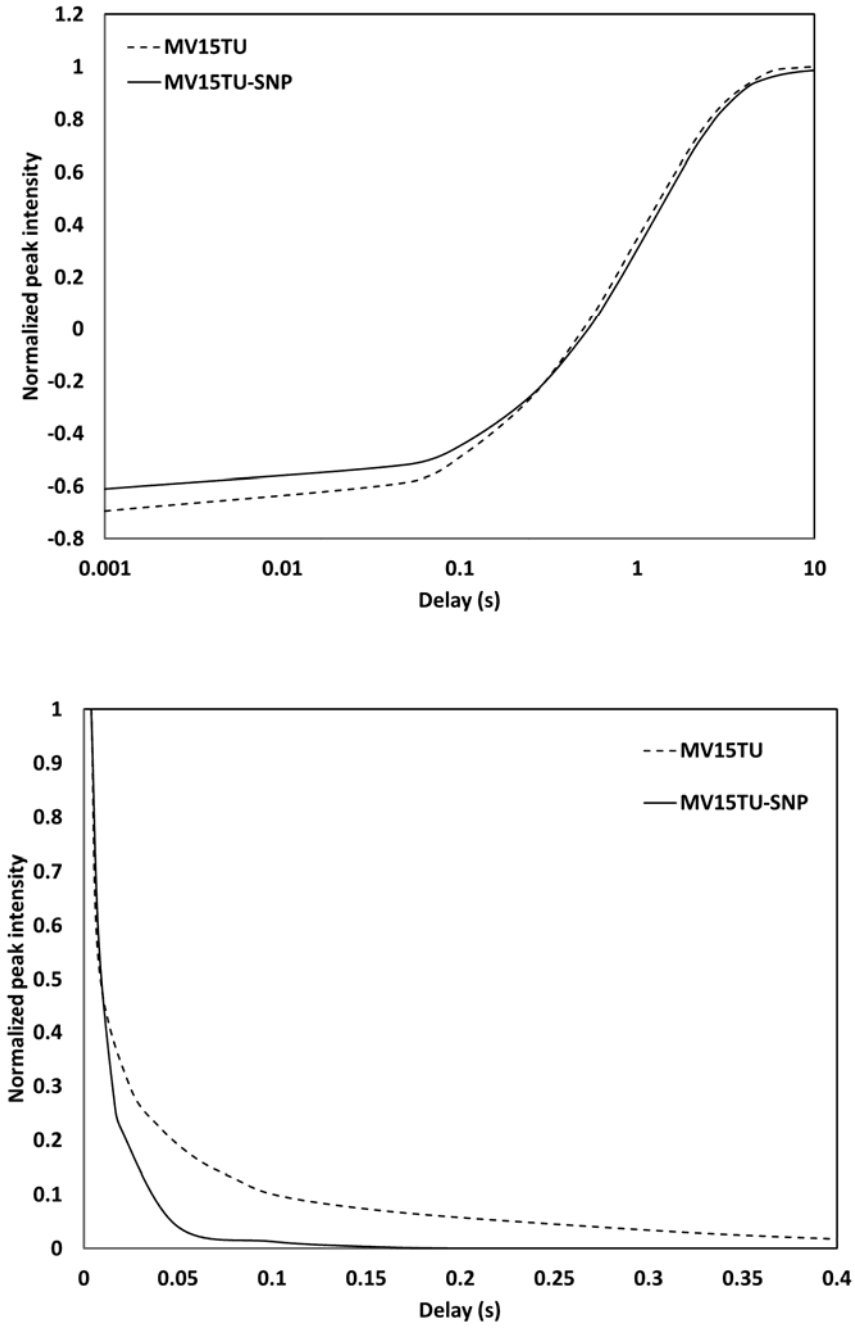

Figure 6.15. Longitudinal (top) and transverse (bottom) relaxation curves of the P_1 signals of MV15TU and MV15-SNP samples.

The application of the proposed two-step method of preparation of SNP encapsulated by various copolymers of VBC was verified by the successful synthesis of silver nanoparticles stabilized with SV15 and BV copolymers, Figures 6.16 and 6.17. The SV15 and BV capped nanoparticles have average diameters of 3.26 ± 0.52 nm and 2.40 ± 0.53 nm, respectively. Unlike the MV15-SNP, these nanoparticles lose their solubility after removal of the reaction solvent. Characterization of the SV15-TU and the BV-TU copolymers using solution NMR and FTIR (Chapter 5, section 5.4) showed that they contain a noticeable amount of unmodified VBC units. The presence of benzyl chloride side groups complicates the reaction and may result in the formation of crosslinks (via intermolecular bonding) that give an insoluble product. Further effort is in progress to improve the quality and the solubility of these nanoparticles.

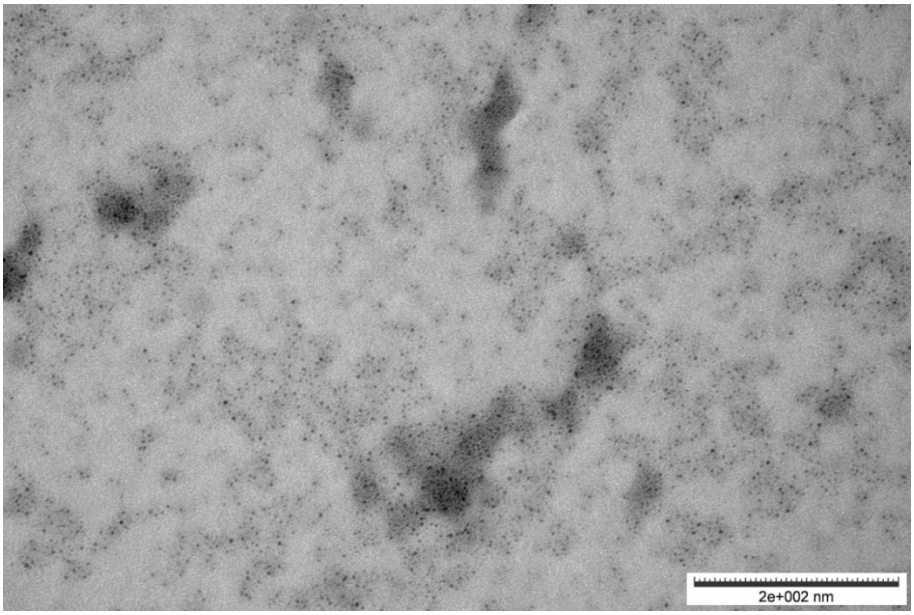

Figure 6.16. TEM micrographs of the SV15 copolymer coated silver nanoparticles.

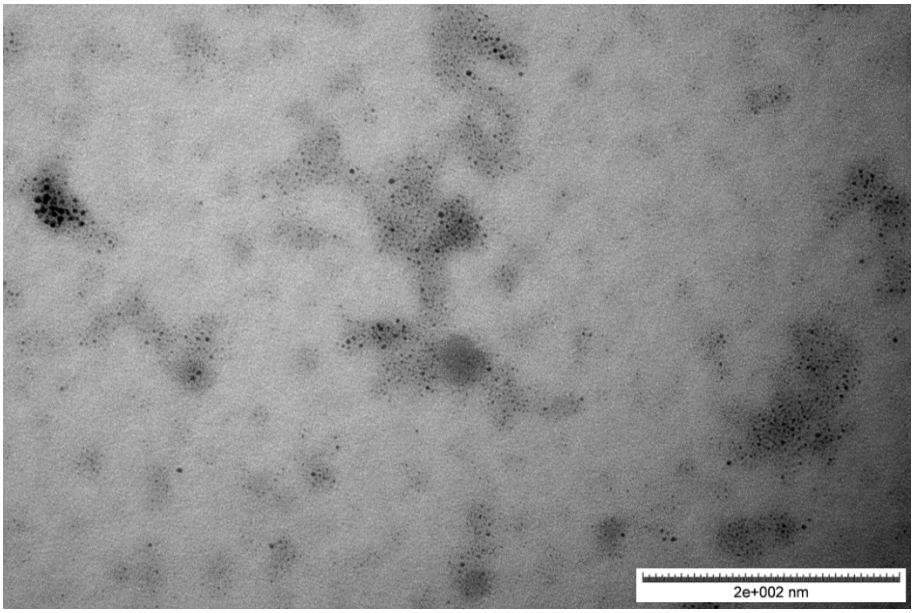

Figure 6.17. TEM micrographs of the BV copolymer coated silver nanoparticles.

6.4. Conclusions

Various synthetic strategies for the preparation of polymer capped SNP with average diameters ranging from 2.73 nm to 5.86 nm were presented. Nanoparticles stabilized with thiol-terminated PMMA were produced by utilizing this polymer as the capping agent in a single-phase reaction. This method suffers from several disadvantages including: the very small proportion of dithioester groups (only one group per polymer chain), their incomplete conversion into thiolate, and the difficulty in dissolving simultaneously the polymer and the silver salt in the same solvent. The resulting nanoparticles were therefore relatively large and less stable.

Better control over the size and dispersity was achieved by developing a two-step method for the synthesis nanoparticles encapsulated with multiple-thiolate functionalized

random copolymers. The synthetic procedure involved a pretreatment step to convert the TU groups of the modified VBC random copolymers into thiolates via either basic hydrolysis or reduction. This was followed by a reduction step where thiolate functionalized copolymer was employed as the capping agent of the growing silver nanocrystals (reduction step). Successful preparation of the MV15 coated nanoparticles via a basic pretreatment step required precise adjustment of the reactant concentrations. Furthermore we observed that a high reaction temperature and an inert atmosphere were necessary to avoid precipitation of the polymer. Our attempts at applying this method for the synthesis of stable nanoparticles protected with modified random copolymers of VBC with styrene (SV15TU) and with butyl acrylate (BVTU) failed.

Unlike basic hydrolysis, pretreatment with $NaBH_4$ was successfully conducted in the presence of air without noticeable precipitation of the copolymer over a much longer time. Furthermore this method was extendable to all VBC copolymers studied here, allowing for the customization of the physical properties of the resulting nanoparticles. The effects of reaction conditions on the average size, dispersity, and solubility of the nanoparticles prepared with this method were evaluated by performing a series of experiments in which just one of the factors was varied, while the rest were kept constant. The nanoparticles were seen to become larger and less uniform with increasing the $NaBH_4$ /TU mole ratio (from 2.50 ± 0.49 nm to 3.88 ± 2.34 nm) and the duration of the pretreatment step (2.73 ± 0.62 nm to 3.82 ± 1.63 nm). Providing a stronger reducing medium by two-step addition of $NaBH_4$ produced smaller and more uniform nanoparticles (e.g. from 4.00 ± 0.91 nm to 3.12 ± 0.76 nm for pretreatment time 90 minutes).

The stability of the nanoparticles dissolved in their reaction mixture was verified by monitoring the time evolution of their UV-visible spectra. An initial red shift in the light absorption wavelength was observed upon ageing in solution over a few weeks, indicating the coalescence of the smaller nanoparticles. The rate of coalescence drastically reduced over longer storage times, as evidenced by a very small variation in the λ_{max} (light absorption peak positon) from three weeks to two months. The solubility of the dried nanoparticles, which is essential for their further applications, was significantly improved by adding the reducing agent in two steps. TEM micrographs of the redissolved nanoparticles showed an increase in their average diameter and a pronounced loss of uniformity with respect to the original nanoparticles (before drying). Solubility of the dried nanoparticles was further improved by either conducting the pre-treatment step for MV15TU under an inert atmosphere or employing MV5TU as the capping agent. Performing the reaction under an inert atmosphere had a negligible effect on the size and uniformity of the nanoparticles, while using MV5TU with lower concentration of TU functionalities increased the mean diameter and dispersity of the nanoparticles.

The observed changes in the size, dispersity, and solubility of the nanoparticles was justified by considering the influence of reaction conditions on the concentration of the thiolate groups and the reducing strength of the reaction medium. Formation of smaller and more uniform nanoparticles at shorter pretreatment times and two-step addition of $NaBH_4$ was attributed to the larger concentration of thiolates and stronger reducing environment, respectively. The loss of solubility of the dried nanoparticles was correlated with the fraction of free thiolates, which depends on the initial concentration of the functional groups and the metal surface available for their grafting.

The solution state ^{1}H NMR spectrum of the re-dissolved nanoparticles showed disappearance of the characteristic resonances of NH_2 groups and the benzylic CH_2 of the MV15TU copolymer. Surface adsorption of the copolymer chains on the nanoparticles was studied by comparing the ^{1}H NMR relaxation times of the MV15TU and MV15-SNP samples. The ^{1}H nuclei of MV15-SNP sample had larger T_1/T_2 ratios over a range of temperatures, which confirmed strong multiple-point grafting of the copolymer chains to the metal surface.

Chapter 7. Conclusions and Future work

7.1. Conclusions

In this thesis, research into the synthesis and characterization of silver nanoparticles coated with alkanethiols and thiolate functional polymer was presented. Some of the major challenges in manufacturing of these hybrid nanomaterials were addressed. A combination of experimental techniques were employed to investigate the preparation methods and to characterize the properties of the nanoparticles.

The two-phase Brust and Schiffrin method was employed for the synthesis of small uniform nonanethiol and octadecanethiol capped SNP. TEM micrographs of the resulting nanoparticles showed their arrangement into ordered 2D or 3D structures through interdigitation of the surface grafted alkane chains. Such interdigitation results in the predominance of all-*trans* conformation and slower bond rotation in the surface grafted alkane chains, as revealed by solid-state NMR spectroscopy.

To gain a better understanding of the two-phase method, samples taken from the intermediate stage of this reaction were characterized by NMR and vibrational spectroscopies and compared with unmodified TAOB and AgNT. The silver-tetraoctylammonium complexes formed during the phase-transfer step of the reaction did not change upon addition of NT, leading to the conclusion that at sufficiently large TOAB/$AgNO_3$ and TOAB/NT mole ratios, they are the predominant intermediate compound and thus must be the precursor to the silver nanoparticles. The phase structure and composition of the phase-transferred compound were further elucidated by observing

the chemical shifts, dynamics, and thermal transitions of the samples with different mole ratios of the reactants. It was shown that with excess amounts of TOAB (TOAB/$AgNO_3 \geq$ 2), the product of the phase-transfer step has at least two distinct phases, due to the interactions between $[TOA]^+$ and a multitude of counterions, such as NO_3^-, $[AgBr_2]^-$, and Br^-. Lower concentration of TOAB (TOAB/$AgNO_3$ < 2) resulted in inefficient phase-transfer and formation of insoluble silver bromide that precipitate from the reaction mixture. The reduction of the TAOB/$AgNO_3$ mole ratio from 4.4 (which is commonly used in the two-phase methods) to 2 did not significantly affect the average size and uniformity of the nanoparticles.

Discrete polymer-capped silver nanoparticles were prepared by synthesis of thiolate functionalized polymers and employing them as capping agents of the metal nanocrystals. The RAFT process was employed for controlled free radical synthesis of PMMA, PVBC, and random copolymers of VBC, which were subsequently converted into thiolate bearing macromolecules by post-polymerization modification. The chain transfer agents employed for RAFT polymerization of MMA and its random copolymers with VBC produced living polymers with narrow molar mass distribution. These RAFT agents were less efficient in controlling the synthesis of PVBC and SV15 random copolymer.

Thiol-terminated PMMA was synthesized via reduction of the terminal dithioester residue of the RAFT agents with $NaBH_4$. Polymers bearing multiple thiolate functionalities were prepared by nucleophilic substitution of chlorine on the homopolymer and copolymers of VBC with TU groups, followed by the conversion of TU into thiolate by basic hydrolysis or reduction. The substitution reaction was investigated by following the changes in the FTIR band of the C-Cl bond, as well as 1D and 2D NMR characterization

of the modified polymers. For PVBC, the substitution did not proceed to completion due to the high concentration of the reactive sites on the homopolymer, which severely reduced their accessibility as the reaction proceeds. Complete substitution of Cl with TU was achieved for the MV15 copolymer.

Basic hydrolysis of PVBC yielded an insoluble product formed as a result of side reactions leading to inter and intra-molecular bonding between the polymer chains. Despite the lower concentration and random distribution of the reactive units in MV15TU chains, introduction of KOH for basic hydrolysis, could induce rapid precipitation of the copolymer from the reaction medium. Precipitation was avoided by carrying out the reaction in DMSO under an inert atmosphere, using a RAFT copolymer with lower molar mass, and carefully adjusting the concentration of the base solution. Characterization of the intermediate and the final product of hydrolysis did not indicate the formation of the thiolate group. Moreover, hydrolysis of SV15TU and BV15TU via the same procedure produced insoluble material.

Conversion of the thiouronium side group into thiolate by reduction with $NaBH_4$ was found to be more facile and more flexible in comparison to basic hydrolysis. The reaction was monitored by NMR at two temperatures. ^1H NMR showed that the copolymer backbone and side-groups of the MMA units remained unaltered, while the signals of the TU functionality and its neighboring benzylic CH_2 disappeared rapidly, and those of the phenyl ring shifted slightly to lower frequencies upon addition of $NaBH_4$. Moreover, new signals emerged in the ^1H and ^{13}C spectra of the modified copolymer. The connectivity of nuclei were determined from 2D COSY and phase-sensitive HSQC spectra. FTIR of the

modified MV15TU showed the disappearance of the thiouronium bands, however it did not shed light onto the structure of the modified side group.

Further insight into the mechanism of the above reaction was obtained by investigating the reduction of benzyl thiouronium, which is the small-molecule analogous of TU-bearing vinylbenzyl repeating units. Monitoring this reaction via 1D and 2D NMR experiments, showed that the TU groups are first converted to thiolates, which subsequently underwent reversible exchange with disulfides. A comparison between the NMR spectra of the BTU/$NaBH_4$ and the MV15TU/$NaBH_4$ reaction mixtures confirmed the presence of thiolates on the modified copolymer. Precipitation of the copolymer from the reaction medium at long reaction times was attributed to the conversion of thiolates into disulfides, which formed crosslinks between the copolymer chains.

Silver nanoparticles ($d_{avg} \approx$ 2.73 nm to 5.86 nm) coated with thiol-terminated PMMA or multi-functional modified random copolymers of VBC were prepared via various "grafting-to" processes. Employing the thiol-terminated PMMA as the capping agent suffered from several disadvantages resulting in the formation of relatively large and less stable nanoparticles. Better control over the size and dispersity was achieved by developing a two-step method for the synthesis of nanoparticles encapsulated by random copolymers with multi-thiolate functionalities. The synthetic procedure involved a pretreatment step to convert the TU groups of the modified VBC random copolymers into thiolates via either basic hydrolysis or reduction. This was followed by a reduction step where thiolate functionalized copolymer was employed as the capping agent of the growing silver nanocrystals (reduction step). Successful preparation of the MV15 coated nanoparticles via a basic pretreatment step required precise adjustment of the reactant

concentrations, high reaction temperatures, and operation under an inert atmosphere. Unlike this reaction, pretreatment with $NaBH_4$ was successfully conducted in the presence of air without noticeable precipitation of the copolymer over much longer periods. Furthermore it was applicable to all VBC copolymers studied in here, which allows for the customization of the physical properties of the resulting nanoparticles.

The effect of reaction conditions on the average size, dispersity, and solubility of the nanoparticles prepared with reductive pretreatment were evaluated by performing a series of experiments. The nanoparticles were observed to become larger and less uniform with increasing $NaBH_4$/TU mole ratio (from 2.50±0.49 nm to 3.88±2.34 nm), and the duration of the pretreatment step (2.73±0.62 nm to 3.82±1.63 nm). A stronger reducing medium, provided by two-step addition of $NaBH_4$, produced smaller and more uniform nanoparticles (e.g. from 4.00±0.91 nm to 3.12±0.76 nm for pretreatment time 90 minutes). The solubility of the dried nanoparticles was also improved significantly by adding the reducing agent in two steps. The observed changes in size, dispersity, and solubility were attributed to the influence of the experimental parameters on the concentration of the thiolate groups and the reducing strength of the reaction medium.

Surface adsorption of the copolymer chains on the nanoparticles was studied by comparing the ^1H NMR relaxation times of the MV15TU and MV15-SNP samples. The ^1H nuclei of the MV15-SNP had larger T_1/T_2 ratios over a range of temperatures, which confirmed strong multiple-point grafting of the copolymer chains to the metal surface.

In summary, fundamental knowledge into the mechanism of the commonly used two-phase Brust and Schiffrin method was provided which is essential to improve its application for synthesis of alkanethiol-capped SNP. A modification to this synthetic

procedure was proposed to simplify the purification process and to improve the solubility of the dried nanoparticles, without compromising the small size and dispersity of the nanoparticles produced. To the best of our knowledge, this is the first report on the solid-state phase structure and dynamics of the material obtained from the phase-transfer step of the two-phase method. Controlled free radical polymerization of the copolymers of VBC, which are versatile precursors for a diverse range of functional polymers, was presented. The knowledge and experience acquired from synthesis of alkanethiol-capped SNP and post-polymerization modification of VBC copolymer, was employed to develop a novel method for preparation of small, uniform and redispersible polymer capped nanoparticles.

7.2. Future work

Based on the knowledge and experience acquired over the course of this research, the following directions are recommended for future work:

1. Further investigation into the reaction mechanism and the microstructure of the intermediate compound of the two-phase method by $^{109/107}$Ag NMR spectroscopy. This technique may reveal valuable information on the fate of the silver ions during the reaction.
2. Detailed characterization of the insoluble portion of the alkanethiol-capped SNP, formed upon work-up or drying the nanoparticles, using powder x-ray scattering and solid-state silver NMR spectroscopy. Knowledge of the composition and structure of this material is essential for solving the precipitation problem which will lead to higher product yield.

3. Employing bulky thiol-bearing ligands in the two-phase method. A bulky group on the capping ligands can prevent their interdigitation, thus may improve solubility of the dried nanoparticles.
4. The development of efficient single phase method for synthesis of silver nanoparticles based on using water soluble thiol capping agents. This eliminates the use of TOAB, which is the major impurity in the product of the two-phase method, while avoiding the problems caused by using common alkanethiols (formation of Ag(I)-thiolate and extensive precipitation) in a single-phase reaction.
5. The search for effective RAFT agents for controlled synthesis of VBC homopolymers and its random copolymers (with monomers other than MMA). Employing such RAFT agents allows for the preparation of di-block or tri-block copolymers with a diverse range of useful properties. For example, a di-block copolymer can be synthesized in which one block is a random sequence of MMA and VBC, which is convertible to a thiolate-bearing block, and the other block is a sequence of BA monomers imparting film forming ability to the copolymer.
6. The synthesis of disulfide functionalized polymeric capping agents through post-polymerization modifications of GMA or VBC containing copolymers. The resulting copolymers are less prone to crosslinking as disulfides are more stable than thiolates under ambient conditions.
7. The optimization of the novel two-step method proposed herein for synthesis of copolymer-capped SNP. This allows for the preparation of nanoparticles with

highly tuned physical characteristics, such as size, size distribution, solubility and shape.

8. The expansion of the two-step method to the production of nanoparticles coated with high performance polymers, with special focus on fluorinated copolymers, such as fluoroacrylates.
9. The development of incorporation strategies for copolymer coated SNP into a variety of polymer matrices, which would allow a systematic method to produce advanced materials for specific applications.

References

1. Gwo, S.; Lin, M.-H.; He, C.-L.; Chen, H.-Y.; Teranishi, T. Bottom-Up Assembly of Colloidal Gold and Silver Nanostructures for Designable Plasmonic Structures and Metamaterials. *Langmuir* **2012,** *28* (24), 8902-8908.
2. Chen, X.; Cheng, X.; Gooding, J. J. Multifunctional Modified Silver Nanoparticles as Ion and pH Sensors in Aqueous Solution. *Analyst* **2012,** *137* (10), 2338-2343.
3. Marsich, L.; Bonifacio, A.; Mandal, S.; Krol, S.; Beleites, C.; Sergo, V. Poly-l-lysine-Coated Silver Nanoparticles as Positively Charged Substrates for Surface-Enhanced Raman Scattering. *Langmuir* **2012,** *28* (37), 13166-13171.
4. Naidu, B. V. K.; Park, J. S.; Kim, S. C.; Park, S.-M.; Lee, E.-J.; Yoon, K.-J.; Joon Lee, S.; Wook Lee, J.; Gal, Y.-S.; Jin, S.-H. Novel Hybrid Polymer Photovoltaics Made by Generating silver Nanoparticles in Polymer: Fullerene Bulk-heterojunction Structures. *Solar Energy Materials and Solar Cells* **2008,** *92* (4), 397-401.
5. Jeong, N. C.; Prasittichai, C.; Hupp, J. T. Photocurrent Enhancement by Surface Plasmon Resonance of Silver Nanoparticles in Highly Porous Dye-Sensitized Solar Cells. *Langmuir* **2011,** *27* (23), 14609-14614.
6. Li, Y.; Wu, Y.; Ong, B. S. Facile Synthesis of Silver Nanoparticles Useful for Fabrication of High-Conductivity Elements for Printed Electronics. *Journal of the American Chemical Society* **2005,** *127* (10), 3266-3267.
7. Niskanen, J.; Shan, J.; Tenhu, H.; Jiang, H.; Kauppinen, E.; Barranco, V.; Picó, F.; Yliniemi, K.; Kontturi, K. Synthesis of Copolymer-Stabilized Silver Nanoparticles for Coating Materials. *Colloid Polym Sci* **2010,** *288* (5), 543-553.
8. Amato, E.; Diaz-Fernandez, Y. A.; Taglietti, A.; Pallavicini, P.; Pasotti, L.; Cucca, L.; Milanese, C.; Grisoli, P.; Dacarro, C.; Fernandez-Hechavarria, J. M.; Necchi, V. Synthesis, Characterization and Antibacterial Activity against Gram Positive and Gram Negative Bacteria of Biomimetically Coated Silver Nanoparticles. *Langmuir* **2011,** *27* (15), 9165-9173.
9. Brown, P. K.; Qureshi, A. T.; Moll, A. N.; Hayes, D. J.; Monroe, W. T. Silver Nanoscale Antisense Drug Delivery System for Photoactivated Gene Silencing. *ACS Nano* **2013,** *7* (4), 2948-2959.
10. Hu, R.; Li, G.; Jiang, Y.; Zhang, Y.; Zou, J.-J.; Wang, L.; Zhang, X. Silver–Zwitterion Organic–Inorganic Nanocomposite with Antimicrobial and Antiadhesive Capabilities. *Langmuir* **2013,** *29* (11), 3773-3779.
11. Taglietti, A.; Diaz Fernandez, Y.; Galinetto, P.; Grisoli, P.; Milanese, C.; Pallavicini, P. Mixing Thiols on the Surface of Silver Nanoparticles: Preserving Antibacterial Properties while Introducing SERS Activity. *Journal of Nanoparticle Research* **2013,** *15* (11), 1-13.
12. Brust, M.; Kiely, C. J. Some Recent Advances in Nanostructure Preparation from Gold and Silver Particles: a short topical review. *Colloids and Surfaces A: Physicochemical and Engineering Aspects* **2002,** *202* (2–3), 175-186.
13. Zhang, S.; Leem, G.; Lee, T. R. Monolayer-Protected Gold Nanoparticles Prepared Using Long-Chain Alkanethioacetates†. *Langmuir* **2009,** *25* (24), 13855-13860.
14. Mari, A.; Imperatori, P.; Marchegiani, G.; Pilloni, L.; Mezzi, A.; Kaciulis, S.; Cannas, C.; Meneghini, C.; Mobilio, S.; Suber, L. High Yield Synthesis of Pure Alkanethiolate-Capped Silver Nanoparticles. *Langmuir* **2010,** *26* (19), 15561-15566.

15. Prasad, B. L. V.; Stoeva, S. I.; Sorensen, C. M.; Klabunde, K. J. Digestive Ripening of Thiolated Gold Nanoparticles: The Effect of Alkyl Chain Length. *Langmuir* **2002,** *18* (20), 7515-7520.
16. Maccarini, M.; Briganti, G.; Rucareanu, S.; Lui, X.-D.; Sinibaldi, R.; Sztucki, M.; Lennox, R. B. Characterization of Poly(ethylene oxide)-Capped Gold Nanoparticles in Water by Means of Transmission Electron Microscopy, Thermogravimetric Analysis, Mass Density, and Small Angle Scattering. *The Journal of Physical Chemistry C* **2010,** *114* (15), 6937-6943.
17. Carotenuto, G. Synthesis and Characterization of Poly(N-vinylpyrrolidone) Filled by Monodispersed Silver Clusters with Controlled Size. *Applied Organometallic Chemistry* **2001,** *15* (5), 344-351.
18. Guo, L.; Nie, J.; Du, B.; Peng, Z.; Tesche, B.; Kleinermanns, K. Thermoresponsive polymer-stabilized silver nanoparticles. *Journal of Colloid and Interface Science* **2008,** *319* (1), 175-181.
19. Brust, M.; Walker, M.; Bethell, D.; Schiffrin, D. J.; Whyman, R. Synthesis of Thiol-Derivatised Gold Nanoparticles in a Two-Phase Liquid-Liquid System. *Journal of the Chemical Society, Chemical Communications* **1994,** (7), 801-802.
20. He, S.; Yao, J.; Jiang, P.; Shi, D.; Zhang, H.; Xie, S.; Pang, S.; Gao, H. Formation of Silver Nanoparticles and Self-Assembled Two-Dimensional Ordered Superlattice. *Langmuir* **2001,** *17* (5), 1571-1575.
21. Johnson, S. R.; Evans, S. D.; Mahon, S. W.; Ulman, A. Alkanethiol Molecules Containing an Aromatic Moiety Self-Assembled onto Gold Clusters. *Langmuir* **1997,** *13* (1), 51-57.
22. Stewart, A.; Zheng, S.; McCourt, M. R.; Bell, S. E. J. Controlling Assembly of Mixed Thiol Monolayers on Silver Nanoparticles to Tune Their Surface Properties. *ACS Nano* **2012,** *6* (5), 3718-3726.
23. Ingram, R. S.; Hostetler, M. J.; Murray, R. W. Poly-hetero-ω-functionalized Alkanethiolate-Stabilized Gold Cluster Compounds. *Journal of the American Chemical Society* **1997,** *119* (39), 9175-9178.
24. Kalfagiannis, N.; Karagiannidis, P. G.; Pitsalidis, C.; Panagiotopoulos, N. T.; Gravalidis, C.; Kassavetis, S.; Patsalas, P.; Logothetidis, S. Plasmonic Silver Nanoparticles for Improved Organic Solar Cells. *Solar Energy Materials and Solar Cells* **2012,** *104* (0), 165-174.
25. Longo, A.; Carotenuto, G.; Palomba, M.; Nicola, S. D. Dependence of Optical and Microstructure Properties of Thiol-Capped Silver Nanoparticles Embedded in Polymeric Matrix. *Polymers* **2011,** *3* (4), 1794-1804.
26. Kang, S. Y.; Kim, K. Comparative Study of Dodecanethiol-Derivatized Silver Nanoparticles Prepared in One-Phase and Two-Phase Systems. *Langmuir* **1998,** *14* (1), 226-230.
27. Goulet, P. J. G.; Lennox, R. B. New Insights into Brust−Schiffrin Metal Nanoparticle Synthesis. *Journal of the American Chemical Society* **2010,** *132* (28), 9582-9584.
28. Sardar, R.; Funston, A. M.; Mulvaney, P.; Murray, R. W. Gold Nanoparticles: Past, Present, and Future†. *Langmuir* **2009,** *25* (24), 13840-13851.
29. Templeton, A. C.; Wuelfing, W. P.; Murray, R. W. Monolayer-Protected Cluster Molecules. *Accounts of Chemical Research* **1999,** *33* (1), 27-36.
30. Li, Y.; Zaluzhna, O.; Xu, B.; Gao, Y.; Modest, J. M.; Tong, Y. J. Mechanistic Insights into the Brust−Schiffrin Two-Phase Synthesis of Organo-chalcogenate-Protected Metal Nanoparticles. *Journal of the American Chemical Society* **2011,** *133* (7), 2092-2095.
31. Farrell, Z.; Shelton, C.; Dunn, C.; Green, D. Straightforward, One-Step Synthesis of Alkanethiol-capped Silver Nanoparticles from an Aggregative Model of Growth. *Langmuir* **2013,** *29* (30), 9291-9300.

32. Polte, J.; Tuaev, X.; Wuithschick, M.; Fischer, A.; Thuenemann, A. F.; Rademann, K.; Kraehnert, R.; Emmerling, F. Formation Mechanism of Colloidal Silver Nanoparticles: Analogies and Differences to the Growth of Gold Nanoparticles. *ACS Nano* **2012,** *6* (7), 5791-5802.
33. Van Hyning, D. L.; Zukoski, C. F. Formation Mechanisms and Aggregation Behavior of Borohydride Reduced Silver Particles. *Langmuir* **1998,** *14* (24), 7034-7046.
34. He, S.; Yao, J.; Xie, S.; Gao, H.; Pang, S. Superlattices of Silver Nanoparticles Passivated by Mercaptan. *Journal of Physics D: Applied Physics* **2001,** *34* (24), 3425.
35. Korgel, B. A.; Fullam, S.; Connolly, S.; Fitzmaurice, D. Assembly and Self-Organization of Silver Nanocrystal Superlattices: Ordered "Soft Spheres". *The Journal of Physical Chemistry B* **1998,** *102* (43), 8379-8388.
36. Badia, A.; Singh, S.; Demers, L.; Cuccia, L.; Brown, G. R.; Lennox, R. B. Self-Assembled Monolayers on Gold Nanoparticles. *Chemistry – A European Journal* **1996,** *2* (3), 359-363.
37. Pawsey, S.; Yach, K.; Halla, J.; Reven, L. Self-Assembled Monolayers of Alkanoic Acids: A Solid-State NMR Study. *Langmuir* **2000,** *16* (7), 3294-3303.
38. Sandhyarani, N.; Pradeep, T. Characteristics of Alkanethiol Self Assembled Monolayers Prepared on Sputtered Gold Films: a Surface Enhanced Raman Spectroscopic Investigation. *Vacuum* **1998,** *49* (4), 279-284.
39. Levin, C. S.; Janesko, B. G.; Bardhan, R.; Scuseria, G. E.; Hartgerink, J. D.; Halas, N. J. Chain-Length-Dependent Vibrational Resonances in Alkanethiol Self-Assembled Monolayers Observed on Plasmonic Nanoparticle Substrates. *Nano Letters* **2006,** *6* (11), 2617-2621.
40. Terrill, R. H.; Postlethwaite, T. A.; Chen, C.-h.; Poon, C.-D.; Terzis, A.; Chen, A.; Hutchison, J. E.; Clark, M. R.; Wignall, G. Monolayers in Three Dimensions: NMR, SAXS, Thermal, and Electron Hopping Studies of Alkanethiol Stabilized Gold Clusters. *Journal of the American Chemical Society* **1995,** *117* (50), 12537-12548.
41. Badia, A.; Demers, L.; Dickinson, L.; Morin, F. G.; Lennox, R. B.; Reven, L. Gold−Sulfur Interactions in Alkylthiol Self-Assembled Monolayers Formed on Gold Nanoparticles Studied by Solid-State NMR. *Journal of the American Chemical Society* **1997,** *119* (45), 11104-11105.
42. Gan, W.; Xu, B.; Dai, H.-L. Activation of Thiols at a Silver Nanoparticle Surface. *Angewandte Chemie International Edition* **2011,** *50* (29), 6622-6625.
43. Bauer, C.; Stellacci, F.; Perry, J. Relationship Between Structure and Solubility of Thiol-Protected Silver Nanoparticles and Assemblies. *Top Catal* **2008,** *47* (1-2), 32-41.
44. Kang, Y.; Taton, T. A. Core/Shell Gold Nanoparticles by Self-Assembly and Crosslinking of Micellar, Block-Copolymer Shells. *Angewandte Chemie* **2005,** *117* (3), 413-416.
45. Andrieux-Ledier, A.; Tremblay, B.; Courty, A. Stability of Self-Ordered Thiol-Coated Silver Nanoparticles: Oxidative Environment Effects. *Langmuir* **2013,** *29* (43), 13140-13145.
46. Cathcart, N.; Mistry, P.; Makra, C.; Pietrobon, B.; Coombs, N.; Jelokhani-Niaraki, M.; Kitaev, V. Chiral Thiol-Stabilized Silver Nanoclusters with Well-Resolved Optical Transitions Synthesized by a Facile Etching Procedure in Aqueous Solutions. *Langmuir* **2009,** *25* (10), 5840-5846.
47. Kassam, A.; Bremner, G.; Clark, B.; Ulibarri, G.; Lennox, R. B. Place Exchange Reactions of Alkyl Thiols on Gold Nanoparticles. *Journal of the American Chemical Society* **2006,** *128* (11), 3476-3477.
48. Caragheorgheopol, A.; Chechik, V. Mechanistic Aspects of Ligand Exchange in Au Nanoparticles. *Physical Chemistry Chemical Physics* **2008,** *10* (33), 5029-5041.
49. Ionita, P.; Gilbert, B. C.; Chechik, V. Radical Mechanism of a Place-Exchange Reaction of Au Nanoparticles. *Angewandte Chemie International Edition* **2005,** *44* (24), 3720-3722.

50. Song, Y.; Huang, T.; Murray, R. W. Heterophase Ligand Exchange and Metal Transfer between Monolayer Protected Clusters. *Journal of the American Chemical Society* **2003,** *125* (38), 11694-11701.
51. Hostetler, M. J.; Templeton, A. C.; Murray, R. W. Dynamics of Place-Exchange Reactions on Monolayer-Protected Gold Cluster Molecules. *Langmuir* **1999,** *15* (11), 3782-3789.
52. Guo, R.; Song, Y.; Wang, G.; Murray, R. W. Does Core Size Matter in the Kinetics of Ligand Exchanges of Monolayer-Protected Au Clusters? *Journal of the American Chemical Society* **2005,** *127* (8), 2752-2757.
53. Kell, A. J.; Donkers, R. L.; Workentin, M. S. Core Size Effects on the Reactivity of Organic Substrates as Monolayers on Gold Nanoparticles. *Langmuir* **2005,** *21* (2), 735-742.
54. Corbierre, M. K.; Cameron, N. S.; Sutton, M.; Laaziri, K.; Lennox, R. B. Gold Nanoparticle/Polymer Nanocomposites: Dispersion of Nanoparticles as a Function of Capping Agent Molecular Weight and Grafting Density. *Langmuir* **2005,** *21* (13), 6063-6072.
55. Silvert, P.-Y.; Herrera-Urbina, R.; Duvauchelle, N.; Vijayakrishnan, V.; Elhsissen, K. T. Preparation of Colloidal Silver Dispersions by the Polyol Process. Part 1 - Synthesis and Characterization. *Journal of Materials Chemistry* **1996,** *6* (4), 573-577.
56. Huang, H. H.; Ni, X. P.; Loy, G. L.; Chew, C. H.; Tan, K. L.; Loh, F. C.; Deng, J. F.; Xu, G. Q. Photochemical Formation of Silver Nanoparticles in Poly(N-vinylpyrrolidone). *Langmuir* **1996,** *12* (4), 909-912.
57. Haryono, A.; Binder, W. H. Controlled Arrangement of Nanoparticle Arrays in Block-Copolymer Domains. *Small* **2006,** *2* (5), 600-611.
58. Balazs, A. C.; Emrick, T.; Russell, T. P. Nanoparticle Polymer Composites: Where Two Small Worlds Meet. *Science* **2006,** *314* (5802), 1107-1110.
59. Shenhar, R.; Norsten, T. B.; Rotello, V. M. Polymer-Mediated Nanoparticle Assembly: Structural Control and Applications. *Advanced Materials* **2005,** *17* (6), 657-669.
60. Willcock, H.; O'Reilly, R. K. End Group Removal and Modification of RAFT Polymers. *Polymer Chemistry* **2010,** *1* (2), 149-157.
61. Shen, W.; Qiu, Q.; Wang, Y.; Miao, M.; Li, B.; Zhang, T.; Cao, A.; An, Z. Hydrazine as a Nucleophile and Antioxidant for Fast Aminolysis of RAFT Polymers in Air. *Macromolecular Rapid Communications* **2010,** *31* (16), 1444-1448.
62. Spruell, J. M.; Levy, B. A.; Sutherland, A.; Dichtel, W. R.; Cheng, J. Y.; Stoddart, J. F.; Nelson, A. Facile Postpolymerization End-Modification of RAFT Polymers. *Journal of Polymer Science Part A: Polymer Chemistry* **2009,** *47* (2), 346-356.
63. Wan, D.; Pu, H.; Yang, G. Highly Efficient Condensation of Hydroxyl-Terminated Polyethylene Oxide with 3-Mercaptopropionic Acid Catalyzed by Hafnium Salt. *Reactive and Functional Polymers* **2008,** *68* (2), 431-435.
64. Nishi, H.; Kobatake, S. Reduction Reaction to Thiol Group of Dithiobenzoate End Group in Polystyrene Polymerized by Reversible Addition–Fragmentation Chain Transfer. *Chemistry Letters* **2008,** *37* (6), 630-631.
65. Kabachii, Y. A.; Kochev, S. Y. Alcoholysis and Aminolysis of Di- and Trithioester Chain-Transfer Agents of Free-Radical Polymerization. *Polym. Sci. Ser. A* **2006,** *48* (7), 717-722.
66. Tsarevsky, N. V.; Matyjaszewski, K. Reversible Redox Cleavage/Coupling of Polystyrene with Disulfide or Thiol Groups Prepared by Atom Transfer Radical Polymerization. *Macromolecules* **2002,** *35* (24), 9009-9014.
67. Lowe, A. B.; Sumerlin, B. S.; Donovan, M. S.; McCormick, C. L. Facile Preparation of Transition Metal Nanoparticles Stabilized by Well-Defined (Co)polymers Synthesized via Aqueous Reversible Addition-Fragmentation Chain Transfer Polymerization†. *Journal of the American Chemical Society* **2002,** *124* (39), 11562-11563.

68. Carrot, G.; Hilborn, J.; Hedrick, J. L.; Trollsås, M. Novel Initiators for Atom Transfer Radical and Ring-Opening Polymerization: A New General Method for the Preparation of Thiol-Functional Polymers. *Macromolecules* **1999,** *32* (15), 5171-5173.
69. Tohyama, M.; Hirao, A.; Nakahama, S.; Takenaka, K. Synthesis of End-Functionalized Polymer by Means of Living Anionic Polymerization, 5. Syntheses of Polystyrenes and Polyisoprenes with Hydroxy and Mercapto end Groups by Reactions of the Living Polymers with Haloalkanes Containing Silyl Ether and Silyl Thioether Functions. *Macromolecular Chemistry and Physics* **1996,** *197* (10), 3135-3148.
70. Bockstaller, M. R.; Mickiewicz, R. A.; Thomas, E. L. Block Copolymer Nanocomposites: Perspectives for Tailored Functional Materials. *Advanced Materials* **2005,** *17* (11), 1331-1349.
71. Darling, S. B. Block copolymers for photovoltaics. *Energy & Environmental Science* **2009,** *2* (12), 1266-1273.
72. Boontongkong, Y.; Cohen, R. E. Cavitated Block Copolymer Micellar Thin Films: Lateral Arrays of Open Nanoreactors. *Macromolecules* **2002,** *35* (9), 3647-3652.
73. Sohn, B.-H.; Seo, B.-W.; Yoo, S.-I. Changes of the Lamellar Period by Nanoparticles in the Nanoreactor Scheme of Thin Films of Symmetric Diblock Copolymers. *Journal of Materials Chemistry* **2002,** *12* (6), 1730-1734.
74. Sohn, B. H.; Seo, B. H. Fabrication of the Multilayered Nanostructure of Alternating Polymers and Gold Nanoparticles with Thin Films of Self-Assembling Diblock Copolymers. *Chemistry of Materials* **2001,** *13* (5), 1752-1757.
75. Nicolay V Tsarevsky, B. S. S. *Fundamentals of Controlled/Living Radical Polymerization*; Royal Society of Chemistry2013. p 364.
76. Matyjaszewski, K. General Concepts and History of Living Radical Polymerization. In *Handbook of Radical Polymerization*; John Wiley & Sons, Inc., 2003, pp 361-406.
77. Gnanou, Y.; Taton, D. Macromolecular Engineering by Controlled/Living Radical Polymerization. In *Handbook of Radical Polymerization*; John Wiley & Sons, Inc., 2003, pp 775-844.
78. Matyjaszewski, K.; Xia, J. Fundamentals of Atom Transfer Radical Polymerization. In *Handbook of Radical Polymerization*; John Wiley & Sons, Inc., 2003, pp 523-628.
79. Hawker, C. J. Nitroxide-Mediated Living Radical Polymerizations. In *Handbook of Radical Polymerization*; John Wiley & Sons, Inc., 2003, pp 463-521.
80. Chiefari, J.; Rizzardo, E. Control of Free-Radical Polymerization by Chain Transfer Methods. In *Handbook of Radical Polymerization*; John Wiley & Sons, Inc., 2003, pp 629-690.
81. Krstina, J.; Moad, G.; Rizzardo, E.; Winzor, C. L.; Berge, C. T.; Fryd, M. Narrow Polydispersity Block Copolymers by Free-Radical Polymerization in the Presence of Macromonomers. *Macromolecules* **1995,** *28* (15), 5381-5385.
82. Zard, S. Z. The Radical Chemistry of Thiocarbonylthio Compounds: An Overview. In *Handbook of RAFT Polymerization*; Wiley-VCH Verlag GmbH & Co. KGaA, 2008, pp 151-187.
83. Mitsukami, Y.; Donovan, M. S.; Lowe, A. B.; McCormick, C. L. Water-Soluble Polymers. 81. Direct Synthesis of Hydrophilic Styrenic-Based Homopolymers and Block Copolymers in Aqueous Solution via RAFT. *Macromolecules* **2001,** *34* (7), 2248-2256.
84. Moad, G.; Barner-Kowollik, C. The Mechanism and Kinetics of the RAFT Process: Overview, Rates, Stabilities, Side Reactions, Product Spectrum and Outstanding Challenges. In *Handbook of RAFT Polymerization*; Wiley-VCH Verlag GmbH & Co. KGaA, 2008, pp 51-104.
85. Fijten, M. W. M.; Meier, M. A. R.; Hoogenboom, R.; Schubert, U. S. Automated Parallel Investigations/Optimizations of the Reversible Addition-Fragmentation Chain Transfer Polymerization of Methyl Methacrylate. *Journal of Polymer Science Part A: Polymer Chemistry* **2004,** *42* (22), 5775-5783.

86. Chong, Y. K.; Le, T. P. T.; Moad, G.; Rizzardo, E.; Thang, S. H. A More Versatile Route to Block Copolymers and Other Polymers of Complex Architecture by Living Radical Polymerization: The RAFT Process. *Macromolecules* **1999,** *32* (6), 2071-2074.
87. Hoogenboom, R.; Schubert, U. S.; Van Camp, W.; Du Prez, F. E. RAFT Polymerization of 1-Ethoxyethyl Acrylate: A Novel Route toward Near-Monodisperse Poly(acrylic acid) and Derived Block Copolymer Structures. *Macromolecules* **2005,** *38* (18), 7653-7659.
88. Davies, M. C.; Dawkins, J. V.; Hourston, D. J. Radical Copolymerization of Maleic Anhydride and Substituted Styrenes by Reversible Addition-fragmentation Chain Transfer (RAFT) polymerization. *Polymer* **2005,** *46* (6), 1739-1753.
89. MARTINEZ, F.; NECULQUEO, G.; TORRES, M.; OLEA, A. Monoestrification of Styrene-Maleic Anhydride Copolymer with Aliphatic Alcohols. *Boletín de la Sociedad Chilena de Química* **2001,** *46*, 137-141.
90. Sun, G.; Cheng, C.; Wooley, K. L. Reversible Addition Fragmentation Chain Transfer Polymerization of 4-Vinylbenzaldehyde. *Macromolecules* **2007,** *40* (4), 793-795.
91. Hwang, J.; Li, R. C.; Maynard, H. D. Well-defined Polymers with Activated Ester and Protected Aldehyde Side Chains for Bio-Functionalization. *Journal of Controlled Release* **2007,** *122* (3), 279-286.
92. Li, X.; Liu, Y.; Xu, Z.; Yan, H. Preparation of Magnetic Microspheres with Thiol-Containing Polymer Brushes and Immobilization of Gold Nanoparticles in the Brush Layer. *European Polymer Journal* **2011,** *47* (10), 1877-1884.
93. Preinerstorfer, B.; Bicker, W.; Lindner, W.; Lämmerhofer, M. Development of Reactive Thiol-Modified Monolithic Capillaries and In-Column Surface Functionalization by Radical Addition of a Chromatographic Ligand for Capillary Electrochromatography. *Journal of Chromatography A* **2004,** *1044* (1–2), 187-199.
94. Wendler, U.; Bohrisch, J.; Jaeger, W.; Rother, G.; Dautzenberg, H. Amphiphilic Cationic Block Copolymers via Controlled Free Radical Polymerization. *Macromolecular Rapid Communications* **1998,** *19* (4), 185-190.
95. Quinn, J. F.; Chaplin, R. P.; Davis, T. P. Facile Synthesis of Comb, Star, and Graft Polymers via Reversible Addition–Fragmentation Chain Transfer (RAFT) Polymerization. *Journal of Polymer Science Part A: Polymer Chemistry* **2002,** *40* (17), 2956-2966.
96. Patra, B. N.; Rayeroux, D.; Lacroix-Desmazes, P. Synthesis of Cationic Amphiphilic Diblock Copolymers of Poly(Vinylbenzyl Triethylammonium Chloride) and Polystyrene by Reverse Iodine Transfer Polymerization (RITP). *Reactive and Functional Polymers* **2010,** *70* (7), 408-413.
97. Jiang, X.; Du, X.; Zhang, L.; Cheng, Z. A Bifunctional Diblock Copolymer from Consecutive RAFT Polymerizations and its Functionalization. *Macromolecular Chemistry and Physics* **2013,** *214* (6), 654-663.
98. Park, S.-G.; Kwak, N.-S.; Hwang, C. W.; Park, H.-M.; Hwang, T. S. Synthesis and Characteristics of Aminated Vinylbenzyl Chloride-co-Styrene-co-Hydroxyethyl Acrylate Anion-Exchange Membrane for Redox Flow Battery Applications. *Journal of Membrane Science* **2012,** *423–424* (0), 429-437.
99. Sun Koo, J.; Kwak, N.-S.; Hwang, T. S. Synthesis and Properties of an Anion-Exchange Membrane Based on Vinylbenzyl Chloride–Styrene–Ethyl Methacrylate Copolymers. *Journal of Membrane Science* **2012,** *423–424* (0), 293-301.
100. Xu, H.; Fang, J.; Guo, M.; Lu, X.; Wei, X.; Tu, S. Novel Anion Exchange Membrane Based on Copolymer of Methyl Methacrylate, Vinylbenzyl Chloride and Ethyl acrylate for Alkaline Fuel Cells. *Journal of Membrane Science* **2010,** *354* (1–2), 206-211.

101. Luo, Y.; Guo, J.; Wang, C.; Chu, D. Quaternized Poly(Methyl Methacrylate-co-Butyl Acrylate-co-Vinylbenzyl Chloride) Membrane for Alkaline Fuel Cells. *Journal of Power Sources* **2010,** *195* (12), 3765-3771.
102. Krajnc, P.; Brown, J. F.; Cameron, N. R. Monolithic Scavenger Resins by Amine Functionalizations of Poly(4-vinylbenzyl chloride-co-divinylbenzene) PolyHIPE Materials. *Organic Letters* **2002,** *4* (15), 2497-2500.
103. Staff, R. H.; Willersinn, J.; Musyanovych, A.; Landfester, K.; Crespy, D. Janus Nanoparticles with both Faces Selectively Functionalized for Click Chemistry. *Polymer Chemistry* **2014,** *5* (13), 4097-4104.
104. Karabacak, R. B.; Tay, T.; Kıvanç, M. Preparation of Novel Antimicrobial Polymer Colloids Based on (+)-Usnic Acid and Poly(vinylbenzyl chloride). *Reactive and Functional Polymers* **2014,** *83* (0), 7-13.
105. MonthÉArd, J. P.; Jegat, C.; Camps, M. Vinylbenzylchloride (Chloromethylstyrene), Polymers, and Copolymers. Recent Reactions and Applications. *Journal of Macromolecular Science, Part C* **1999,** *39* (1), 135-174.
106. Tseng, C.-R.; Wu, J.-Y.; Lee, H.-Y.; Chang, F.-C. Preparation and Characterization of Polystyrene–Clay Nanocomposites by Free-Radical Polymerization. *Journal of Applied Polymer Science* **2002,** *85* (7), 1370-1377.
107. Strube, O. I.; Schmidt-Naake, G. Synthesis of Reactive Triblock Copolymers via Reversible Addition-Fragmentation Chain Transfer (RAFT) Polymerization. *Macromolecular Symposia* **2009,** *275–276* (1), 13-23.
108. Couture, G.; Améduri, B. Kinetics of RAFT Homopolymerisation of Vinylbenzyl Chloride in the Presence of Xanthate or Trithiocarbonate. *European Polymer Journal* **2012,** *48* (7), 1348-1356.
109. Fei, G.; Shin, J.; Kang, S.-A.; Ko, B.-S.; Kang, P.-H.; Lee, Y.-S.; Nho, Y. C. Preparation and Characterization of a Poly(vinylbenzyl sulfonic acid)-Grafted FEP Membrane. *Journal of Polymer Science Part A: Polymer Chemistry* **2010,** *48* (3), 563-569.
110. Saha, K.; Agasti, S. S.; Kim, C.; Li, X.; Rotello, V. M. Gold Nanoparticles in Chemical and Biological Sensing. *Chemical Reviews* **2012,** *112* (5), 2739-2779.
111. Elghanian, R.; Storhoff, J. J.; Mucic, R. C.; Letsinger, R. L.; Mirkin, C. A. Selective Colorimetric Detection of Polynucleotides Based on the Distance-Dependent Optical Properties of Gold Nanoparticles. *Science* **1997,** *277* (5329), 1078-1081.
112. Ghosh, P.; Han, G.; De, M.; Kim, C. K.; Rotello, V. M. Gold Nanoparticles in Delivery Applications. *Advanced Drug Delivery Reviews* **2008,** *60* (11), 1307-1315.
113. Naoi, K.; Ohko, Y.; Tatsuma, T. TiO2 Films Loaded with Silver Nanoparticles: Control of Multicolor Photochromic Behavior. *Journal of the American Chemical Society* **2004,** *126* (11), 3664-3668.
114. Hideyuki, I.; Koichiro, T.; Ichiro, T.; Toshiaki, H.; Hiroki, N. Ultrafast Optical Switching in a Silver Nanoparticle System. *Japanese Journal of Applied Physics* **2000,** *39* (9R), 5132.
115. Quinten, M.; Leitner, A.; Krenn, J. R.; Aussenegg, F. R. Electromagnetic Energy Transport via Linear Chains of Silver Nanoparticles. *Opt. Lett.* **1998,** *23* (17), 1331-1333.
116. Tseng, R. J.; Huang, J.; Ouyang, J.; Kaner, R. B.; Yang. Polyaniline Nanofiber/Gold Nanoparticle Nonvolatile Memory. *Nano Letters* **2005,** *5* (6), 1077-1080.
117. Gehan, H.; Mangeney, C.; Aubard, J.; Lévi, G.; Hohenau, A.; Krenn, J. R.; Lacaze, E.; Félidj, N. Design and Optical Properties of Active Polymer-Coated Plasmonic Nanostructures. *The Journal of Physical Chemistry Letters* **2011,** *2* (8), 926-931.
118. Levitt, M. H. *Spin Dynamics: Basics of Nuclear Magnetic Resonance, 2nd Edition*; John Wiley & Sons2007.

119. Schmidt-Rohr, K.; Spiess, H. S. *Multidimensional Solid-state NMR and Polymers*; Academic Press: London, 1994.
120. James Keeler; *Understanding NMR Spectroscopy*, John Wiley & Sons2010.
121. Cavanagh, J.; Fairbrother, W. J.; Palmer Iii, A. G.; Rance, M.; Skelton, N. J. Chapter 4 - Multidimensional NMR spectroscopy. In *Protein NMR Spectroscopy (Second Edition)*, Cavanagh, J.; Fairbrother, W. J.; Palmer, A. G.; Rance, M.; Skelton, N. J., Eds.; Academic Press: Burlington, 2007, pp 271-332.
122. Duer, M. J. *Solid-State NMR Spectroscopy Principles and Applications*; Blackwell Science Ltd2005.
123. Kowalewski, J.; Mäler, L. *Nuclear Spin Relaxation in Liquids: Theory, Experiments, and Applications* 2006; Vol. Taylor & Francis Group, LLC.
124. Sperling, L. H. *Introduction to Physical Polymer Science, 4th Edition*; Wiley2005. p 880.
125. Faghihi, F.; Hazendonk, P.; Montina, T. Investigation into the Mechanism and Microstructure of Reaction Intermediates in the Two-Phase Synthesis of Alkanethiol-Capped Silver Nanoparticles. *Langmuir* **2015,** *31* (11), 3473-3481.
126. Bensebaa, F.; Ellis, T. H.; Kruus, E.; Voicu, R.; Zhou, Y. Characterization of Self-Assembled Bilayers: Silver−Alkanethiolates. *Langmuir* **1998,** *14* (22), 6579-6587.
127. Cha, S.-H.; Kim, J.-U.; Kim, K.-H.; Lee, J.-C. Preparation and Photoluminescent Properties of Gold(I)−Alkanethiolate Complexes Having Highly Ordered Supramolecular Structures. *Chemistry of Materials* **2007,** *19* (25), 6297-6303.
128. Bryant, M. A.; Pemberton, J. E. Surface Raman Scattering of Self-Assembled Monolayers Formed from 1-Alkanethiols: Behavior of Films at Gold and Comparison to Films at Silver. *Journal of the American Chemical Society* **1991,** *113* (22), 8284-8293.
129. Hammann, P. E.; Habermehl, G. G.; Kluge, H. γgauche Effects in the ^{1}H and ^{13}C NMR Spectra of Steroids. *Magnetic Resonance in Chemistry* **1988,** *26* (1), 85-88.
130. Subbotin, O. A.; Sergeev, N. M. Pulsed carbon-13 Fourier Transform Nuclear Magnetic Resonance Spectra of Monohalo-Substituted Cyclohexanes at Low Temperatures. *Journal of the American Chemical Society* **1975,** *97* (5), 1080-1084.
131. Cheney, B. V.; Grant, D. M. Carbon-13 Magnetic Resonance. VIII. Theory of Carbon-13 Chemical Shifts Applied to Saturated Hydrocarbons. *Journal of the American Chemical Society* **1967,** *89* (21), 5319-5327.
132. Pajak, Z.; Szafrańska, B. Plastic Phase in Tetrabutylammonium Bromide. *physica status solidi (a)* **1993,** *136* (2), 371-377.
133. Texter, J. Stability Constants for Aqueous Silver/Bromide/Thiocyanate Complexes. *Analytica Chimica Acta* **1988,** *215* (0), 187-201.
134. Neugebauer, D.; Bury, K.; Wlazło, M. Atom Transfer Radical Copolymerization of Glycidyl Methacrylate and Methyl Methacrylate. *Journal of Applied Polymer Science* **2012,** *124* (3), 2209-2215.
135. Jermakowicz-Bartkowiak, D.; Kolarz, B. N. Gold Sorption on Weak Base Anion Exchangers with Aminoguanidyl Groups. *European Polymer Journal* **2002,** *38* (11), 2239-2246.
136. Luo, Y.; Guo, J.; Liu, Y.; Shao, Q.; Wang, C.; Chu, D. Copolymerization of Methyl Methacrylate and Vinylbenzyl Chloride towards Alkaline Anion Exchange Membrane for Fuel Cell Applications. *Journal of Membrane Science* **2012,** *423–424* (0), 209-214.
137. Mascagna, D.; d'Ischia, M.; Costantini, C.; Prota, G. A Convenient Access to Dihydroxybenzenethiols via Reduction of Iso-Thiouronium Salts with Sodium Borohydride. *Synthetic Communications* **1994,** *24* (1), 35-42.

138. Sahu, J. N.; Mahalik, K.; Patwardhan, A. V.; Meikap, B. C. Equilibrium and Kinetic Studies on the Hydrolysis of Urea for Ammonia Generation in a Semibatch Reactor. *Industrial & Engineering Chemistry Research* **2008,** *47* (14), 4689-4696.
139. Evanoff, D. D.; Chumanov, G. Size-Controlled Synthesis of Nanoparticles. 1. "Silver-Only" Aqueous Suspensions via Hydrogen Reduction. *The Journal of Physical Chemistry B* **2004,** *108* (37), 13948-13956.
140. Jelić, D.; Penavin-Škundrić, J.; Majstorović, D.; Mentus, S. The Thermogravimetric Study of Silver(I) Oxide Reduction by Hydrogen. *Thermochimica Acta* **2011,** *526* (1–2), 252-256.

Appendix

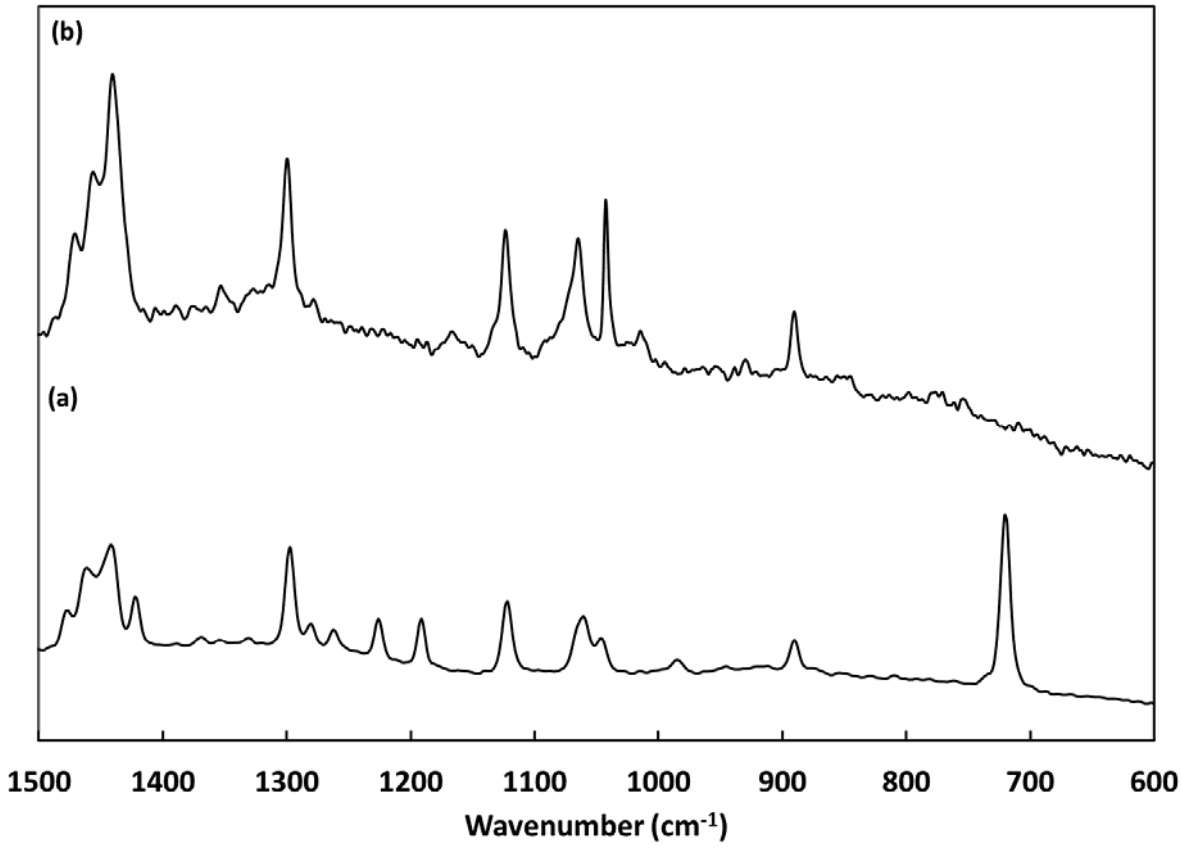

Figure A.1. Raman spectra of (a) ATNT-24 and (b) AgNT.

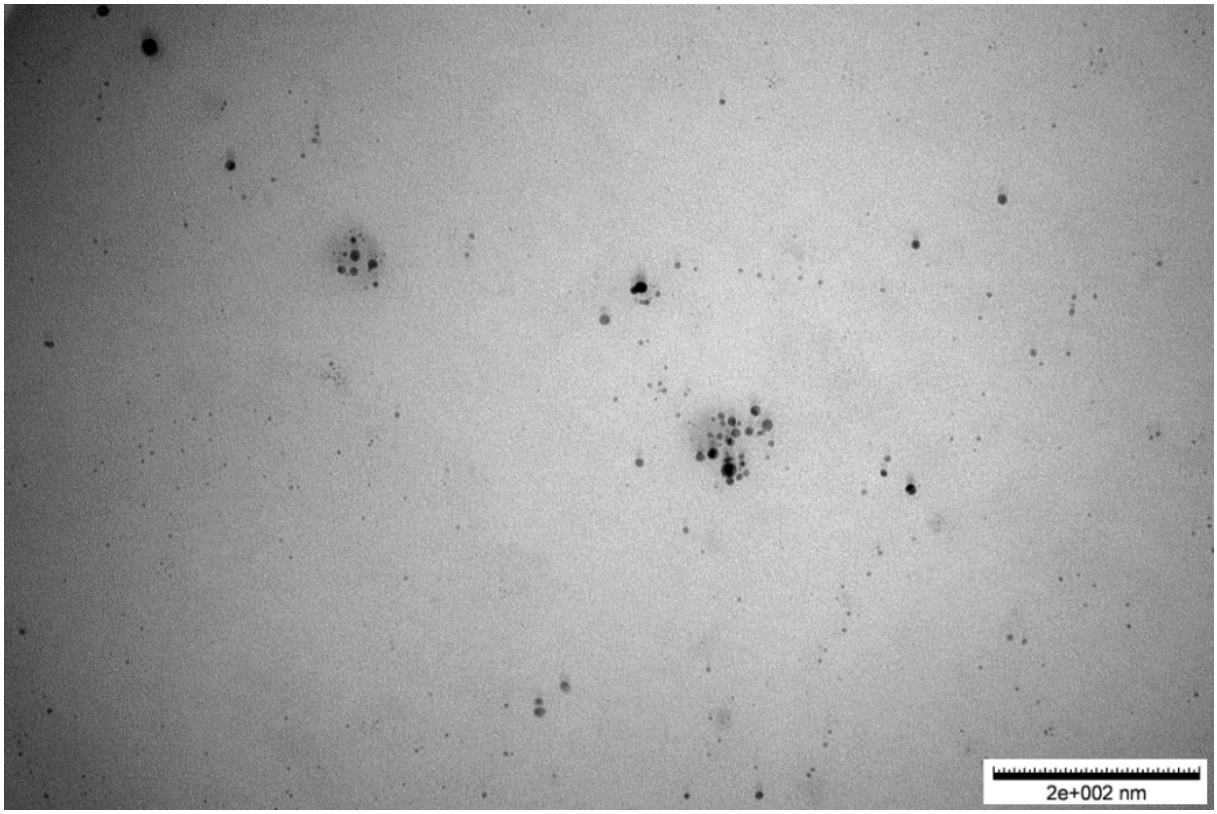

Figure A.2. TEM micrograph of TOAB-capped silver nanoparticles stored four 4 days.

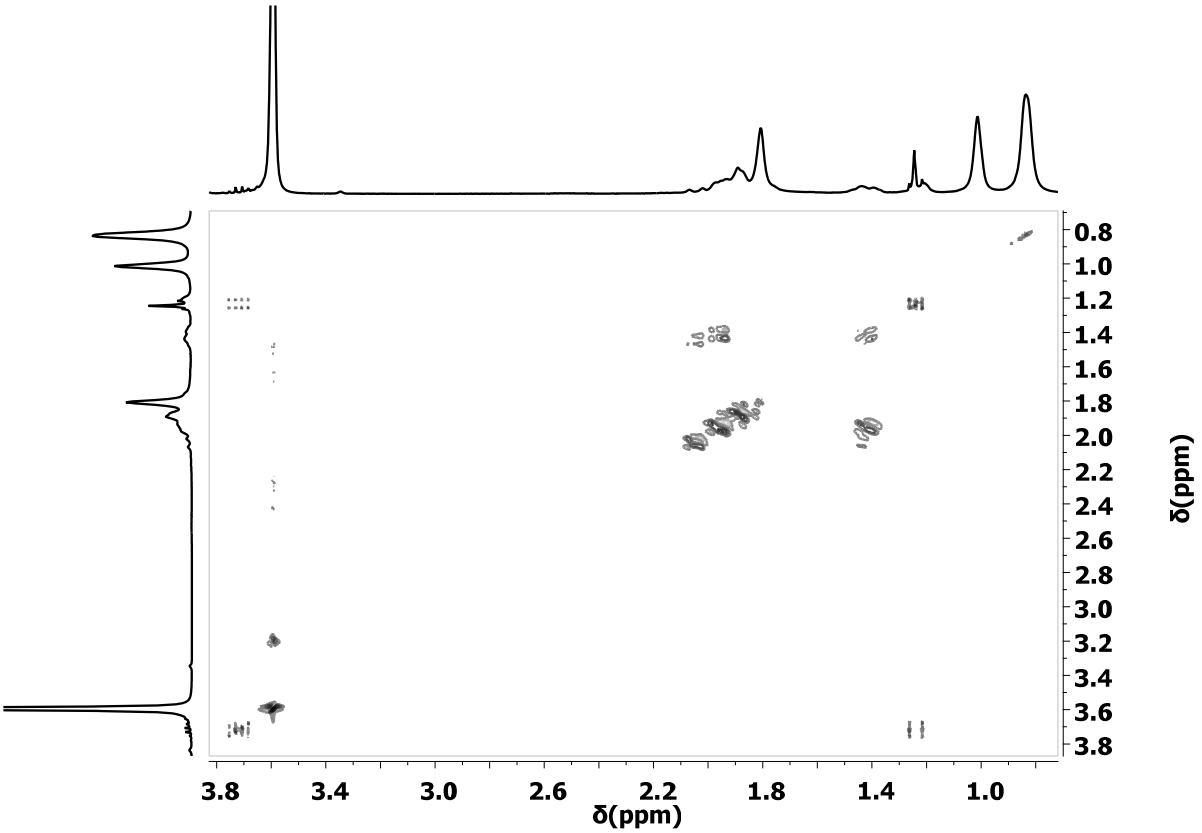

Figure A.3. 2D ^{1}H COSY spectrum of RAFT polymerized PMMA (CTA/I=10) in chloroform-d.

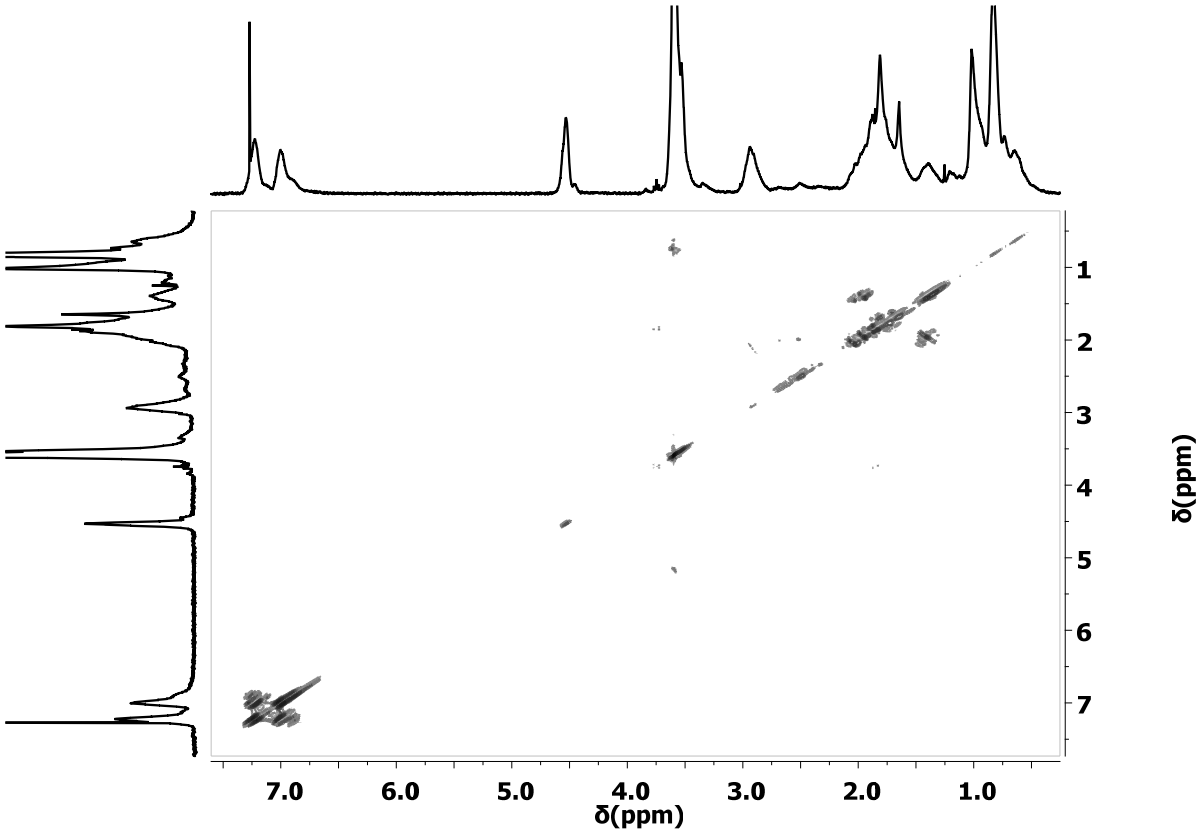

Figure A.4. 2D ^{1}H COSY spectrum of MV15 prepared by free radical polymerization in chloroform-d.

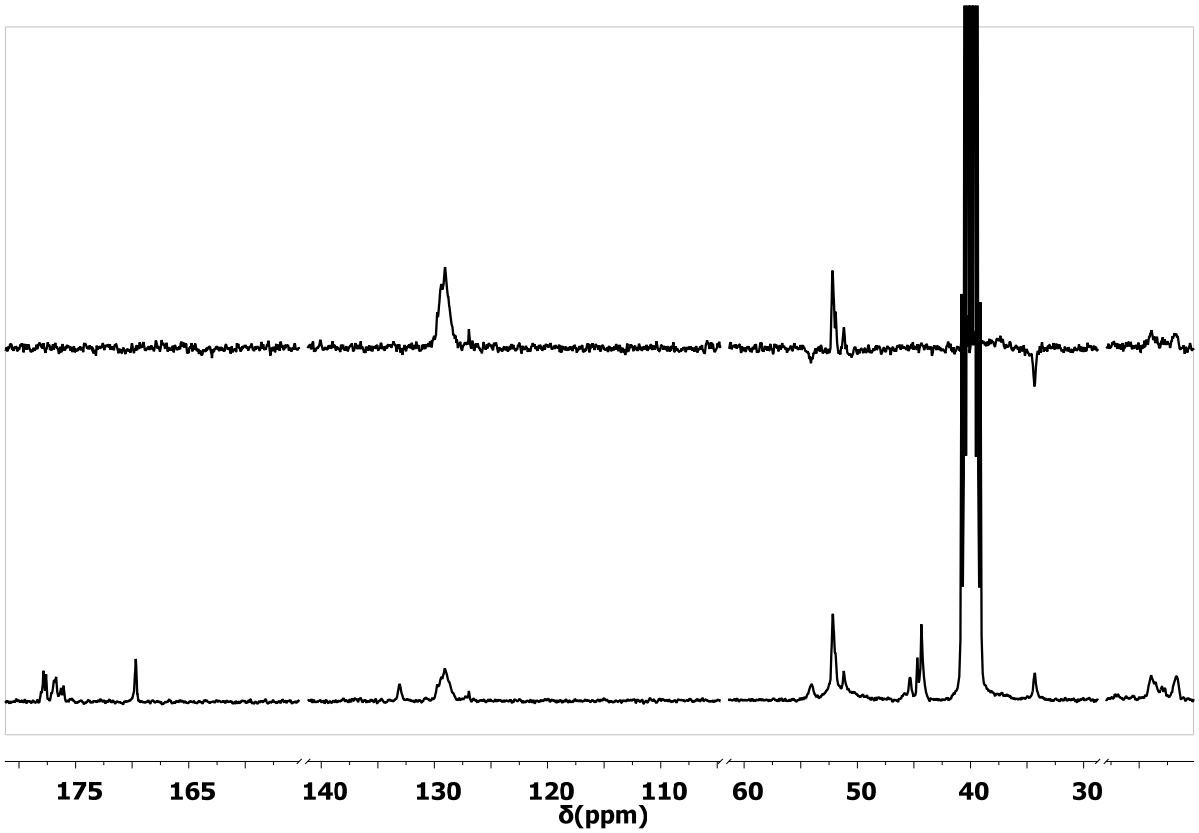

Figure A.5. ^{13}C (bottom) and DEPT135 (top) NMR spectra of MV15-TU in DMSO-d_6.

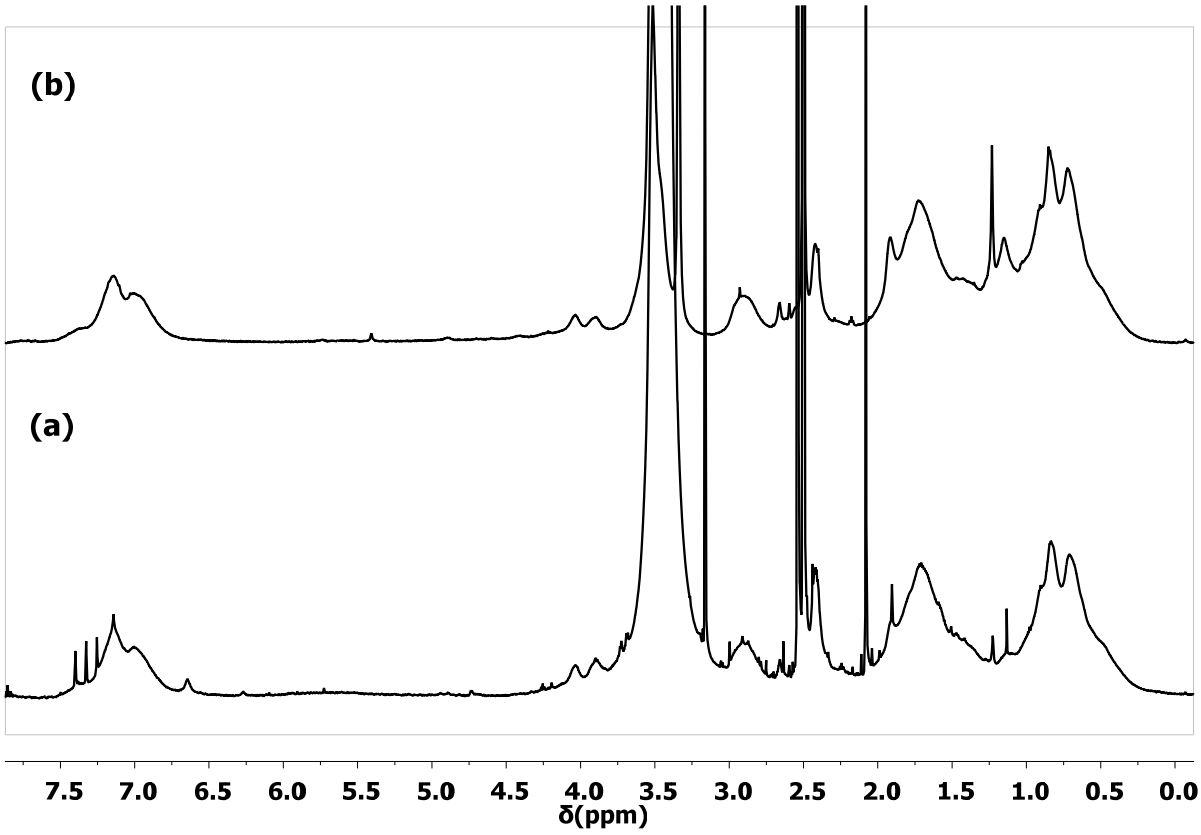

Figure A.6. ^{1}H NMR spectra of hydrolyzed MV15-TU in DMSO-d6 before (a) and after (b) work-up.

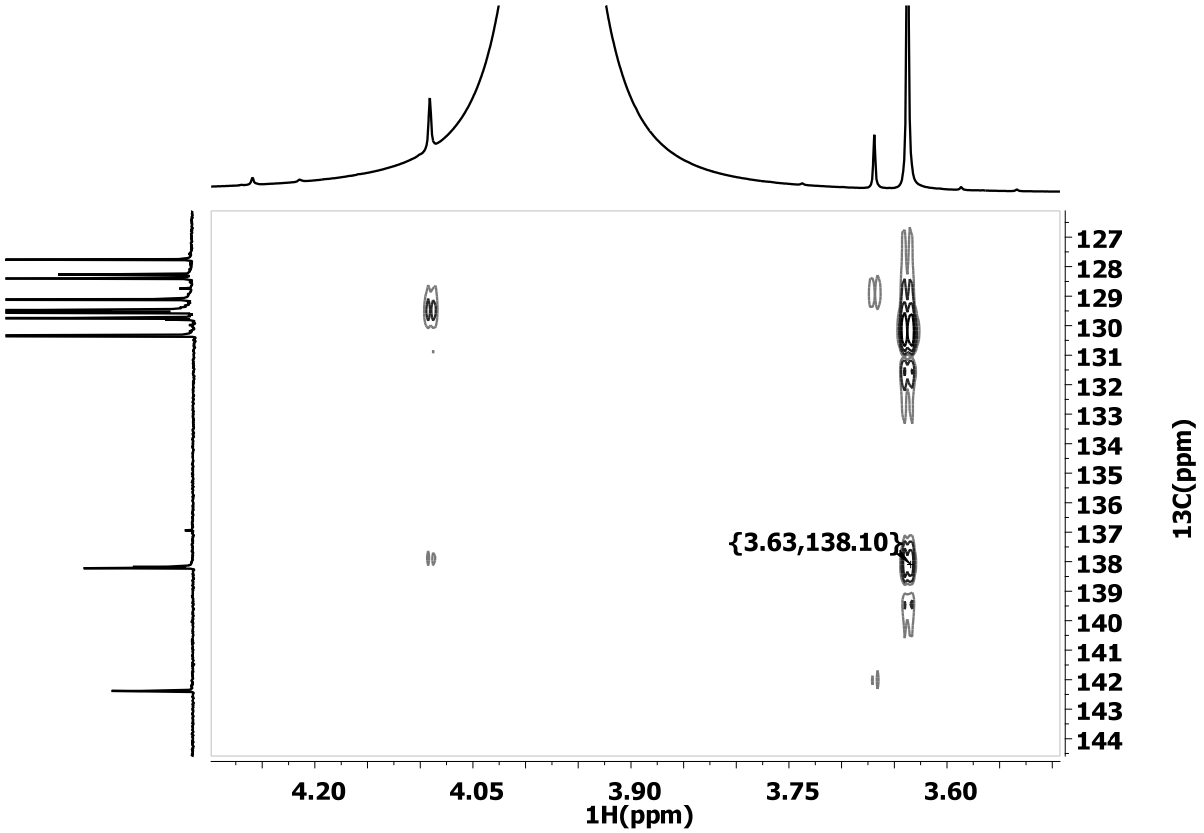

Figure A.7. 2D NMR HMBC spectrum of BCTU/$NaBH_4$ reaction mixture acquired at T=22 °C in DMSO-d_6.

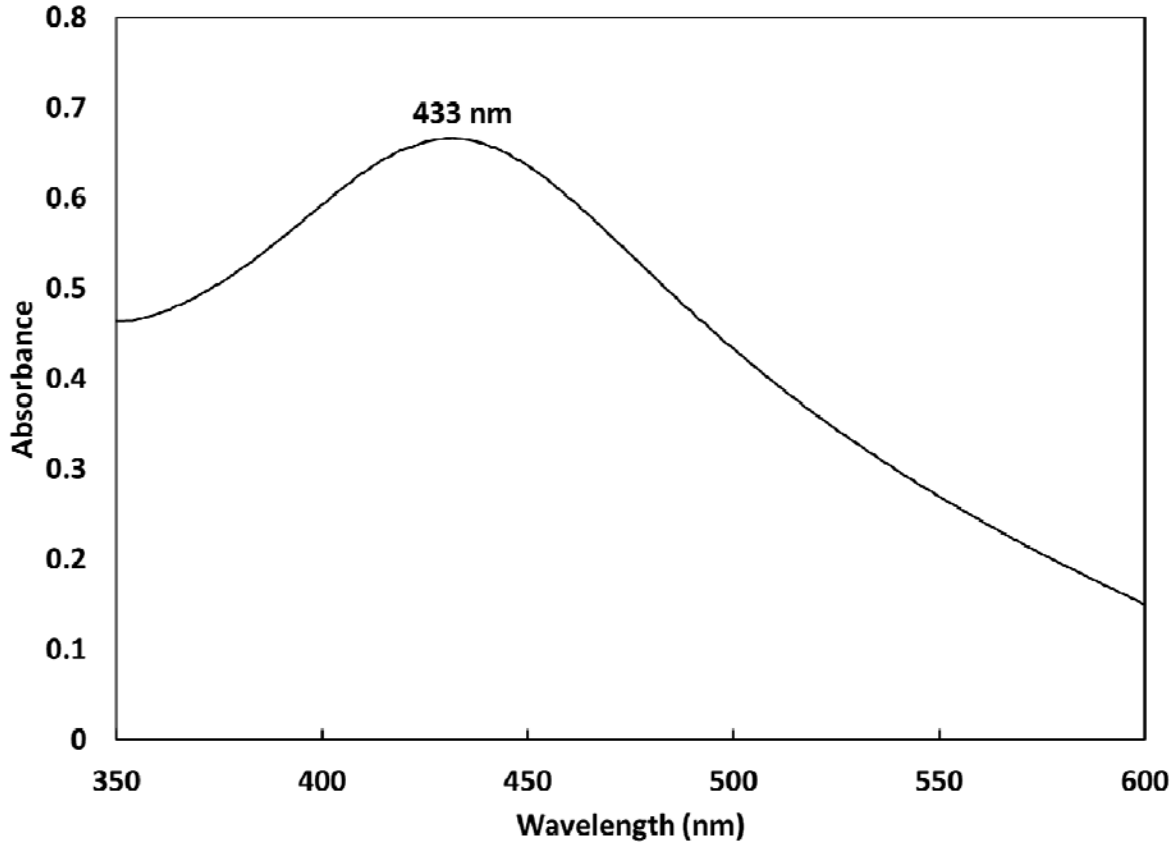

Figure A.8. UV-visible spectrum of the MV15-SNP solution stored under ambient condition for nine weeks. The nanoparticles were synthesized with 90 min pretreatment time and two-step addition of $NaBH_4$.